STUDY ON MICRO SPACE PROPULSION
マイクロ宇宙推進機に関する研究

A doctoral dissertation
submitted in partial fulfillment of the requirements
for the degree of Doctor of Engineering

Department of Aeronautics and Astronautics
University of Tokyo

By
Hiroyuki Koizumi
July 2006

Abstract

In recent years, as microspacecraft has increasingly attracted the interest by government agencies, industries and universities, the requirement for micropropulsion has been enlarged. In this dissertation, two micropropulsions are proposed and developed for 1-100 kg microspacecraft and the fundamental characteristics are revealed. In extremely small spacecraft, less than 10 kg, the weight, size and power allowed for propulsion are strictly limited, less than a few 100 g and 1 W. There the best suited is a diode laser microthruster with dual propulsive mode, laser ablation mode and laser ignition mode. That thruster has the ability controlling lower thrust of micro-Newton and providing higher thrust of milli-Newton with compact size and low power. In this study, fundamental characteristics of the newly proposed laser microthruster are investigated. As a result, it is verified that the laser ablation mode can control 1-30 μN thrust and the laser ignition mode can generate 10 to 500 mN thrust. In a little larger microspacecraft, less than 100 kg, the limitations for the size and power are a little relaxed, and more challenging and advanced missions are enabled. They requires higher delta-v for micropropulsion, and miniaturized electric propulsion is needed. In the electric propulsions, a pulsed plasma thruster is the most attractive due to its low power, compact size, and digital impulse. Here, a pulsed plasma thruster using water propellant is proposed and investigated for the adequate micropropulsion, That thruster can accomplish high performance and contamination free. In this study, the cause of the major problem on that thruster, low thrust power ratio, is clarified and the improvement methods are proposed, which increased the performance at most 30 %. In addition to these two thrusters, a thrust stand to measure micro-Newton thrust is developed. Thrust measurement is inevitable for the study on micropropulsion. It measures the thrust with the resolution less than 1.0 μNs and the uncertainty within 2 %.

Contents

List of Tables

List of Figures

Chapter 1

Introduction

1.1 Microspacecraft

Microspacecraft have increasingly attracted the interest of researchers in recent years[1]. Here *microspacecraft* mean miniaturized spacecraft down to less than 100 kg. In the early days of space exploration, the spacecraft were very light, Sputnik weighed a little over 83 kg. It was because of the restrictions by a launcher. Subsequent tremendous growth of technologies on aeronautics and astronautics made it possible to increase the mass and size of spacecraft to acquire higher functions, and the development had been directed toward highly functional, larger spacecraft. However, these days the direction has started toward the miniaturization.

The miniaturization of spacecraft is motivated by the need to reduce in the cost of developing and launching spacecraft. Up to date, space exploration had been mainly conducted by government agencies in the world. Enormous cost associated with the space exploration had prevented industry from the development, whereas the importantness of the space is increasingly recognized. The expensiveness is caused by developing and launching spacecraft. Spacecraft are constructed using specially made components with extremely high reliability and durability. The miniaturization will reduce the cost and also reduce the developing cycle, which accelerates the growth of space development. Moreover, the most saving by the microspacecraft will be the launch cost due to the mass and size reduction. For instance, piggyback launch dramatically decreases the hurdle to launch spacecraft for university and industry. Indeed, several universities have succeeded to launch

their microspacecraft in a last decade [2, 3, 4, 5].

The miniaturization improves in the mission capability, flexibility, and redundancy using microspacecraft constellations. Partitioning the functions of a single, large, highly functional spacecraft into a number of smaller spacecraft has a lot of potentials. Cluster of spacecraft cooperatively conduct missions with orbiting in close each other. Changing the role of each spacecraft according to the situation increases the probability of success for the mission. A trouble on one spacecraft would not affect the other spacecraft and that role is covered by the others. The increasing redundancy also enables to construct spacecraft using ordinary available components, which causes the reducing cost again. Moreover such cluster or platoon of microspacecraft enables advanced missions that otherwise could not be performed. Several studies using the formation flying are studied [6, 7, 8, 9]. Terrestrial Planet Finder (TPF) [10] by National Aeronautics and Space Administration (NASA) and Darwin[11] by European Space Agency (ESA) are missions to search Earth-like planets outside the solar system. They use multiple spacecraft with telescopes as a large telescope with a diameter of several 100 meters using interferometric imaging, which provide high sensitivity and resolution. Laser Interferometery Space Antenna (LISA) [12] (joint mission by NASA and ESA) is a space-based gravitational wave observatory using laser interferometry with large distance. Although such advanced missions are not to use microspacecraft (they are over 100 kg), the technologies can be applied to microspacecraft and increase the variety of microspacecraft missions.

In addition to the formation flying, microspacecraft is expected to perform health management of the mother spacecraft or to probe planets and asteroid in deep space exploration. Microspacecraft could not have the capability to orbit far away from the earth by themselves. However they can be carried on a large spacecraft because of their small size, and deorbited in deep space to conduct such various missions.

1.2 Micropropulsion

1.2.1 Role of micropropulsion

A key element for microspacecraft operations is a practical micropropulsion system. These days microspacecraft have been studied, developed, and launched by government agency, industry, and universities. However, their missions remain in the state of the demonstration for microspacecraft. Strictly limited weight and size for the microspacecraft leads to various constrictions for spacecraft hardware. Especially the lack of propulsion systems reduces the variety of missions. Attitude control of spacecraft is attainable by passive systems such as momentum wheels and magnetic torqueres. Actually, state-of-the-art microspacecraft perform their attitude control using such systems as minimum as possible (whereas unloading of the momentum wheel requires propulsion). In contrast, translation motion of the spacecraft inevitably requires propulsive capability. Advantages of microspacecraft will be developed conducting cooperrative works by the constellation or orbiting by themselves, which essentially need translation motion. Therefore in order to enable advanced microspacecraft missions, a small propulsion system suitable for microspacecraft, namely a microthruster, is needed.

Microspacecraft dealt in this study have the weight ranging from 1 to 100 kg. That class spacecraft is categorized into class I/II microspacecraft by NASA and Micro/Nano spacecraft by AFRL. The corresponding spacecraft's dimension and power are 0.1 to 1 m and 1 to 100 W. State-of-the-art propulsion hardware can be applicable to more than 100 kg spacecraft in most cases. Hence, newly developed technology is required to accomplish such small miniaturized spacecraft.

1.2.2 Problems to the miniaturization

Micropropulsion systems must be designed to overcome a number of challenges associated with the miniaturization. The difficulties of micropropulsion system are manufacturing and integrating complexity, degenerating efficiency according to the scaling low, propellant leakage and clogging, contamination problems from the plume, and limited power for electric propulsions. Which factor affects most

depends on the variety of the thruster. The manufacturing and integrating complexity is included in all thrusters. The complexity mainly comes from the propellant feeding system, pressurizing or mixing the propellant, and plasma confinement. Some researchers expect MEMS as a key technology to solve those problems. However, state-of-the-art MEMS technology has not reached to the level for practical applications. Decreasing the scale leads to several inefficiency because of increased boundary layer, heating loss, and plasma loss. Concerns of the propellant leakage and clogging are associated with microspacecraft unless using solid phase propellant. With the scaling down, leakage rate of the propellant will remain in the same level, or may be worse. Hence the percentage of the leakage in the total propellant mass becomes larger with decreasing the size. Also miniaturization will increase the probability of clogging, which often becomes a cause of the failure of propulsion system. Contamination becomes concern for spacecraft system, degenerating the solar cell, as well as usual spacecraft. The miniaturization consequently leads to less power, and it increases the difficulty using electric propulsion. A lot of electric propulsion work most effectively using power more than a few 100 W.

1.2.3 Required propulsive capabilities

Requirements for thrust level

The propulsive capabilities required for micropropulsion will be widely varied according to the mission and size of the spacecraft. The requirement is roughly said as the lower range thrust and the higher range thrust. In the case of attitude control, lower thrust is required for precise positioning and higher thrust is for slew maneuvers. In the case of formation flying, they need lower thrust for the constellation controls and higher thrust for the re-arrangement of their formation patterns. Tables 1.1 and 1.2 summarize representative thrusts required for the attitude control and translation motion of microspacecraft. Those thrusts (impulses) were evaluated assuming several dead bands and time interval between thrust firings, where dead band is angle or distance by which spacecraft moves during the time interval, namely resolutions for spacecraft control. In the case of the evaluation of attitude control, cubical spacecraft shape was assumed, and the typical dimension and impulse were calculated based on the spacecraft mass. It should

Table 1.1: Representative thrust requirement for attitude control.

Dead band angle (deg):		0.1	0.1	180	180
time interval (s):		20	100	60	300
Microspacecraft					
Mass (kg)	Dimension* (m)	Lower impulse (μNs)		Higher impulse (mNs)	
1	0.10	2.9	0.58	1.8	0.35
10	0.22	64	13	38	7.7
50	0.37	540	110	320	65

* Assume cubical spacecraft shape

Table 1.2: Representative thrust requirement for translation motion.

Dead band distance (m):		1.0×10^{-4}	1.0×10^{-4}	1.0	1.0
time interval (s):		20	100	60	300
Microspacecraft					
Mass (kg)	Dimension* (m)	Lower impulse (μNs)		Higher impulse (mNs)	
1	0.10	5.0	1.0	17	3.3
10	0.22	50	10	170	33
50	0.37	250	50	830	170

* Assume cubical spacecraft shape

be noted that the minimum impulse requirement is very small, micro-Newton second range. In the case of 10 kg spacecraft, the required minimum impulse is at most 12 μNs to maintain the attitude of spacecraft withing 0.1 deg during 100s and at most 10 μNs to maintain the separation distance between spacecraft with the deviation within 0.1 mm during 100 s. Actually more precise positioning control is necessary to spacecraft constellations for interferometry missions, aiming to detect gravity waves or search for planets around distant solar systems. For instance, above mentioned LISA mission must maintain the precise constellation against solar disturbance torques. It requires thrust levels of 2 - 20 μN to be controllable within 0.1 μN. On the other hand, the maximum impulse is more than

mili-Newton second range. In the case of 10 kg spacecraft, the required impulse is 38 mNs to rotate the spacecraft in the opposite direction in 1 min and 170 mNs to translate the spacecraft with the velocity of 1 m/min. Such huge impulse would not be accomplished without certain micro-chemical propulsion.

The most important for state-of-the-art microspacecraft is the further miniaturization to expand the varieties of missions. Therefore, the requirement for micropropulsion is in first the ability to be installed on such microspacecraft rather than their performance. Additionally their missions are like demonstrations and the life times are relatively shorter than commercially available spacecraft. Therefore large delta-v is not required. However, in the next stage, highly functional microspacecraft would be required, and long mission time, hence large delta-V, will be necessary. In such advanced long-term missions, micropropulsion with high specific impulse becomes very attractive. The propellant tank must be eventually miniaturized, because of the high percentage of spacecraft mass and volume. Moreover, future challenging missions would require microspacecraft proceed in deep space by themselves using primary micropropulsion system. Small-body rendezvous and outer planet orbiters have substantially higher delta-v requirements. In those large delta-V missions, micro-electric propulsion system become necessary.

Micropropulsion is used for not only microspacecraft but also large spacecraft to control and restrain the deformation of the huge structure. In the stream of increasing the size and function of spacecraft, spacecraft have increasingly required larger power, which is accomplished enormous solar cell. Such enormous solar cell will be expanded in the space and the deformation should be prevented. Several micropropulsion system would be suitable to help expanding the cell and keep the formation due to their compactness.

Requirements for delta-V

Next, propulsive capability for microspacecraft is discussed in terms of delta-V. It is strongly related to the life time of spacecraft and specific impulse of the propulsion system. The requirement will be widely changed according to the mission as well as the thrust requirement. Here, only a few representative missions are considered as the examples for 5 kg and 50 kg microspacecraft missions.

In the case of 5 kg microspacecraft, the mission life time will be short. Actually, in the current stage of this class microspacecraft, most of the missions are like demonstrations (not long life time). Even in the future where several practical missions are conducted, the life time of the such microspacecraft will be limited in short time (at most one year) because of the extremely limited spacecraft functions. As examples of their missions, two kinds of demonstrative missions are considered, which are shown in Fig. 1.1 [13]. One is an example of formation flying, where two spacecraft fly together on slight different orbits. In order to keep the fixed relative position, the compensation using thrusters are necessary. In the case of, the distance of both spacecraft is 3 m and the orbit altitude is 800 km, the required thrust is 50 μN and one round flying requires the delta-V of 1.5 m/s. The other is orbiting around a mother spacecraft, which is simulation for health management of other spacecraft or exploring planets and asteroid deorbited from mother spacecraft. It should be conducted in a limited time, for instance linkage time to the base station on the ground. Figure 1.1 shows the square orbit. In the case of side length of 6 m and limited time of 5 minutes, the required impulse is 31 Ns and the delta-V is 6.3 m/s for 30 rounds.

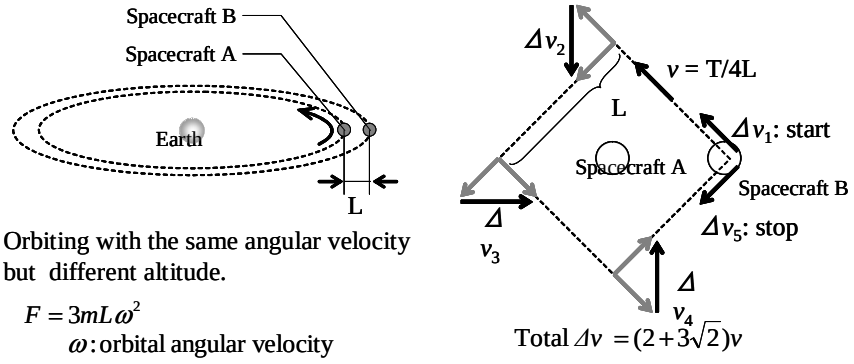

Figure 1.1: Example missions for 5 kg microspacecraft; a) Formation flying keeping a distance on slight different orbits (L m) and b) Orbiting around a mother ship drawing a square orbit.

In 5 kg microspacecraft ($\sim$ 20 cm cubic size), the size allowed for propulsion system would be typically within 250 cm^3 and 0.5 kg. Additionally, the most of fractions would be dominated by not propellant but other bus systems (controlling systems). As a result, the useful propellant mass would be less than 100g. For

instance, in the case of a cold gas thruster with xenon gas, 100 cm^3 would be used for high pressure (100 atm) gas tank and the propellant mass would be about 40 g. The other space must be used for pressure regulator, valves, nozzle, and so on. In the case of a laser ignition thruster, which is addressed in this study (see Chapter 3), five solid propellant cartridges would be allowed and the mass of solid propellant is also 40 g. The other space must be used for laser diode driver and propellant feeding system.

Figure 1.2 shows the relation of specific impulse and acquired delta-V for 5 kg spacecraft. Within the limit of propellant mass (20, 40, 100 g cases are shown in the figure), at least Isp of 50 s is necessary to conduct above-mentioned microspacecraft missions. Therefore, low Isp thruster like a vaporizing liquid thruster would not be adequate for this class mission, unless bringing a lot of propellant mass. Laser ablation thruster, also addressed in this study, with low thrust but high Isp of 100-150 s would be suited for keeping formation flying and laser ignition thruster with high thrust but low Isp will be suited for the maneuver in very short time.

In the case of 50 kg microspacecraft ($\sim$ 40 cm cubic size), the size allowed for propulsion system would be typically within 2500 cm^3 and 5 kg. There the missions would be close to those of conventional highly functional spacecraft with more than a few years of the life time for practical use. For instance, let us consider North-South maneuver in GEO (geostationary orbit) which is the most practical orbit for spacecraft. Large, highly functional spacecraft currently used in GEO can be replaced by constellation of microspacecraft to increase the system redundancy. Of course these microspacecraft should be brought by other large spacecraft or transfer rocket supplying high delta-V because transfer from LEO (low earth orbit) to GEO requires huge delta-V about 4 km/s.

In GEO most important propulsion task would be North-South maneuver. It is compensation of the orbit inclination due to the several disturbances on the orbit. The most causes are gravitations from the sun and moon. Both accelerations are 8.6×10^{-6} and 3.4×10^{-6} m/s^2 by the moon and sun respectively. As a result, the required delta-V for the N/S maneuver for one year is usually about 50 m/s[14].

Solar pressure is another disturbance forces for spacecraft, which is about 4.5×10^{-6} N/m^2 near the earth. In the case of 40 cm cubic microspacecraft, the applied force is 7×10^{-7} N and much smaller than the gravitational disturbances. Also, the atmospheric drag is much smaller than solar pressure in GEO.

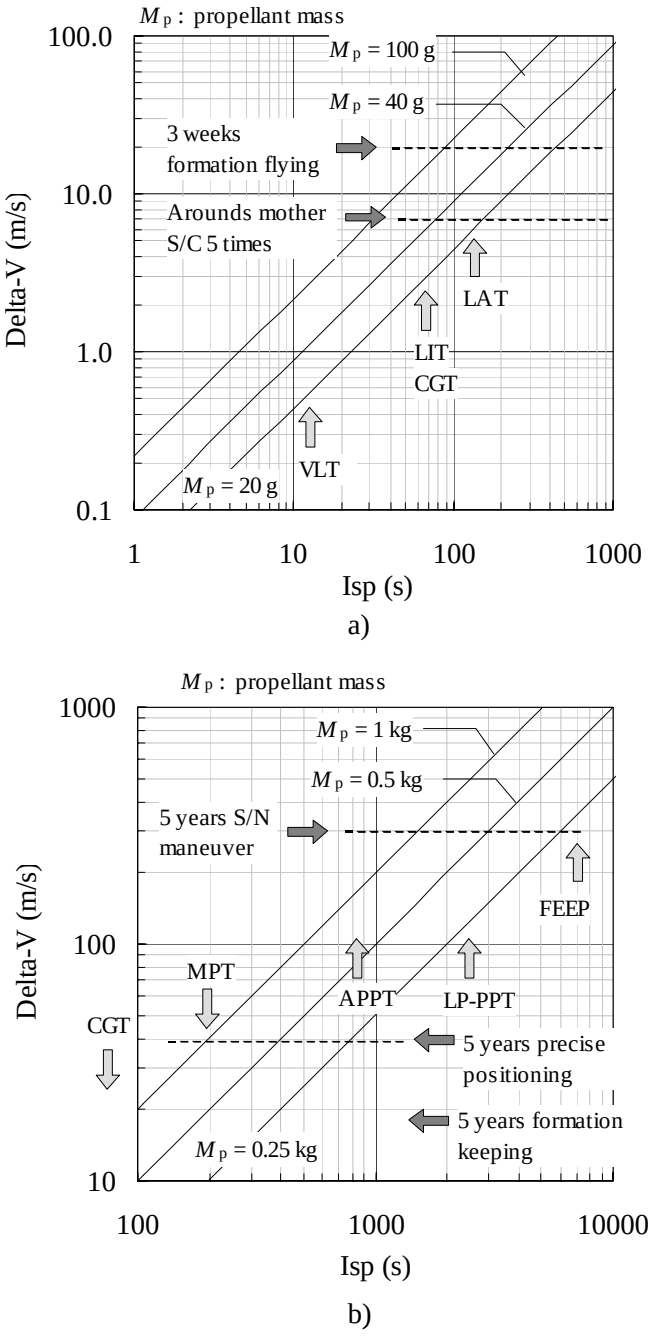

Figure 1.2: Relation of delta V and specific impulse; a) 5 kg spacecraft and b) 50 kg spacecraft. LAT: laser ablation thruster, LIT: laser ignition thruster, CGT: cold gas thruster, VLT: Vaporizing liquid thruster, FEEP: field emission thruster, LP-PPT: liquid propellant PPT, APPT: ablative PPT, MPT: monopropellant thruster.

Microspacecraft constellation will also need the force to keep the formation as well as the above 5 kg spacecraft, see Fig 1.1 a). However, the required delta V for keeping the formation in GEO is much smaller than that in low earth orbit because of the small orbital angular velocity. In the case of 50 kg spacecraft, 10 m distance, and 5 years life time, the required delta-V is 8 m/s.

Moreover, very precise positioning of formation flying will need additional delta-V. For instance, in the missions requiring precise positioning like LISA and Darwin, the delta V is about 30 m/s for 5 years (they are not in GEO).

As a result, microspacecraft in GEO requires delta-V of about 300 m/s for 5 years life time. Figure 1.2 shows the relation of specific impulse and acquired delta-V for 50 kg spacecraft. In the case of a cold gas thruster, the most fraction of space will be used for the gas tank, and for instance 1 kg gas can be reserved in a 2000 cm^3 and 100 atm tank. However, the low specific impulse is not suited for higher delta-V requirement. May be, micro-mono propellant engine would be better whereas several additional components must be prepared. These chemical propulsions are suited for re-arrangement of formation requiring higher thrust.

When micro-electric propulsion is selected, the mass for the propellant would be less than 1 kg (other spaces for thruster head and power source). In a lot of electric propulsions, only PPTs are suitable for this class microspacecraft. However, the low specific impulse cannot supply enough advantage by using an electric propulsion. Liquid propellant PPT, addressed in this study, has enough high specific impulse and compact size due to liquid propellant. FEEP can deliver quite high specific impulse, but the high voltage (10 kV) power conditioner and ion neutralizer are are suited for over 100 kg spacecraft.

1.3 Review of microthrusters

Because of the above mentioned backgrounds and motivations, a number of varieties of microthrusters have been proposed and developed in a last decade. In this section, those microthrusters are reviewed to select the ones most suited with microspacecraft. More details are reviewed well by Muller in elsewhere[15].

1.3.1 Micro-chemical propulsion

Up to date almost all propulsion systems used for the space exploration are chemical propulsions due to their simpler physics, and higher completeness, than electric propulsion. The interests are focused on the developing and fabricating the commercial products rather than the fundamental research. Therefore they are conducted mainly by government agency and industry. However, the miniaturization of those propulsion includes a number of unknown problems and characteristics, and many researchers in universities have started the studies.

In comparison with electric propulsion, chemical propulsion is characterized by the higher thrust and no need of an electrical power source. Therefore, it would be suitable with extremely small and short life time microspacecraft.

Cold gas thruster

Cold gas thrusters simply exhaust gas with no chemical reaction from a pressurized propellant tank. In the tank, the propellant is stored with 1 to 200 atms. Hence the specific impulse is small, usually ranged from 30 to 100 s, unless very light gas like H_2 and He is used. Nitrogen is the most frequently used propellant, which gives the specific impulse around 70 s.

The most advantage is the simplest structre in the other gas thrusters. It has been miniaturized already over the other thrusters. Moreover, when using benign gas, the cold gas thruster is relieved from spacecraft contamination problems. Nevertheless, propellant leakage and clogging problems and heavy, high-pressure propellant storage still remain as disadvantage. Use of ammonia as the propellant is interesting and promising idea because it will enable the liquid storage and reduce the tank size and mass.

Mono/Bi-propellant engines

Bipropellant engines are frequently considered for primary propulsion applications on conventional spacecraft because of their high thrust and high specific impulse. They mix two gaseous (fuel and oxidizer) and get high specific impulse, up to 300 s. Nitrogen tetroxide (NTO) and monomethylhedrazine (MMH) as oxidizer and fuels are used in the most cases. However, its complexity using separate feeding systems for fuel and oxidizer is disadvantage. Also leakage and clogging of

propellants becomes concern as well as or more than cold gas thrusters due to the complex system. Moreover, combustion efficiency and mixing losses are affected by the miniaturization, and the associated degradation of the performance would be worse than cold gas thrusters.

Using power MEMS technology for micro-bipropellant engine have been proposed and examined [16]. They accomplished the chamber pressure up to 12 atm (over the pressure failed the motor) and got the 1 N thrust. The most problems of such thrusters using power MEMS are suitable valve development, which should be fabricated using MEMS. Several MEMS based thruster suffers from the lack of suitable micro-valve.

Micro monopropellant engines are positioned between bipropellant engines and cold gas thrusters in the specific impulse and complexity. Hence the advantages and disadvantages are also middle of them. However, from the view point of the contamination, they have worse than both thrusters. It is because that they use most commonly hydrazine as monopropellant, which have high toxicity. It also costs the ground test and propellant loading procedure.

Recently HAN-based monopropellant engines have attracted interests, which uses a mixture of an oxygenrich component called HAN (hydroxylammonium nitrate) and a fuel-rich component. It is characterized by the non-toxicity.

Digital microthruster array

Solid rocket motors have advantages of the that compact size, no propellant feeding system, high specific impulse. However, the obvious disadvantage is difficulty to use arbitrary of quantity, that is they are not restartable. One of the methods to solve the problem is partitioning solid propellant into small pellets and installing them into a numbmer of micro chambers, whereas the installing micro-chamber leads to decrease of the energy density. Several researchers have examined that idea using power MEMS technology [17, 18, 19, 20], which are called as digital microthruster or micro solid rocket array. Micro-chambers with the dimension of 1 mm or below are fabricated and arrayed on a single chip. Every micro solid propellant is ignited by a heat element. Their solid rockets have very high energy density, namely small propellant tank volume, and are released from the propellant

feeding concerns. However, they suffer from low ignition probability and low combustion efficiency. Inexact touching of heat element on the propellant caused the failure of the ignition. Also another disadvantage is the change of the trust vector by shot-to-shot. In the propulsive task of translation motion, the synchronous firing of multiple propellants with symmetry at the center (thrust point) would solve the problem to some extent.

1.3.2 Micro-electric propulsion

In contrast to long history of the practical use of the chemical propulsions, electric propulsion has started to be applied in a last decade. The research on electric propulsions started since the early days (1960s) [21, 22]. However, in the space exploration which needs high reliability, they hardly changes already-established-systems into novel systems, even if they are superior than old ones. In last decades, several missions have started installing electric propulsions in challenging deep space missions [23, 24, 25, 26, 27].

Micro-electric propulsion systems are characterized by the high specific impulse over the micro-chemical propulsion. High specific impulse decreases the size and weight of propellant tank, which had dominated the fraction in the size and mass of spacecraft subsystems. On the other hand, electric propulsions are disadvantaged by the need of a high voltage power source. Then the reduction of propellant tank must be enough to compensate the increase of the power source.

The scaled-down of electric propulsion would lead to several inefficiency as well as chemical propulsion. Increased surface to volume ratio by the miniaturization increases the plasma losses to walls.

Pulsed Plasma Thruster

In electric propulsions, Pulsed Plasma Thrusters (PPTs) [28] have very simple structures and robustness in comparison to others. They utilize solid polymer Teflon®(PTFE) as the propellant. The polymer surfaces which contacts to plasma are ablated by the plasma and fed into it as propellant (discharge ablation feeding). Such PPTs are sometimes called as ablative PPTs or ablation fed PPTs (APPTs) to distinguish PPTs using gas or liquid as the propellant. The receded propellant is re-fueled by simply pushing the back using a spring. Then they are

released from the complex propellant feeding system and concern of propellant leakage. Moreover their capability to work with low energy (1 to 10 J) is suitable with power-limited microspacecraft. The thrust is generated in very short time (5 μs), and that impulsive thrust enables digital control of the impulse with high resolution. A dditionally, the thrust efficiency is independence on the firing frequency, and the thrust can be arbitrarily throttled within the allowed electric power.

On the other hand, associated problems with PPTs are their low thrust performance and concern of contamination from the ablated gas. Most electric propulsions currently used for several missions have the thrust efficiency of 50 % and the specific impulse of 1500 to over 3000 s. However typical flight qualified PPTs have the performance of less than 10 % and 800 s. Many researchers have considered that those poor performance comes from the excessive propellant feeding due to discharge ablation. The ablated propellant is kept to be evaporated from the solid surface even after the discharge termination.

Micro electrostatic thruster

Electrostatic propulsions, represented by ion engines and Hall thrusters, are leading thrusters in electric propulsions, and used in several missions as primary engines [23, 24, 25, 26, 27]. Neutral particles are ionized into ions in a discharge chamber and they are electrostatistically accelerated by voltage difference of 300 (Hall thruster) to 1000 (ion engine) V. The extracted ion beam is neutralized using a neutralizer, where hollow cathodes are often used due to their low electron cost. Xenon is frequently used as the propellant, because of the relative low ionization potential of heavy and benign gaseous.

Their great achievement in several missions have attracted researchers' interest to apply them to micropropulsions. Then micro-ion-engine and micro-Hall-thrusters have been proposed and developed [29, 30, 31, 32, 33]. However, the scaled-down causes the performance decreasing. Electrostatic propulsions confine plasma using magnetic field, where Larmor radius of the particles should be less than the characteristic length. Hence the decreasing size of thrusters requires stronger magnetic field to confine plasma. Even if enough magnetic field is applied, the increased surface volume ratio leads to more plasma losses. Also decreased

power causes the higher ion beam cost. In addition, the need of ion beam neutralizer leads to system complexity and make the miniaturization difficult.

Field emission thruster

Field emission electric propulsions (FEEPs) are also electrostatic thrusters but with unique characteristic on the plasma generation processes [34, 35]. They directly extract atomic ions from the free surface of liquid metal at the edge of an emitter. The emitter has needle or slit shape and liquid metal is fed through or wetted on it by the action of capillary forces. High voltage of 10 kV range is applied at the edge and the strong electric field is generated. When the field reaches a threshold value ($\simeq 10^6$ V/mm), atoms on the liquid surface are eventually extracted and electrostatistically accelerated. Cesium or indium are usually selected as the propellant.

The FEEPs are characterized by their ultra high specific impulse of 4000-10000 s range because of the high applied voltage. Also they can deliver extremely small thrust in the 1-10 μN range. It is suitable for accurate positioning of the spacecraft. Their unique plasma generation method, with no discharge chamber, inherently avoids the plasma losses into walls and leads to high efficiency (over 70 %). Moreover it removes the concern related to volume surface ratio and suitable for the scaled-down.

The disadvantages of FEEPs are concerns on electromagnetic interaction (EMI) due to their high voltage. Additionally use of high applied voltage requires heavier power supply than lower voltage devices with the same power range. As well as the other electrostatic thrusters, FEEP requires an neutralizer for the ion beam.

Colloid thruster

Colloid thrusters have similar acceleration mechanism as FEEPs and were studied in 1960s to 1970s proceeding in FEEPs [36, 37]. High voltage is applied to a capillary tube with liquid propellant, and not atomic ions but charged liquid droplets are extracted from the emitter. They use solutions as propellant, for instance glycerol doped with sodium iodine to produce positive droplets and glycerol doped with sulfuric to produce negative droplets. In the development of colloid thrusters, specific charge, defined as charge per droplets mass, is a key factor to

determine the performance. The typical values are in the range of 10^2 to 10^5 Coul/kg. Recently, application of MEMS technology [38] and examinations of alternative propellants [39, 40] are studied.

The using no discharge chamber gives the similar characteristics as FEEPs. In comparison to FEEPs, colloid thrusters have higher thrust (200 μN/W) and lower specific impulse (500 - 1500 s). In addition, unique ability to produce both positive and negative droplets according to the solutes enables self-neutralizing colloid thruster with bipolar array. It eliminates the disadvantage of needing a neutralizer.

Micro Resisto/arc-jet thruster

resistojet or arcjet thrusters convert the electric energy into the thermal energy using a resistive heater or arc discharge respectively, and electrothermally accelerate the propellant. They provide higher thrust than other electric propulsions but lower specific impulse around 200-500 s. Resist/arc-jets provide specific impulse as well as bipropellant engine without the complexity of such engines. However they requires an additional power source. Difficulty in the miniaturization is similar to chemical propulsions, inefficiency of scaled-down and propellant leakage and clogging. In recent years, a very low power arcjet (a few W) has been studied [41, 42, 43].

Laser ablation microthruster

Laser ablation microthrusters are sometimes categorized into a beaming propulsion rather than electric prpulsions. The beaming propulsion is to transmit the energy from outside of the spacecraft using beam (as laser, microwave, or solar window) [44, 45, 46]. It has the potential for significant weight reduction and improved the payload ratio. The beaming propulsion can be categorized into several types, by the laser types or the energy conversion processes. A laser ablative propulsion is one of those [46, 47], which focuses and irradiates the laser beam on the surface of a solid propellant (metals and polymers). The heated and evaporated propellant by the laser beam is ejected from the surface (laser ablation) to provide thrust.

Phipps et al. proposed the use of laser diodes for the laser ablative propulsions

as a micropropulsion [48, 49], as the miniaturization of spacecraft increasingly attracted attentions, The thruster is referred as a diode laser ablation microthrusters in this study. The propulsion system includes diode lasers, optical system, and solid ablative propellant. The compactness of laser diodes and the associated optical system enable an onboard laser beam source. Actually, typical diode lasers weigh 1-2 g and less than 10 g even with the optical system. In addition to the compactness, laser diodes have advantages of low operation voltage and high convergent efficiency. Diode lasers require the operation voltage less than 5 V and have the convergent efficiency over 40 %. Solid polymer is commonly used as the propellant (ablative material) for the diode laser ablation microthruster, because most diode lasers do not have enough intensity to ablate metals.

The diode laser ablation microthrusters are characterized by the compactness, the use of solid propellant, and the accurate thrust control. The compactness of diode lasers and the low operating voltage enable the higher miniaturization than other electric propulsions. The use of solid propellant solves the problem of the propellant leakage and clogging as well as PPTs. The thrust can be widely and precisely adjusted by varying the laser pulse width.

In contrast, the disadvantages are their feeding system and lens fouling. They must equip a certain mechanism to feed solid propellant for the laser irradiation. The propellant feeding system should be compact, light weight, and long life time. Developing such a feeding system is essential to realize the diode laser ablation microthruster. Lens fouling by the plume jet becomes severe problem for propulsions using beaming energy. Phipps et al. have proposed and examined the transparent mode ablation to defeat that problem, where laser beam irradiate the propellant from the opposite direction to the plume jet through transparent material. However that mode decreased the thrust by half and limits the varieties of usable propellant.

1.3.3 MEMS based propulsion

MEMS based propulsion systems allow extremely small devices to be applied to microspacecraft less than 1 kg. Hence several MEMS-based thrusters have been proposed; MEMS-based, cold gas thruster, resistojet, FEEP, and ion engine. It will allow to integrate different propulsion components on a single MEMS chip,

saving the size and weight for thrusters. However many of these concepts are still in the very early development stage. The most important component is a valve controlling the propellant. The valve with low leakage rate and long life-time should be developed to apply MEMS based propulsion to microspacecraft.

Additionally, excessive miaturization using MEMS would have less benefit. It is because that the most dominate size and weight in propulsions is not a thruster head but propellant and its feeding system. The minimum size allowed for a thruster head would be determined by the propellant. Then the head should be designed to provide as high efficiency as possible within the range. The excessive miaturization would only increase disadvantages associated with the scaled-down.

1.4 Microthrusters for 1-100 kg microspacecraft

In this study, a diode laser microthruster with dual propulsive mode and pulsed plasma thruster using liquid propellant are selected as promising micropropulsions for 1-10 kg and 10-100 kg microspacecraft respectively.

1.4.1 Dual propulsive mode diode laser microthruster

The ability required for propulsion of 1-10 kg microspacecraft is first the compactness rather than high specific impulse. The missions expected for such microspacecraft would be commonly simple and short-time missions, because the function is quite restricted due to severe limits of the size, weight, and power. The bus system dominates most of the volume and weight, and only a small fraction would be provided for sensing devices and propulsions. The electric power that such microspacecraft provide for propulsion system is restricted at most a few Watts in the current stage, at most 20 W even in the near future. Orbit raising needing large delta-v or constellation controlling in long time, over a few years, are not required (impractical) for this class spacecraft.

Therefore high specific impulse of electric propulsions are not so attractive for that class microspacecraft. Additionally loading an additional power source for propulsions would prevents them from the application in such small spacecraft. Chemical propulsions using gas propellant, cold gas thrusters and mono/bi-propellant engines, are also not suitable due to their propellant feeding system.

Those systems need strict, complex, and heavy components by handling and storing highly pressurized propellant. Moreover they gives several risks of propellant leakage and clogging. MEMS-based microthrusters may have the most advantage in the scale. However, their technologies are not in the practical stage. After all digital microthruster array and laser ablation microthruster are suitable for 1-10 kg microspacecraft (whereas laser ablation microthrusters are categorized in electric propulsions but they need a power source with only a few W).

The propulsion capable to generate both the lower range and higher range thrust is very attractive for 1-10 kg microspacecraft. The applications of the propulsion are represented by accurate constellation positioning and attitude control using lower thrust and re-arrangement of the constellation and slew manevver using higher thrust. In order to limit the weight and size of the microspacecraft, it is essential to satisfy the requirement of lower and higher range thrusts with the same propulsion system. To our knowledge, there is as yet no single propulsion system which can supply such a wide range of thrust for the 1-10 kg class microspacecraft.

In this study, a novel type of microthruster enabling multiple propulsive tasks is proposed. That microthruster has dual propulsive modes using a diode laser: laser ablation mode and laser ignition mode. Its propellant consists of polymeric material and pelleted pyrotechnic. In other words, it is the thruster combining a diode laser ablation microthruster and laser ignited digital microthruster array. It works as laser ablation microthruster when the laser irradiates the ablative material, and works as micro solid rocket when the laser irradiates a pelleted pyrotechnic. That thruster is referred as a dual dropulsive mode laser microthruster or simply laser microthruster in this thesis. The study on that thruster will be described in Chapter 3.

1.4.2 Liquid Propellant Pulsed Plasma Thruster

In the case of 10-100 kg microspacecraft, propulsion system with high delta-v would be required to conduct more practical and advanced missions. Whereas such missions have not been expected for 1-10 kg microspacecraft, they would become practical when the scpacecraft are scaled up to 10-100 kg. Of course, however, the compactness is still required, but the limits on the propulsion system

will be relaxed up to 1-10 kg and 10-100 W. Those allows the selection of electric propulsions.

In electric propulsions, both PPTs and FEEPs are released from the concerns of propellant feeding system. Whereas FEEPs use liquid metal as propellant and need the valves, that handling is much better than highly pressurized gas propellant. However, high voltage applied for FEEPs (5-20 kV) causes the heavy power source and electromagnetic interference and the need of neutralizer causes additional system weight and complexity. Therefore PPTs have the most potential to be applied in 10-100 kg microspacecraft. Nevertheless PPTs are sometimes defeated by their very poor performance. The typical flight model PPTs have the thrust efficiency of less than 8 % and the specific impulse of less than 800s. They are much lower than the values of typical electric propulsions. Researchers on PPTs believe that the low performance comes from the excessive feeding of the solid propellant. A lot of Teflon would be vaporized after the main discharge. That gas is not electromagnetically accelerated and leads to decrease of the spectrum efficiency, or propellant utilization efficiency.

Exhaust plume contamination issues are always associated with electric propulsions. The plasma generated and exhausted by thrusters has the potential to affect solar cells. The plasma in the vicinity of the cell causes shorting them or arcing between spacecraft and plasma by the raised spacecraft potential difference. In addition to such plasma contamination, use of toxic or reactive propellant leads to further issues. PPTs use commonly Teflon®(PTFE, $-CF_2CF_2-$) including carbon and fluorine. The carbon causes charring of spacecraft and it can degradate solar cells and optical instruments. Charring of the thruster itself can decrease the life-time of thruster by shorting the insulation of electrodes or spark plug. The high toxicity of fluorine would also causes such contaminations. Cesium that is used as the propellant of FEEPs also results in potential contamination problems due to that high reactivity. In long missions, those contaminations concerns would be important problem. In actual, it is one of the reasons why ion engines and hall thrusters most commonly use benign gas, xenon, as the propellant.

PPTs with high performance and little contamination are very attractive and promising microthruster for 10-100 kg microspacecraft. Here, use of liquid propellant for PPTs is studied to achieve such a microthruster. Liquid droplets are intermittently supplied by an liquid injector into the interelectrode space. The

main discharge is initiated using a spark plug or directly by the pressure rise in the interelectrode. Water is selected as the promising propellant due to the clean constitution, handling ability, safety concern, and capability sharing with life-support system. A pulsed plasma thruster using liquid as the propellant is referred as a liquid propellant pulsed plasma thruster (LP-PPT). The study on a liquid PPT will be described in Chapter 4.

1.4.3 Thrust Stand for Micropropulsion

Accurate thrust measurement is the most important on the research of micropropulsions. The thrust generated by and required for micropropulsions is ranged from very low (micro Newtons) to high (mili Newtons) levels. Thrust measurement of mili Newton orders has been performed since the early days of the space exploration. However, need of extremely small thrust measurement is newly emerged in a last decade with micropropulsions, and it is difficult to accurately measure those thrusts. Hence, studying on the above-mentioned two microthrusters, a thrust stand to measure micro Newtons thrust is designed and developed. The stand is designed not to measure thrust of a special thruster but to be commonly used for any micropropulsion. The study on a thrust stand will be described in Chapter 2.

1.5 Objectives

1.5.1 Objectives of this study

The objective of this study is to develop micropropulsions suitable for 1-100 kg microspacecraft, and the following studies are performed: developing a highly accurate thrust stand for microthrusters, studying a dual propulsive mode laser microthruster for 1-10 kg microspacecraft, and studying a liquid propellant pulsed plasma thruster for 10-100 kg microspacecraft.

1.5.2 Outline of the contents

Succeeding this chapter, first development of thrust stand for micropropulsions is introduced in Chapter 2. Study on a dual propulsive mode laser microthruster is reviewed in Chapter 3. Study on a liquid propellant pulsed plasma thruster is

reviewed in Chapter 4. Conclusions obtained by this study are given in Chapter 5.

In Chapter 2, firstly the detailed explanations are introduced for every components of the thrust stand. Then the dynamics of a thrust stand and analysis method of thrust measurement are given, where a new analysis method for micro Newton thrust measurement is proposed and that effect is verified. The measurement of thrust widely ranged from lower to higher level is verified using two microthrusters described in the succeeding chapters. Finally the error associated with the stand is discussed in the view points of the resolutions and the accuracy.

In Chapter 3, follwing to the introduction of the laser microthruster, experimental setup in common with laser ablation and ignition modes are reviewed. There After that the results and discussions on the both modes are given in different sections. In the laser ablation mode, first the most appropriate ablative material was surveyed of several materials. The fundamental thrust performance of that mode was evaluated using the thrust stand. The ablation processes of the best material was investigated by the effect of carbon density in PVC and mass spectroscopy. In the discussion, to clarify the ablation mechanism, analysis of heat conduction problem was conducted. In the laser ignition mode, first the laser ignition of pyrotechnic in vacuum was examined and the threshold power for the ignition was clarified. In the discussion section, the laser ignition threshold and the ignition processes of boron/potassium nitrate were investigated. There numerical calculation to predict the threshold was performed.

The objective of the study in Chapter 4 is to increase the thrust to power ratio of a liquid propellant pulsed plasma thruster. The fundamental verification of LP-PPT was conducted in Kakami and the author [50, 51, 52, 53], where the successful operation using liquid and the high specific impulse were verified. In this study, the clarification of the acceleration processes is conducted to increase the performance. To specify the characteristics of a LP-PPT, a liquid PPT and ablative PPT with the same electrodes and external circuits were designed. First, the performance and the energy partition on both PPTs were compared. There the resistances in a PPT circuit was mainly investigated by the current waveform and observation using a ultra high speed camera. As a result, two methods to improve the thrust to power ratio were proposed. The proposed two improvement methods were experimentally examined and the effects are discussed.

Chapter 2

Thrust Stand for Micropropulsion

2.1 Introduction

Thrust measurement is most essential to validate the performance of thrusters. However it is difficult to accurately measure extremely low thrust produced by microthrusters. In the early stage of space development, few studies have addressed low thrust measurement of microthrusters, since the main focus at that time was on developing primary propulsion systems. Stark et al.[54] performed a study of low thrust measurement during the early 1970s. They developed a torsional type thrust stand that oscillates horizontally and measured thrust of ion engines ranging from 5 μN to 200 mN. Notwithstanding, that thrust stand was quite complex and expensive. Recently, several studies of low thrust measurement using a thrust stand have been done [55, 56, 57, 58, 59, 60] because of the increasing interest in microthrusters. Haag [55] designed a thrust stand with the same mechanism of Stark's, but with simpler components. He measured impulse of Pulsed Plasma Thruster (PPT) of 300 μNs. Cubbin et al.[56] developed an optical interferometric proximeter for measuring impulse from PPTs within the range of 100 μNs to 10 Ns. However, most of microthrusters produce lower impulse (order of 10 μNs) than 100 μNs. Although there are other thrust stands [57, 58, 59, 60] allowing measurement of such low thrust, most are specialized for very lightweight thrusters.

In this study a thrust stand has been designed to accurately measure impulse produced by microthrusters. The stand has the same mechanism as Haag's one [55], horizontally swinging torsional balance. In order to estimate the performance, lower impulse (1 - 80 μNs) was measured and two types of microthrusters: a liquid propellant PPT and a diode laser ablation microthruster were used. The impulses of a PPT used here ranged from 20-80 μNs and a laser microthruster had lower impulse of 1-30 μNs in laser ablation mode and higher impulse of 10 mNs or 500 mNs in laser ignition mode. The mechanical noise induced from the background vibration is a crucial problem for low impulse measurement. A data analysis method to more accurately evaluate such low impulse was established. By adding additional term into a fitting function, actual response from microthruster was separated from mechanical noise. Our method reduced the variance down to one-third that of a normal fitting method.

2.2 Thrust stand

A thrust stand addressed here is separated into five components: torsional balance, displacement sensor, electromagnetic damper, counter weight, and calibration system. Figure 2.1 is a schematic diagram and picture of the thrust stand. A thruster is installed on the torsional balance and the reaction force is measured as displacement of the balance.

In this study, mainly impulse measurement was conducted. Impulse measurement is strongly required because a number of microthrusters are repetitively operated in pulses. In whole of this work, thrust measurement means impulse measurement in exact meaning.

2.2.1 Torsional balance

A balance for a thrust stand measuring micro-Newton thrust requires the following characteristics.

- small restoring force
- no affected by environmental disturbance
- no static friction, no slippage, and high endurance for rotational axis

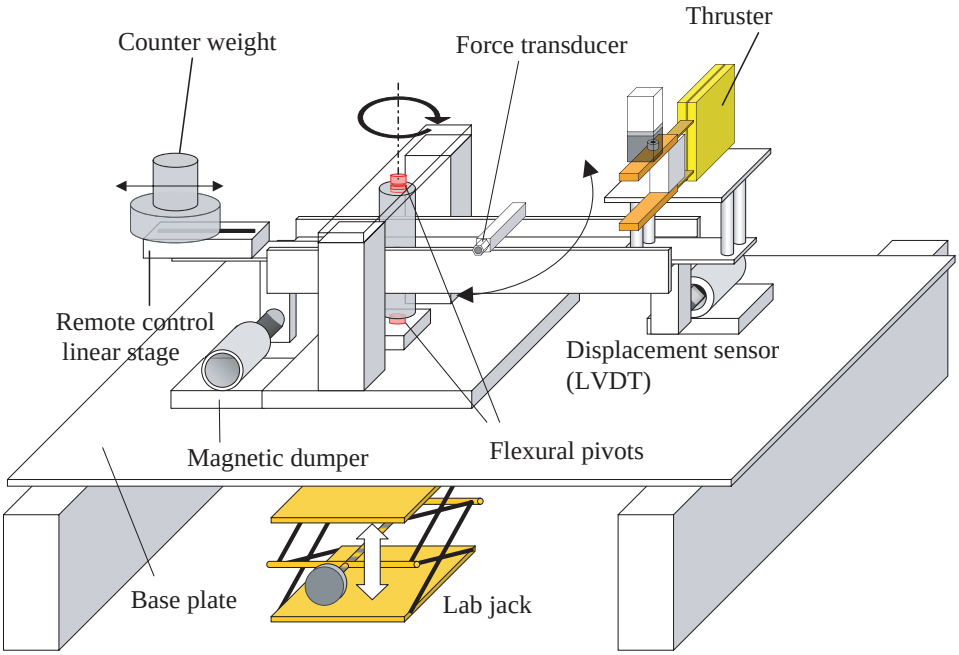

a)

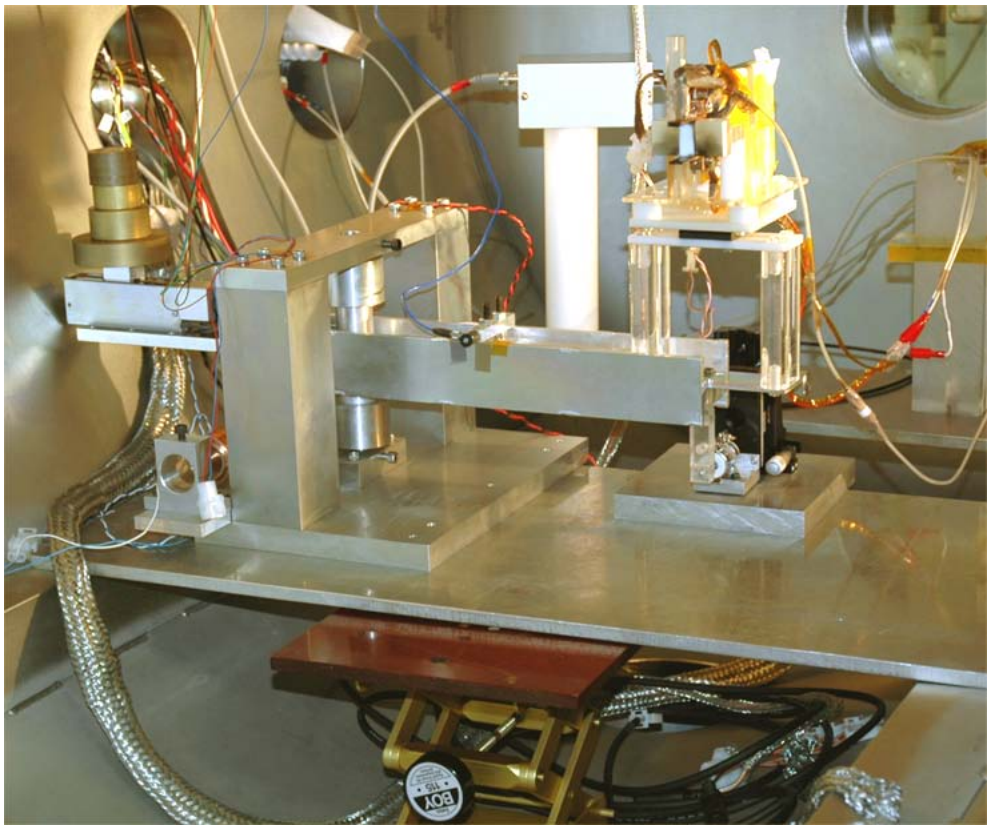

b)

Figure 2.1: Schematic drawing and photograph of the thrust stand system.

Impulse from microthrusters are generally very small, and high sensitivity, large displacement against small impulse, is required for the balance. Hence small restoring force is necessary. Moreover impulse measurement requires long oscillation period for the balance in order to assume the force as impulsive force. Small restoring force is suitable also with that requirement. It is unrealistic that we require a perfectly quiescent environment for the place to carry out experiment. In most cases the environment has several disturbances, like minute shaking of a chamber, floor, and building. Then the balance should not be affected by those disturbance. Static friction applies a threshold to displace the balance and breaks the linearity for a very small thrust response. Slippage of rotational axis causes the misleading of the impulse, because the displacement of balance from microthruster is extremely small, micro-meter levels.

A horizontally swinging torsional balance using flexural pivots was selected to satisfy the above requirements. It has the following advantages. Firstly, a torsional balance can adjust its gravity center on the axis using counter weight and make itself insensitive to the environment disturbance. In contrast, a ballistic pendulum, which is sometimes used for thrust stand, is directly affected by those disturbance (if the gravity center matches to the axis, it can not work). Secondly, horizontally swinging structure gives good property to set a thruster on that arm. Arms of vertically swinging balance sometimes induce the difficulty to install a thruster on it. Thirdly, a flexural pivot provides very good rotational abilities. The flexural pivot is made of flat crossed springs supporting rotating sleeves, and has the characteristics, high radial and axial stiffness, frictionless, stiction-free, low hysterisis, low center-shift, and long (infinite) life time. A knife edge is sometimes used for the rotational axis, and would be suited with a light-weight, simple balance. However, it has the potentials of stiction and hysterisis due to the wear and deformation of the edge. We have to care every time to those effects.

The balance designed in this study is built in three parts: a swinging arm with H cross section, rotational axis with flexural pivots, and stationary framework supporting the axis. The H-cross-sectional arm has the height of 50 mm and the width of 55 mm, with the each plate thickness of 2.4 mm. The vertical plate is strengthened by welding 3.0-mm-thickness-plates on the both sides. The arm is vertically penetrated by and welded to the rotational axis with a circular tube, which has the outer/inner diameter of 30/24 mm. The rotational axis is

supported by two commercially available flexural pivots, which connect the axis to the stationary framework. The flexural pivots made by Lucas Aerospace Ltd.

Figure 2.2: Photograph of a flexural pivot with the rotational spring constant of 0.191 Nm/rad.

have the rotational spring constant of 0.191 Nm/rad, the diameter of 15.88 mm, and the length of 25.4 mm. The picture of the flexural pivot is shown in Fig. 2.2. The above three parts (except for the flexural pivot) are made of aluminum to provide light weight structure. That balance swings with the natural period of 4 - 5 s with a thruster, counter weights, and several mounting structures, whereas natural period of 1.3 s without those parts. The design of the thrust stand was shown in details in the reference[50].

Several electrical feed lines are connected from the balance to the outer framework. Standard feed lines are five vinyl coating copper wires of 0.8 mm in diameter and one coaxial cable 2.0 mm in diameter for a linear stage of counter weight and a force transducer respectively, which are described in the following sections. Pulsed

plasma thrusters need two vinyl coating wires 1.2 mm in diam. to charge the capacitor, one high voltage endurance wire 3.5 mm in diam. for a spark plug, and two pair of twisted vinyl coating wires 1.0 mm in diam. for a Rogowski coil and liquid injector. Diode laser thrusters need two pairs of twisted vinyl wires 1.0 mm in diam. for a diode laser and propellant feeding system. These feed lines are slacked off as much as possible in an effort to minimize the friction force.

The electrical feed lines cause the damping force to the balance. Figure 2.3 shows the balance oscillation under the situation of a PPT setting (a magnetic damper was not worked). The balance has the damping time constant of 60 s and the natural period of 4.2 s. The small damping ratio of 0.07 gives little effect to the estimation of the oscillation amplitude in the first cycle (see Section 2.3).

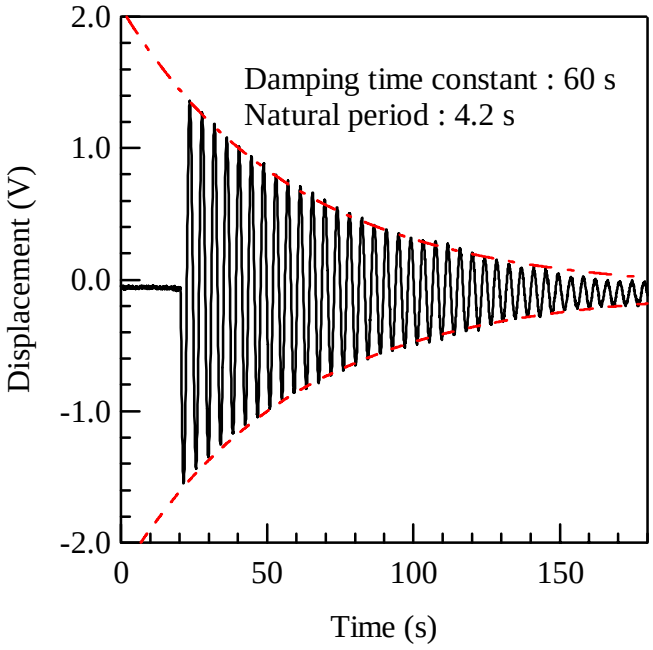

Figure 2.3: Sample waveform of the oscillation of the balance with damping by electrical feed lines (no magnetic damper).

2.2.2 Displacement sensor

A linear variable differential transformer: LVDT was used as displacement sensor. The thrust stand dealt here is oscillated with the amplitude of 2 μm by the 10

μNs impulse. Then sub-micro-meter resolution is required for a displacement sensor. A LVDT can supply such high resolution. Additionally a LVDT is a contact-free displacement sensor and has no effect on thrust measurement. In general, it consists of magnetic core, first excitation, and second receiving coils. The displacement of the core gives change of the mutual inductance between two coils. A LVDT made by Shinko Electric Co., LTD was used (type:1301-2; size: CC-36). A signal conditioner HM100-5.0 provided by the same company was used. It supplies an excitation signal and convert the output AC signal of second receiving coil to DC signal. Its circuit diagram is shown in Appendix, Fig. F.1. The sensitivity can be set in four different levels and the third highest sensitivity was used in all thrust measurement. Table 2.1 shows the specifications of the LVDT system used in this study.

Table 2.1: Specifications of a LVDT from Shinko Electric Co., LTD.

Average sensitivity	12.4 μm/V
Movable range	$\pm$3 mm
Excitation voltage	5 kHz

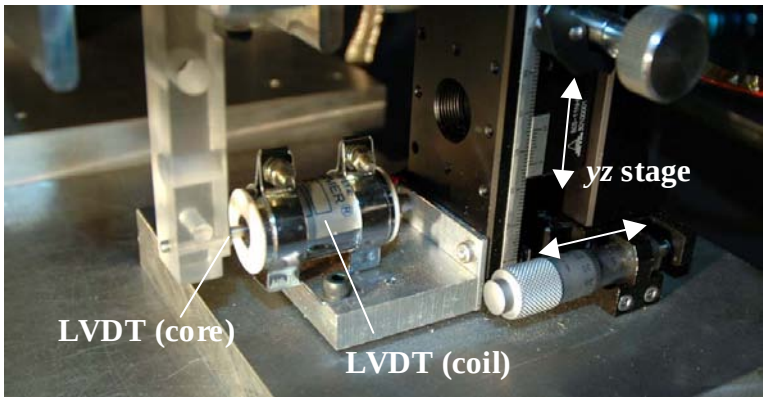

Figure 2.4: Picture of the displacement sensor, LVDT: Linear Variable Differential Transformer, on the $y-z$ stage.

The magnetic core of the LVDT is installed at the edge of and below the balance arm. First and second coils in the same housing are set on a yz stage.

The yz stage has rough alignment for z (height) and tight alignment for y (balance moving direction). The picture is shown in Fig. 2.4.

2.2.3 Electromagnetic damper

An electromagnetic damper was installed to suppress the undesirable oscillations, which are mechanical noise induced by background vibrations and remained thrust oscillations after the measurement. Displacement signal of the LVDT was fed back to the electromagnetic damper to generate the force proportional to the derivative of the displacement as damping force. The electromagnetic damper consists of an iron core and coil. The iron-core is installed on the opposite side of balance to a thruster, which is made of soft iron and has the diameter of 20 mm. The coil was set on the stand base, which was wounded on a acrylic circular tube with the 40 mm diameter with the number of turns of about 200.

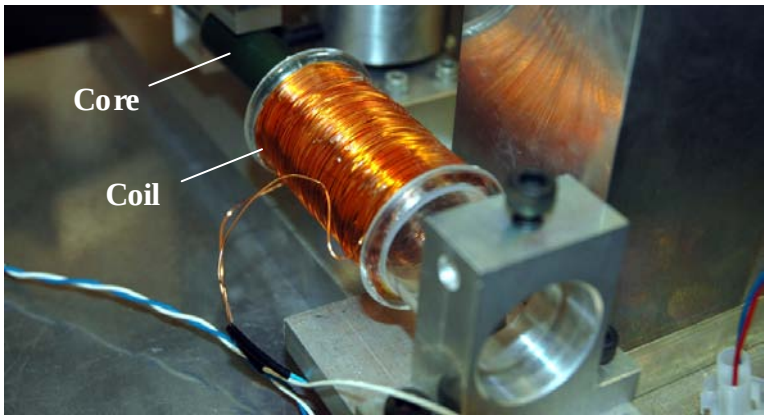

Figure 2.5: Picture of the magnetic damper.

The force produced by a solenoid coil is linearized by adding bias current. Applying current:J to the coil produces the force: F_{damper}

$$F_{\text{damper}} = \frac{1}{2}L'J^2 \tag{2.1}$$

to the iron-core, where L' is the inductance derivative of coil along the moving direction. The squared dependence of the force on the current is not useful to construct a simple feedback system. Then the current is biased at the working

point J_0, and the electromagnetic force becomes

$$F_{\text{damper}} = \frac{1}{2}L'(J_0 + J_1)^2 \tag{2.2}$$

$$= \frac{1}{2}L'J_0^2 + L'J_0J_1 + O(J_1^2) \tag{2.3}$$

, where J_1 is the current proportional to the derivative of the displacement of the balance. The first term of bias curernt J_0 works only to displace the balance point. The second term is proportional to the derivative of the displacement, and works as the damping force. The third term of J_1^2 is negligible, if the bias current: J_0 is much larger than J_1.

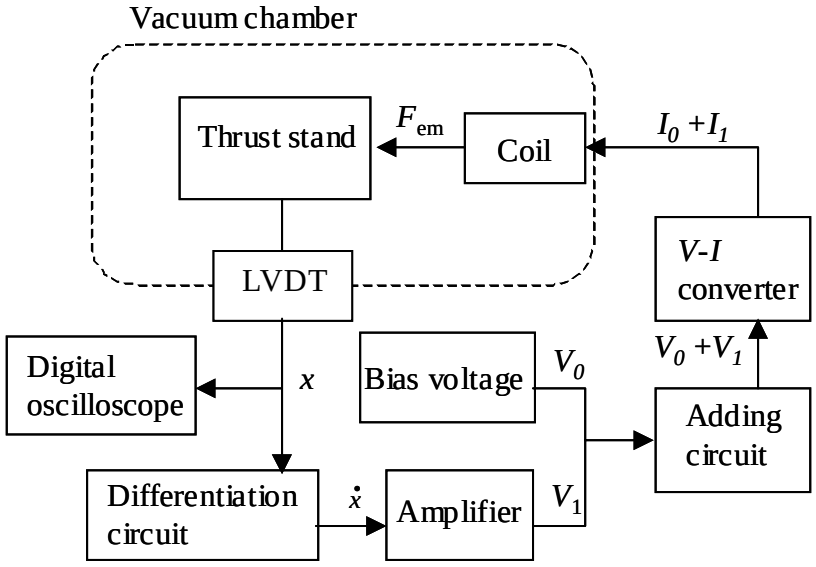

Figure 2.6: Magnetic damper feed back system.

Figure 2.6 shows the flow chart diagram of the active damping system. The output from a displacement sensor (LVDT) is differentiated and amplified using an analog circuit. Bias voltage is added to that signal and the summation is converted to the current. By changing the gain of the amplifier, damping force can be arbitrarily controlled, remote on-off control. Its circuit diagram is shown in Appendix F.

The magnetic damper was turned off a few second before firing a thruster. All thrust measurements were conducted under only minute damping by feed lines. After recording oscillation waveform by the thrust, The damper was re-worked and the oscillation was suppressed for the succeeding thrust measurement.

The bias current J_0 was set about 200 mA and the maximum amplitude of the derivative current J_1 was about 100 mA. They supplied enough force to damp the balance oscillation (over damped waveform was obtained with increasing the gain a little). Figure 2.7 shows the oscillation waveform damped by the magnetic damper. Although J_0 is not much larger than J_1, and the third term in r.h.s. of Eq. 2.3 worked. However, the effect was not severe at all, because the measurement was performed wit no damping. If the damped oscillatory waveform is to be measured, the damping force should be precisely exerted.

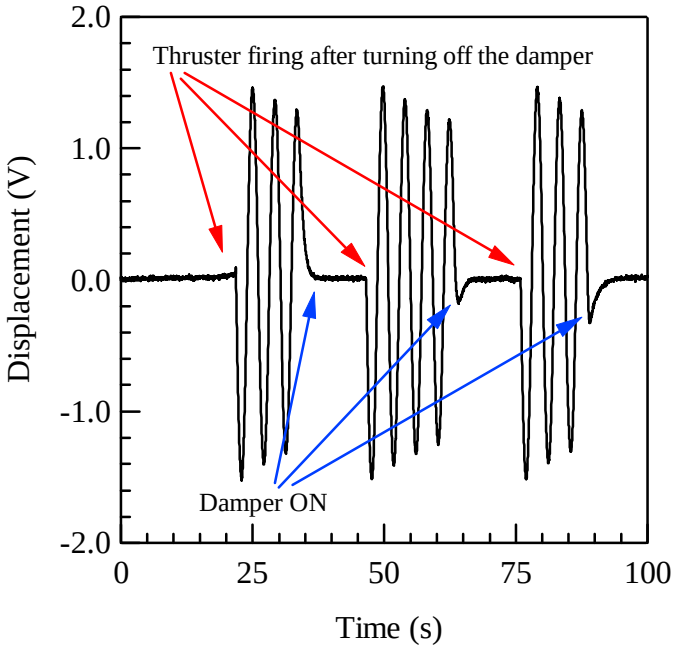

Figure 2.7: Oscillation of the thrust stand by the thruster firing and its damping using the electromagnetic damper.

2.2.4 Counter weight

Adjustment of gravity center on the rotational axis is one of the most effective methods to avoid mechanical noise induced by background vibrations on a torsional type thrust stand. If the gravity center of the torsional balance is just on the axis, the background vibrations does not affect the balance at all. It only sways the whole of the thrust stand. For instance, the base motion (acceleration):

$\ddot{X}$ induces the torque: T_{noise} on the balance, and

$$T_{\text{noise}} = l_G M \ddot{X} \tag{2.4}$$

where l_G is the position of gravity center from the rotational axis and M is the total weight of the balance. Then the torque is directly affected by l_G. Other types of base accelerations, like rotation, are also proportional to the position of the gravity center.

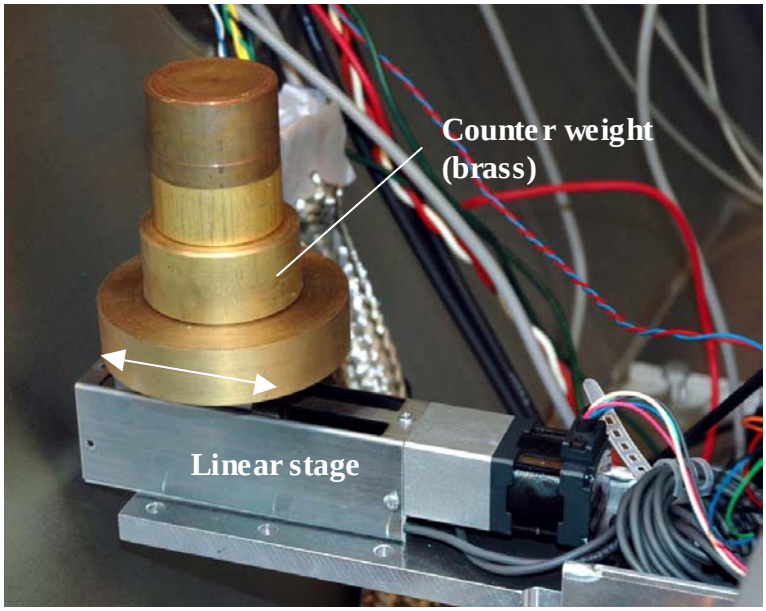

Figure 2.8: Picture of the linear stage and counter weights to control the gravity center of the balance.

In this study, a counter weight was used to adjust the gravity center on the rotational axis, whereas it is sometimes used just to balance the stand. Generally a thrust stand balance has a long arm to increase the sensitivity to thrust, and consequently the other side has a shorter distance from the axis due to the limited space in a space chamber. Thereafter the gravity center is largely shifted from the axis. The thrust stand dealt here has the gravity center +20 cm away from the axis with no counter weight, assumed 1 kg thruster. Then 2 kg counter weight -20 cm away from the axis will shift the gravity center to the axis. However, it is difficult to perfectly set the gravity center just on the axis.

The position of the counter weight was adjusted using a linear stage, which is shown in Fig. 2.8. The linear stage is SPL28T08B-06C2T made by ORIENTAL

MOTOR Co., Ltd.. Rough alignment of the counter weight was conducted by cumulating several weights (100 - 800 g), and tight alignment was performed using the linear stage.

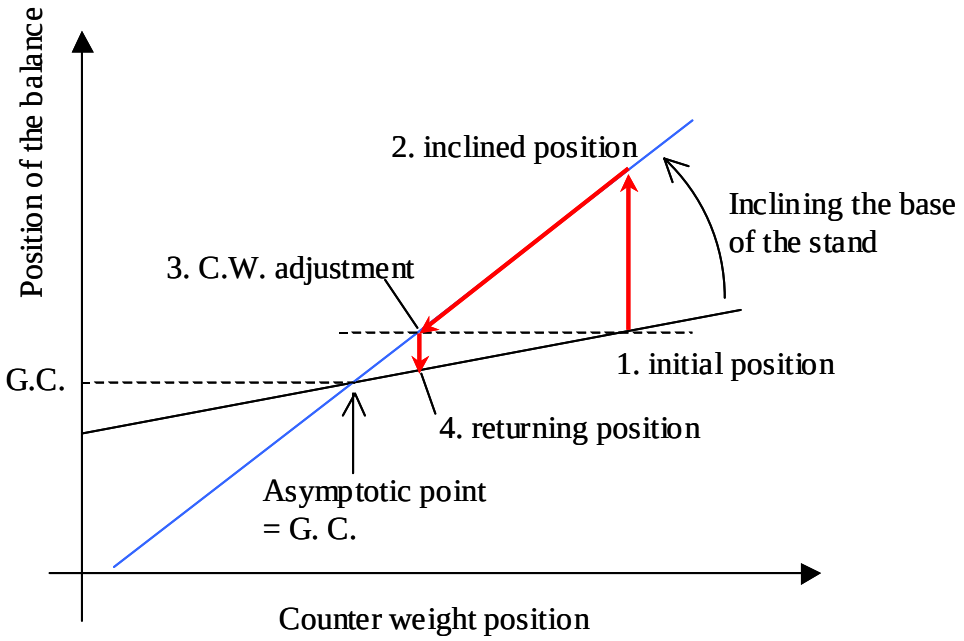

Figure 2.9: Limit cycle of counter weight adjustment.

Fine adjustment of the counter weight was carried out as the balance does not move even if the base plate on which the stand was placed was inclined. Figure 2.9 shows the limit cycle of the counter weight adjustment. In the figure, a horizontal and vertical axis show the position of] the counter weight and balance respectively. In general, the base of the stand is not perfectly horizontal and a little inclined. Hence the changing the position of counter weight produces the displacement of the balance. That relation can be expressed by a line in the plot of the counter weight position and the balance displacement, as shown in the figure. At the initial state, the gravity center is out of the axis, and inclining the base shifts the position of the balance ($1 \rightarrow 2$ in fig. 2.9). Secondly the position of the balance is made back to the origin by moving the counter weight ($2 \rightarrow 3$). Thirdly, the base inclination is removed ($3 \rightarrow 4$). By repeating the processes several times, the gravity center comes close to the axis (just on the axis, the balance is not affected by the base inclination).

The gravity center was set up within less than 10 μm off the axis. Inclining the base causes the displacement of the balance, $x$incline, as

$$x_{\text{incline}} = l_{\text{measure}}\ l_{\text{G}} \sin(\alpha) Mg/k \tag{2.5}$$

where α is the inclination angle of the base plate in radian. The thrust stand typically has the total weight of 4 kg with 1 kg thruster and 1.5 kg counter weights. Typical base inclination angle was 1 - 2 degrees in this study. That inclination applies the force of about 1 N at the gravity center. Adjustment of the counter weights by the above-described method was conducted for the shifts x_{incline} to be less than 12 μm (1 V output). It means the approximately 11 μm deviation of gravity center from the rotational axis. Corresponding counter weight motion is 30 μ m, and it must be controlled with the resolution less than 30 μm.

2.2.5 Calibration system

Calibration is performed by striking the thrust stand with an impact pendulum. The impact pendulum strikes a force transducer attached on arm of the thrust stand. The force transducer records the history of the impulsive force, whose integral yields the impulse. After every thrust measurement, the thrust stand was calibrated. Electrical feed lines from microthrusters had a little different configurations every time, which led to a little change of the spring constant of the balance. Sample of calibration plots is shown in Fig. 2.10. For every calibration, 20 pairs of impulse and amplitude were measured and its regression line through origin was determined by the least-square method. The coefficient of determination was always higher than 0.99. The calibration coefficient was typically ranged from 50 to 80 μNs/V, according to a thruster.

A high resolution force transducer, ICP®quartz force sensor made by PCB Piezotronics, Inc., was used, whose specifications are shown in Table 2.2. It uses piezoelectric element with built-in IC, and has high sensitivity and high frequency response. An electrical line from the force transducer is connected to a handmade signal conditioner outside the chamber. The electrical circuit diagram is shown in Appendix F.

The impact was varied from 80 to 300 μNs by changing the initial angle of the pendulum. The transducer is 120 mm distant from the rotational axis on the

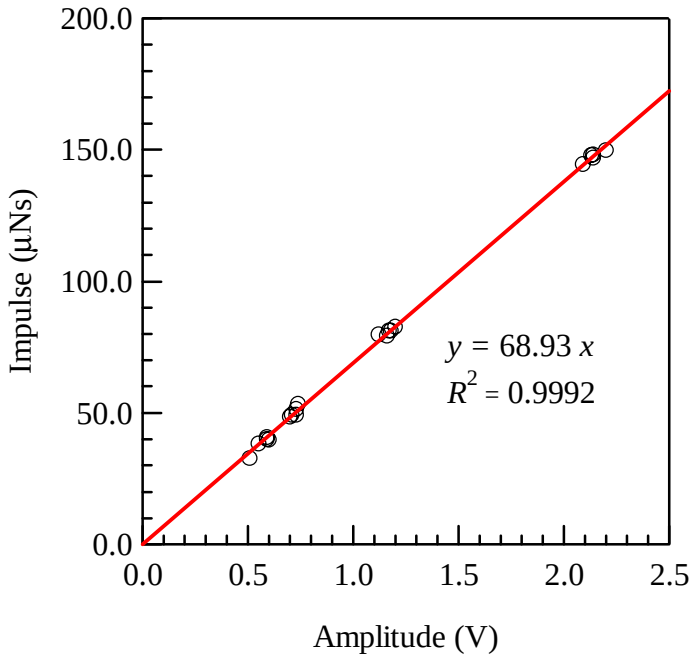

Figure 2.10: Sample of calibration; 20 sets of impulses measured by the force transducer and the associated oscillation amplitude.

balance; a thruster was from 305 mm according to the thruster configuration. The effective impulse delivered to the thrust stand was 20-80 μNs. Figure 2.12 shows the picture of the impact pendulum. The impulse delivered from a pendulum can be written as

$$I_{\text{pendulum}} = \frac{\sqrt{2JMgl_G(1-\cos\phi)}}{l_{\text{hammer}}} \tag{2.6}$$

where l_{hammer} is the distance of the hitting point from the rotational axis, ϕ is the initial angle. Therefore, to carry out small impact to a thrust stand, short l_G and light M are required. The pendulum is made of an aluminum plate with 300 mm length, 10 mm width, and 2 mm thickness. The rotational axis of the pendulum is set at almost center of the plate. On the impact position to a stand, a piece of tape is wrapped in order to extend the impact time between the pendulum and force transducer. Figure 2.13 shows a typical output of the force transducer struck by the impact pendulum. The typical impact time was 2 - 4 ms, which is enough slow impact to detect by the force transducer 209C01. The force waveform of the impact is not a single peak but multiple peaks as shown in the figure. This

Table 2.2: Specifications of a PCB force transducer 209C01.

Average sensitivity	490.7 mV/N
Maximum static force: compression	48.9 N
Broadband resolution (0 to 10 kHz)	0.09 mN
Low frequency response	0.5 Hz
Upper frequency limit	100 kHz
Discharge time constant	$\geq$ 1 s

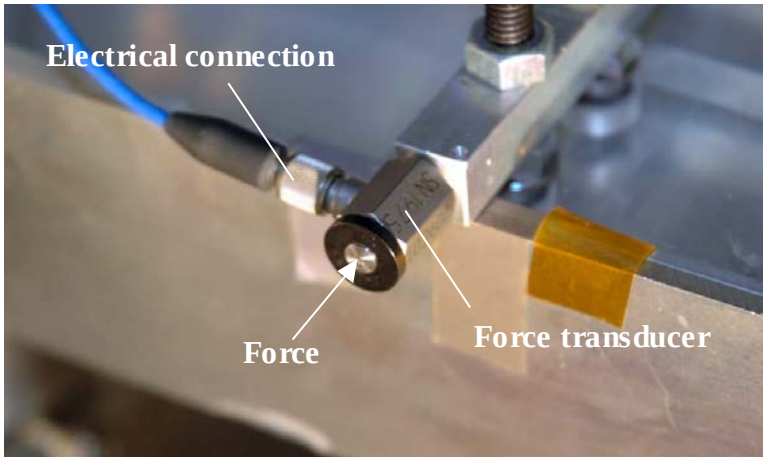

Figure 2.11: Picture of the force transducer 209C01.

multiple impacts would be caused by elastic oscillations of the pendulum during the impact.

The impact pendulum was remotely controlled by rotating a propeller using a DC motor. The remote controlling is necessary because the thrust stand has very high sensitivity and is easily disturbed by the air convection from someone's closing it to operate the pendulum. The propeller can rotate up to the position of a stopper stick and the pendulum is sustained at that position, that determines the initial angle. The position of stopper stick was manually changed, which gives varieties of the impulse. When the propeller was rotated in the counter direction, the pendulum starts to swing and impacts the force transducer. Right after the hitting, the propeller was returned to the initial position in order to prevent the second hit of the pendulum to the stand.

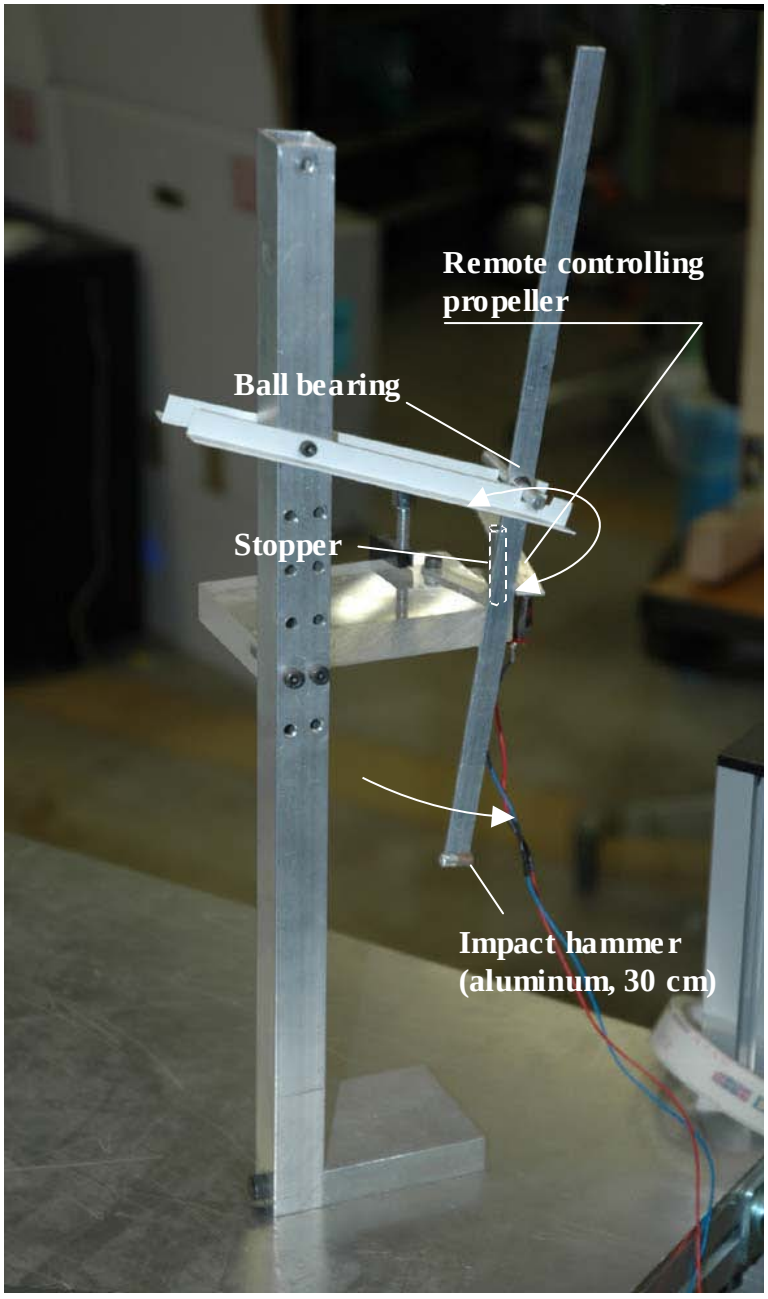

Figure 2.12: Picture of the impact pendulum to strike a force transducer. The pendulum is manipulated by remotely controlling a propeller set on a DC motor.

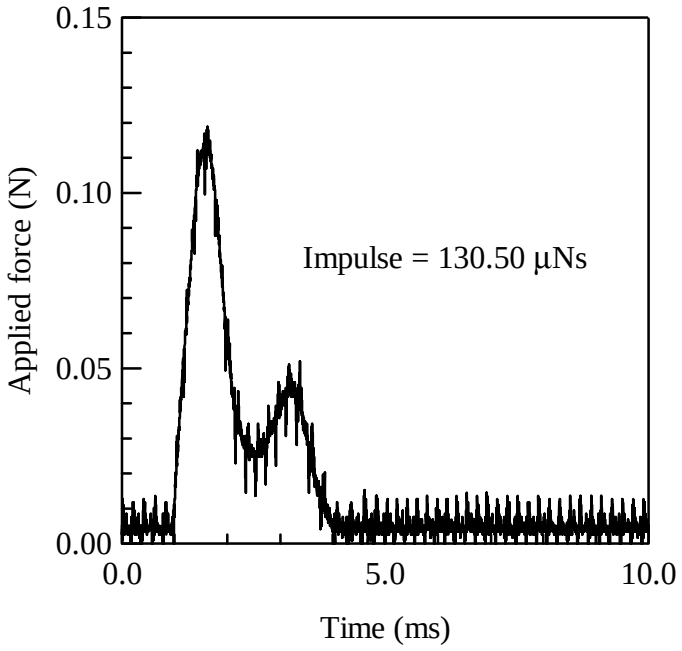

Figure 2.13: Sample of raw output of the force transducer.

It should be noted that it is hopeless to directly measure the force from microthrusters by using a force transducer. The response frequency of the force transducer is determined by its natural frequency of the elastic body (in the case of 209C01, quarts body). The direct measurement requires the higher natural frequency than the characteristic time of the thruster. However, for instance, the force transducer used here had the upper frequency limit of 100 kHz, and thrust of PPTs changes with the frequency of 1 MHz. Thus it is impossible to directly measure the thrust from PPTs. In addition, to directly measure the thrust from thrusters, the force transducer should be mounted to the thruster. The attachment drastically decreases the natural frequency, and response frequency, may be down to a few hundreds Hz. In the case of steady thrust or extremely low thrust frequency, a force transducer can be used to measure the thrust if the following two conditions are satisfied. First, thrusters must be installed on a force transducer, which leads to a lot of difficulty to design thrusters and perform experiments. Secondly, the force transducer must have enough low frequency responce. Some transducers do not have such low frequency resoponse. For instance, the transducer dealt here has the discharge time constant of 1 s and can not be used for

that use (*discharge time* is explained in Appendix A).

2.3 Dynamics of thrust stand

2.3.1 Basic analysis

The momentum equation for the torsional balance is

$$J\frac{d^2}{dt^2}\theta + c\frac{d}{dt}\theta + k\theta \;\; = \;\; l_{\text{force}}F(t) \tag{2.7}$$

where θ is the displacement angle of the balance, J is the moment of inertia of the balance about the rotational axis, c is the coefficient of viscous damping for rotation, k is the coefficient of torsional spring constant, and $F(t)$ is the applied force to the distance l_{force} away from the rotational axis. A displacement sensor measures the distance l_{sensor} away from the axis, and there displacement x can be expressed as $l_{\text{sensor}}\theta$ if $\theta \ll 1$. By introducing the natural angular frequency ω_0 and the viscous coefficient μ, the momentum equation can be written as

$$\frac{d^2}{dt^2}x + 2\mu\frac{d}{dt}x + \omega_0^2 x = \frac{l_{\text{sensor}}l_{\text{force}}}{J}F(t) \tag{2.8}$$

$$\text{where} \quad \omega_0 = \sqrt{\frac{k}{J}} \quad \text{and} \quad \mu = \frac{c}{2J} \tag{2.9}$$

In this study, only impulsive force with $\tau_{\text{force}} \ll \tau_0$ or short time force with $\tau_{\text{froce}} < \tau_0$ is measured, where τ_{force} is the characteristic time of the applied force and τ_0 is the natural period of the balance, $2\pi/\omega_0$. In the special case of the impulsive force, $F(t) = I\delta(t)$, and the stationary initial conditions, $x(0) = 0$ and $\dot{x}(0) = 0$ (short time force is considered in the succeeding section), the solution is

$$x(t) = A\exp(-\mu t)\sin(\omega' t) \tag{2.10}$$

$$\text{where,} \qquad A = \frac{l_{\text{sensor}}l_{\text{force}}}{J\omega'}I \quad \text{and} \quad \omega' = \sqrt{\omega_0^2 - \mu^2} \tag{2.11}$$

If there is no damping,

$$x(t) = A_0\sin(\omega_0 t) \tag{2.12}$$

$$\text{where,} \qquad A_0 = \frac{l_{\text{sensor}}l_{\text{force}}}{J\omega_0}I \tag{2.13}$$

In the operations of the thrust stand, the electromagnetic damper was turned off before the thruster fire, and the oscillation of the balance was measured under

small damping due to some feed lines. Under such small damping effect, the amplitude with damping A and without damping A_0 are related as

$$A = \frac{l_{\rm sensor} l_{\rm force} I}{J\omega_0\sqrt{1-\zeta^2}} = \frac{1}{\sqrt{1-\zeta^2}} A_0 \tag{2.14}$$

$$\simeq \left(1+\frac{\zeta^2}{2}\right) A_0 \quad (\zeta \ll 1) \tag{2.15}$$

$$\zeta = \frac{\mu}{\omega_0} \tag{2.16}$$

where ζ is the damping ratio. Then the damping force affects the amplitude by the second order, and small damping like $\zeta \ll 1$ can be neglected. Actually typical value of ω_0 and μ is 1.5 and 0.01 1/s, and the damping ratio is $0.007 \ll 1$. The associated difference between A and A_0 less than 0.01 %. Therefore the damping is neglected in the following sections, and Eq. (2.12) is used to obtain the impulse.

2.3.2 Analysis for short time force

Here let us to extend the above analysis to the short time force, that is, impulsive force approximation is not valid but the time of applied force is shorter than the natural period. The following force with finite pulse width:$\tau_{\rm pulse}$ is considered

$$F(t) = \begin{cases} I/\tau_{\rm pulse} & , \quad 0 < t \le \tau_{\rm pulse} \\ 0 & , \quad t \le 0,\ \tau_{\rm pulse} < t \end{cases} \tag{2.17}$$

where I means the delivered total impulse. Then the solution for Eq. 2.9 under the force Eq. 2.17 is

$$x(t) = \begin{cases} A_0 \dfrac{1-\cos\omega_0 t}{\omega_0 \tau_{\rm pulse}} & , \quad 0 < t \le \tau_{\rm pulse} \\ A_0 \dfrac{\sin(\omega_0\tau_{\rm pulse}/2)}{\omega_0\tau_{\rm pusle}/2} \sin\omega_0(t-\tau_{\rm pulse}/2) & , \quad t \le 0,\ \tau_{\rm pulse} < t \end{cases} \tag{2.18}$$

A thrust stand has the oscillation amplitude

$$A_{\rm pulse} = A_0 \frac{\sin(\omega_0\tau_{\rm pulse}/2)}{\omega_0\tau_{\rm pusle}/2} \tag{2.19}$$

The comparison of A_0 and $A_{\rm pulse}$ is shown in Fig. 2.14. If the applied force can not be regarded as impulsive force, the oscillation amplitude should be corrected according to Eq. (2.19). In the processes, however, we assumed the rectangular waveform for the applied force and estimate its period. The uncertainties of those lead to error of thrust measurement.

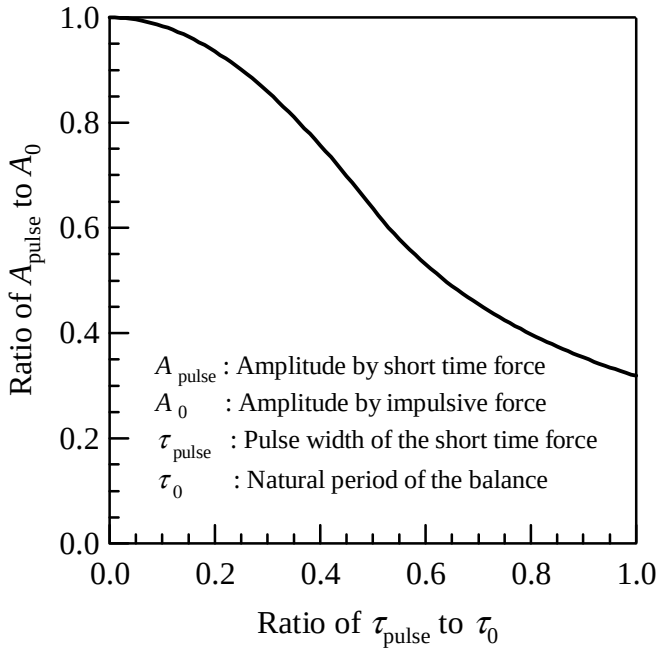

Figure 2.14: Comparison of the oscillation amplitude with impulsive force and short time force.

2.3.3 Analysis for micro-Newton thrust

The most serious problem for micro-Newton thrust measurement is a mechanical noise that is induced on the balance by background vibrations. The oscillation amplitude A_0 is usually obtained by fitting the ideal thrust stand response Eq.(2.12) on the measured displacement history of the balance. However, such measured data always includes the background vibration noise. It includes many components around the natural frequency of the balance that cannot be excluded by a low-pass filter. The associated error becomes serious in case of low impulse measurement, micro-Newton thrust, or on the condition of large mechanical noise.

Herein, a method separating the actual response of the thrust stand from the mechanical noise is established to accurately measure micro-Newton thrust. An additional term which expresses the mechanical noise is added in a fitting function. The real mechanical noise includes a number of harmonic components. It is assumed that the noise can be expressed as a sinusoidal wave with the natural frequency, because mechanical noise includes a harmonic component of the natural

frequency most of all. Let us express the amplitude of the sine component as A_{noise}. Its cosine component is obtained from the position at $t = 0$, namely $x(0)$. Then assume a function

$$x_{\mathrm{f}}(t) = A_0 \sin(\omega_0 t) + A_{\mathrm{noise}} \sin(\omega_0 t) + x(0) \cos(\omega_0 t) \tag{2.20}$$

which is the sum of an ideal thrust stand response and a simulated noise. Constants A_0 and A_{noise} are determined when this function is fitted on measured data. Consequently, the obtained A_0 would include less effect from the noise. The period of this curve-fit should be ranged before the thruster firing to reflect the information of the noise. Hence the curve fit was performed from $-\tau_0$ to τ_0, where τ_0 is the natural period of the balance. The effect of that method and the optimum fitting period will be discussed in Section 2.6.

2.4 Verification of thrust measurement

2.4.1 Pulsed Plasma Thruster

Pulsed plasma thrusters (PPTs) produce electromagnetic force by the interaction of discharge current and its self-induced magnetic field. In 10J class PPTs, the discharge terminates within 10 μs. The period when the thrust is applied is much less than the natural period of the thrust stand developed here (typically 4 s). Therefore PPT thrust can be regarded as impulsive force.

Measured oscillation waveform of the stand was fitted on Eq. (2.12). Stand oscillation by PPT thrust is much larger than noise induced on the thrust stand by background vibration. The impulse of a 10 J class PPT is from 10 to 100 μN, which is controlled by the capacitor-stored energy. The thrust stand addressed here had the mechanical noise corresponding to a few μNs thrust.

Figure 2.15 shows samples of the oscillation waveforms of the thrust stand by a PPT single shot fire. Figure 2.15 a) is the case of 11.5 J capacitor-stored energy and b) is the 2.9 J. Before the firing, the stand was maintained to be quiescent by working the electromagnetic damper. At a few seconds before the firing, the damper was turned off and the stand was set free. At the moment of the PPT fire, the stand starts to move downward (the negative direction of the signal has no mean). Fitted sinusoidal curves show the good agreement with the measured

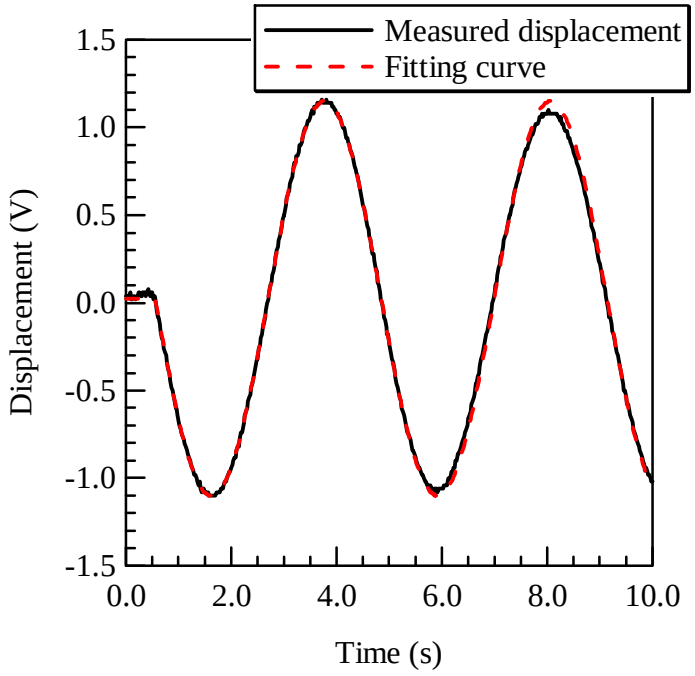

a)

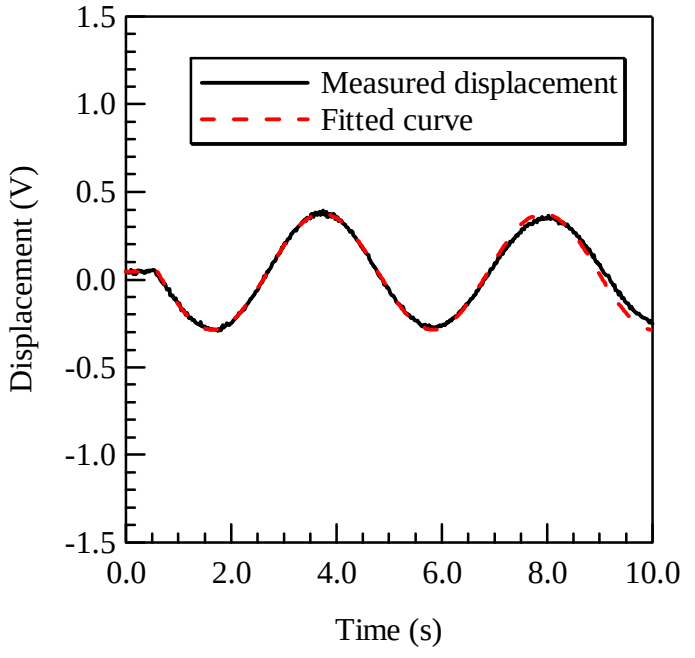

b)

Figure 2.15: Sample of the oscillation waveforms of the thrust stand by PPT firing, capacitor-stored energy of a) 11.5 J and b) 2.9 J.

displacement. In the second cycle of the oscillation, the fitted curve starts to deviate from the measured line a little. The curve-fit was performed only during the first cycle of the oscillation (in precise a little longer than the cycle), and the damping had no effect on the curve fit.

2.4.2 Diode Laser Ablation Thruster

A diode laser ablation thruster generates the thrust by the laser ablation jet and the impulse is mainly adjusted by its laser pulse width. In this study, the pulse was controlled up to one second. Hence the impulsive force approximation is not valid, and short time force analysis Eq. 2.18 should be applied.

In addition, the analysis method described in Section 2.3.3 was used because the impulse level was comparative with the mechanical noise. The maximum thrust of the laser ablation ranged from 10 to 30 μNs according to the ablation materials. Accurate thrust measurement was required to conduct reliable examination for the material selection.

Figure 2.16 shows a sample waveform of measured oscillation and its fitting curve by laser ablation thrust. Figure 2.16 a) is the pulse width of 0.8 s and b) is 0.2 s. In the figure, the damper was turned off before $t = 0$ s and the laser microthruster was fired at $t = 2.0$ s. You see the existence of mechanical noise before the firing. There, noise fitting curve, second and third terms on the right hand side of Eq. (2.20) is also drawn. In the case of Fig. 2.16 a), the noise affected the actual response to decrease the signal, and, in b), affected one to enhance. Introducing the noise curve helped to remove the noise effect from the actual response.

Figure 2.17 shows the effect of the analysis method including noise fitting curve, where the relation of ablated mass and produced impulse is shown. The measured impulses from laser ablation had some variations due to actual variations of exhaust velocity but also mechanical noise. The latter variations were decreased by the data analysis method described in 2.3.3. In the case of normal fitting, namely using Eq. (2.12) as the fitting function, R^2: the coefficient of determination was 0.918. On the other hand, using Eq (2.20), R^2 improved to 0.977.

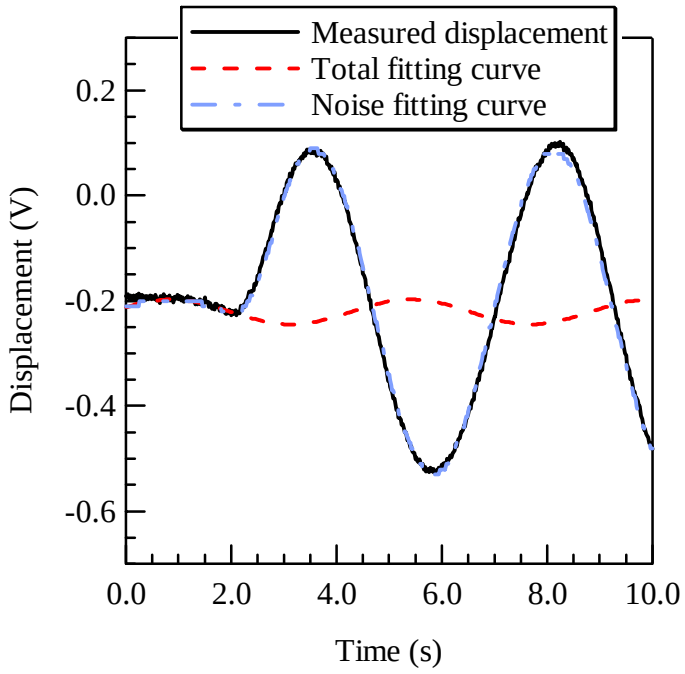

a)

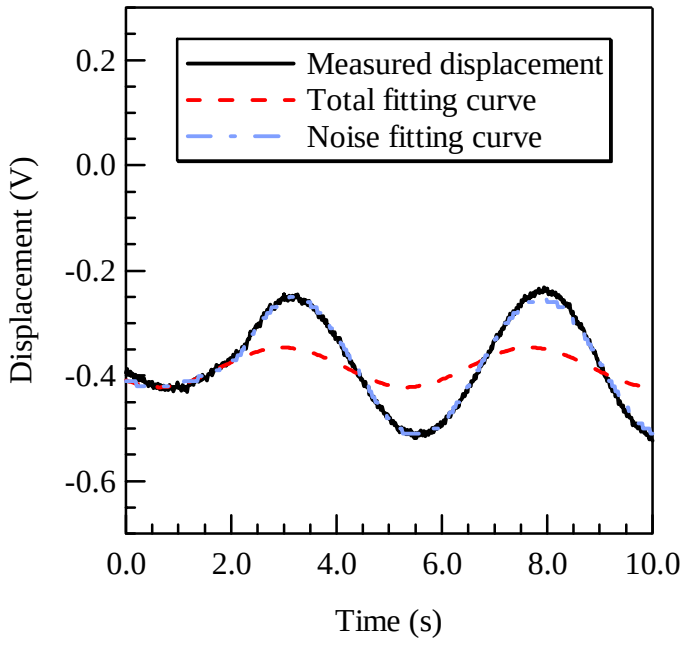

b)

Figure 2.16: Sample of the oscillation waveforms of the thrust stand by laser ablation, the pulse width of a) 0.8 s and b) 0.2 s.

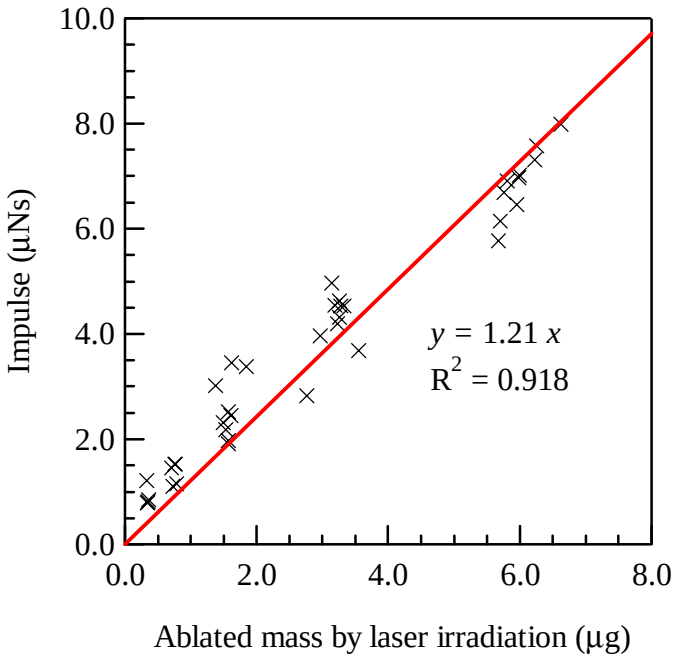

a)

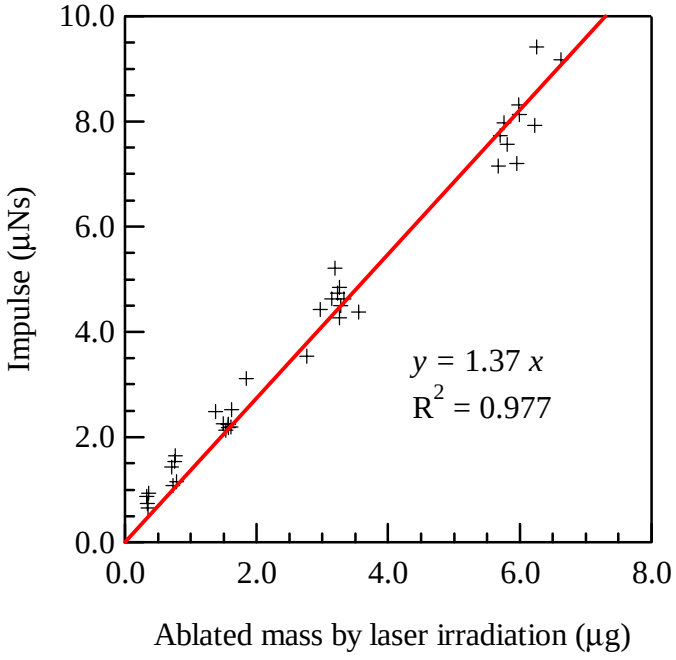

b)

Figure 2.17: Comparison of the analysis methods. The relation of the ablated mass and the impulse, a) result by the normal sinusoidal fitting and b) result by the analysis method including the noise fitting curve.

2.5 Application to huge impulse measurement

Here the thrust stand was customized to measure higher thrust of 10 to 1000 mNs produced by the laser ignition mode. The thrust stand addressed here was designed to measure very small, micro-Newton thrust and the measurable range is up to 10 mNs. It is limited by the movable range of the displacement sensor. When huge impulses over 100 mNs are applied to the thrust stand, the balance oscillates too much, exceeding 100 mm ! Such large deflection will damage the flexural pivots. Hence an alternative displacement sensor and increase of the stiffness are necessary for higher impulse measurement. Moreover, the impact pendulum for the calibration carry the impulse up to 10 mNs even with additional weight, and another impact pendulum for huge impact is necessary.

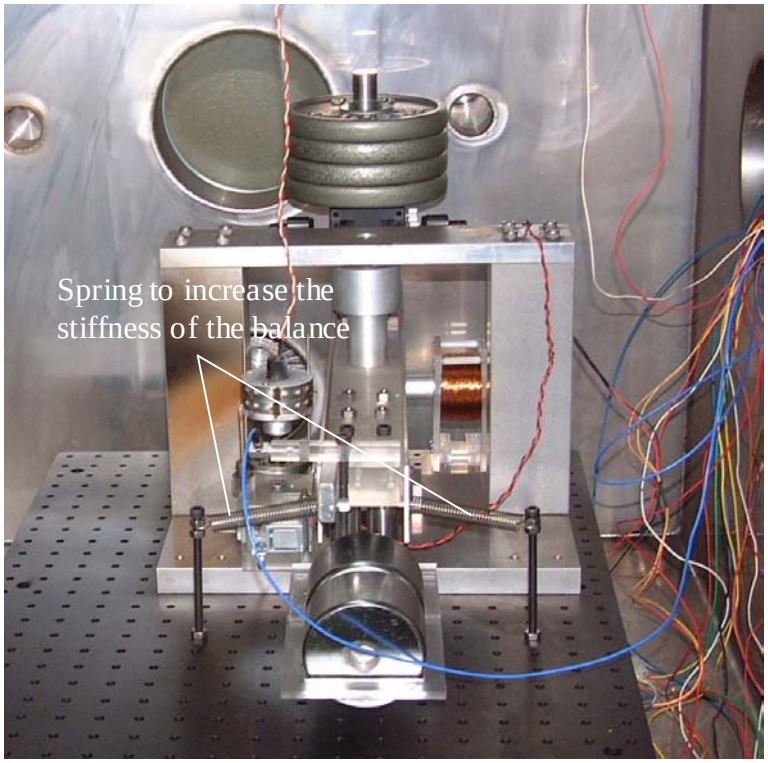

Figure 2.18: Picture of the thrust stand with additional springs and weights to increase the stiffness of the balance.

In order to increase the stiffness of the balance and decrease the sensitivity to the impulse, additional helical springs are installed. The sensitivity of the thrust

stand for micro-Newton thrust was about 0.2 μm/μNs, which means the 0.2 m displacement in the case of 1 Ns. The displacement must be decreased at least down to the level which flexural pivot can endure. The flexural pivot use here has the cycle life of infinite when its deflection angle is within 10 degrees (under light radial loading). It corresponds to the 50 mm displacement of the balance at 300 mm away from the axis. The sensitivity of the stand is inversely proportional to square root of the stiffness and moment of inertia. Thus additional helical springs and 2 - 4 kg weight were installed, shown in Fig. 2.18. Moreover, a thruster was installed at the position of 120 mm. Those decreased the sensitivity of the thrust stand by one tenth, namely down to about 0.02 m/Ns at the edge of the arm.

A laser displacement sensor was used to measure the large deflection of the balance, because the LVDT used here cannot measure the displacement more than 3 mm. It irradiates laser beam on a target and detects its scattering light. Table 2.3 shows the specifications of the laser displacement sensor used here, LK-500 made by Keyence Corporation. The laser beam was irradiated from outside of the chamber through a view port, The sensor was operated using a long range mode with low resolution due to the long distance by the chamber (see Table 2.3). Displacement of the stand was measured at 320 mm away from the rotational axis to increase the resolution.

Table 2.3: Specifications of a laser dispacement senosr (Keyence Corp.).

Model	LK-500 (sensor head) LK-2500 (amplifier)	
Mode	Fine	Long
Detecting distance	350 mm	500 mm
Detecting range	$\pm$100 mm	$\pm$250 mm
Detecting distance	350 mm	500 mm
Light source	Visible red semiconductor laser (690 nm)	
Spot diameter	D 0.7 mm	D 0.3 mm
Resolution	10 μm	50 μm
Sensitivity	10 μm/mV	50 μm/mV

A new calibration hammer was designed for over 100 mNs impulse. The impact

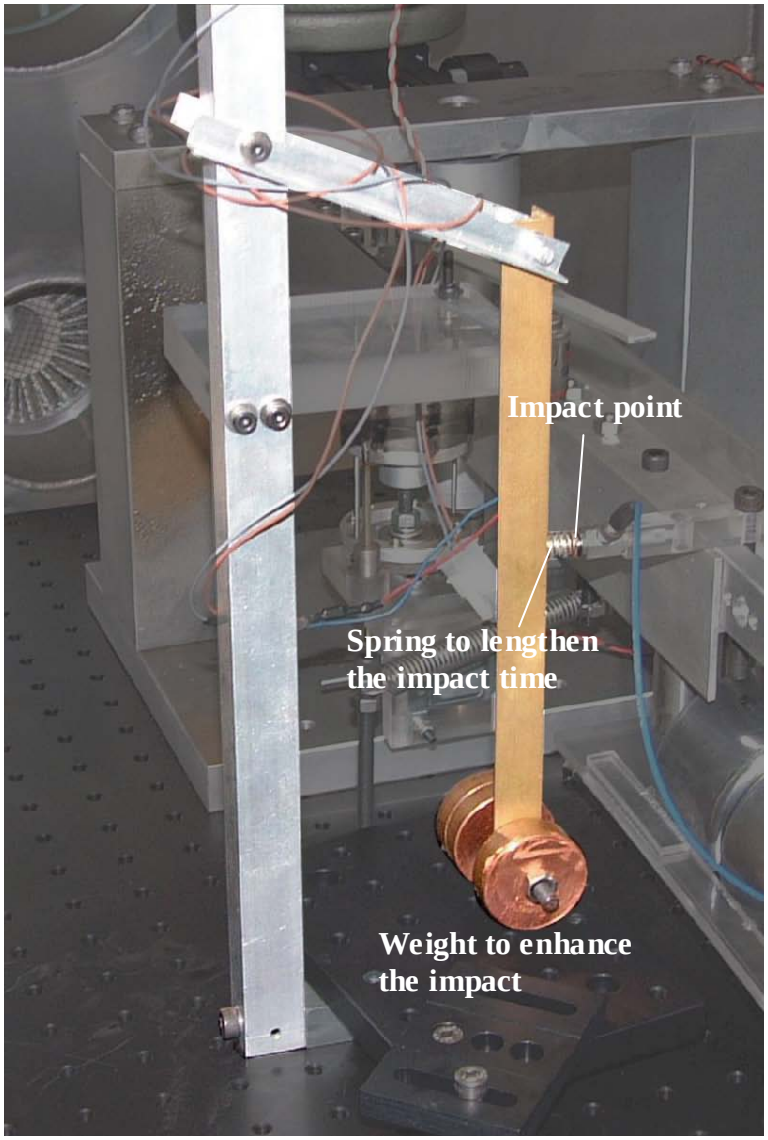

Figure 2.19: Picture of the impact pendulum providing 100 mNs impulse.

hammer shown in Fig.2.12 was designed to deliver very small impulse, which cannot deliver the impulse of over 100 mNs. Impulse delivered from an pendulum is expressed by Eq. 2.6. In the case that the mass M is concentrated at a point l_{mass} away from the axis,

$$l_G \simeq l_{\mathrm{mass}}, \qquad J \simeq M l_G^2, \tag{2.21}$$

and

$$I_{\mathrm{pendulum}} = \frac{M l_G^{3/2} \sqrt{2g(1-\cos\phi)}}{l_{\mathrm{hammer}}}. \tag{2.22}$$

Hence, the shorter the impact point and the longer the gravity center, and the impulse become larger. Figure 2.19 shows the picture of an impact pendulum for huge impulse. It has a long arm with large weight and impact point close to the axis. The pendulum can deliver the impulse from 100 to 300 mNs.

The impact point of the pendulum is made of a spring, copper plate, and silicon rubber plate in order to increase the impact time. In general, impact time against metals is order of 1 ms. The maximum static force of the transducer used here is 48.9 N, and the maximum impulse allowed for the transducer is restricted within about 50 mNs. Therefore, long impact time is necessary to increase that impulse. Here a helical spring of the 4 mm diameter was installed at the hitting point. Figure 2.19 shows the picture of the hammer. That hammer gave enough long impact time. The typical waveform of the force transducer is shown in Fig. 2.20, which has the impact time of about 60 ms. However, this longer impact time induces drift on the output of a force transducer. It is caused by the finite discharge time of a piezo electric force transducer. The correction was performed to correctly remove that drift, whose method is described in Appendix A.

2.6 Error associated with the sinusoidal curve-fit

In this section, we analytically evaluate the error associated with the sinusoidal curve-fit on the measured data. The effect of the analysis method proposed in Section 2.3.3 is compared with the normal sinusoidal curve-fit method in the analysis and experiment.

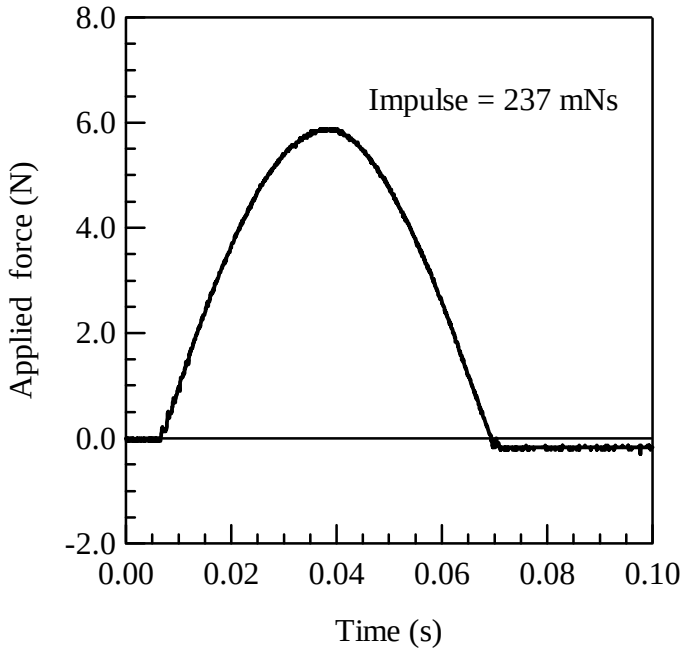

Figure 2.20: Time history of the force transducer output striked by the huge impulse pendulum (Fig. 2.19).

2.6.1 Normal sinusoidal fitting

When an impulsive force is applied to the balance of stationary state, the displacement history of the balance becomes

$$\text{Signal}: \ x_s(t) \ = \ \begin{cases} 0 & t < 0 \\ A\sin(\omega_0 t) & t > 0 \end{cases} \tag{2.23}$$

which is measured as the signal. The amplitude A is related to the applied impulse by Eq. 2.13. However, the balance is not actually stationary. Mechanical vibrations and other kinds of noise are included in the actual data. Then the measured signal always includes noise, which causes error of the impulse measurement. Here this error is analytically discussed for the case in which the amplitude is determined by the least-squares method. First let us express an arbitrary noise of the period $[-l/2, l/2]$ as the Fourier series,

$$\text{Noise}: \ x_N(t) \ = \ \sum_{n=1}^{\infty} A_n \sin(\omega_n t + \delta_n) \ , \ \omega_n \ = \ \frac{2n\pi}{l} \tag{2.24}$$

Amplitudes and phases of its harmonic components are determined from the Fourier series of the noise data. The actually measured signal is the summation of the ideal wave and noise waves, that is $x_s(t) + x_N(t)$. When a fitting function:

$$\text{Fitting curve}: \; x_f(t) \;=\; A_f \sin(\omega_0 t) \tag{2.25}$$

is fitted on the data with the period $[0, NT_0]$, where N is the arbitrary natural number ($N = 1, 2, 3 \ldots$), the squared deviations is

$$\Pi \;\equiv\; \int_0^{NT_0} dt \left[x_s(t) + x_N(t) - x_f(t)\right]^2 \tag{2.26}$$

$$\;=\; \int_0^{NT_0} dt \left[(A - A_f)\sin\omega_0 t + \sum_{n=1}^{\infty} A_n \sin(\omega_n t + \delta_n)\right]^2 \tag{2.27}$$

Differentiating Eq.2.27 with respect to A_f and setting it equal to 0 give the amplitude A_f such that the squared-deviations achieves the minimum value. After a few algebraic manipulations, the amplitude is obtained as

$$A_f \;=\; A + \sum_{n=1}^{\infty} A_n I_n^{(0,NT_0)} \tag{2.28}$$

$$I_n^{(T_1,T_2)} \;\equiv\; \frac{2}{T_0}\int_{T_1}^{T_2} \sin\omega_0 t \sin(\omega_n t + \delta_n) dt \tag{2.29}$$

where the first term of Eq. 2.28 is the actual amplitude and the second term indicates the error caused by the noise Eq. 2.24. Our interest is in the ensemble averages and variances of the obtained amplitude. Phases of the harmonic components are random within 0 to 2π because the noise is assumed to be a random process. Hence,

$$< \sin(\omega_n t + \delta_n) > \;=\; 0 \tag{2.30}$$

$$< I_n^{(0,NT_0)} > \;=\; 0 \tag{2.31}$$

where $< \cdot >$ denotes the ensemble average; hence

$$< A_f > \;=\; A \tag{2.32}$$

The mean value determined by the least-squares method agrees with the real value (trivial). Next, we calculate the mean square to obtain the variance.

$$< A_f^2 > \;=\; < \left(A + \sum_{n=1}^{\infty} A_n I_n^{(0,NT_0)}\right)\left(A + \sum_{m=1}^{\infty} A_m I_m^{(0,NT_0)}\right) > \tag{2.33}$$

$$= A^2 + \sum_{n,m}^{\infty} < A_n A_m >< I_n^{(0,NT_0)} I_m^{(0,NT_0)} > \quad (2.34)$$

$$= A^2 + \sum_{n}^{\infty} < A_n^2 > w_{(0,NT_0)}(\omega_n/\omega_0) \quad (2.35)$$

$$w_{(0,NT_0)}(x) \equiv \frac{2}{N^2\pi^2}\frac{\sin^2(N\pi x)}{(1-x^2)^2} \quad (2.36)$$

where

$$< I_n^{(0,NT_0)} > = 0 \quad (2.37)$$

$$< I_n^{(0,NT_0)} I_m^{(0,NT_0)} > \text{ and } = \begin{cases} 0 & , \quad n \neq m \\ w_{(0,NT_0)}(\omega_n/\omega_0) & , \quad n = m \end{cases} \quad (2.38)$$

were used. To consider non periodic random process noise, let $l \to \infty$. Then the summation becomes an integral. Using the relation

$$\lim_{l\to\infty} \frac{l}{4} < A_n^2 > = 2\pi S(\omega) \quad (2.39)$$

the means-squared of the amplitude becomes a power spectrum density S(ω). The definition and detailed explanation on the power spectrum density is described in the reference[61]. Hence,

$$\frac{1}{2} < A_f^2 > = \frac{1}{2}A^2 + \int_{-\infty}^{\infty} w_{(0,NT_0)}\,(\omega/\omega_0)\, S(\omega) d\omega \quad (2.40)$$

Derivations of Eqs. 2.39 and 2.40 are shown in Appendix C.

Finally, we obtain the expression of the variance

$$\sigma^2 = \int_{-\infty}^{\infty} w_{(0,NT_0)}\,(\omega/\omega_0)\, S(\omega) d\omega \quad (2.41)$$

Generally the integral of power spectrum of the random process gives its mean-square value of it. The function $w_{(0,NT)}(x)$ can be regarded as a weighting function, which is shown in Fig. 2.21. Therefore the weighting function for $N = 1$: $w_{(0,T_0)}(x)$ has a large peak at $x = 0.8374$ with width of 0.4 to 1.3. Hence, noise near the natural frequency contributes greatly to the variance. In contrast, the higher frequency component contributes little to the curve fit error because the function decreases biquadratically (see Eq. 2.36). The position of the peak shifts toward $x = 1$ as the fitting period increases, with touching on the curve of $N = 1$; the peak width becomes narrow.

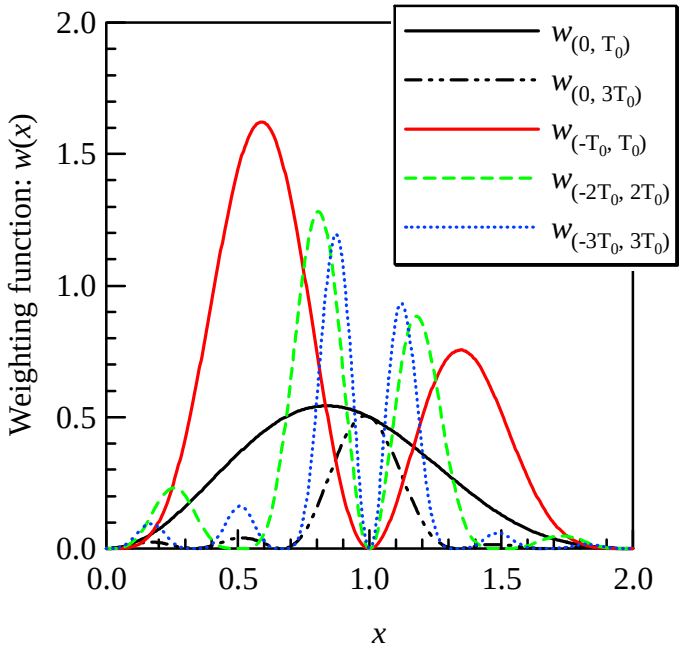

Figure 2.21: Weighting functions according to fitting periods; $[0, T_0]$, $[0, 2T_0]$, $[-T_0, -T_0]$, $[-2T_0, -2T_0]$, and $[-3T_0, -3T_0]$.

2.6.2 Curve-fit including noise effect

Next, let us consider the case in which a function:

$$x_f^*(t) = \begin{cases} 0 \quad + A_N \sin\omega_0 t + x(0)\cos\omega_0 t & t < 0 \\ A_f^* \sin\omega_0 t + A_N \sin\omega_0 t + x(0)\cos\omega_0 t & t > 0 \end{cases} \tag{2.42}$$

is used as a fitting function and the fitting range is $[-NT0, NT0]$, where N is again arbitrary natural number. Then the squared deviations is

$$\Pi^* \equiv \int_{-NT_0}^{NT_0} dt \left[x_s(t) + x_N(t) - x_f^*(t)\right]^2 \tag{2.43}$$

Amplitude A_f^* is determined in the same way, as

$$A_f^* = A + \frac{1}{N}\sum_n^{\infty} A_n \left(I_n^{(0,NT_0)} - I_n^{(-NT_0,0)}\right) \tag{2.44}$$

where 2.43 is differentiated with respect to both A_f^* and A_N and the simultaneous equations are solved for A_f^*. The mean value also agrees with the real value and the variance becomes

$$\sigma^2 = \int_{-\infty}^{\infty} w_{(-NT_0,NT_0)}^*(\omega/\omega_0)\, S(\omega) d\omega \tag{2.45}$$

$$w^*_{(-NT_0,NT_0)}(x) \equiv \frac{8}{N^2\pi^2}\frac{\sin^4(N\pi x)}{(1-x^2)^2} \tag{2.46}$$

The variance is again expressed as the integral of the power spectrum and another weighting function, $w^*_{(-NT_0,NT_0)}(x)$. The weighting functions for $N = 1$, 2, and 3 are shown in Fig. 2.21. All those functions become zero at $x = 1$. Thereby the contribution of the noise of the natural frequency is greatly eliminated. They have two larger peaks on both sides of it than the peak of normal fitting. In general, the mechanical noise has a sharp peak at the natural frequency, and contributions from those side peaks are not serious.

Figure 2.22 shows the power spectrum calculated from the measured noise. It has a strong and sharp peak at the natural frequency. The integral of Eq. 2.45 was calculated for each weighting function using this spectrum. Table 2.4 shows the result with variances obtained from the actual fitting of the 210 data. Variances calculated from the theory using Eq. 2.45 agreed well with variances obtained by fitting the Eq. 2.25 or 2.42 to the 210 artificial data. Therefore, Eq. 2.45 was shown to be valid to estimate the variance which would be generated when the amplitude was obtained by the actual curve fit.

Table 2.4: Mean values and variances of obtained amplitudes from three different analysis methods: a normal fitting and a sinusoidal wave with a noise wave.

Fitting range	$[0, T_0]$		$[-T_0, T_0]$		$[-2T_0, 2T_0]$	
	μ	σ^2	μ	σ^2	μ	σ^2
Predicted value*	1.0000	0.0299	1.0000	0.0122	1.0000	0.0105
Measured value	1.0020	0.0306	0.9995	0.0124	Na	Na

* using Eq. 2.45

Here we conclude that the variance of the amplitude determined by least-squares method can be obtained as the integral of power spectrum density times an appropriate weighting function. Therefore, in order to minimize the associated error, we should measure the power spectrum of the mechanical noise on the balance and then select the best fitting function and period that minimize the integral of Eq. 2.45. For instance, in our experiment, the optimum fitting method

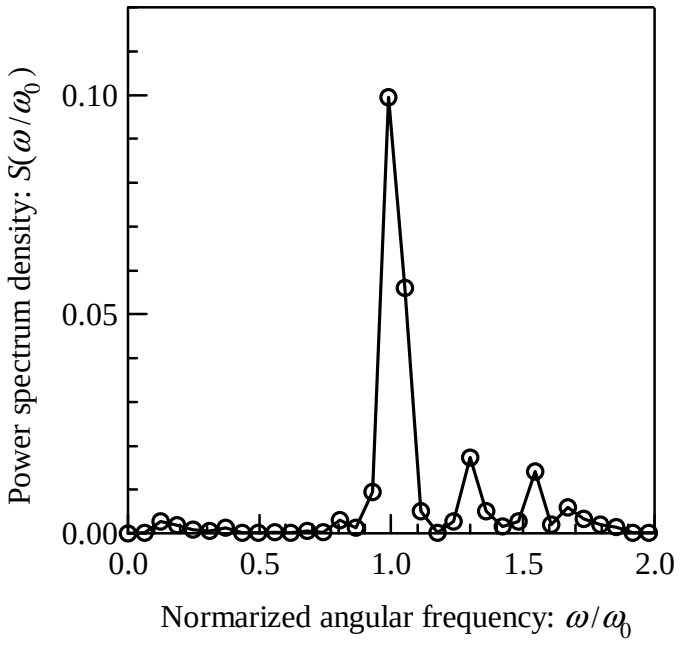

Figure 2.22: Power spectrum density of the mechanical noise, calculated by FFT from measured displacement of the balance.

was the fitting function Eq. 2.42 and fitting period $[-2T_0, 2T_0]$ which would reduce the variance down to 0.0105 (see Table 2.4).

2.7 Accuracy of the impulse measurement

Error of impulse measurement would be induced by the following causes: noise on the displacement sensor, resolution of a force transducer, resolution of a digital oscilloscope, accuracy of the position of a thruster and force transducer, deviation of angle of the thrust vector, etc. Noises on the displacement sensor include mechanical noise and other electrical noises. However, only a low frequency mechanical noise induces errors on the curve fitting procedure and the other high frequency noises contribute little (see the previous section). In experimental conditions dealt in this study, the standard deviation of the mechanical noise was 1.1 μNs against the thruster impulse of 1 to 80 μNs. The force transducer resolution was 90 μN from Table 2.2. The digital oscilloscope resolution corresponded to 0.4 μNs of

impulse. Both position of the force transducer and the angle of the thrust vector axis of thruster were set within the accuracy of 0.3 mm and 5 degrees respectively.

First, presume an error caused by a mechanical noise, inducing shot to shot variation when the amplitude of the balance is estimated from displacement data. The accuracy of the amplitude determined by the curve fitting under arbitrary noise was discussed theoretically in the above section. According to that result, if normal sinusoidal fitting is performed, the associated error of the amplitude would be 1.0 μNs. In contrast, if a fitting function of Eq. 2.20 is used, this error would be decreased down to 0.6 μNs of impulse

Secondly, the accuracy of the calibration constant is addressed. It is given as

$$\alpha = \frac{I_{\text{pendulum}} l_{\text{sensor}}}{A l_{\text{pendulum}}} \tag{2.47}$$

where I_{pendulum} is impulse measured by the force transducer and l_{pendulum} is its position from the rotating center of the balance. The uncertainty of the averaged value of I_{pendulum} over A can be reduced by increasing the number of measurement points. Actually the measurement was performed about 20 times in the every experiment, and those effects was found almost negligible. Uncertainty arose mainly from the error of position measurements of l_{sensor} and l_{pendulum}. Consequently, a typical calibration constant was 49.5$\pm$1.2 μNs/V. The total error of impulse measurement is affected by the errors of both calibration constant and measured amplitude,

$$\Delta I^2 = \Delta\alpha^2 A^2 + \Delta A^2 \alpha^2 \tag{2.48}$$

where ΔA and $\Delta\alpha$ are the uncertainties of the amplitude and calibration constant respectively. If $\Delta A/A > \Delta\alpha/\alpha$, the amplitude error becomes dominant; thereby, the improved analysis method, curve fit including noise data, would be valid, and vice versa. For instance, for impulse of 10 μNs, where the error from the measured amplitude was dominant, the total error would be 1.0 μNs if normal sinusoidal fitting were used. If the fitting function Eq. 2.20 were used, this value would be decreased down to 0.6 μNs. On the other hand, for impulse of 100 μNs, the total error was 2.6 μNs, where the error caused by calibration constant was dominant. Accuracy of positions of the thruster and force transducer becomes particularly important.

2.8 Conclusions of Chapter 2

In this chapter, a thrust stand for micropropulsion was developed and the following conclusions were obtained.

- It is shown that the thrust stand has high resolution and high accuracy and it can be applied for wide varieties of micropropulsions. The resolution was less than 1.0 μNs and the accuracy is within 2.0 %. That thrust measurement was examined using thrusters of the weight up to 2.0 kg (the stand was designed to endure thruster weight over 10 kg). The measured thrust was 1 to 30 μNs in the laser ablation thrustr, 20 to 100 μNs in a pulsed plasma thruster, and 10 and 500 mNs in a laser ignition thruster.

- To increase the resolution on micro-Newton thrust measurement, accurate adjustment of the gravity center ($<$10 μ m) and effective damping of the stand are essential.

- A fitting-curve was newly proposed to removing the mechanical noises induced by background vibrations. That effect was analytically clarified and experimentally verified.

Chapter 3

Dual Propulsive Mode Laser Microthruster

3.1 Introduction

3.1.1 Micropropulsions for 1-10 kg Microspacecraft

Recently several laboratory and flight models of 1-10 kg class microspacecraft have been developed and successfully launched by several researchers and universities' students team[2, 3, 4, 5]. Those microspacecraft have conducted the observation of the earth, measurement of the upper atmosphere, and so on. Increasing activities to develop such 1-10 kg microspacecraft is motivated by their reasonable cost for the launching and developing. They are manufactured using commercially available components, in contrast to highly functional spacecraft using, extremely expensive, special components. The microspacecraft are launched as piggy-back satellite or using an economical rocket of Russia. They make universities' student teams possible to design, fabricate, and launch the microspacecraft, which is also expected as an effective educational course.

In the current stage, however, most of such microspacecraft conducts only very simple missions as demonstrations. Severe limit of weight and size restricts the functions of spacecraft. Especially lack of the propulsion systems make the mission variety to be limited. In order to enable advanced microspacecraft missions, such as formation flying, a microthruster suitable for such microspacecraft is needed. The micropropulsion installed to the spacecraft would realize a number

of advanced and attractive missions as described in Chapter 1, like formation flying, maintenance of mother spacecraft, probe satellite for deep space exploration expected as promising utilization of microspacecraft.

3.1.2 Dual propulsive mode microthruster

Here, a novel type of microthruster enabling multiple propulsive tasks is proposed, that is a dual propulsive mode laser microthruster. Recently several types of microthrusters are proposed and developed as reviewed in Section 1.3. However, there has been no microthruster which has enough compact size and provides widely ranging thrust yet. The microspacecraft envisioned here has a weight of less than 10 kg and characteristic length of 10-20 cm. In such microspacecraft, the space allowed for the propulsion system would be strictly limited, typically less than 0.5-1.0 kg and dimensions of 5-10 cm including a power source used for the propulsion. With satisfying such limits, propulsion system must provide thrust ranging from lower to higher thrust of 1 μN to 1 Ns. Therefore it is essential to satisfy the requirement with the same propulsion system. To our knowledge, there is as yet no single propulsion system which can supply such a wide range of thrust for the 1-10 kg class microspacecraft.

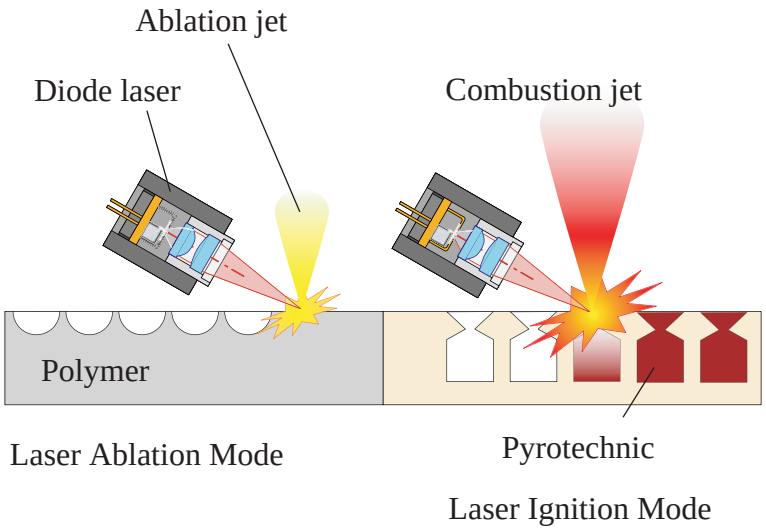

Figure 3.1: Conceptual diagram of the laser abaltion mode and laser ignition mode.

Our microthruster has dual propulsive modes using a diode laser. Its propellant consists of polymeric and pyrotechnic materials. When the laser beam irradiates the surface of the polymer propellant, the laser ablation jet generates low thrust: laser ablation mode. The thrust is controlled by the laser pulse width, and fine adjustment of the thrust is enabled. When the laser irradiates and ignites the pyrotechnic material, which is loaded in the arrayed small chambers, higher thrust is generated by the solid propellant combustion: laser ignition mode. The thrust is roughly controlled by the mass of the loaded pyrotechnic material, and it is predetermined during the thruster design process. Figure 3.1 shows a conceptual diagram of the two modes. In the laser ablation mode, the laser beam provides energy to the ablation jet, and in the laser ignition mode, it plays a role of an ignitor for the solid propellant.

The two modes can be easily interchanged by changing the location irradiated by laser beam. The greatest benefits of our thruster are "compactness" and "wide thrust range." We believe that compactness is the most important feature for the microthruster and, to our knowledge, there is no thruster which can supply thrust over the four orders of magnitude using a single propulsion system and can be installed in a 1-10 kg microspacecraft.

3.1.3 Propellant Feeding System

One of the most important components for a laser microthruster is a propellant feeding system. The solid propellant or diode laser must be translated after every shot. That function is always necessary in the laser ignition mode. In the ablation mode, it will be shown in the experiment that the multiple shots at the same beam spot decreases the impulse. Hence we must have a certain mechanical system feeding new propellant for laser beam, and such system should be compact, light, and tough. In very small micropropulsion less than a few hundreds grams, such mechanical systems will dominate a large fraction of the system. Therefore proposing the effective feeding mechanism is essential to develop a superior micropropulsion system.

A prototype laser microthruster designed by Phipps and Luke [48] was using polymer tape as the propellant. Rolling up the tape-shaped propellant saves the space for propellant storage. However, it needs two axes motions of the propellant,

rolling and traversing the tape. Otherwise only a fraction of entire tape can be utilized. Additionally, more than two rollers (pinch and extension rollers) are needed to effectively roll the tape, which causes increase of the construction weight. Moreover, the most problem of such tape-shaped propellant is the difficulty to loading pyrotechnic propellant in the same propellant with ablative material.

We propose a new type of propellant feeding system which enables the effective use of propellant by a simple mechanism, suited with the laser ignition mode. The propellant has a cylinder shape. Ablative materials are rolled on it or the cylinder itself is made of ablative materials. Pyrotechnics of laser ignition mode are loaded into chambers prepared inside the cylinder. It means that both laser modes can coexist in a single feeding system. Additionally, it requires only one rotational axis to use the whole cylinder sufrace, because the cylinder rotates and proceeds along axis by screw motion. The conceptual diagram is shown in Fig. 3.2. This propellant feeding system makes it possible to effectively use the entire surface of the cylinder using a single rotating mechanism. We have designed a prototype thruster with that feeding mechanism and used it to demonstrate the operation of laser ablation and ignition.

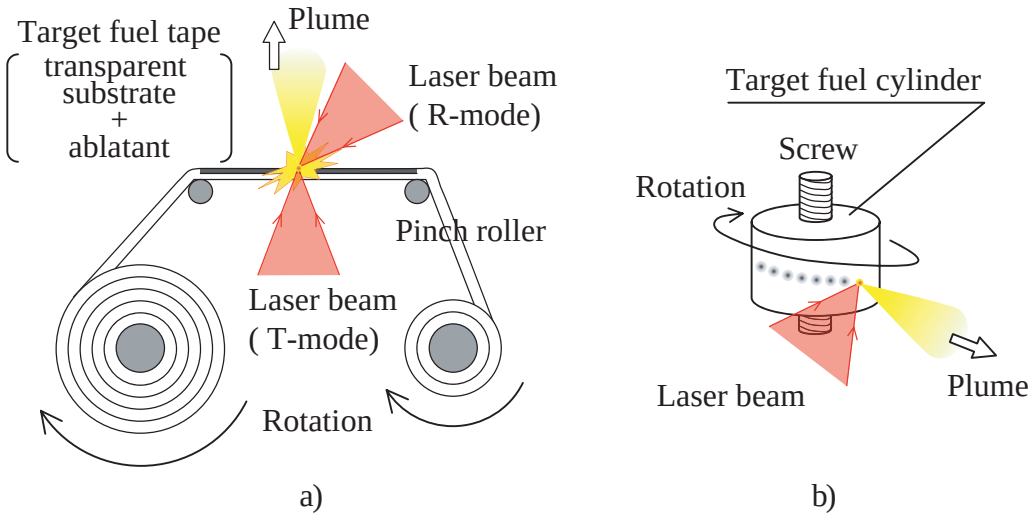

Figure 3.2: Conceptual drawings of propellant feeding systems; a) tape-shaped propellant and b) cylinder-shaped propellant.

3.1.4 Lens Fouling Problems

Lens fouling could be a crucial problem for laser-using thrusters. In this work, a transparent wall was installed between the optical assembly and the propellant. In the laser ablation experiment, it was confirmed that at least 1500 shots of laser ablation gave no effect on the laser optical system and thruster performance. On the other hand, the combustion of pyrotechnics largely affected the transparency of the protection wall. Hence the circular protection wall was rotated after every shot and supplied new transparent surface for the laser beam.

However, such protection system used here is not practical to the actual application. That protection window needs somewhat large system, and other simpler and more reliable protection system is necessary. Here we present three ideas to protect the optical system:

- Use of optical system with long focal length.
- Use of moving protection wall or tape.
- Application of *transmission mode*

Long focal length decreases the lens fouling because contamination to lens system would quadratically decrease with the focal length. However, this is not a perfect protection, and durability test should be performed for each thruster. Moving protection wall or tape can solve the fouling problem. A rolled transparent tape would be useful because of the comapactness. As mentioned above, however, such system needs another mechanics, and leads to the down of the durability and reliability. *Transmission mode* means laser irradiation through a transparent material from the opposite direction to the plume-generated side, whose conceptual diagram is shown in Fig. 3.3. In this mode, there is no matter about lens fouling. Phipps et al. [48, 49] proposed the transmission mode for diode laser ablation thrusters and investigated the difference from the reflection mode (irradiation from the same direction as the plume). The disadvantage is the reduction of the thrust performance in the laser ablation when using the transmission mode, which was shown by Phipps et al. in the reference[48, 49].

One Newtown class microthruster addressed in Section 3.6 utilizes the transmission laser irradiation in laser ignition mode. The laser was irradiated from the

axis toward the outward in radial. Figure 3.3 is an illustration of an application of transmission mode for laser ablation and ignition.

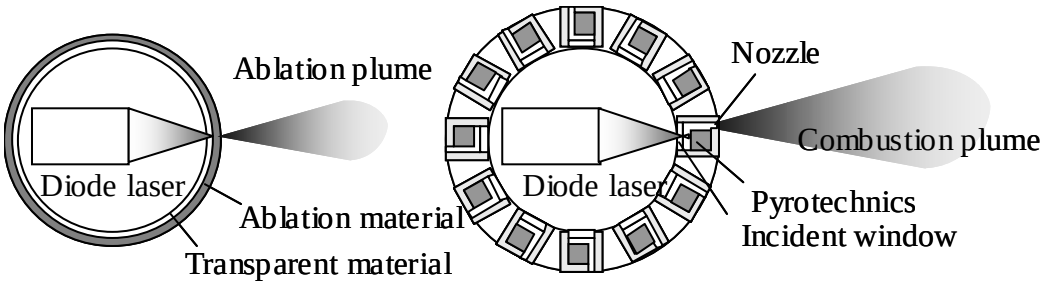

Figure 3.3: Conceptual drawings of transmission modes for laser ablation and ignition.

3.1.5 Objectives of this chapter

The objectives of this chapter are verifying the operation and clarifying the fundamental characteristics of a dual propulsive mode laser microthruster. The characteristics of above-mentioned laser ablation and laser ignition modes are separately investigated. Both modes use the same propellant feeding system and can be interchanged by the variety of the propellant, polymer or pyrotechnic.

Laser ablation mode

A number of studies have been conducted in the field of laser ablation. They are commonly not for the laser ablative propulsion but for various industrial applications, laser machining, laser hardening, laser deposition and so on. Then physical processes included in the laser ablation have been well studied [62, 63, 64, 65, 66, 67]. The processes include absorption of laser irradiation, heating the ablative material by the energy, and the phase transformations. However, there are a few studies on the characteristics unique on propulsions (thrust and Isp) and those dependence on the laser parameters. Moreover, most studies on the laser ablation are using high intensity lasers (CO_2, excimer, and YAG) and with extremely short pulse. The typical laser intensity is over 10^8 W/m^2 and the laser pulse width is less than 10^{-6} s in many researches. In contrast, laser beam dealt here is an infrared

laser with lower laser intensity (1 MW/m^2) and longer pulse width (100 ms). The laser ablation physics of those levels has not been focused in this field.

Therefore in this study, first the ablative materials are selected to generate ablative plume using a diode laser. As a result polyvinyl chloride is considered as the best material and the fundamental thruster performances: plume direction, momentum coupling coefficient, specific impulse, and multiple shots effect are measured with changing the laser pulse width. Next, to clarify the ablation mechanism, effect of doped carbon density and mass spectroscopy of the exhausted plume are investigated. In the discussion, photothermal ablation model is applied in the diode laser ablation processes. It consists of thermal heating and ablating processes. Analytical expressions are derived and compared with the experimentally measured results.

Laser ignition mode

Several researchers have studied on the laser ignition of chemical propellants [68, 69, 70, 71, 72, 73]. The ignition using laser benefits from the high intensity and the electrical insulation. They observed that the ignition depends on a thermal mechanism, and the incident laser energy and the laser power density control the ignition threshold. They also noticed that the laser energy required for the ignition decreases as the laser power is increased. However, most of them have conducted the experiments in the atmosphere. Only a few studies were carried out in the lower background pressure [70]. Additionally, different kind of lasers, focusing, and pyrotechnics were used in those studies.

The objectives are first to verify the laser ignition of pyrotechnic in vacuum, secondly to measure the thrust provided by the combustion, and thirdly to clarify the required laser conditions for the ignition. In the experiment, after examining several pyrotechnics, only boron/potassium nitrate succeeds to be ignited in vacuum. The laser ignition characteristics are investigated against by laser pulse width and laser power. The obtained threshold laser parameters should be adequate to coexist with laser ablation mode to veryfy the concept of a dual propulsive mode. Thereafter the thrust measurement is performed. In the discussions, the reason why boron/potassium nitrate is adequate to the laser ignition in vacuum is considered. It is shown that the measured threshold laser power and period for the

ignition is explained by three dimensional numerical calculations with exothermic reaction.

3.2 Experimental Setup

3.2.1 Vacuum facilities

Experiments on the laser ablation mode were performed in a 1.1-m-diam, 1.8-m-long vacuum chamber, referred as UT cyrindrical chamber in this thesis. The chamber is made of stainless steel and evacuated using two stage pumps: rotary pump and turbo molecular pump. The base pressures were between $2 - 5 \times 10^{-5}$ Torr. The inner pressure was measured using a ionization vacuum gauge.

Experiments on the laser ignition mode were performed in a 0.9-m-cubic stainless steel vacuum chamber, which is in Tokyo Metropolitan of Aeronautical Engineering. That chamber is referred as TMAE cubic chamber in this thesis. The base pressures was between $1.4 - 3.0 \times 10^{-4}$ Torr.

More explanations about those vacuum facilities are described in Appendix B.

3.2.2 Diode laser and optical system

The optical assembly employed a 1 W diode laser with the wavelength of 980 nm and the focal length of 14 mm, the beam waist size of 1.0 mm $\times$ 0.05 mm, and the maximum power density of 5 MW/m^2. A one Watts multi mode diode laser L9801E3P1 made by Thorlabs inc. was used and its characteristics is shown in Table 3.1. Focusing assembly consisted of focusing tube optics, LT2302260P-B (Thorlabs inc.), which includs a lens pair C230260P-B (Thorlabs Inc.). The picture

Table 3.1: Optical, electrical characteristics of the diode laser, L9801E3P1.

Power	1 W	Wavelength	980±5.0 nm
Threshold current	160 mA	Beam divergence (FWHM)	8 × 40 deg.
Operating current	1100 mA	Emitter size	100 × 1 μm
Operating voltage	1.8 V	Slope efficiency	0.9 W/A

and schematic diagram of the laser optical system: laser, optics, and holding tube are shown in Figs. 3.4 and 3.5. The focal length can be adjusted changing the position of the lens pair, and here the typical length was 15.3 mm as shown in the figure.

Figure 3.4: Picture of the diode laser optical system: diode laser, collimation tube, and focusing lens.

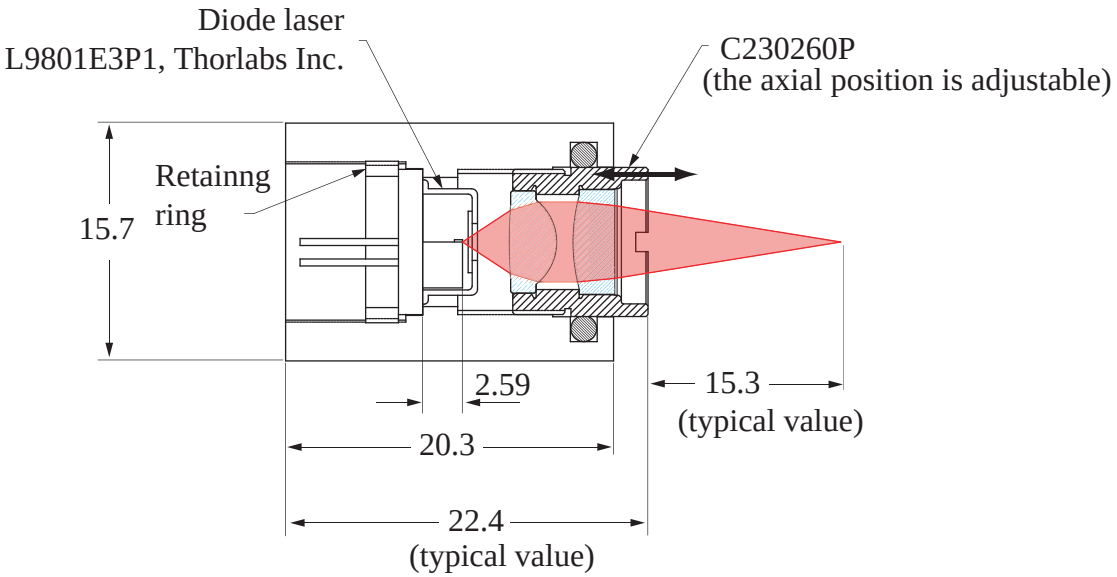

Figure 3.5: Schematic diagram and dimensions of the diode laser optical system: diode laser, collimation tube, and focusing lens.

3.2.3 Laser diode driver

Two varieties of laser diode drivers are used to drive the diode laser. In the experiments on the laser ablation mode, WLD3343 made by Wavelength Electronics Inc. was used. It can supply laser diode current up to 2 A from a single +5 V power supply and operate with constant current mode or constant power mode. The output current and the operation mode were selected by the external connections. The laser pulse width is controlled by TLT signal from a controlling PC. The output current from the driver dealt here had a lot of high frequency ripples with DC current. However, the ripples were neglected and the driver was used to perform the experiment, because the laser pulse width was more than 50 ms and much lower than the frequency of those ripples. The laser beam power emitted from the diode laser was about 300 mW, which was measured using a power meter (LM-10 from Coherent Inc.).

In the early stage of the experiments on the laser ignition mode, the same laser driver as the laser ablation mode was used. Thereafter, another diode laser driver, LP3000 made by Thorlabs inc. was used. The laser pulse width was determined by a controlling PC as well as the laser ablation mode. The diode laser was operated with the beam power ranged from 300 to 1000 mW.

3.2.4 Beam profile of diode laser

Beam profile from the diode laser was taken using a CCD beam profiler. Generally laser beam emitted from a diode laser has astigmatic elliptical wavefront profile, because the lasing cavity has rectangular configuration with high aspect ratio (the diode laser used here had the emitting size of 100×1 μm). Figure 3.6 is a drawing of typical diode laser beam. The beam has larger divergence angle perpendicular to the emitting stripe of diode laser than the angle parallel to it. Then the wavefront of the laser becomes elliptic as shown the figure. In this study, the perpendicular and parallel axes are refrred as vertical and horizontal axes.

In order to evaluate the effect of laser intensity on the laser ablation performance, beam profile of such elliptical laser beam should be measured. The beam profiler used here is Beam Star-V from Ophir Optronics Ltd., and its characteristics is shown in Table 3.2. The beam profiler was set in front of the laser diode system on a linear sage. By changing the position of the laser diode against the

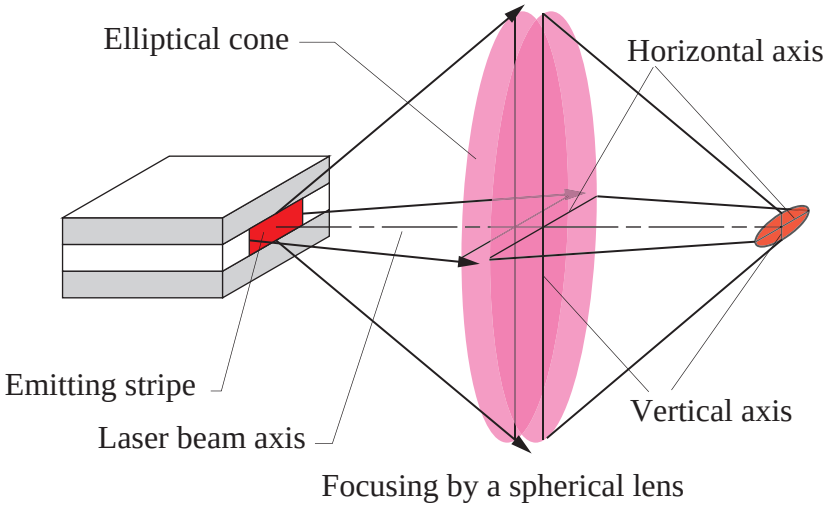

Figure 3.6: Drawing of typical diode laser beam.

Table 3.2: Characteristics of the CCD beam profiler, Beam Star-V.

Spectral responce	350 - 1100 nm
Number of pixels	320×240
Pixel resolutions	18.09 μm/pixel (Horizontal)
	20.05 μm/pixel (Vertical)
CCD sensitivity	$\sim$ 0.1 μW/cm^2
Damage threshold	$\sim$1 W/cm^2 (CW), $\sim$0.05 J/cm^2
Distance between a front glass and sensor	4.3 mm

profiler, 3D beam profile was measured.

The laser beam emitted from the diode laser was weakened by 1/8000 using ND filters. The finally measured laser spot size was more than 500 μm × 10 μm. In the case of 100 mW laser power, the intensity did not increased than 6000 W/cm^2. Hence to decease the intensity less than the damage threshold, 1 W/cm^2, three 5 % ND filters were attached in front of the focusing lens. However, ND filters change the optical path length due to its refractive index. The measured distance from the laser diode to the beam profiler was collected according to the refractive index of ND filters.

Figures 3.7-3.9 shows the measured 2D and 1D beam profiles at the position

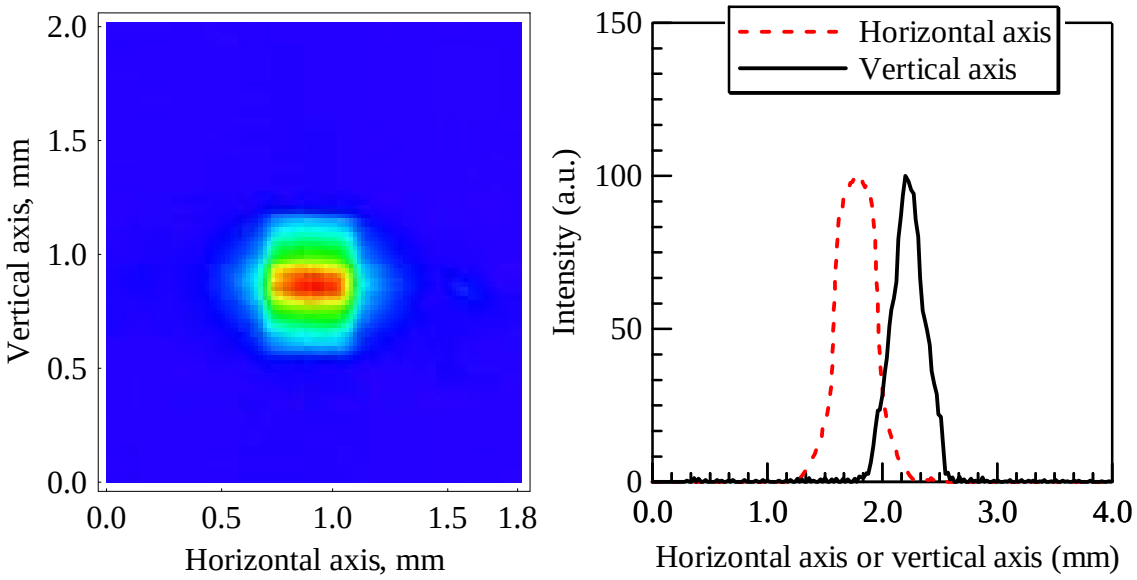

a) b)

Figure 3.7: Beam profile at -2.0 mm from the focal point, a) 2D profile and b) 1D profile along the horizontal and vertical axis.

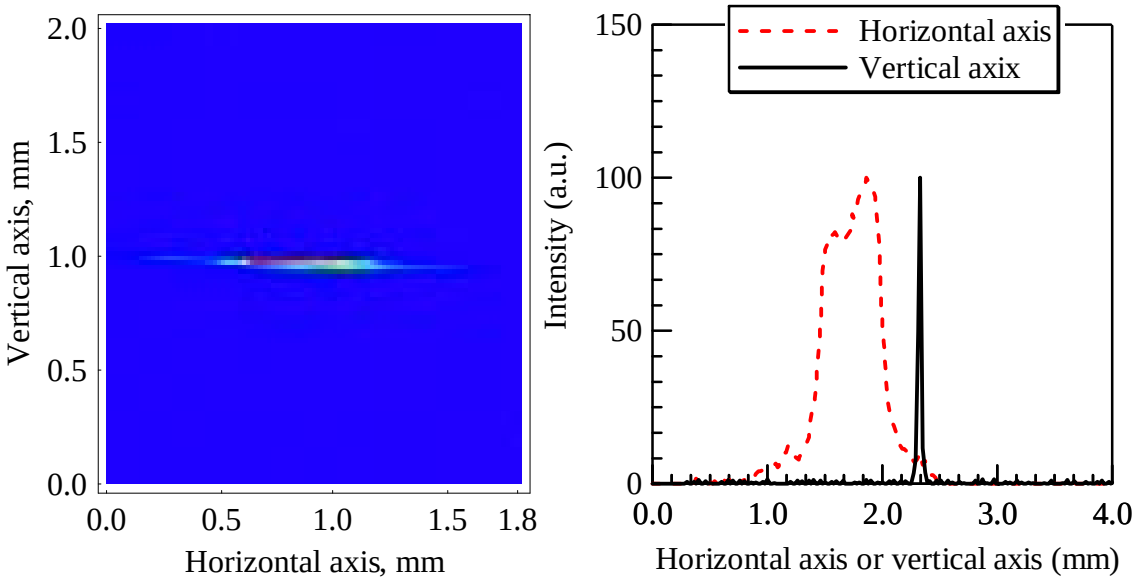

a) b)

Figure 3.8: Beam profile at the focal point, a) 2D profile and b) 1D profile along the horizontal and vertical axis.

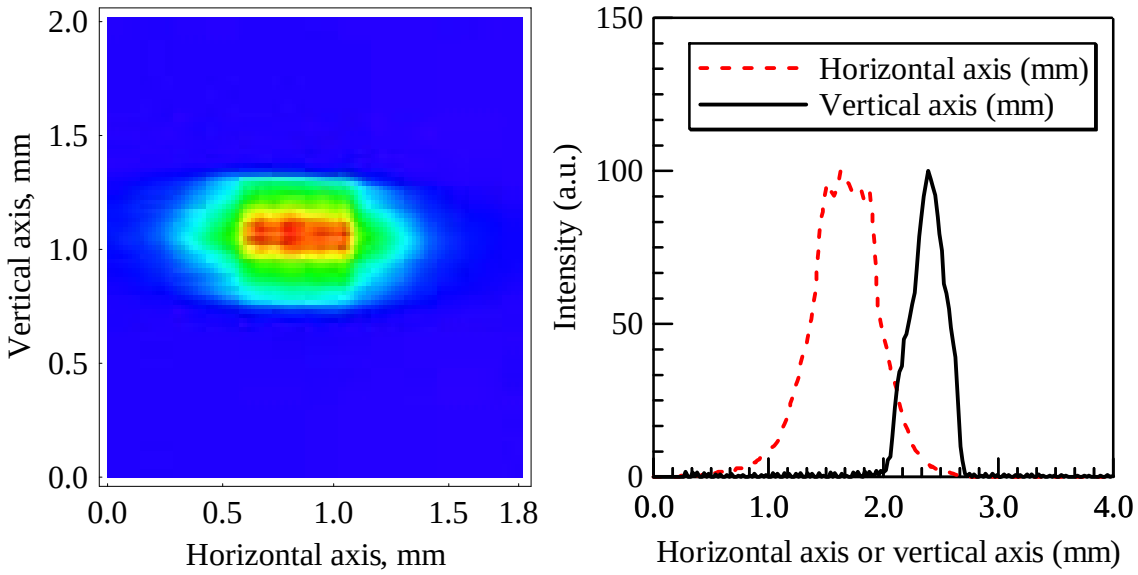

a) b)

Figure 3.9: Beam profile at +2.0 mm from the focal point, a) 2D profile and b) 1D profile along the horizontal and vertical axis.

-2, 0, 2 mm away from the focal point. 1D profiles are along the horizontal and vertical axes. Figure 3.8 is the profile at the focal point, where the laser intensity becomes maximum. The beam profile becomes rectangular with high aspect ratio. Figure 3.7 and 3.9 are the profile at -2 mm and +2 mm from the focal point. There the beam spot become close to a square due to the increase of the beam radius along vertical axis.

Laser beam of diode laser can be roughly assumed as Gaussian beam with different beam width on vertical and horizontal axes. The beam has a Gaussian profile transverse to the beam axis and a hyperbolic profile along the axis. Let us take z along the beam axis and x and y along the horizontal and vertical axes. The beam profile on $z = z'$ plane: $f(x, y, z')$ and the prowile of beam width: $w(z)$ are

$$f(x, y, z) \sim \exp\left(-\frac{x^2}{w_x(z)^2/4} - \frac{y^2}{w_y(z)^2/4}\right) \tag{3.1}$$

$$w_i(z) = w_{0i}\sqrt{1 + \frac{(z - z_{0i})^2}{k_i^2 w_{0i}^2/4}} \quad , \quad i = x, y \tag{3.2}$$

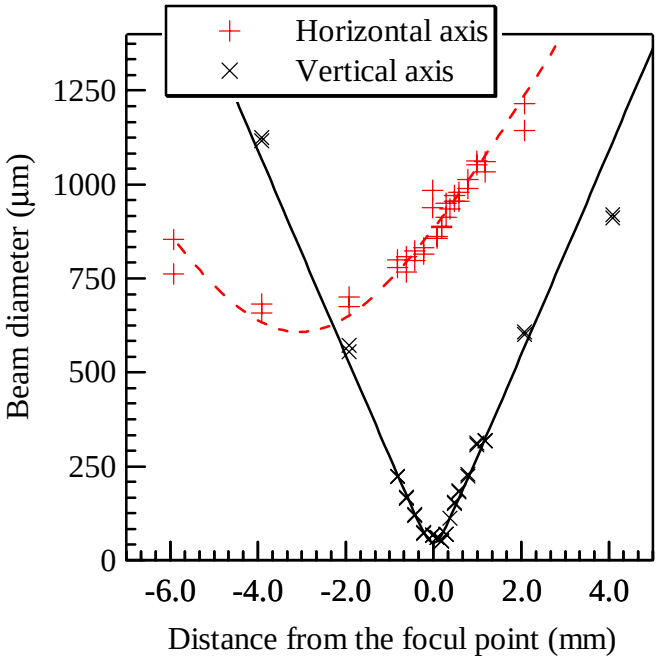

Figure 3.10: Profiles of beam widths along the beam axis. The solid and dashed lines are fitted hyperbolic curves for vertical and horizontal axis respectively.

where subscript $_i$ means x or y direction, k is the wave number, z_{0i} is the focul point, and w_{0i} is the minimum beam width, namely $w_i(z_{0i})$.

First a beam profile is measured on a plane with a given z (profile along the vertical and horizontal axes). Secondly, that profile is fitted on Eq. 3.1, and the beam widths are obtained along x and y axes. Here the beam width means the $1/e^2$ point in the profile. Repeating the process, profiles of laser beam width along the beam axis z was obtained, which is plotted in Fig. 3.10. Those beam width profiles are fitted on Eq. 3.2 respectively, and hyperbolic parameters are obtained as shown in Table 3.3.

Table 3.3: Gaussian beam width parameters along the beam axis.

	ω_0	$k\omega/2$	z_0
Vertical axis	46 μm	0.17 mm	0 mm
Horizontal axis	607 μm	2.89 mm	-3.05 mm

Figure 3.11 shows the laser beam intensity calculated from the beam width profiles (fitted hyperbolic curves). The intensity was defined as incident power over rectangle area (horizontal beam width times vertical beam width). The intensity has the maximum of 740 W/cm^2 and the FWHM (full width at half maximum) of 0.59 mm.

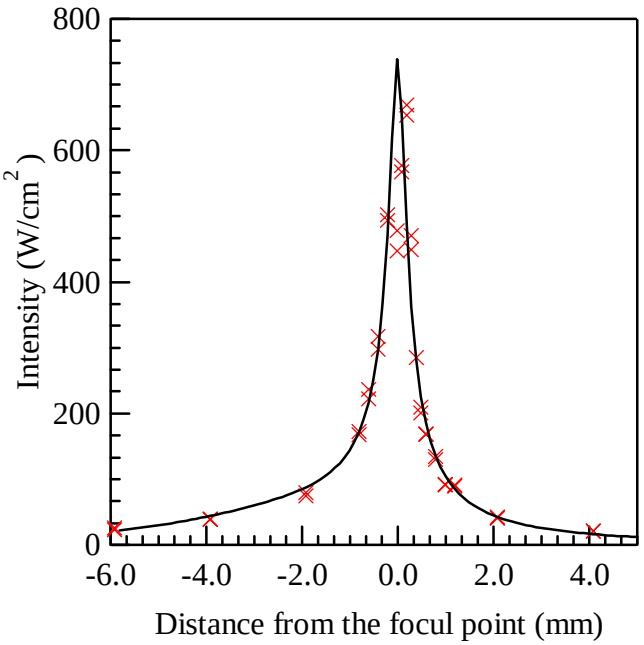

Figure 3.11: Laser beam intensity claculated from the beam width profiles.

3.2.5 Propellant feeding system

As described in the above section, cylindrical propellant feeding system was selected to supply new ablative surface or new pyrotechnic pellet to laser beam. Polymer or pyrotechnic propellants were installed on a cylinder, which was installed on a screw fixed on the mounting stage. The laser optical assembly was aligned such that the laser beam was focused on the surface of the cylindrical propellant with a certain angle of incidence. The configurations are shown in Fig. 3.12. After every shot (laser ablation or laser ignition), the cylinder was rotated upwards (or downwards) by the screw pitch (DC motor and gearbox were installed above the cylindrical propellant).

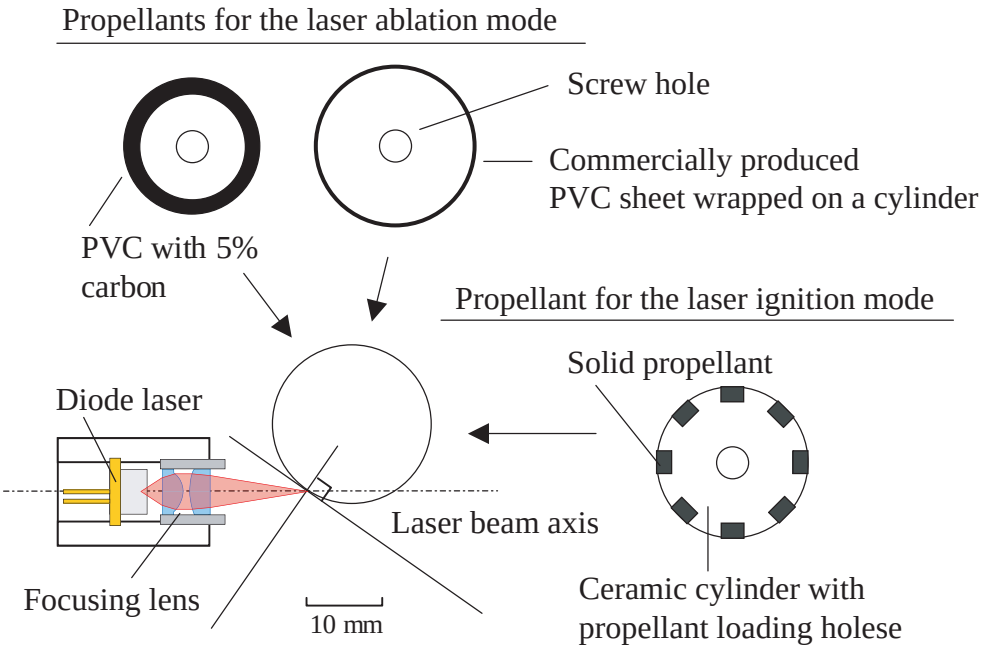

Figure 3.12: Configuration diagram of the laser beam and propellant.

3.2.6 Impulse measurement

The impulses generated by laser ablation jet were measured using a thrust stand, which is described in Chapter 2. It is a horizontally swinging torsional balance with a 30-cm-long arm and 10-cm-extension arm to increase the sensitivity. A laser ablation thruster was installed on the extension arm to make the normal vector on the ablation surface perpendicular to the thrust stand arm. Force-acting period, the period when the thrust is generated, was assumed to be equal to the laser pulse width. It is because finally measured impulse by laser ablation showed high proportionality to the laser pulse width. Because the impulse generated by laser ablation is very small and noise removing method was used to analysis the displacement, which is described in Section 2.3.3. The resolution of the thrust stand measurement was ± 1.0 μNs and the accuracy of the calibration was ± 2 %.

The huge impulse generated by laser ignition mode was measured by the thrust stand improved for huge impulse measurement described in Section 2.5. However, in the laser ignition mode, it is more difficult to accurately determine the period during which the thrust is generated than laser ablation mode. The ablation and combustion of pyrotechnics were longed over 500 ms, but its condition changed in

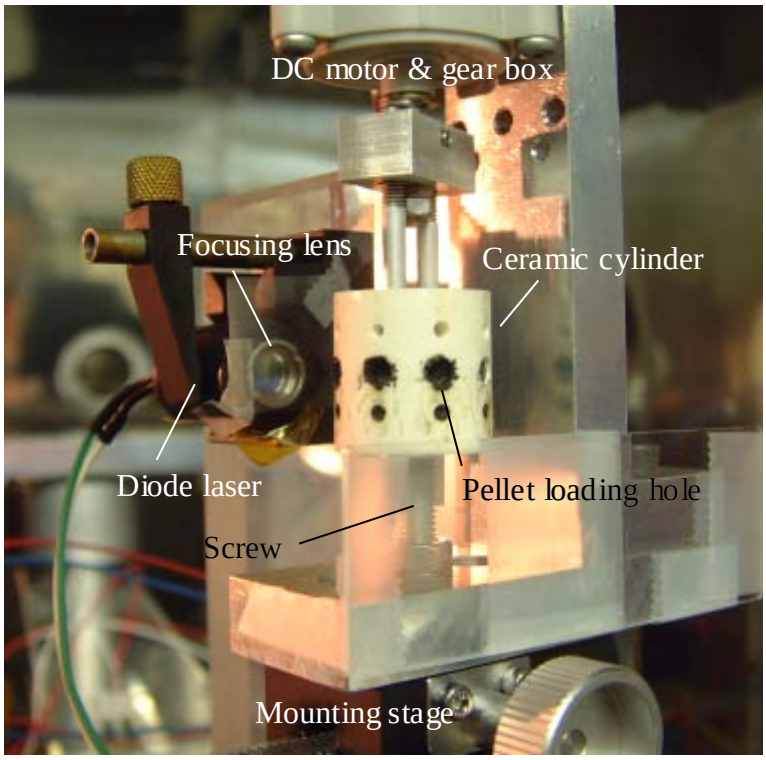

Figure 3.13: Picture of the experiment setup used for both laser ablation and laser ignition mode (the propellant in the picture is B/KNO_3 pyrotechnics of laser ignition mode).

a few ten ms. The strongest combustion lasted about 40 - 60 ms. This uncertainty of the force-acting time caused the error of the impulse measurement, which would be up to 15 %.

3.2.7 Laser-ablated mass measurement

In the experiments on the laser ablation mode, in order to evaluate the specific impulse, the mass ablated by each laser irradiation Δm was estimated from the pressure increase in the vacuum chamber ΔP using the equation $\Delta m = C\Delta P$, where C is the proportionality constant. The proportionally constant C was determined by the averaged ablated mass as determined from the difference in the weight of the propellant before and after the 1550 shots experiments, divided by the averaged pressure increase during the experiment. The weight difference of the propellant was 29.4 mg after 1550 shots, and the uncertainty of the weight

measurement was at most ±5%. The accuracy of individual pressure measurements was ±15%. The specific impulse was evaluated from impulse and ablated mass over 20 shots; measurement accuracy was better than ±10%.

3.3 Experimental Results on Laser Ablation Mode

3.3.1 Selection of ablation material

In the atmosphere, to investigate the effect of propellant material, several types of propellants were examined for laser ablation: PVC (Poly Vinyl Chloride), ABS (Acrylonitrile Butadiene Styrene polymer), POM (Poly Oxy Methylene), NR (Natural Rubber), PMMA(Poly Methyl Methacrylate). Table 3.4 shows that result. Of

Table 3.4: Laser ablation on several materials in the atomosphere.

Name	Color	Shaping	Ablation	Light emission
Paper	black	sheet	yes	yes
Paper	white	sheet	weak	no
PVC	gray	cubic	yes	weak
PVC	black	sheet	yes	yes
NR	black	sheet	weak	weak
ABS	black	cylinder	yes	no
POM	black	cylinder	yes	no
POM	white	cylinder	no	no
PMMA	black	cylinder	weak	no

those polymer materials, PVC showed the best performance, that is, the emission from the plasma produced by the laser ablation was the strongest and the resulted crater was the largest. However, even if the main component was PVC, there was large difference between commercially available PVCs. It would be because of additives. Commercially available polymers usually include several additives in it for the coloring or improving the properties.

Figure 3.14 shows the thrust performance using the commercially available black PVC sheet as propellant. The effect of laser pulse width was investigated,

with maintaining the laser power as 280 mW (as a result incident laser energy was changed). The impulse was proportionally increased up to 8.1 μNs with the increase of the pulse width up to 800 ms. The ablated mass was also increased up to 6.0 μg.

The proportionality of impulse and mass to the energy means the constant specific impulse and momentum coupling coefficient. Momentum coupling coefficient, abbreviated as C_{m}, is defined as the impulse provided by laser ablation over the incident energy. It is often used to evaluate the performance in the field of laser propulsion and is the same quantity as thrust to power ratio which is used in the field of electric propulsion. In this chapter, according to the custom in that field, momentum coupling coefficient is used to express the generated impulse over consumed energy. In Fig. 3.14 b), the specific impulse and coupling coefficient are shown. They are almost constant against the laser energy with the averaged value of 134 s and 42 μNs/J respectively. Both of the Isp and C_{m} in Fig. 3.14 b) shows slight increase with the decrease of laser pulse. It was confirmed also by Phipps et al. [49, 74].

3.3.2 Effect of the carbon density in PVC

The effect of the carbon density in PVC was investigated. It should be noted that black color material showed the best performance. It can be easily understood by the fact that the wavelength of the laser beam was close to the visible light. Hence the absorption coefficient, shown as color, would drastically affect the thruster performance. Three PVC cylinders with the carbon density of 0, 2.5, and 5.0 % were prepared and the thruster performance for them was measured. Picture of those PVC cylinders is shown in Fig. 3.15. PVC with 0 % carbon is almost transparent and the others are opaque (black).

Increase of the carbon density in PVC showed dramatic increase of the performance. The measured thrust performances are shown in Fig. 3.16. The measurement was carried out for 5.0 and 2.5 % carbon PVC, and 0 % carbon PVC showed no reaction to the laser focusing. PVC with 5.0 % carbon showed 5.9 times of coupling coefficient than that of 2.5 %. In contrast, specific impulse for 5.0 % carbon was 1.7 times than 2.5 %. Therefore the increasing of the impulse was mainly caused by the increase of the ablated mass. As a result, using PVC

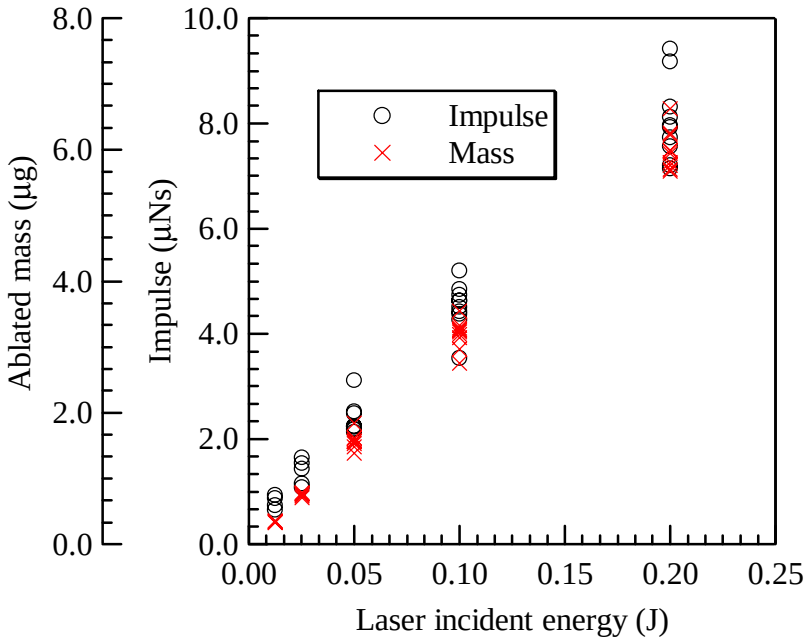

a)

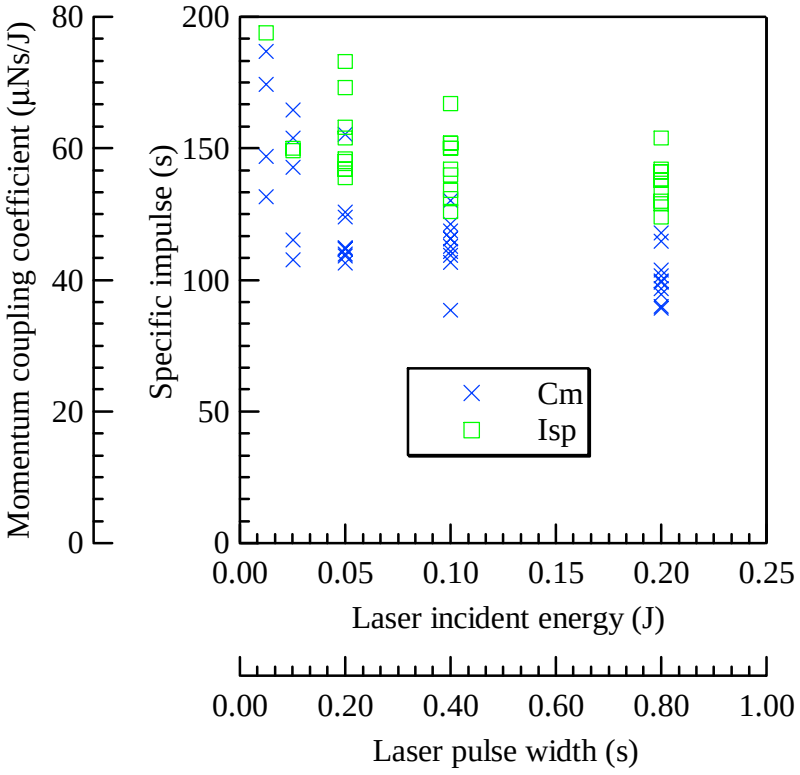

b)

Figure 3.14: Thrust performance of laser ablation mode using commercially available black PVC sheet as propellant; a) generated impulse and ablated mass and b) specific impulse and momentum coupling coefficient.

Figure 3.15: Picture of the PVC cylinders with different doped carbon density: 0, 2.5, and 5.0 %.

with 5.0 % carbon as propellant, specific impulse of 104 s and coupling coefficient of 152 μNs were obtained as the thrust performance. Those values are higher than using the commercially available PVC shown in Fig. 3.14. Especially, the coupling coefficient was increased by three times from 42 to 152 μNs/J. It would be also the additives in the PVC, whereas the additives included in the commercial PVC were not claryfied.

The effect of the carbon density can be explained as follows. The Laser beam dealt here was low intensity and long pulse width. Then photothermal reaction would prevail, and it can be treated as the simple problem of heat conduction. Carbon additive gives opaque black color for PVC as shown in Fig. 3.15. It means that carbon additive makes the laser absorption length short. The shorter is the absorption length, the more narrow region is heated. PVC heated up to the boiling or degradation temperature starts to exhaust itself as gas with that temperature. Only the temperature of gas determines the exhaust velocity, because it is the only the acceleration mechanism. Hence the specific impulse was essentially not affected a lot by the carbon additive. However, polymers have no clear boiling temperature and various degradations occur depending the temperature. It would be a reason of the increase of specific impulse (1.7 times). Heating rate of polymer is increased by the carbon additives, and the degradations at higher temperature may be occurred.

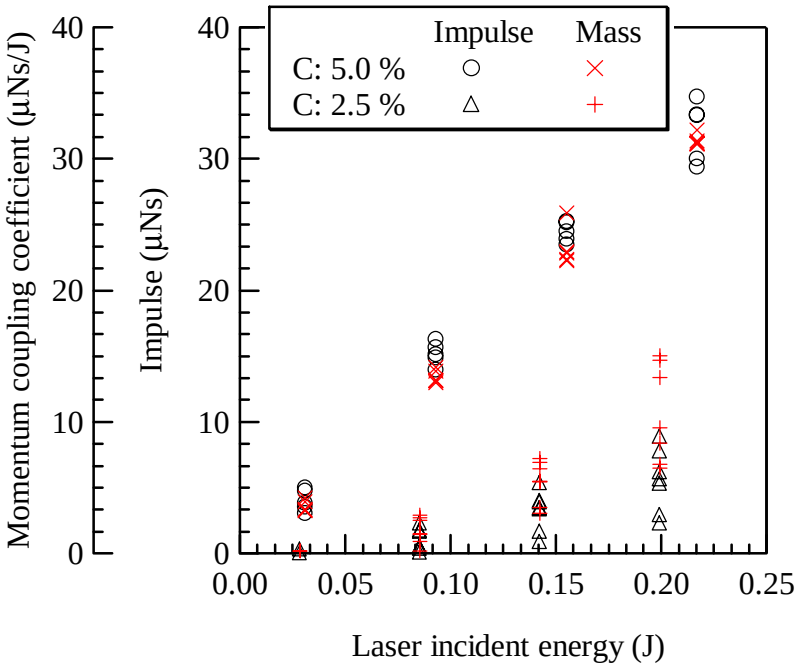

a)

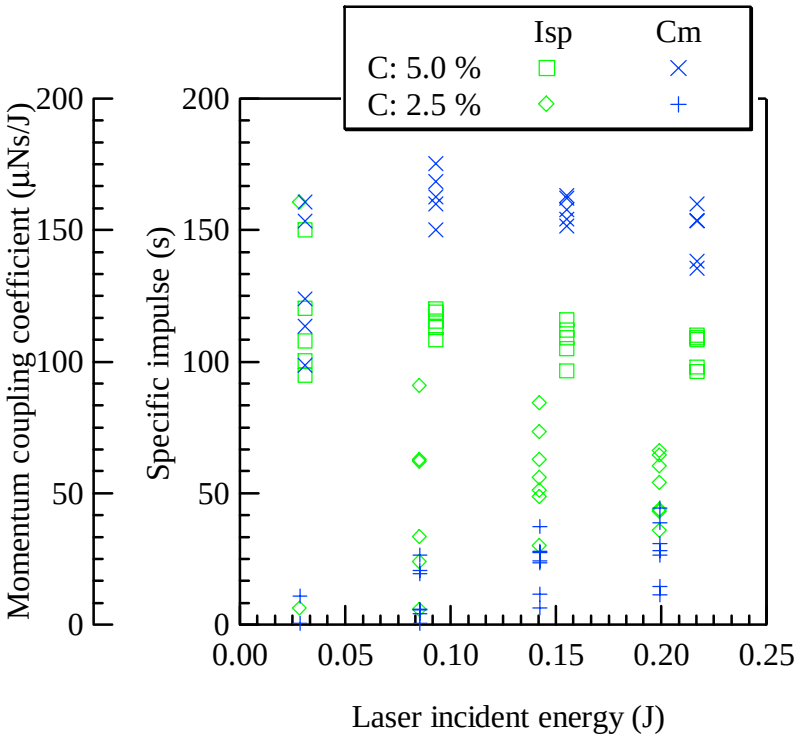

b)

Figure 3.16: Thrust performance of laser ablation mode using custom-made PVCs with carbon additives of 2.5 % and 5.0 %, a) generated impulse and ablated mass and b) specific impulse and momentum coupling coefficient.

3.3.3 Variations of thrust

Precise positioning of microspacecraft requires not only small thrust but also its accuracy (resolution). As mentioned in chapter 1, precise attitude or translation controle keeping sub degrees or sub milli meters will require the accuracy of micro Newton order. For instance, LISA which comprises the laser interferometer requires very severe accuracy, 5-30 μN thrust with the resolution less than 0.1 μN.

Thrust measurement of the above laser ablation mode showed the linearlity of the thrust to the laser pulse width, and the thrust (impulse) will be predicted by the width. In the experiment using commercially available PVC (Fig. 3.14), the relation is $I(\mu\text{Ns}) = 9.59 \times \text{pulse (s)} + 0.48$. The standard deviation from that proportionality was 0.48 μNs with the impulse range of 1 to 8 μNs. In the experimetn using other material with higher coupling coefficient (Fig. 3.16), the standard devitation was 1.5 μNs with the impulse range of 5 to 35 μNs.

3.3.4 Direction of the ablation plume

It is very important to know the direction of the thrust. In most thrusters, its direction is obvious and the interest is in the deviation of the thrust vector. However, in the laser ablation of cylinder surface, the direction is not claryfied, and it is necessary to know the direction of laser ablation thrust.

Up to date, a number of studies on the laser ablation plume have been conductd in the field of laser ablation. They concluded that the plume has two distinct components: one a cosine component and the other a highly normal directed component [64, 75, 76]. Most of those studies on laser ablation have focused on ultraviolet laser beam (ex. excimer laser) with high power intensity (100 kW/cm^2) or a short pulse (10 ns). In contrast, the laser used here is infrared laser with low laser intensity (<1 kW/cm^2) and long pulse width (>50 ms).

Here profile of the laser ablation plume was estimated measuring the distribution of the contamination by the exhaust gas. A white PVC sheet target was placed downstream of the ablation point in two configurations: one was parallel to the ablation surface and 30 mm downstream from the ablation point (forward target), the other was perpendicular to the ablation surface and 14 mm under the ablation point (bottom target). The configurations of the sheets are shown in Fig. 3.17. For each target configuration, a thruster was fired over 1000 shots with the

pulse width of 500 ms.

Figure 3.18 shows a typical contour of the contamination on the targets by the exhaust gas. The contaminated original targets were scanned in the scanner and the contour plots of color intensity were drawn. On the contour plot, the configuration of the cylindrical propellant, laser beam axis, and normal and tangent to the ablation surface are drawn. The profile on the forward sheet, Fig. 3.18 a), has good axial symmetry. The line from the ablation point to the center of that contour plot almost agreed with the normal to the ablation surface. Figure. 3.18 b) also shows that the exhaust plume was symmetrical for the normal to the ablation surface.

The thrust vector was measured from the impulse measurement. A rotational stage was installed between a thruster and a beam of the thrust stand. The normal to the ablation surface was rotated 45 or -45 degrees from the perpendicular to the beam axis. For the each case, the impulse bits were measured and the thrust deflection angle from the normal, α, was calculated by the equation

$$\alpha = \mathrm{Tan}^{-1}\left(\frac{v_{45}}{v_{-45}}\right) - \frac{\pi}{4} \tag{3.3}$$

where v_{45} and v_{-45} are the exhaust gas velocities in the case of the rotation angle: 45 or -45 degrees respectively. The exhaust velocities was obtained from impulse and ablated mass. The thrust deflection was measured with the laser pulse width of 400 or 800 ms and the laser beam incident angle of 60 or 70 degrees.

Figure 3.19 shows the measured deviation angle of thrust vector from the normal to the ablation surface. As a result, the thrust vector was deviated by 15-35 degrees from the normal. It indicates that the exhaust gas plume is declined opposite to the laser beam from the normal. This result conflicted to the measured contamination profile, which concluded that the center of the exhaust plume was directed to the normal. One of the reasons would be the effect of the plume attachement on the laser assembly (laser holding tube etc.). Several part of the exhaust gas was adhered on the laser assembly. Large shadow due to that effect is confirmed in the contour (Fig. 3.18). The thrust deviation was alway directed to outward.

In all of the experiment of impulse measurement, the normal to the ablation surface was placed perpendicular to the beam of the thrust stand. The thrust angle

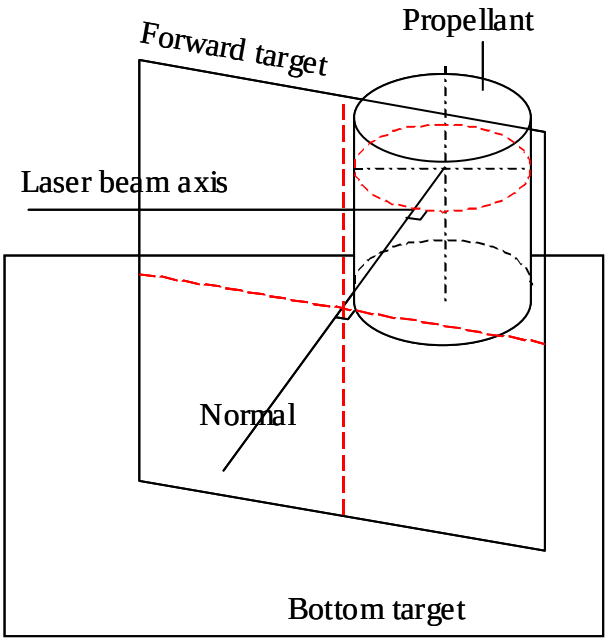

a)

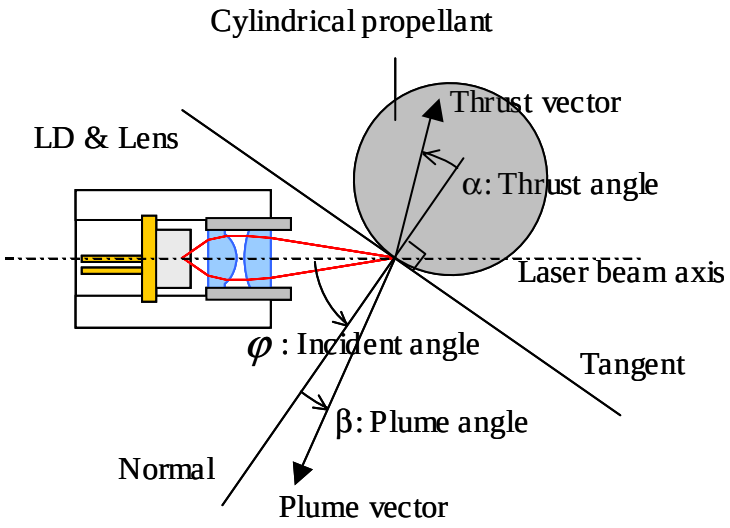

b)

Figure 3.17: Schematic diagram of plume direction measurement a) configuration drawing and b) top view and definition of terms.

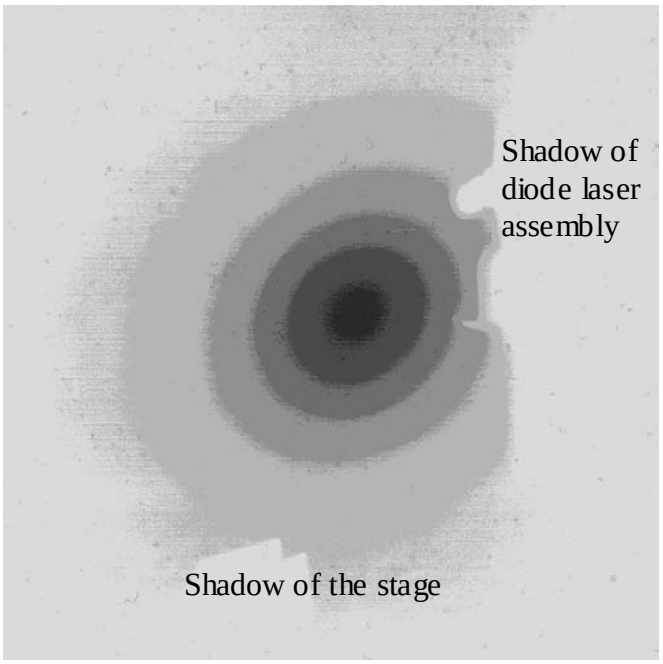

a)

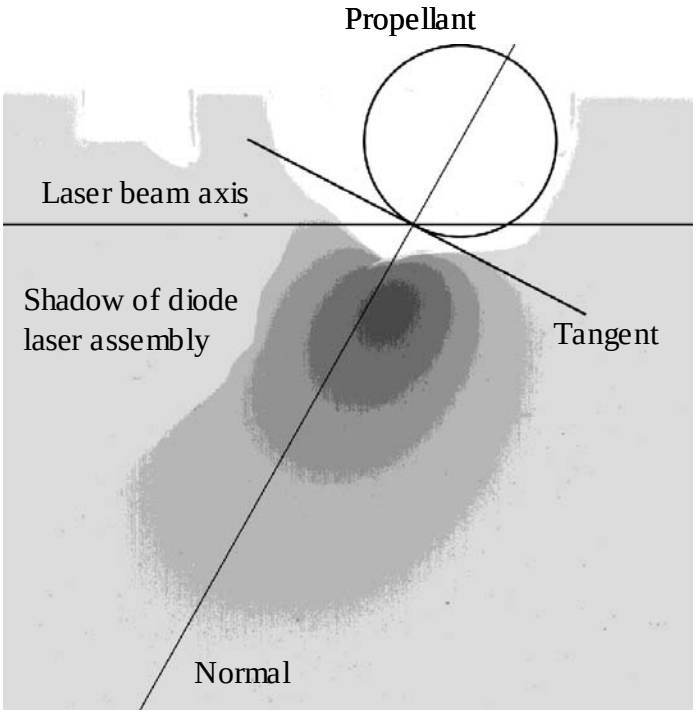

b)

Figure 3.18: Scanned images contaminated by the exhaust gas: a) forward target and b) bottom target.

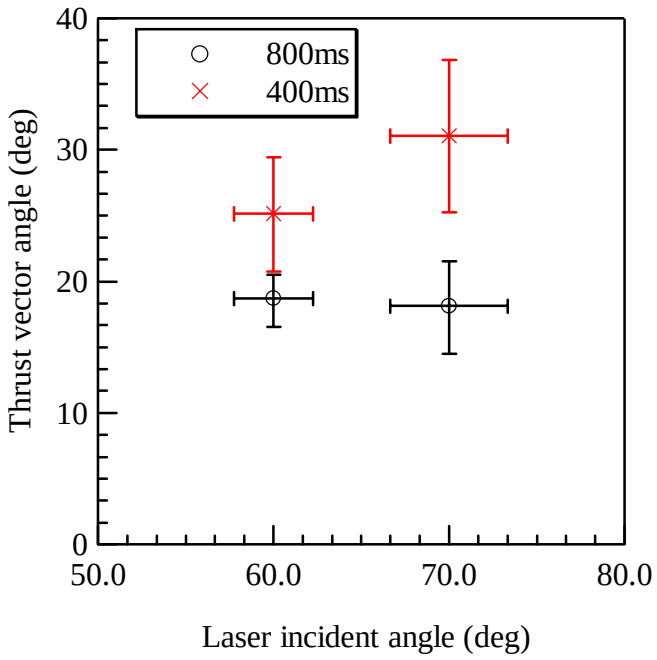

Figure 3.19: Deviation angle of thrust vector from the normal to the ablation surface.

measurement indicates that the thrust direction is deviated from the normal, and the impulse is estimated lower than its absolute value by 5 to 20 %.

3.3.5 Multiple-shots effect

In microspacecraft, it is important to utilize as much propellant as possible in limited space and mass. In the above experiment, new surface was supplied for the succeeding laser irradiations after every shot. Howiever, if the same ablation surface can be utilized many times, namely multishots, the propellant will be utilized more effectively.

Here, propellant surface was irradiated three times at the same point and with the same pulse width to investigate the multishots effect at the same ablation point. The pulse widths of 100, 300, 500, and 800 ms were examined. Figure 3.20 a) shows result of the impulses on the number of shots. It is clear that the impulse of first shot is the highest and multi-shots at the same point decreases the performance. The decrease from second to third shot is lower than from first to

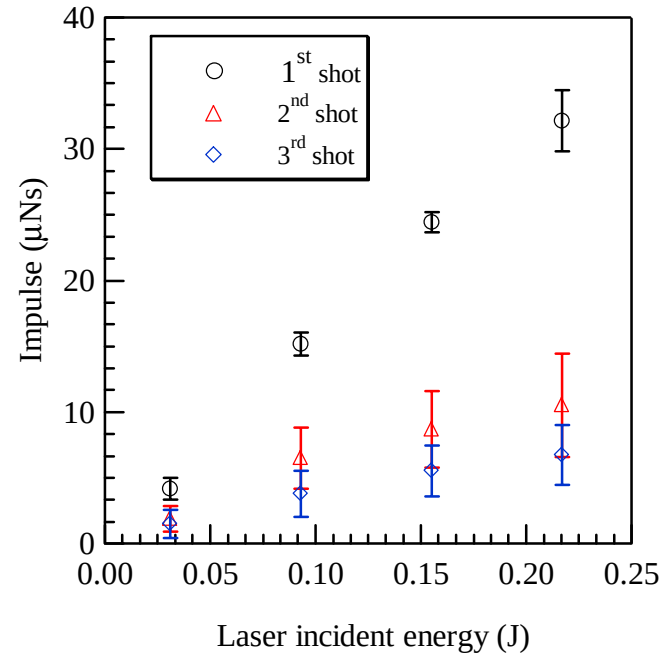

a)

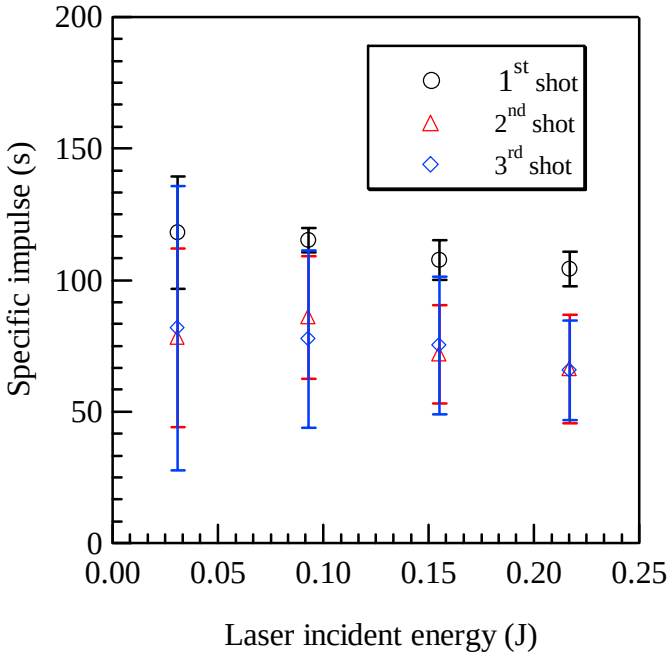

b)

Figure 3.20: Effect ot the multiple shots at the same point.

second.

It should be noted that the summation of impulses of first and second shot is lower than impulse of only first shot of the twice pulse width. It means that, for any given total laser pulse width, single continuous laser irradiation is more effective than multiple irradiations with intervals. In addition, the specific impulse was also decreased from first to second shot, although the decrease rate was not larger than impulse.

3.3.6 Mass spectroscopy

To investigate the mechanism of the laser ablation on PVC material, mass spectroscopy of the exhaust plume was performed using a quadruple mass spectrometer. The spectrometer was AGA-100 made by ANELVA Corporation, whose specifications are shown in Table 3.5.

Table 3.5: Specifications of the mass spectrometer AGA-100.

Mass number range	1-100 amu
Operation pressure range	$10^{-4} \sim 2\times10^{-11}$ Torr
Minimum detective partial pressure	2×10^{-11} Torr
Sweeping time	$0.1 \sim 1000$ s
Sensitivity	1×10^{-3} A/Torr
	at 5 mA emission current
Electro meter	$10^{7\sim12}$ V/A
Recorder output voltage	$0 \sim 10$ V
Error of mass number	$\pm$ 0.05 amu
Error of peak	$\pm$ 1.5 %

Figure 3.21 shows measured mass spectrum during the repulsive operation of the thruster (PVC with 5 % carbon was used). Mass spectrum of residual gases (background) was also measured, where intense peaks of 1, 17, and 18 attributed from water H_2O were observed. The background spectrum was subtracted from one during the thruster operation. Hence the contributions from residual gases were eliminated and only ablated gas from PVC remains. The spectrums were

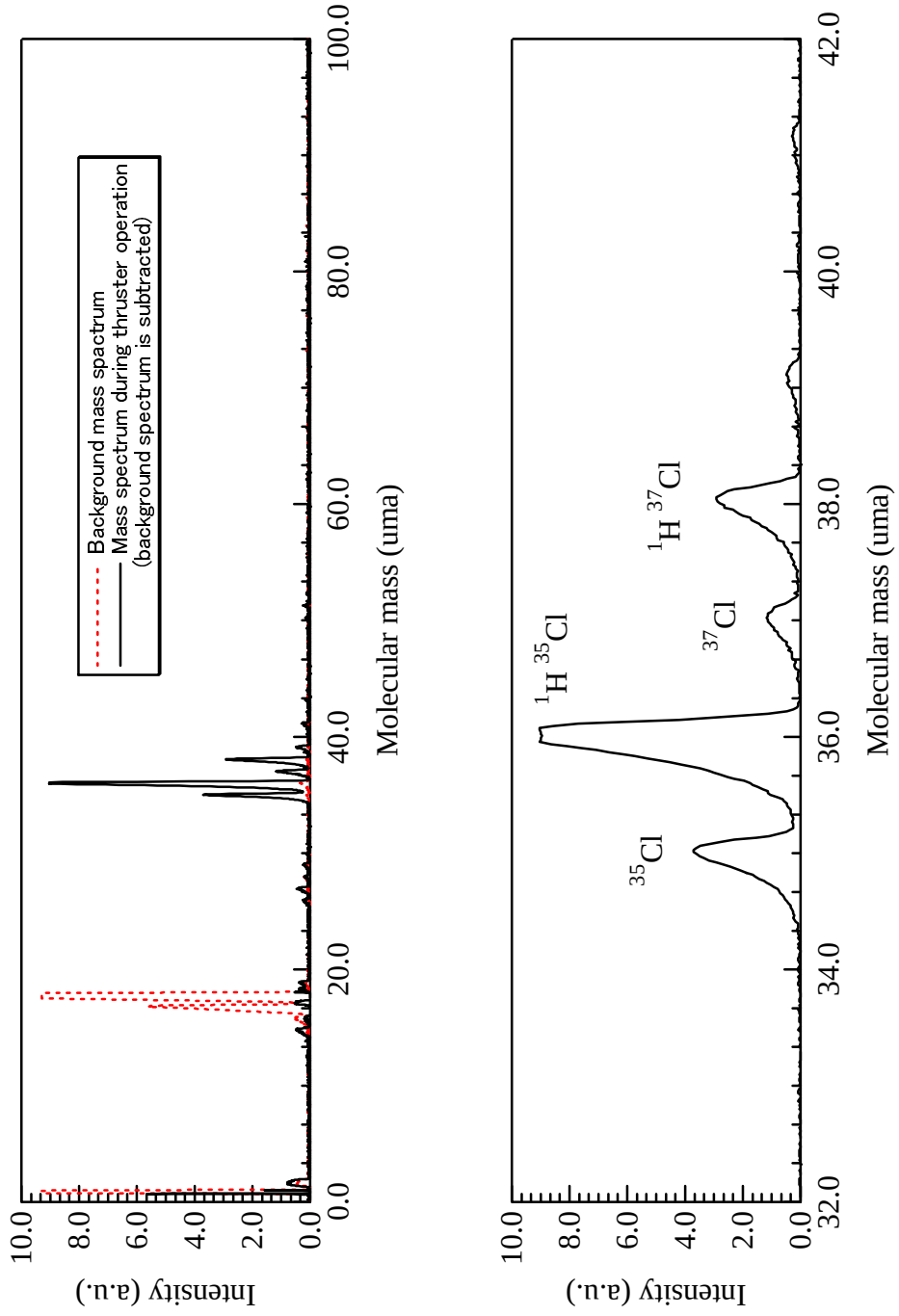

a) b)

Figure 3.21: Mass spectrum during the repulsive operation in the laser ablation mode: a) 1-100 amu and b) 32-42 amu.

searched in the range of 1 - 100 amu.

Table 3.6: Comparison of the experimentally measured peaks and abundance ratio of Cl and HCL isotope.

Mass number (u.m.a)	Experimental result	Chemical composition	Fraction of isotope
35	0.72	^{35}Cl	0.76
37	0.28	^{37}Cl	0.24
36	0.86	$^{1}H^{35}Cl$	0.76
38	0.14	$^{1}H^{37}Cl$	0.24

In Fig. 3.21, four strong peaks of 35 to 38 are identified. These peaks correspond to HCl and Cl with those isotope from the literature [77]. The ratio of measured peaks and abundance ratio of HCl and Cl are listed in Table. 3.6, which shows good agreement. Such strong emissions of HCl from PVC by laser or heating is in agreement with a lot of other studies [78, 79, 77]. They have shown that the thermal degradation of PVC proceeds in the following two stages. The

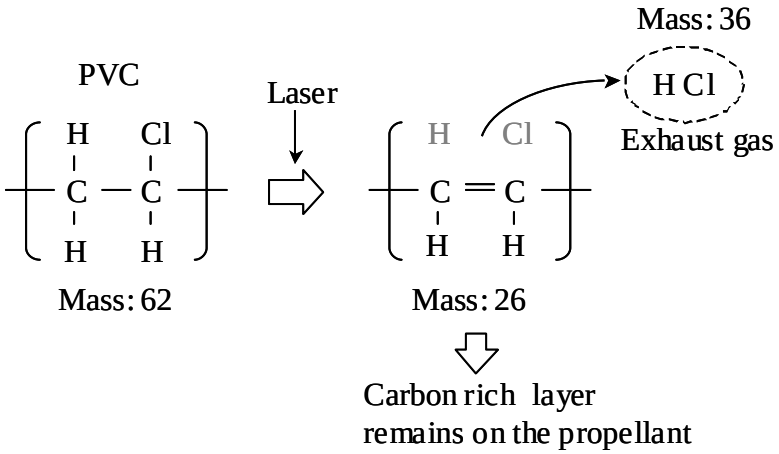

Figure 3.22: Dehydrochlorination of PVC with subsequent formation of conjugated double bonds.

first stage proceeds in the temperature range of 470 to 640 K. It corresponds to dehydrochlorination with subsequent formation of conjugated double bonds, as

shown in Fig 3.22. The second stage proceeds in 640 - 770 K, which is scission of polyene sequences formed during the first stage. Therefore the ablated gas by a diode laser would mainly consist of HCl, at least in the early stage of the ablation.

This preferential degradation of HCl in low temperature would explains the reason for the decrease of impulse by multiple shot at the sample point. During the laser ablation, HCl is degraded and other components are remained in PVC as residuals. Once the heating is stopped, the residuals are cooled. When the same point is again irradiated by laser, the residuals have to be heated again and, after the re-heating, HCl would begin to degrade. On the other hand, if the same point is continuously heated, laser can continuously heat the solid since residuals are kept hot. Hence the duration time between shots would be important factor determining the impulse bit of second shot.

3.4 Discussion on Mechanism of Diode Laser Ablation.

3.4.1 Analytical solutions of heat conduction by laser irradiation

To clarify the ablation mechanism by diode laser irradiation, photothermal ablation model is applied on the laser ablation processes. Here, it is assumed that laser beam irradiated on the ablative propellant is converted from photo energy to thermal energy by the absorption. It is because the laser intensity of diode laser is not enough high to occur photochemical reaction. Hence the beam behaves as heat source in the ablative material, and it is analyzed as heat conduction problem.

The laser ablation processes is assumed to be constructed by the following regimes. First laser beam is absorbed in the ablative material and all the energy is used to raise the inner temperature: heating regime. When the maximum temperature, generally surface temperature, reaches to the boiling or degrading temperature, the laser energy is used for both temperature raising and material vaporization. This is transition regime. After enough time is pasted, the ablation reaches to the stationary ablation, where the temperature profile recedes inward with maintaining its shape, which is stationary ablation regime.

In this section, the above regimes are analyzed by the method of heat conduction problem where laser is treated as a heat source.

Heating regime

Heating of ablative material by laser irradiation can be described as one dimensional semi-infinite heat conduction. The absorption of radiation in the first approximation obeys the Bouguer-Lambert-Beer law, that is the beam exponentially decays. Hence the governing equation is

$$\frac{\partial T}{\partial t} = \kappa \frac{\partial^2 T}{\partial x^2} + \frac{q}{\rho c_p \lambda_a} e^{-x/\lambda_a} \tag{3.4}$$

$$\text{i.c.} \qquad T(x,0) = 0, \qquad x \geq 0 \tag{3.5}$$

$$\text{b.c.} \qquad \left.\frac{\partial T}{\partial x}\right|_{x=0} = 0, \quad \left.\frac{\partial T}{\partial x}\right|_{x=\infty} = 0 \tag{3.6}$$

where T is the temperature, ρ is the density, c_p is the specific heat, λ_a is the laser absorption length, and q is the total power absorbed in the material. Figure 3.23 shows a conceptual drawing of the problem. The solution of Eq. 3.4 is

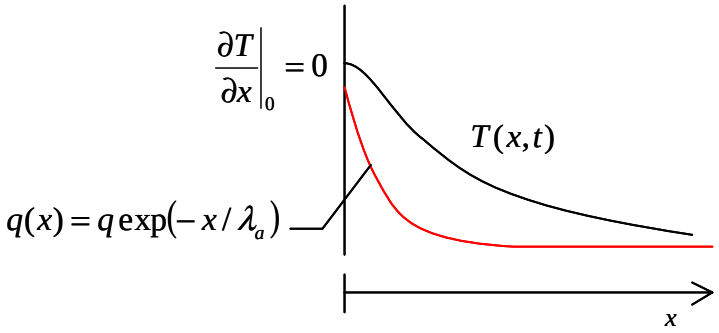

Figure 3.23: Heating of solid by absorption of laser radiation.

$$T = \frac{2q\lambda_h}{K}\,\mathrm{ierfc}(\frac{x}{2\lambda_h}) + \frac{q\lambda_a}{K}\left[\frac{1}{2}e^{(\lambda_h/\lambda_a)^2}\left\{e^{x/\lambda_a}\,\mathrm{erfc}\left(\frac{\lambda_h}{\lambda_a}+\frac{x}{2\lambda_h}\right)\right.\right.$$
$$\left.\left.+e^{-x/\lambda_a}\,\mathrm{erfc}\left(\frac{\lambda_h}{\lambda_a}-\frac{x}{2\lambda_h}\right)\right\} - e^{-x/\lambda_a}\right] \quad (3.7)$$

where λ_h is the heat depth and $\mathrm{ierfc}(x)$ is the integral complementary error function [80]. Those are defined as

$$\lambda_h = \sqrt{\kappa t} \quad (3.8)$$
$$\mathrm{ierfc}(x) \equiv \int_x^\infty \mathrm{erfc}\,x\;dx \quad (3.9)$$
$$= \frac{1}{\sqrt{\pi}}e^{-x^2} - x\,\mathrm{erfc}\,x \quad (3.10)$$

To clarify the characteristics of the phenomena, dimensionless form is effective, which becomes

$$\Theta = \mathrm{ierfc}(X) + \frac{1}{2D}\left[\frac{1}{2}e^{D^2}\left\{e^{2XD}\,\mathrm{erfc}(D+X)\right.\right.$$
$$\left.\left.+e^{-2XD}\,\mathrm{erfc}(D-X)\right\} - e^{-2XD}\right] \quad (3.11)$$

where

$$X = \frac{x}{2\lambda_h},\quad D = \frac{\lambda_h}{\lambda_a},\ \text{and}\quad \Theta = \frac{KT}{2q\lambda_h} = \frac{KT}{2q\lambda_a D} \quad (3.12)$$

are dimensionless parameters. X is the dimensionless length normalized by the heat depth, D is the ratio of the heat depth to laser absorption length, and T is normalized by the temperature which gives the heat flux equal to q by the gradient over the λ_h.

Time when the wall temperature reaches to the boiling point

The temperature at $X = 0$ in dimensionless form is

$$\Theta_0 = \frac{1}{\sqrt{\pi}} + \frac{1}{2D}\left[e^{D^2}\,\mathrm{erfc}(D) - 1\right]. \tag{3.13}$$

By using the definition of Θ: Eq.(3.12),

$$\frac{2}{\sqrt{\pi}}D + e^{D^2}\,\mathrm{erfc}(D) - 1 = \frac{KT_w}{q\lambda_a} \equiv \frac{1}{A}. \tag{3.14}$$

where A is a dimensionless form of the laser ablsorption length. It should be cared that the variable of time is included in the λ_h in term of the D. Hence the time when T_w reaches an arbitrary temperature is obtained by solving the Eq. 3.14 for the variable D. Figure 3.24 shows the numerically solved function $D^*(A)$. The

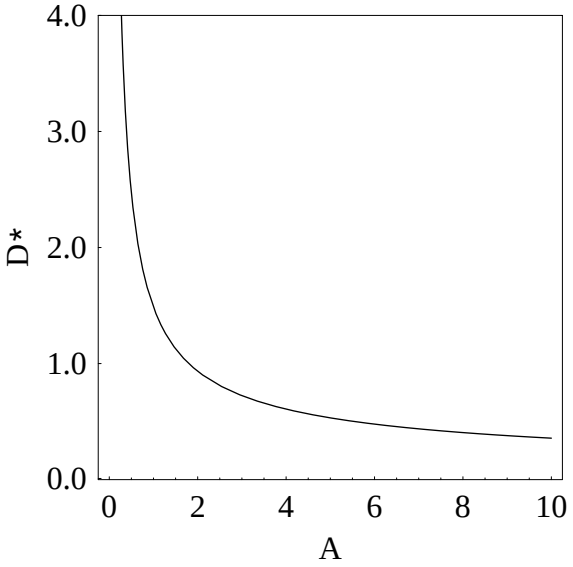

Figure 3.24: Numerically obtained plot of $D^*(A)$.

behavior of $D^*(A)$ around zero or infinity is expressed as

$$D^*(A) = \begin{cases} 1/\sqrt{A} & , \quad A \gg 1 \\ \\ \dfrac{1}{4}\left\{\sqrt{\pi}(1+1/A) + \sqrt{\pi(1+1/A)^2 - 4}\right\} & , \quad A \ll 1, \end{cases} \tag{3.15}$$

where the following series expansion was used.

$$\mathrm{erfc}(x) = \begin{cases} \dfrac{1}{\sqrt{\pi}}\left(\sqrt{\pi} - 2x + \dfrac{2}{3}x^3 - \dfrac{1}{5}x^5 + \dfrac{1}{21}x^7 + O(x^9)\right) & , \quad x \ll 1 \\ \\ \dfrac{1}{\sqrt{\pi}}e^{-x^2}\left(\dfrac{1}{x} - \dfrac{1}{2x^3} + \dfrac{3}{4x^5} - \dfrac{15}{8x^7} + O(x^{-9})\right) & , \quad x \ll 1 \end{cases} \tag{3.16}$$

After all, the time when the wall temperature reaches to the boiling temperature: T_b is

$$t_b = \frac{1}{\kappa}\left[\lambda_a D^*\left(\frac{q\lambda_a}{KT_b}\right)\right]^2 \tag{3.17}$$

$$= \frac{1}{\kappa}\left(\frac{\sqrt{\pi}}{2}\frac{KT_b}{q}\right)^2 f(A) \tag{3.18}$$

$$f(A) \equiv \left(\frac{2}{\sqrt{\pi}}AD^*(A)\right)^2, \text{ where } A = \frac{q\lambda_a}{KT_b}. \tag{3.19}$$

Note that the term in front of $f(A)$ in Eq. 3.18 is the boiling time in the case of infinite short laser absorption length ($A \to 0$), which is the heat flux problem with Neoumann boundary condition. Therefore, the function $f(A)$ is a deviation factor of the arrival time to the boiling temperature from the surface heat flux approximation. Figure 3.25 shows the $f(A)$ dependence on A and its asymptotic curves,

$$f(A) = \begin{cases} 1 + 2A + \left(1 - \dfrac{2}{\pi}\right)A^2 & , \quad A \ll 1 \\ \\ \dfrac{4}{\pi}A\left(1 + \dfrac{8\sqrt{A} - 3\sqrt{\pi}}{6(\sqrt{\pi} - 2\sqrt{A} + A\sqrt{\pi})}\right) & , \quad A \gg 1, \end{cases} \tag{3.20}$$

As shown in Eq. 3.18, the time when the wall reaches to the boiling temperature has the essential characteristic of quadratical decrease with the increase of the incident laser intensity: q. If the absorption length λ_a is longer than the characteristic length of the system, KT_b/q, the time is extended by the factor $f(A)$. Thereafter the material starts to be ablated.

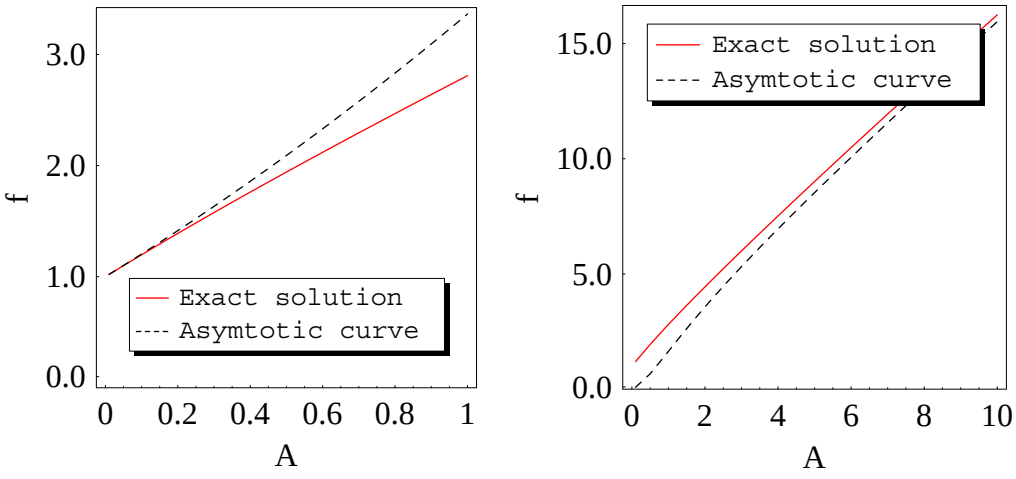

a) b)

Figure 3.25: Approximation of a deviation factor from the surface heat flux approximation.

The case of heat flux into pre-sheath

Here, a heat conduction if the radiation is uniformly absorbed in the thickness δ region set in front of the ablative material. Its drawing is shown in Fig. 3.26. This problem simulate the situation that carbon layer is established on PVC ablative material by multiple shots. In the carbon layer, the temperature profile is assumed constant, because carbon has high absorption coefficient and thermal conductivity. There the governing equation is

$$\frac{\partial T}{\partial t} = \kappa \frac{\partial^2 T}{\partial x^2} \tag{3.21}$$

$$\text{i.c.} \qquad T(x,0) = 0, \qquad x \geq 0 \tag{3.22}$$

$$\text{b.c.} \qquad \begin{cases} T(0,t) = T_s(t) \\ \delta \rho_s c_{p,s} \dfrac{d}{dt} T_s = q + K \left. \dfrac{\partial T}{\partial x} \right|_0 \end{cases} \tag{3.23}$$

The solution is

$$T = \frac{2q\lambda_h}{K} \operatorname{ierfc}\left(\frac{x}{2\lambda_h}\right) \tag{3.24}$$

$$+\lambda_s \frac{q}{K} \left[e^{\frac{x}{\lambda_s} + \left(\frac{\lambda_h}{\lambda_s}\right)^2} \operatorname{erfc}\left(\frac{x}{2\lambda_h} + \frac{\lambda_h}{\lambda_s}\right) - \operatorname{erfc}\left(\frac{x}{2\lambda_h}\right) \right] \tag{3.25}$$

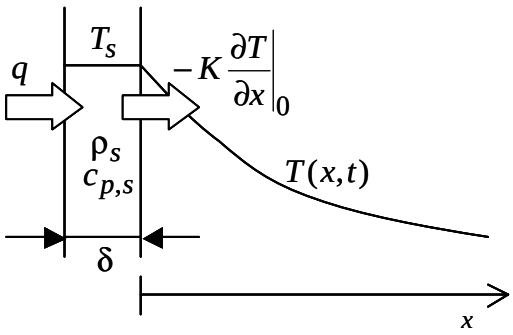

Figure 3.26: Pre-sheath heat conduction.

$$\Theta = \text{ierfc}(X) + \frac{1}{2D_s}\left[e^{2XD_s+D_s^2}\,\text{erfc}(X+D_s) - \text{erfc}(X)\right] \tag{3.26}$$

where

$$\lambda_s = \frac{\rho_s c_{p,s}}{\rho c_p}\delta, \quad \Theta = \frac{KT}{2q\lambda_s}, \quad X = \frac{x}{2\lambda_h}, \quad D_s = \frac{\lambda_h}{\lambda_s}. \tag{3.27}$$

$$\Theta = \frac{2}{\sqrt{\pi}} + \frac{1}{2D_s}\left[e^{D_s^2}\,\text{erfc}(D_s) - 1\right] \quad \text{at } x = 0 \tag{3.28}$$

This equation is the same as Eq. 3.14 except for D_s instead of D. Therefore the behavior of the temperature profile is the same as the case of Bouguer-Lambert-Beer law absorption.

Stationary ablation

Next, recession velocity of the ablated surface is obtained in the stationary ablation regime. The recession velocity during stationary ablation is independent on the absorption length of laser, more generally, independent on the profile of heat injection. Consider an arbitrary temperature distribution: $T(x)$, which recedes in the x direction with keeping the shape at the velocity of v, because now the stationary ablation is assumed. After the surface recession of Δx, the temperature distribution becomes $T(x-\Delta x)$ as shown in Fig. 3.27. At the point of x, to perform this recession, the temperature must be raised up to $T(x-\Delta x)$ from $T(x)$. Therefore, over the all x, the heat of

$$\rho c_p \int_{x_w}^{\infty} T(x-\Delta x) - T(x)\; dx \tag{3.29}$$

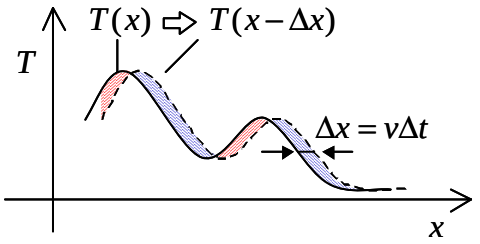

Figure 3.27: Shift of temperature profile during stationary ablation.

is necessary. The heat injected during this recession: $q\Delta t = q\Delta x/v$ is used for both the ablation of the material and the heating. Hence

$$q\Delta x/v = \rho c_p \int_{x_w}^{\infty} T(x-\Delta x) - T(x)\; dx + \rho \Delta h_{\rm PT} \Delta x \tag{3.30}$$

$$q = \rho c_p \int_{x_w}^{\infty} -\frac{dT}{dx} v\; dx + \rho \Delta h_{\rm PT}\; v \tag{3.31}$$

$$q = \rho \left(c_p (T_{x_w} - T_\infty) + \Delta h_{\rm PT} \right) v \tag{3.32}$$

where $\Delta h_{\rm PT}$ is the heat of phase transformation (ablation, decomposition, melting, or vaporization).

$$v = q \,/ [\rho \left(c_p (T_{x_w} - T_\infty) + \Delta h_{\rm PT} \right)] \tag{3.33}$$

This recession velocity is independent on both profile of the heat source and stationary distribution of the temperature.

Let us obtain the temperature profile during the stationary ablation. The governing equation is

$$\frac{\partial T}{\partial t} = \kappa \frac{\partial^2 T}{\partial x^2} + \frac{q}{\rho c_p \lambda_a} e^{-(x-vt)/\lambda_a}, \qquad x \geq vt \tag{3.34}$$

$$\text{B.C.} \left\{ \begin{array}{ll} \left. \dfrac{\partial T}{\partial x} \right|_{x=vt} = \Delta h_{\rm PT}\; \rho v, & T(x=vt) = T_b \\ \left. \dfrac{\partial T}{\partial x} \right|_{\infty} = 0, & T(\infty) = T_\infty \end{array} \right. \tag{3.35}$$

where v is the recession velocity. At the recession surface at $x = vt$, the surface is cooled by the latent heat $\rho v \Delta h_{\rm PT}$. On putting $\xi = x - vt$, we have an ordinary differential equation on the temperature profile

$$-v\frac{dT}{d\xi} = \kappa \frac{d^2 T}{d\xi^2} + \frac{q}{\rho c_p \lambda_a} e^{-\xi/\lambda_a} \tag{3.36}$$

Solving the equation,

$$T - T_\infty = (T_b - T_\infty)e^{-\xi/\lambda_x} + \frac{q}{K}\frac{\lambda_x\lambda_a}{\lambda_x - \lambda_a}(e^{-\xi/\lambda_x} - e^{-\xi/\lambda_a}) \tag{3.37}$$

$$v = q\,/\rho\,(\Delta h_{\rm PT} + c_p T_b)\,, \tag{3.38}$$

$$\lambda_x = \frac{\kappa}{v} = \frac{K}{qc_p}(\Delta h_{\rm PT} + + c_p T_b) \tag{3.39}$$

3.4.2 Comparison to the experimental results

In the first approximation of the thrust generation by laser ablation, the transition regime of the ablation is neglected. In short, it is assumed that stationary ablation starts just after the laser-irradiated surface reaches to its boiling (or degradation) temperature. In that case, the mass ablated by irradiation is simply

$$m(t) = \begin{cases} 0 & , \quad t < t_b \\ \rho v S(t - t_b) & , \quad t \geq t_b \end{cases} \tag{3.40}$$

$$\rho v S = Q/(\Delta h_{\rm PT} + c_p T_b) \tag{3.41}$$

$$t_b = \frac{1}{\kappa}\left(\frac{\sqrt{\pi}}{2}\frac{KT_b}{q}\right)^2 f(A) \tag{3.42}$$

where S is the area irradiatd by laser beam and Q is the laser power, namely qS. Equation 3.40 means that mass ablated by laser irradiation mainly depends on the total incident power, and little on the intensity. The intensity affect the time when the ablation starts.

In order to experimentally validate that expression, laser ablated mass was measured with changing the laser intensity. The position of the target was shifted around the focal point. The change of the position gives different laser intensities according to the measured beam profile, shown in Fig. 3.11. The ablative material used here was PVC with 5 % carbon additives, The relation of the position of target surface from the focal point and the ablated mass is shown in Fig. 3.28, where laser intensity was calculated from the position using the realtion of Fig. 3.11. The distance from the optical system to the target surface would have uncertainty because of the oblique surface of cylindrical propellant. The associated error would be ± 1.0 mm in maximum. That relation says that the laser ablated mass is gradually changed with the position, whereas laser intensity has an abrupt peak at the focal point. It means that laser ablated mass has no strong dependence

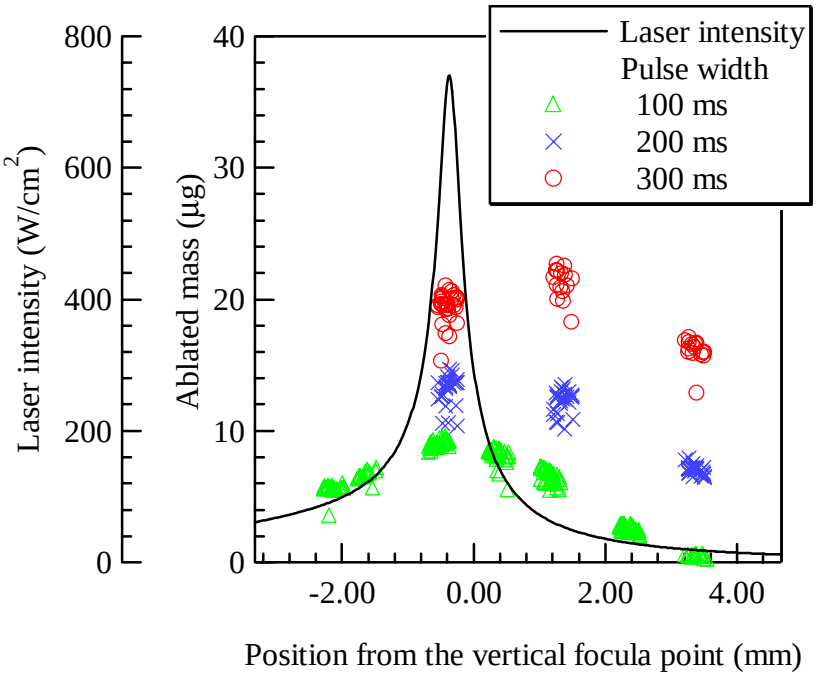

Figure 3.28: Relation of tge target position and ablated mass.

on laser intensity. It is the fact predicted from the thermal analysis of laser ablation. From the engineering view point, the weak dependence of intensity on the ablated mass, namely the performance, means that the integration of laser ablation thruster does not require tight alignment for optical system.

Figure 3.29 is re-drawing of the same data as the relation of laser intensity and ablated mass, where the theoretical curves of ablated mass, Eq. 3.40, is drawn as a function of the intensity q. Those curves are in the case of zero laser absorption length ($\lambda_a = A = 0$). The properties used in the calculation are shown in Table 3.7. It should be cared that characteristics of polymer largely depends on the experimental conditions and additives. Of the properties the heat of fusion was experimentally estimated. As shown from the mass spectrum, laser ablation mostly relies on the degradation of HCl in PVC, and there is few reliable data about the heat of degradation. Then the effective heat of degradation was determined from the ratio of ablated mass to laser pulse width at high laser intensity (>300 W/cm^2), where the ablation would reach to the stationary regime.

The theoretical curves show the qualitative behavior of the ablation. The

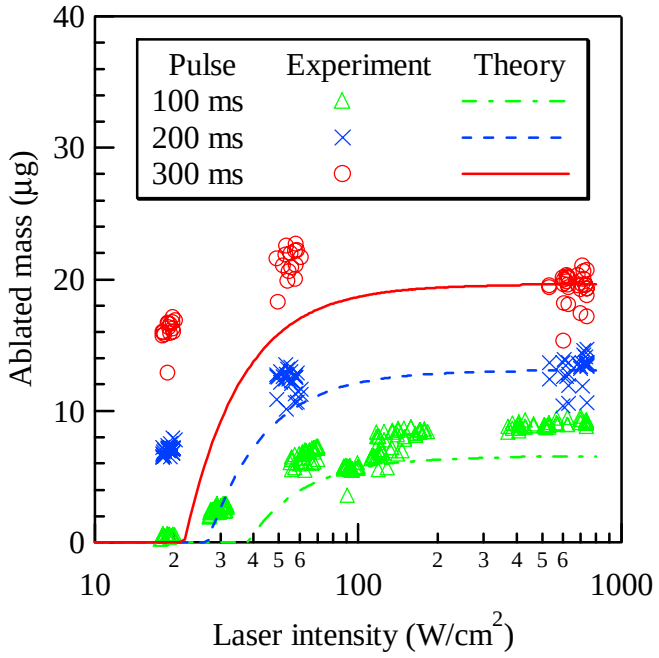

Figure 3.29: Relation of the laser intensity and ablated mass.

ejected mass increases with the laser intensity and it saturates in high intensity region. However, the rising is slower than measured mass, in spite of no consideration of the transition regime here. The rising time is determined by density, specific heat, thermal conductivity, and laser intensity. Uncertainty included in the thermal properties and the intensity would cause that difference. Especially the intensity would include large error, and additionally it affect the rising time quadratically.

Table 3.7: Properties of PVC used in the calculation.

Density[81]	1.35 kg/m^3
Specific heat[81]	952 J/kgK
Thermal conductivity[81]	0.21 W/mK
Decomposition point[78, 79, 77]	553 K
Fraction of carbon additives	5 %

3.5 Experimental Results on Laser Ignition Mode

3.5.1 Laser ignition of pyrotechnics

Three varieties of pyrotechnics were prepared for the laser ignition mode experiments: composite propellant, double-base propellant, and pelleted boron/potassium nitrate(B/KNO_3). These pyrotechnics were loaded into the holes on the ceramic cylinder (shown in Fig. 3.13). The composite and double-base propellants were cut to the appropriate size and pressed into the 2.0-mm-diam, 1.0-mm-long holes. Pelleted B/KNO_3 cylinders of 3.2-mm-diam and 2.0-mm-long were installed in holes of the corresponding size. The pellet weighed 0.03 g. Pictures of the three pyrotechnics are shown in Fig. 3.30.

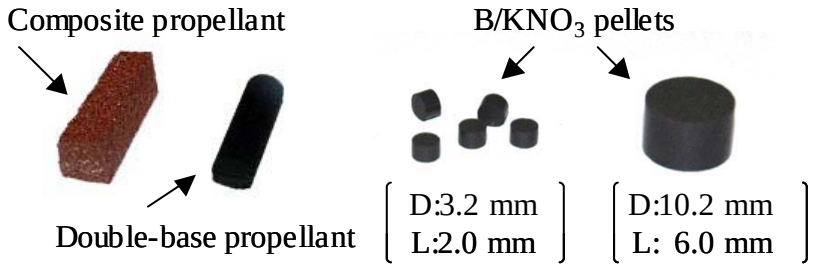

Figure 3.30: Pictures of the pyrotechnics: composite propellant, double-base propellant, and pelleted boron/potassium niterate (B/KNO_3).

In the atmosphere, all pyrotechnics were successfully ignited by the irradiation from a diode laser. Figure 3.31 a) shows images of laser ignited combustion of the composite propellant in the atmosphere. The origin of the time in the figure is when the laser irradiation starts. Initially, laser beam irradiates the propellant and there is no reaction ($t = 0 \sim 400$ms). After 500 ms, the propellant undergoes combustion with exhausting intense plume and it lasts to $t = 1000$ ms.

However, in vacuum, composite and double-base propellants were not ignited. Figure 3.31 b) shows images when the composite propellant was irradiated by laser in vacuum. Self-sustained combustion was not performed, whereas several small sparks were scattered from the laser irradiation point. The scattering of sparks goes only under laser irradiation. Generally, the combustion speed of pyrotechnics decreases with decrease of the background pressure, and several pyrotechnics have

a threshold pressure for the self-combustion.

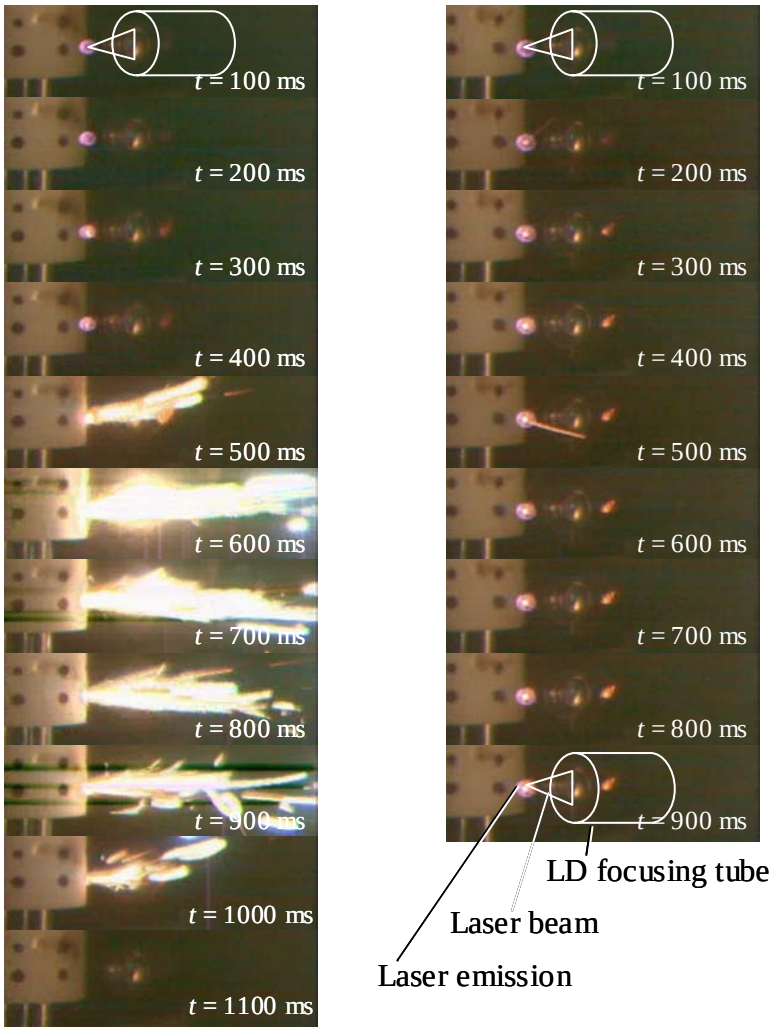

Figure 3.31: Laser irradiation of composite propellant; a) Laser ignited combustion in the atmosphere and b) no self-sustained combustion in vacuum.

In contrast, B/KNO_3 was successfully ignited by diode laser beam under a background pressure of 1.4 - 3.0 $\times$ 10^{-4} Torr. Figure 3.32 shows images of the laser ignition of a B/KNO_3 pellet. Initially, the laser beam irradiates the pellet (t = 30 ms in Fig. 3.32). The pellet then undergoes combustion at the focal point of the laser beam (t = 90 ms). The combustion front spreads over the surface of the pellet and steady combustion lasts during t = 270 $\sim$ 690ms. Thereafter the combustion becomes weak and terminates at approximately 1000 ms. Table 3.8

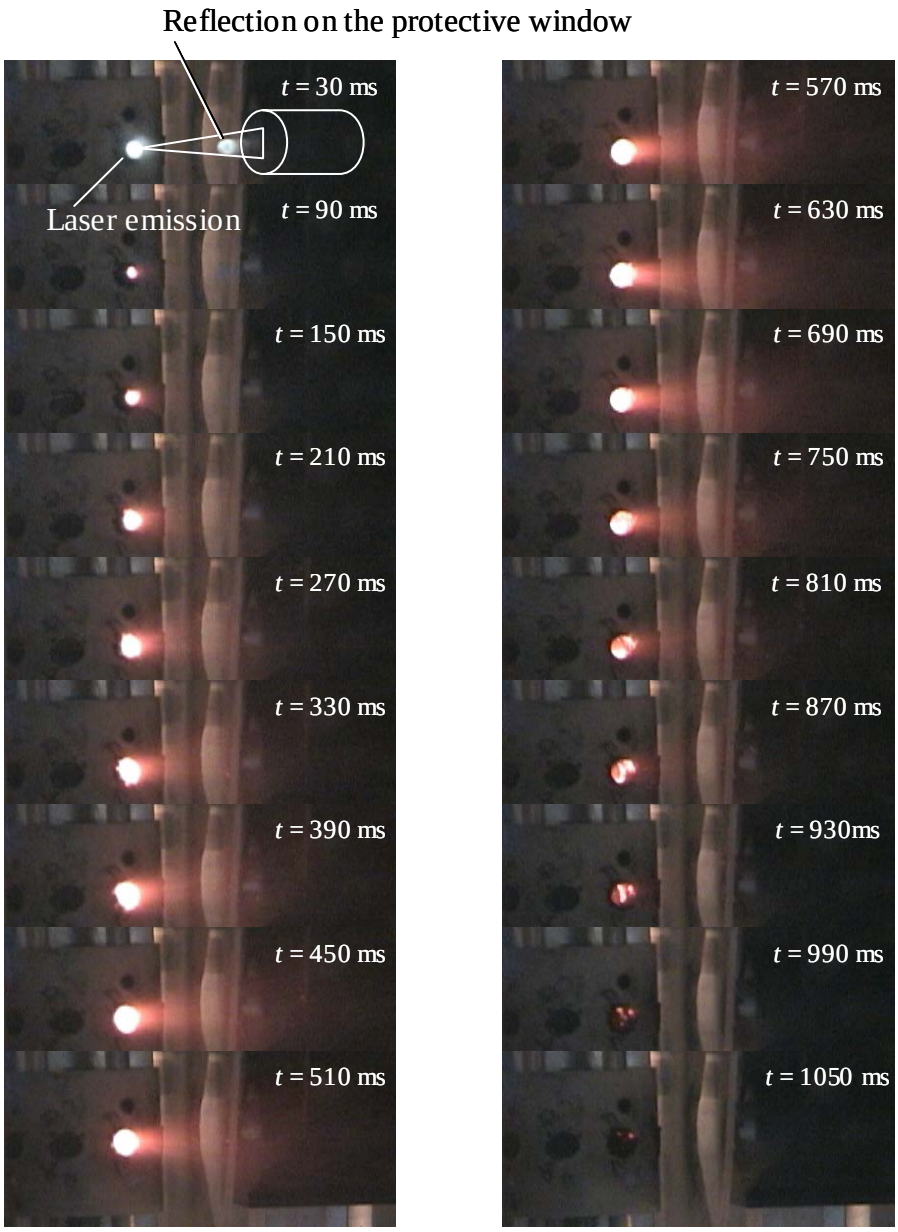

Figure 3.32: Laser ignited combustion of B/KNO_3 in vacuum.

summarizes the results of laser irradiation of pyrotechnics.

Table 3.8: Summery of 300 mW laser irradiation on pyrotechnics.

Pyrotechnics	in the atmosphere	in vacuum ($< 10^{-3}$ Torr)
Composite propellant	Combustion	No self-sustained combustion
Double-base propellant	Combustion	No self-sustained combustion
Boron/potassium nitrate	Combustion	Combustion

3.5.2 Laser ignition probability of B/KNO_3 in vacuum

Effect of laser pulse width

The ignition threshold of B/KNO_3 was investigated against the laser pulse width; the results are shown in Figure 3.33. The laser power was 250 mW. There the ignition probability is defined as the number of ignitions over number of trials. At laser pulses shorter than 50 ms, no propellant was ignited. Between 50 to 150 ms, the propellants were ignited only after several attempts. When the laser pulse width exceeded 150 ms (38 mJ), all the propellants were successfully ignited. The ignition threshold of our solid propellant was therefore about 100ms. The uncertainty of the ignition around the threshold was caused by slight differences in the experimental conditions, surface position and angle of propellants, and so on, and depends on the alignment accuracy of the optical system. A pulse width of 1000 ms (250 mJ) would be enough for spacecraft applications.

Effect of laser power

The effect of laser power on the ignition probability was investigated. To remove the variation of the position and angle of the pellets, another propellant feeding system was prepared. It was designed not for the thruster but only for accurate evaluation of the ignition probability dependence of the power. Figure 3.34 shows the picture of the experiment setup. Twenty pellets are installed into holes aligned on a line, and each pellets are separated by plastic walls. Laser beam enters through a acrylic window which prevents the optical system from fouling. The

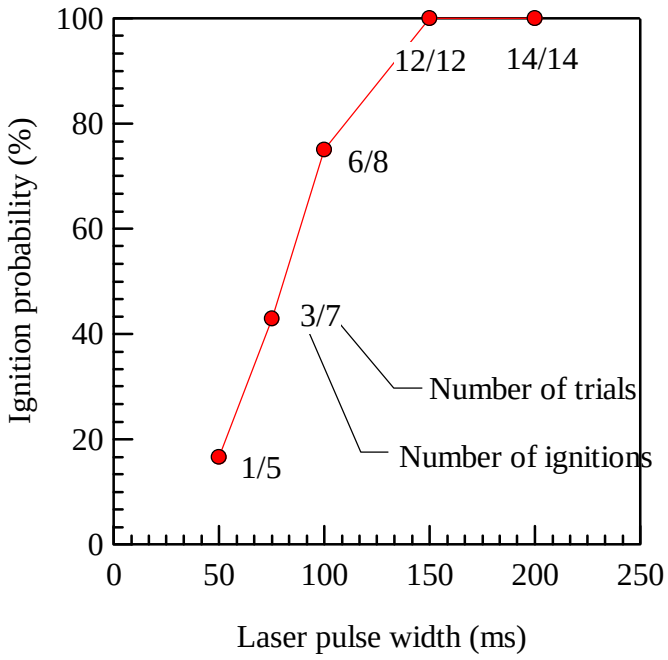

Figure 3.33: Laser ignition probability of B/KNO_3 in vacuum, dependence on the laser pulse width.

stage was shifted after every shot using a linear transverse stage. The distance from the diode laser to the pellet's surface was set as 16 mm, which includes the increase of light pass due to the acrylic window. The variation of the position of the pellets was at most ± 0.2 mm (standard deviation), which was measured using a laser displacement sensor. Here it should be noted that in this experiment a diode laser different from one above-described was used. Therefore, the focal length measured using a beam profiler can not be applied for the laser beam dealt here. The focus lens was newly adjusted to give the maximum light emission on the position of 16 mm.

The measured ignition probability is shown in Fig. 3.35, which was obtained after the ignition trials using 40 pellets. The definition of the probability is the same as before. The laser pulse width was constant of 1 s in all trials. The base pressure was under the 2×10^{-3} Torr.

The threshold of the laser ignition was between 265 and 340 mW. No pellets was ignited under the 200 mW of power, and all pellets were combusted over

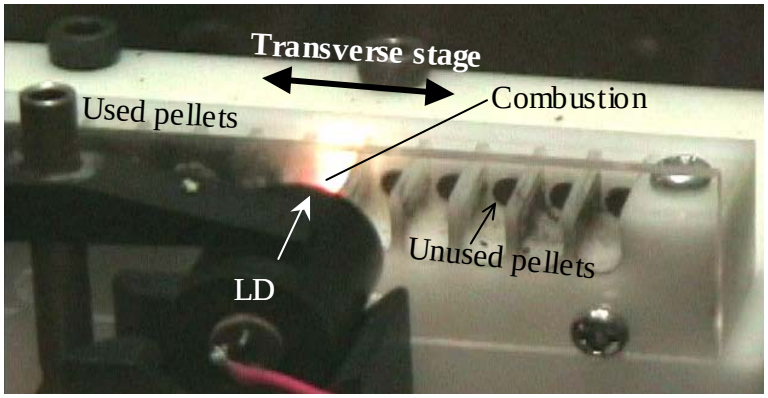

Figure 3.34: Picture of the experiment setup for measuring the ignition probability.

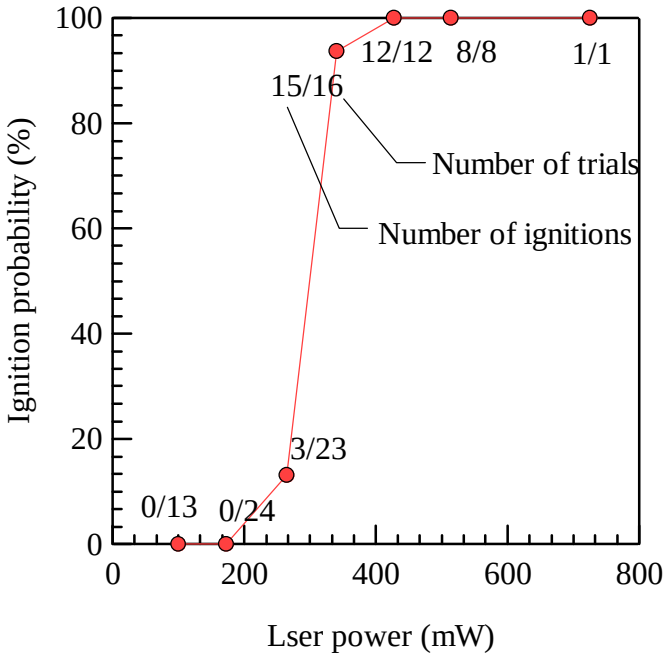

Figure 3.35: Laser ignition probability of B/KNO_3 in vacuum, dependence on the laser power.

the 400 mW. The observed combustion processes were the same as Fig. 3.32. After the laser irradiation and the ablation of the surface, the pellets started the combustion, which lasts about 1s.

The obtained threshold power for the laser ignition was a little inconsistent in the experiment of previous section 3.5.2, where the laser power 250 mW and width 1 s gave exact ignition. The discrepancy would be caused by the difference of configurations of laser optical assembly and feeding system. At most 500 mW power, however, is enough power to ignite B/KNO_3 pyrotechnics in vacuum. These results says that the laser ignition mode can easily coexist with the laser ablation mode because the energy required for ignition was lower than or comparable to that for laser ablation.

3.5.3 Thrust measurement of laser ignition mode

Thrust measurement for laser ignition mode was performed to evaluate the thrust produced by the combustion of laser ignited B/KNO_3 pellet. The thruster used for the thrust measurement was shown in Figs. 3.13 and 3.12. The B/KNO_3 pellet used here weighed 32 mg and installed into a ceramic hole without any nozzle.

Table 3.9 indicates performance in the laser ignition mode using B/KNO_3 propellant in vacuum. The averaged impulse was 11±2 mNs and the specific impulse, which was calculated using the weight of the pellet, was 36±7 s. The theoretical predicted maximum specific impulse of B/KNO_3 in vacuum was higher than 100 s. This discrepancy probably arose because the propellant and the nozzle were not optimized in shape. The consumed energy here for the laser ignition was 38 mJ using 250 mW laser power and 150 ms laser power.

Table 3.9: Result of thrust measurement of laser ignition mode using 30 mg B/KNO_3 pellets.

Impulse	11±2 mNs
Specific impulse	36±7 s
Laser energy	38 mJ (250 mW, 150 ms)

The thrust measurement described here have shown that dual operational

modes, laser ablation of polymer propellants and laser ignition of solid propellants, can be achieved using the same laser optical assembly. The two modes of operation generated impulses over the four orders of magnitude, impulses of 1-40 μNs in the laser ablation mode and 10 mNs in the laser ignition mode. Figure 3.36 shows a conceptual diagram of a dual propulsive mode microthruster. The propellant is fabricated from several kinds of materials, namely, ablation material with low and high C_{m} and solid propellant of small and large size. It is reoriented to the fixed laser optical assembly in order to provide the appropriate material and vary the propulsive mode according to the required thrust level. This single propulsion system thus perform multiple propulsive tasks with a single propulsion system.

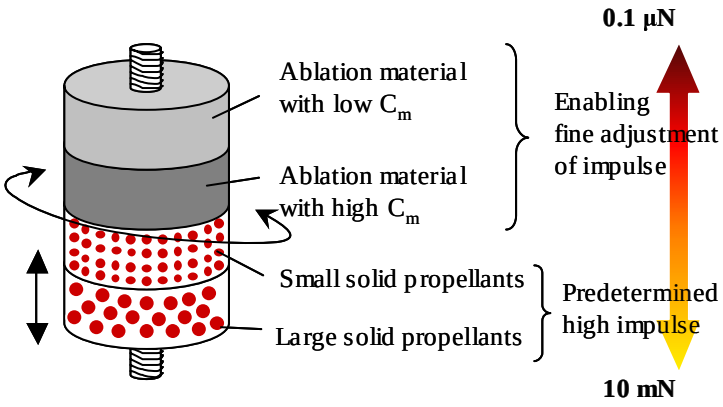

Figure 3.36: Conceptual diagram of a dual propulsive modes microthruster.

3.6 Development of a One Newton Laser Microthruster

A laser ignition microthruster was designed and developed to provide high total impulse over 20 Ns. The objective of that thruster is to verify the concept of laser ignition mode by actually developing a thruster. The thruster was designed to be installed in 10 kg microspacecraft with 20 cm cubic dimensions and 5 kg weight, in a private meeting with Nakasuka lab. and Arakawa lab.. There the allowed volume for the thruster was a rectangular space of $5\times5\times20$ cm^3. For instance, mission suggested in the meeting is to orbit around another microspcecraft with the distance of 5 m, which is a demonstrative mission of formation flying. That orbiting should be conducted during communication period of 400 s. A spacecraft in low earth orbit rapidly passes over the base station on the earth. In the case, at least the total impulse of 5.6 Ns is necessary to orbit around. In the demonstration stage of formation flying, only the huge thrust translating spacecraft is needed.

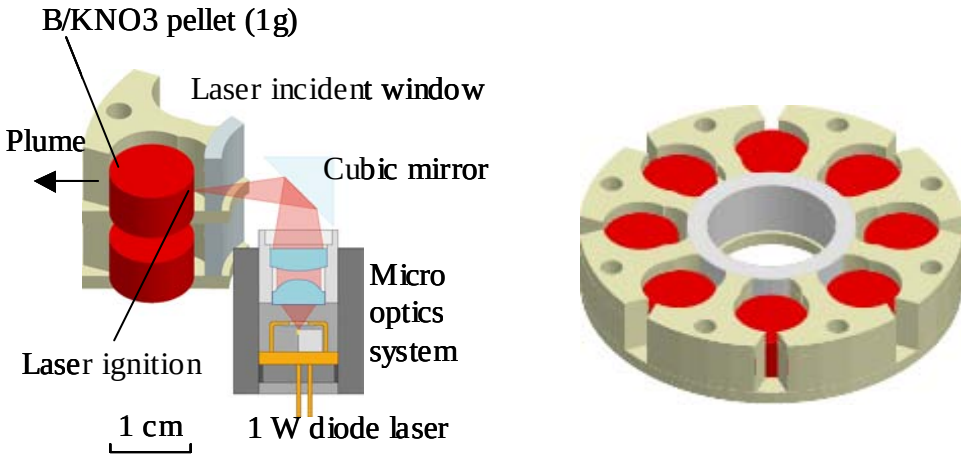

Figure 3.37: Schematic diagrams of a one Newton class laser microthruster, a) cross section of the single combustion chamber and b) a single prpellant cartridge.

To solve the lens fouling problems, a transmission mode was used (see Fig. 3.3) The conceptual diagram of the thruster is shown in Fig. 3.37. A diode laser and optics system is installed inside the propellant along the axis. Laser beam emitted along the axis is reflected by a cubic mirror, and introduced into a combustion

chamber through a transparent incident window. A pyrotechnic pellet is loaded in that combustion chamber, which has the same diameter and a little more height as the pellet. To provide high total impulse, larger pellets than those used for the above experiment were used, which has the diameter of 10.2 mm, the length of 6.0 mm, and the weight of 1.02 g (see Fig. 3.30). The combustion plume is exhausted from a throat to the outside. Eight pellets are installed in a single disc as shown in Fig. 3.37 b). The single disc is referred as a propellant cartridge here. The propellant cartridges are accumulated to provide required total impulse.

The fabricated propellant cartridges are made of stainless steel, urethane resin, or epoxy resin. The stainless steel body was designed for initial examinations, reusable material was selected. The latter was designed for the actual use. The bodies had very light weight of 8.6 and 9.4 g for urethane and epoxy bodies respectively, whereas those cartridge can be used only once. The incident window is made of an acrylic tube with the thickness of 2 mm. The picture and drawing of an epoxy resin cartridge are shown in Fig. 3.38.

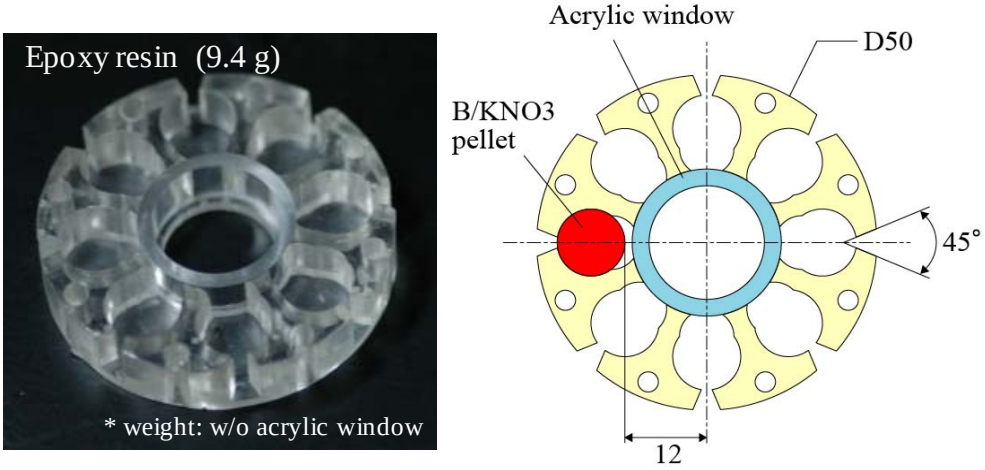

Figure 3.38: Picture a) and dimension b) of the one Newton class laser microthruster.

First, laser ignition using cubic mirror reflection, no-sympathetic combustion with the neighbor pellets, and the generated thrust by a large pellet were examined using a stainless steel cartridge body. As a result, the most problem was the sympathetic combustion. It was sometimes observed that the combustion gas was leaked out into the neighbor chamber, and made the pellet there be ignited. It was

solved adhering and sealing the gap of cartridges using an epoxy resin adhesive (Araldite®).

Next, urethane and epoxy resin bodies were examined. The most concern was whether resin bodies endured the combustion. As a result, the urethane body showed the sympathetic combustion but the epoxy body showed no such combustion. There were observed extended gap between the urethane cartridges due to the combustion. Figure 3.39 shows the combustion plume when the epoxy resin cartridge was used. The better result using epoxy resin would be caused by higher durability of epoxy resin and better compatibility with the used adhesive.

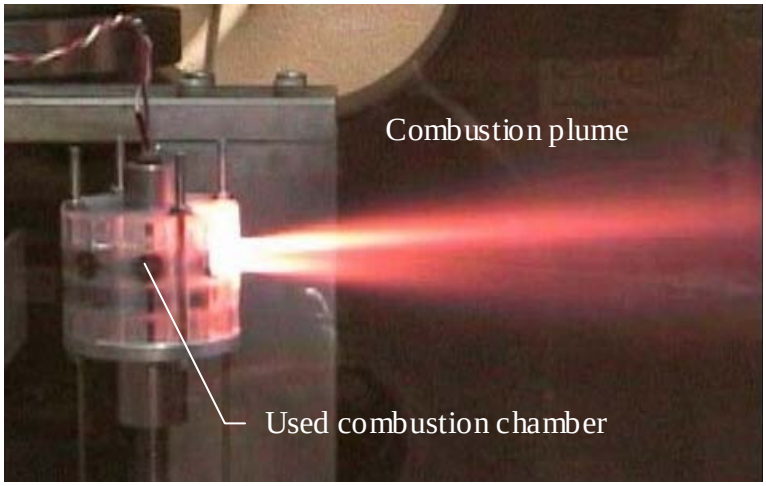

Figure 3.39: Combustion plume of the one Newton class laser microthruster.

Thrust measurement was carried out using the stainless steel and epoxy bodies. The thrust measurement was described in detail in Section 2.5. The result is shown in Fig. 3.40. The averaged impulse of a single shot was 452 mNs for stainless steel cartridge and 655 mNs for epoxy resin cartridge. The reason of higer impulse of epoxy resin would be the additional mass by the ablation of cartridge body itself. In contrast shot-to-shot variation was larger using epoxy resin. The standard deviation was 21 mNs for SUS and 60 mNs for epoxy resin. It would also be caused by the ablation of the polymer.

Using the laser ignited propellant addressed here, the propulsion system can provide more than 30 Ns of total impulse within the volume of $5\times5\times10$ cm^3. The propellant cartridge has the diameter of 50 mm and the thickness of 10 mm. Then

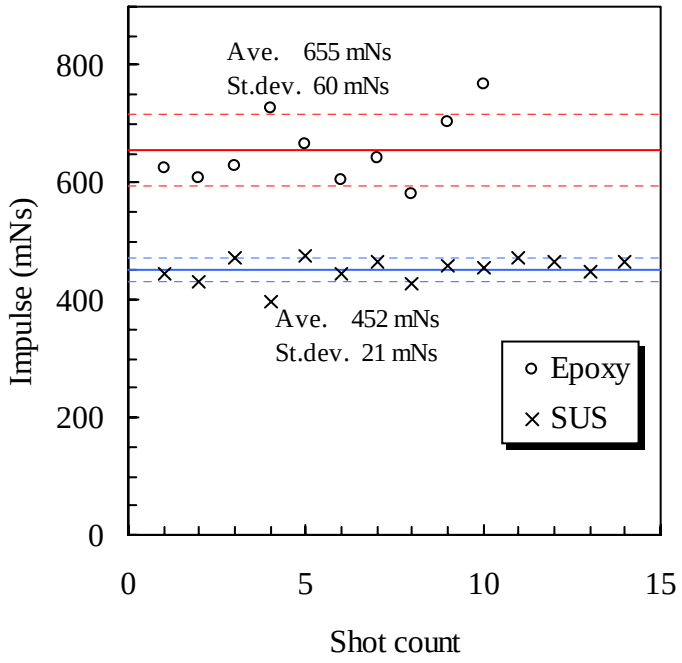

Figure 3.40: Impulse generaed by the one Newton class laser microthruster, using two materials for the cartridge bodies.

the accumulation of the six cartridges has the height of 60 mm. The residual 40 mm height can be used for the rotational mechanism and diode laser module.

3.7 Discussion on Ignition threshold of B/KNO_3 pyrotechnic.

3.7.1 Reaction processes of B/KNO_3

Boron and potassium nitrate showed good ignition performance in vacuum in comparison with composite and double-base propellant. To clarify its ignition capability, why it has good ignition characteristic in vacuum, it is necessary to understand the reaction processes.

Generally, the burning rate of pyrotechnics decreases with the decrease of the background pressure as above mentioned. It is because the gas phase reaction

speed is strongly depends on the background pressure. Figure 3.41 shows the mechanism of typical solid propellant combustion. Vaporization of solid propellant

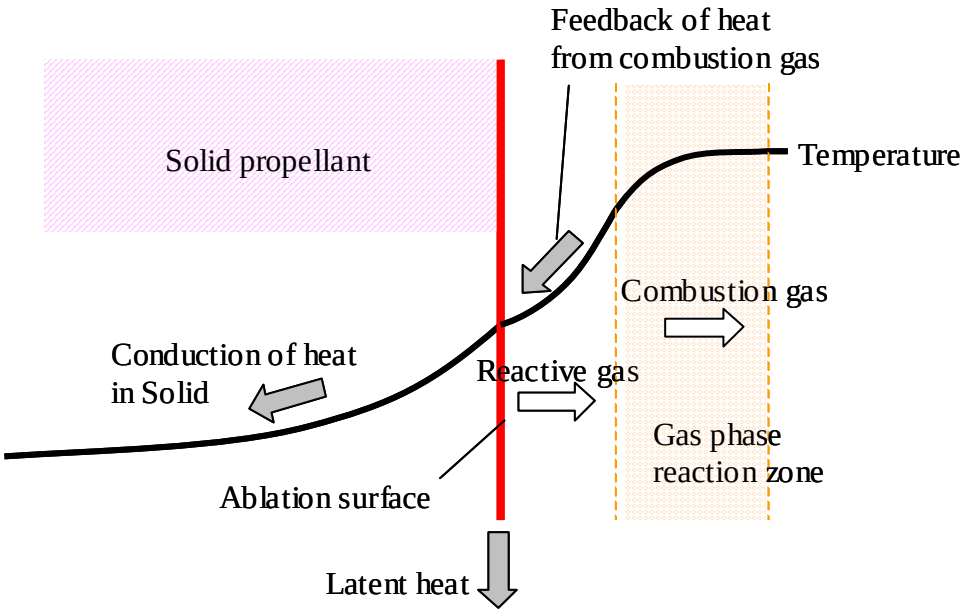

Figure 3.41: Thermal feed back mechanism of typical solid propellant combustion.

gives reaction gas in the vicinity of the ablation surface. The reaction gas goes under combustion zone which is a little apart from the surface (sometimes the boundary is vague). The heat produced in the combustion zone is fed back to the solid by heat conduction and radiation. The feed back of the heat causes the ablation of the solid surface. The burning rate depends on the reaction rate in the gas phase, and it increases with the background pressure. As a result, burning rate is expressed as a function of pressure as

$$r_{\mathrm{b}} = ap_c^n \tag{3.43}$$

where r_{b} is the burning rate, a is the constant, p_c is the background pressure, and n is also constant called pressure exponent. Equation 3.43 is called as Vielle's law. Therefore decreasing background pressure, the burning rate decreases and eventually the combustion is quenched [82].

Reaction processes of boron and potassium nitrate had been investigated by Yano in 1980s by thermochemical alaysis [83, 84, 85, 86]. The processes consist of

a three-stage reaction. A significant heat is produced in the first-stage process by the reaction

$$B + KNO_3 \rightarrow KBO_2 + NO. \tag{3.44}$$

In the second-stage process, the remaining un-reacted potassium nitrate decomposes to produce gaseous oxidizing fragments. In the third stage, the KBO_2 produced in the first-stage process decomposes.

The first-stage process is the reaction of condensed phase potassium nitrate and boron particle. Boron potassium nitrate dealt here was the mixture of boron particle of less than 1.0 μm diameter and potassium nitrate. Boron has the melting point of 2340 K and potassium nitrate has the melting point at 612 K. Yano showed by his thermochemical analysis that the exothermic reaction of Eq. 3.44 was occurred between 720 and 810 K [83, 84]. Hence in the reaction of Eq. 3.44, the boron particles are oxidized with liquefied potassium nitrate around. The oxidation forms the oxide shell around the particle surface, which prevents the oxidation. Thus the reaction of boron particles is terminated when the thickness of the oxide shell reaches to certain value. The thermal reaction processes of boron/potassium nitrate is summarized in Table 3.10.

The exothermic reaction of Eq. 3.44 is not largely effected by the background pressure because the main reaction is not the gaseous phase reaction but condensed phase reaction. It is the reason that B/KNO_3 pyrotechnic is successfully ignited by laser irradiation in vacuum. Yano showed that the burning rate of B/KNO_3 with high boron weight fraction is insensitive to the background pressure, namely the pressure exponent is close to zero. Actually, B/KNO_3 pellet dealt here, supplied from Nichiyu Giken Kogyo Co., Ltd., has the pressure exponent of 0.08 (measured from 1 to 50 atm).

3.7.2 Numerical calculation of the exothermic reaction

It is important in an engineering view point to know what power is necessary to successfully ignite the pyrotechnics by laser irradiation. In short it is required to clarify the mechanism oflaser ignition and to determin what is the most important factor. In this section, numerical calculation was conducted to clarify that mechanism.

Table 3.10: Thermal reaction processes of B/KNO_3.

Temperature(K)	Reaction
300-620	Temperature rising
620	Melting of KNO_3
720-810	Exothermic reaction
	($B+KNO_3 \rightarrow KBO_2 + NO$)
810-930	Decomposition of excess KNO_3
1000	Decomposition of KBO_2 ($\rightarrow K_2O$, B_2O_3)

B/KNO_3 pellets used here are mixture of boron and potassium nitrate, and the thermal properties are different from them. In this study, following thermal properties were used to evaluate the ignition capability of B/KNO_3 pyrotechnic. The density was calculated from the size and weight of the pellets. The specific

Table 3.11: Thermal properties of B/KNO_3.

Born weight fraction: p	0.3
Density: ρ	2228 kg/m^3
Specific heat: c_p	1142 J/kgK
Thermal conductivity: k	1.6 W/mK
Reaction threshold: T_{R}	720 K
Heat of reaction: Δh_{R}	4 MJ/kg

heat was calculated by the mass average of boron and potassium nitrate. Reaction threshold temperature and heat of fusion were sited from Yano's result [83, 84, 85]. However, the heat of reaction depends on the boron weight fraction and the diameter of the boron particles. It is because that the effective total surface area of boron particles depends on the weight fraction and diameter. Hence that accurate value could not be known.

The thermal conductivity is the most important parameter. However, it is difficult to accurately predict the thermal conductivity of mixture solid of two components, because it depends on not only the volume fraction but also the arrangement

of the components with respect to the mean heat flow. Then a lot of researchers have worked on this field and proposed the several theories [87, 88, 89, 90, 91]. Nevertheless, there are several discrepancies of those results according to the thermal conductivity and mixture ratio. In this study, empirical formulae obtained by Kobayashi et. al was used to predict the thermal conductivity [87]. It based on the result of their numerical calculation of heterogeneous solid mixture. Thermal conductivity of mixture solid predicted by other authors and the comparison with those are shown in Appendix D.

To ignite the B/KNO_3, firstly, laser beam must heat up the pyrotechnics to the reaction temperature, which is necessary condition for the ignition. However, even if several fractions reach to the reaction point and there reaction occurs, the reaction can be quenched if the initial reaction is too small. Hence, enough reaction to maintain the reaction must occur, which is another condition for the ignition.

Here it should be noted that heating by laser during about 1 s leads to not the bulk heating but very local heating. The heat depth at 1 s is about 0.8 mm which is less than the characteristics length of the pellet (2-3 mm). The bulk heating of pellet by our laser power rises the temperature only a few tens of Kelvins. Actually, the pulse width longer than 17 s is required to bulky heat up the pellet up to the reaction point.

One dimensional analysis with spherical symmetry

Laser beam emitted from a diode laser has very distorted ellipse shape as shown in Fig. 3.6. Then the heating has nor spherical or cylindrical symmetry and three dimensional analysis is required. Nevertheless simple analysis using spherical symmetry will give the fundamental knowledge about the local heating by laser beam.

In the spherical symmetry, the governing equation of heat conduction is described as

$$\frac{\partial T}{\partial t} = \kappa \left(\frac{\partial^2 T}{\partial r^2} + \frac{2}{r} \frac{\partial T}{\partial r} \right), \qquad r \geq r_0 \tag{3.45}$$

$$\text{b.c.} \qquad -k \left. \frac{\partial T}{\partial x} \right|_{r=r_0} = q, \quad T(\infty) = T_\infty \tag{3.46}$$

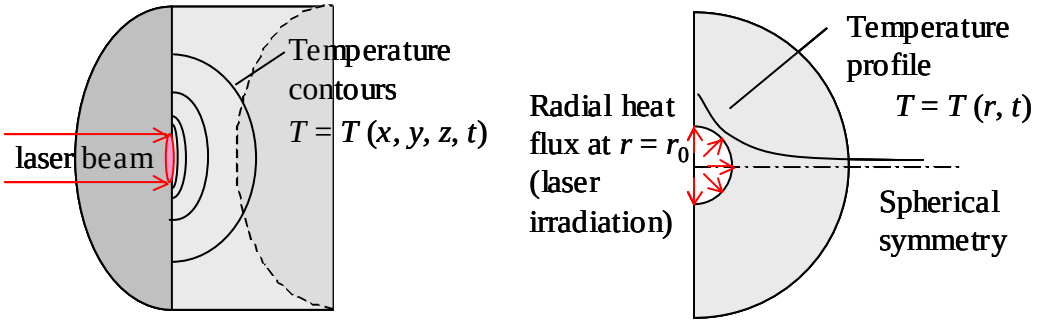

Figure 3.42: Conceptual drawings of a) three dimensional heating and b) heating under spherical symmetry.

where q is the intensity of laser beam and r_0 simulates the half beam width at the irradiation surface. Conceptual diagram of the system is shown in Fig. 3.42. The transit solution of those equation can be expressed by the series expansion [80], and the steady state solution has a simple form

$$T(r) - T_\infty = \frac{Q}{2\pi k r}, \qquad Q = 2\pi r_0^2\, q \tag{3.47}$$

where Q is the incident laser power. The maximum temperature of the system appears at $r = r_0$. Equation 3.47 says that small thermal conductivity or small beam width gives high maximum temperature under constant laser power.

For instance, in our case of the thermal conductivity of 1.60 W/mK and the minimum radius of 98 μm ($= \sqrt{\omega_x \omega_y / \pi}$, averaged width of the horizontal and vertical laser widths), 0.30 W laser power is required to heat up 430 K at $r = r_0$ (reaching reaction point of 720 K). In the actual case, the laser irradiation area has a distorted ellipse. Therefore the Eq. 3.47 can not be used for the quantitative estimation. Nonetheless, the estimation of 0.30 W power is well consistent with the experimental result.

Numerical calculation of heating

To accurately predict the threshold of laser ignition, three dimensional numerical calculation was conducted. A rectangular solid is selected as the calculation domain in stead of the actual cylindrical pellet. It is due to the simplicity of fabricating the calculation grid. However, that difference can be neglected because the characteristic length of the heat conduction is less than the one of the pellet.

Incident power by laser beam was treated as heat flux into the boundary surface. The laser absorption length was assumed to be zero. Exothermic reaction was included in the calculation. It is assumed that the reaction rate is constant and it starts when the point reaches to the reaction temperature T_R. It means the reaction rate is independent on the temperature and density of the reactant. The last assumption is valid because the exothermic reaction of B/KNO_3 is in the condensed phase and insensitive to the background pressure.

The governing equation is

$$\rho c_p \frac{\partial T}{\partial t} = k \frac{\partial^2 T}{\partial \mathbf{x}^2} + \rho \Delta h_{\mathrm{R}} \omega s(t, \mathrm{x}) \tag{3.48}$$

$$0 \le x \le L_x,\ 0 \le y \le L_y,\ 0 \le z \le L_z \tag{3.49}$$

$$\text{B.C.} \qquad \left.\frac{\partial T}{\partial z}\right|_{z=0} = -q(x,y)/k \tag{3.50}$$

$$\left.\frac{\partial T}{\partial n}\right|_{\text{wall}} = 0 \tag{3.51}$$

where x is taken along the horizontal axis and y is along the vertical axis, and z is along the beam axis (see Fig. 3.6). Laser beam irradiates the $z = 0$ plane and the intensity profile $q(x, y)$ is given as

$$q(x,y) = Q \frac{4}{\pi w_x w_y} \exp\left\{ -\left(\frac{x}{w_x/2}\right)^2 - \left(\frac{y}{w_y/2}\right)^2 \right\} \tag{3.52}$$

As mentioned in Section 3.2.4, $w_x \simeq 0.6$ mm and $w_y < 0.1$ mm. Second term on right hand side of Eq. 3.48 expresses the exothermic reaction, where Δh_{R} is the heat of reaction, ω is the reaction rate (constant), and $s(t, \mathbf{x})$ is a function which determines the reaction period, defined as.

$$s(t,\mathbf{x}) = \begin{cases} 1 & , \quad t_R < t \le t_R + 1/\omega \\ 0 & , \quad \text{otherwise} \end{cases} \tag{3.53}$$

$$t_{\mathrm{R}}\text{: the time when } T(\mathbf{t}, \mathbf{x}) \text{ reaches to } T_{\mathrm{R}} \tag{3.54}$$

It means that the reaction at a certain point, $\mathbf{x}$, starts when the temperature $T(t, \mathbf{x})$ reaches to T_{R} and it lasts during $1/\omega$. The calculation domain is taken as a quarter of the actual rectangular solid from the symmetry on $x = 0$ and $y = 0$ planes.

Figure 3.43 shows the calculation domain and grid. Here, irregular mesh, namely variable grid spacing, was employed to obtain the desired accuracy and resolution in the vicinity of the laser beam spot. Laser beam width along the vertical axis (y direction) is very narrow, 30 - 100 μm. In addition, the heat depth is also narrow, 100 μm. Hence using fine grid is required there. However, it is desired to use coarser grid far away from the beam spot. The each node point is determined by the equation

$$x_\xi(i) = L_\xi \frac{\sinh(\alpha_\xi\, i/N_\xi)}{\sinh(\alpha_\xi)} \qquad (\xi = x,\ y,\ \text{or}\ z) \tag{3.55}$$

where α_ξ is the parameter to decide the degree of the irregularity and N_ξ is the number of partitions in ξ direction. In this calculation,

$$L_x = 1.5,\ L_y = 1.0,\ \text{and}\ L_z = 2.0\ (\text{mm}) \tag{3.56}$$

$$\alpha_x = 3.0,\ \alpha_y = 2.5,\ \text{and}\ \alpha_z = 2.5 \tag{3.57}$$

$$N_x = 25,\ N_y = 50,\ \text{and}\ N_z = 25 \tag{3.58}$$

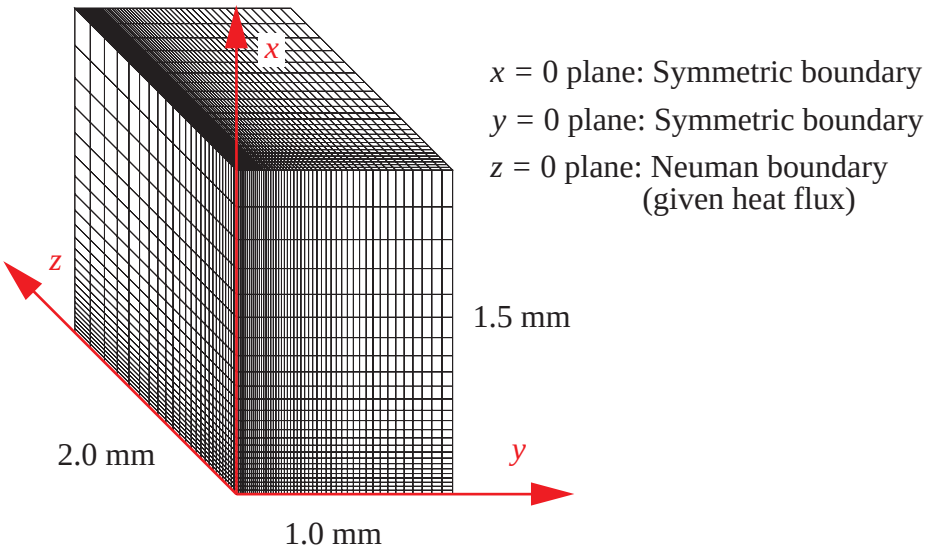

Figure 3.43: Claculation grid and domain.

Space discretization was performed according to finite differential method with irregular grid.

$$\left.\frac{\partial^2 T}{\partial {x_\xi}^2}\right|_i = \frac{sT_{i+1} - (s+h)T_i + hT_{i-1}}{hs(h+s)/2} + O(s,h) \tag{3.59}$$

$$h = x_\xi(i+1) - x_\xi(i) \ , \ s = x_\xi(i) - x_\xi(i-1) \tag{3.60}$$

which is second order in space in the case $s = h$. Discretization on the boundary was derived assuming a controlled volume method on the boundary. For instance, on the $z = 0$ plane,

$$\rho c_p \Delta x \Delta y \frac{\Delta z_1}{2} \frac{T_0^{n+1} - T_0^n}{\Delta t} = \Delta y \Delta z \left\{ kq - \left(-k \frac{T_1^n - T_0^n}{\Delta x_1} \right) \right\} \tag{3.61}$$

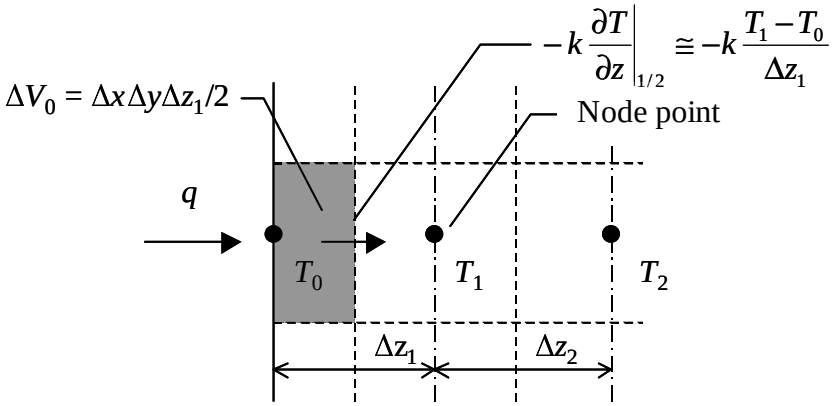

Figure 3.44: Descretization on boudary.

Time marching method was fourth order Runge-Kutta method.

$$T^{n+1} = T^n + \left(\frac{k_1}{6} + \frac{k_2}{3} + \frac{k_3}{3} + \frac{k_4}{6} \right) \Delta t \tag{3.62}$$

$$k_1 = f(T^n, t^n) \tag{3.63}$$

$$k_2 = f(T^n + k_1 \Delta t/2, t^n + \Delta t/2) \tag{3.64}$$

$$k_3 = f(T^n + k_2 \Delta t/2, t^n + \Delta t/2) \tag{3.65}$$

$$k_4 = f(T^n + k_3 \Delta t, t^n + \Delta t) \tag{3.66}$$

where $f(T, t)$ means the right hand side of Eq. 3.48. The time step Δt is selected as

$$\Delta t = 0.5 \ \frac{\mathrm{Min}(\Delta x, \Delta y, \Delta z)^2}{2\kappa} \tag{3.67}$$

to satisfy Stephan condition.

Results with no reaction

Firstly calculation results with no reaction is shown in Fig. 3.45, which is a pure heat conduction problem. There the beam width along the vertical axis was varied from 20 to 150 μm with the laser powr of 300 to 500 mW. The temperature decays with increaseing the beam width as predicted. It is interesting that the decay is slower than the spherical symmety where the maximum temperature decays reciprocally. The result of Fig. 3.45 shows slower decaying.

As a result, in the case of 300 mW laser power, the temperature does not reach the reaction point 720 K, unless the beam width is narrower than 20 μm. On the other hand, 400 mW laser relaxt the limit up to 120 μm.

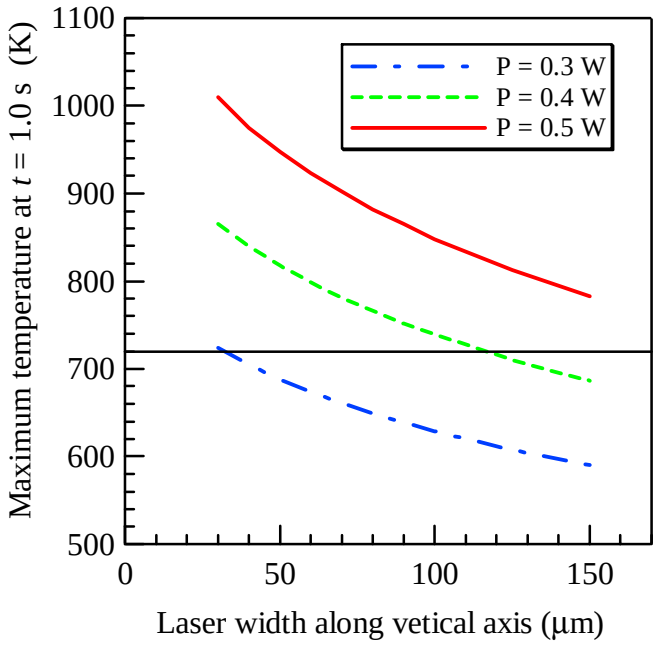

Figure 3.45: Calculated maximum temperature of B/KNO_3 pyrotechnic after one second laser heating, obtained by numerical simulation with no exothermic reaction. The laser width along the horizontal axis is 600 μm.

Estimation of the reaction rate using burning rate

The reaction rate is very important parameter for judging self-sustained combustion of the pyrotechnics. In general, an equation of Arrhenius type

$$\omega(T) = A \exp\left(-\frac{E}{RT}\right) \tag{3.68}$$

is used to describe the reaction rate [82, 72, 92], where E is the activation energy and A is a constant. However, it was difficult to obtain actual properties of A and E and there were no available data for B/KNO_3 pyrotechnic.

In this study, a constant reaction rate ω_c is estimated using a burning rate instead of Eq. 3.68. A number of authors have investigated the burning rates of several pyrotechnics, and also for B/KNO_3 [85, 86, 93, 94]. The burning rate v_b and constant reaction rate ω_c is related in the steady state combustion as follows.

The governing equation is Eq. 3.48

$$\frac{\partial T}{\partial t} = \kappa \frac{\partial^2 T}{\partial x^2} + \Delta T_R \omega s(x,t) \tag{3.69}$$

$$\Delta T_R \equiv \Delta T_R / c_p \tag{3.70}$$

Exothermic reaction of B/KNO_3 starts when the temperature reaches to the threshold T_R. The reaction lasts during $1/\omega_c$ by the definition of ω_c, and the length of the reaction regime is v_b/ω_c. The schematic drawing of the system is shown in Fig. 3.46. In the steady state combustion, putting $\xi = x - v_b t$ can be applied as well as Eq. 3.36, and

$$-v_b \frac{dT}{d\xi} = \kappa \frac{\partial^2 T}{\partial \xi^2} + \Delta T_R \omega_c s(\xi) \tag{3.71}$$

$$s(\xi) = \begin{cases} 0 \quad , & v_b/\omega_c < \xi \\ 1 \quad , & 0 < \xi < v_b/\omega_c \end{cases} \tag{3.72}$$

$$B.C. \qquad T(\infty) = T_\infty, \ \left.\frac{dT}{d\xi}\right|_0 = \frac{\rho \Delta h_{PT} v}{k}, \ T(v_b/\omega_c) = T_R \tag{3.73}$$

Moving ξ frame was taken to have the reaction regime $0 < \xi < v_b/\omega_c$. In the region of $\xi > v_b/\omega_c$, B/KNO_3 is simply heated with maintaining $T = T_R$ at $\xi = v_b/\omega_c$. At the $\xi = 0$ surface, KNO_3 decomposes to gas, which needs positive temperature gradient corresponding to the heat of phase transformation (decomposition). In

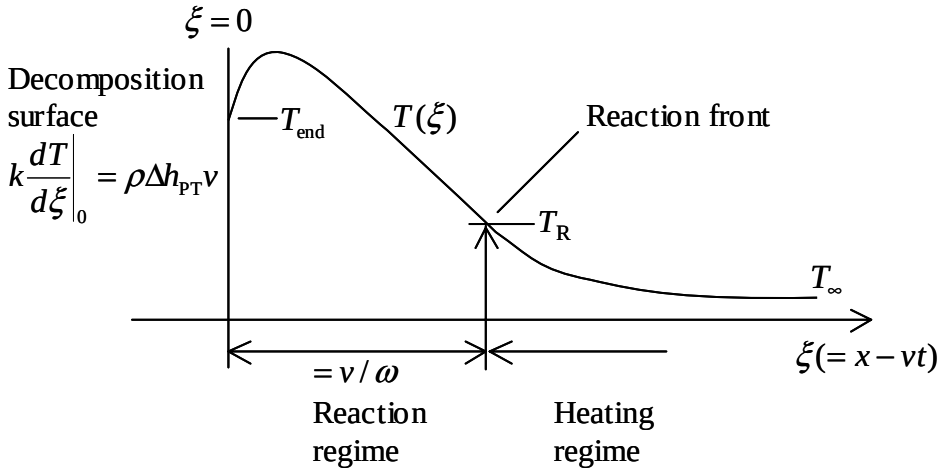

Figure 3.46: Schematic drawing of temperature profile in a combusting pyrotechnic.

the actual burning phenomena, however, the decomposition will occurs according to the reaction of an Arrhenius type equation before the all of the reaction is terminated.

The solution for Eq. 3.71 is

$$T = C_1 \exp\left(-\frac{v_b}{\kappa}\xi\right) + C_1' - \frac{\omega_c}{v_b}\Delta T_R \qquad 0 < \xi < v/\omega \tag{3.74}$$

$$T = C_2 \exp\left(-\frac{v_b}{\kappa}\xi\right) + C_2' \qquad v_b/\omega_c < \xi \tag{3.75}$$

Using the boundary conditions Eq. 3.73,

$$T - T_R = \Delta T_R \left[1 - \frac{\omega_c}{v_b}\xi - \left(\frac{\kappa\omega_c}{v_b^2} + \frac{\Delta h_{PT}}{\Delta h_R}\right)\left\{e^{-\frac{v_b}{\kappa}\xi} - e^{-\frac{v_b^2}{\kappa\omega_c}}\right\}\right] \tag{3.76}$$
$$, \ 0 < \xi < v_b/\omega_c$$

$$T - T_\infty = T_R \exp\left(-\frac{v_b}{\kappa}\left(\xi - \frac{v}{\kappa}\right)\right), \ v_b/\omega_c < \xi \tag{3.77}$$

Recession of the reaction front by the combustion is essentially the same mechanism as the ablation with a heat source at $0 < \xi < v_b/\omega$. Hence the equation of the stationary ablation Eq. 3.33 can be applied. Here T_{end} is used instead of T_{x_w} and heat flux q equals to $\rho\Delta h_R \omega_c v_b/\omega$. Therefore

$$v_b = \frac{\rho\Delta h_R v_b}{\rho\left(c_p(T_{end} - T_\infty) + \Delta h_{PT}\right)} \tag{3.78}$$

$$\Delta h_{\mathrm{R}} = c_p(T_{\mathrm{end}} - T_\infty) + \Delta h_{\mathrm{PT}} \tag{3.79}$$

Putting $\xi = 0$ into Eq. 3.76,

$$\left(\frac{\omega\kappa}{v^2} + \frac{\Delta h_{\mathrm{PT}}}{\Delta h_{\mathrm{R}}}\right)\left(1 - \exp\left(-\frac{v^2}{\omega\kappa}\right)\right) = \frac{c_p(T_{\mathrm{R}} - T_\infty) + \Delta h_{\mathrm{PT}}}{\Delta h_{\mathrm{R}}} \tag{3.80}$$

Solving Eq. 3.80 for ω_{c}, the reaction rate can be expressed as a function of v_{R}. However, that solution can not be expressed by an algebraic way. Fortunately, in the most cases of pyrotechnic combustion, $v_{\mathrm{b}}^2/\omega_{\mathrm{c}}\kappa$ is much larger than one and the exponential term in the left hand side of Eq.3.80 can be neglected. In that case, the reaction rate is simply related to the burning rate as

$$\omega_{\mathrm{c}} = \frac{c_p(T_{\mathrm{R}} - T_\infty)}{\Delta h_{\mathrm{R}}} \frac{v_{\mathrm{b}}^2}{\kappa} \tag{3.81}$$

The boron/potassium nitrate pellet used in this study is supplied from Nichiyu Giken Kogyo CO., LTD. It contains 30 % boron particle by the weight fraction. The diameters of the particles are less than 1.0 μm. They have the data on the burning rate of

$$v_{\mathrm{b}}\ (\mathrm{mm/s}) = 24\ p^{0.08}\ ,\ (5 < p < 50\mathrm{kg/cm}^2) \tag{3.82}$$

The low pressure exponent of 0.08 means very weak dependence of the burning rate on the pressure as expected above. Whereas that rate is for higher pressure than the atmosphere and not for low pressure environment like this study, the burning rate of 24 mm/s is used. Using the properties in Table 3.11, the constant reaction rate is obtained as

$$\omega_{\mathrm{c}} = 97\ (1/\mathrm{s}) \tag{3.83}$$

It should be noted that that reaction rate can contain large error, because the reaction rate is quadratically affected by the burning rate. Additionally, in several studies measuring the burning rate of B/KNO_3, other values were measured at 30 % weight fraction and 0.1 MPa, 10 mm/s [85], 25 mm/s [93], and 10 mm/s [94]. In the case of 10 mm/s the burning rate, the reaction rate becomes one fifth, 16 1/s. The difference would be caused by particle size and environment conditions. In the calculation, the reaction rate was changed from 10 to 130 /s to check the dependence.

Results with reaction

Three dimensional heat conduction problem with an exothermic reaction, described in Section 3.7.2, was calculated with changing the laser power from 0.2 to 0.7 W, vertical laser width from 30 to 110 μm, and reaction rate from 10 to 130 1/s, and thermal conductivity from 0.9 to 1.8 W/mK. As a result, three kind of results are obtained: no reaction, quenching, and self-sustained combustion. *No reaction* means that any point does not reach to the threshold temperature T_{R} =720 K in 1.0 s. In the case of *quenching*, several points reach to and over the threshold and exothermic reaction occurs, but that reaction cannot be sustained (quenched). In the last case, *self-sustained combustion*, chain reaction of the exothermic reaction occurs, and the whole volume is reacted. Figure 3.47 shows the temperature profiles on $y = 0$ plane for the three cases. In the case of 0.25 W power (left side), there is no reaction. In 0.40 W power and 30 /s reaction rate, at $t = 50$ ms the maximum temperature reaches to 720 K and exothermic reaction starts. However, the reaction did not grow any more even after one second has passed. By increasing the reaction rate to 80 /s, chain reaction is accomplished and the combsution propagated to whole volume at $t = 140$ ms. In this section, unless noted otherwise, the horizontal laser width w_x is 600 μm and the thermal conductivity is taken as 1.6 W/mK.

Figure 3.48 shows an ignition map which means the calculated results after one second laser irradiation. Every symbol shows one of the regimes of no reaction, quenching and self-combustion, with a certain power and reaction rate. Figure 3.48 a) is in the case of the vertical laser width of 50 μm and b) is 110 μm. In the case of $w_y = 50$ μm, laser power less than 0.30 W can not heat the body up to 720 K, and there is no ignition with no relation to the reaction rate. It was indicated from Fig. 3.45. Between laser power of 0.325 to 0.450, certain points are reached to the threshold. However, if the reaction rate is too low, the reaction is quenched and self-combustion can not be accomplished. Once a point starts to exothermic reaction, the heat of reaction keeps to be supplied there according to the reaction rate. The generated energy is escaped around due to the diffusion. If the energy is enough to heat neighbor cells up to the threshold temperature, the reaction will be into a chain reaction (self-comustion). Otherwise, the reaction maintains only several points and can not be propagated to around (quenching).

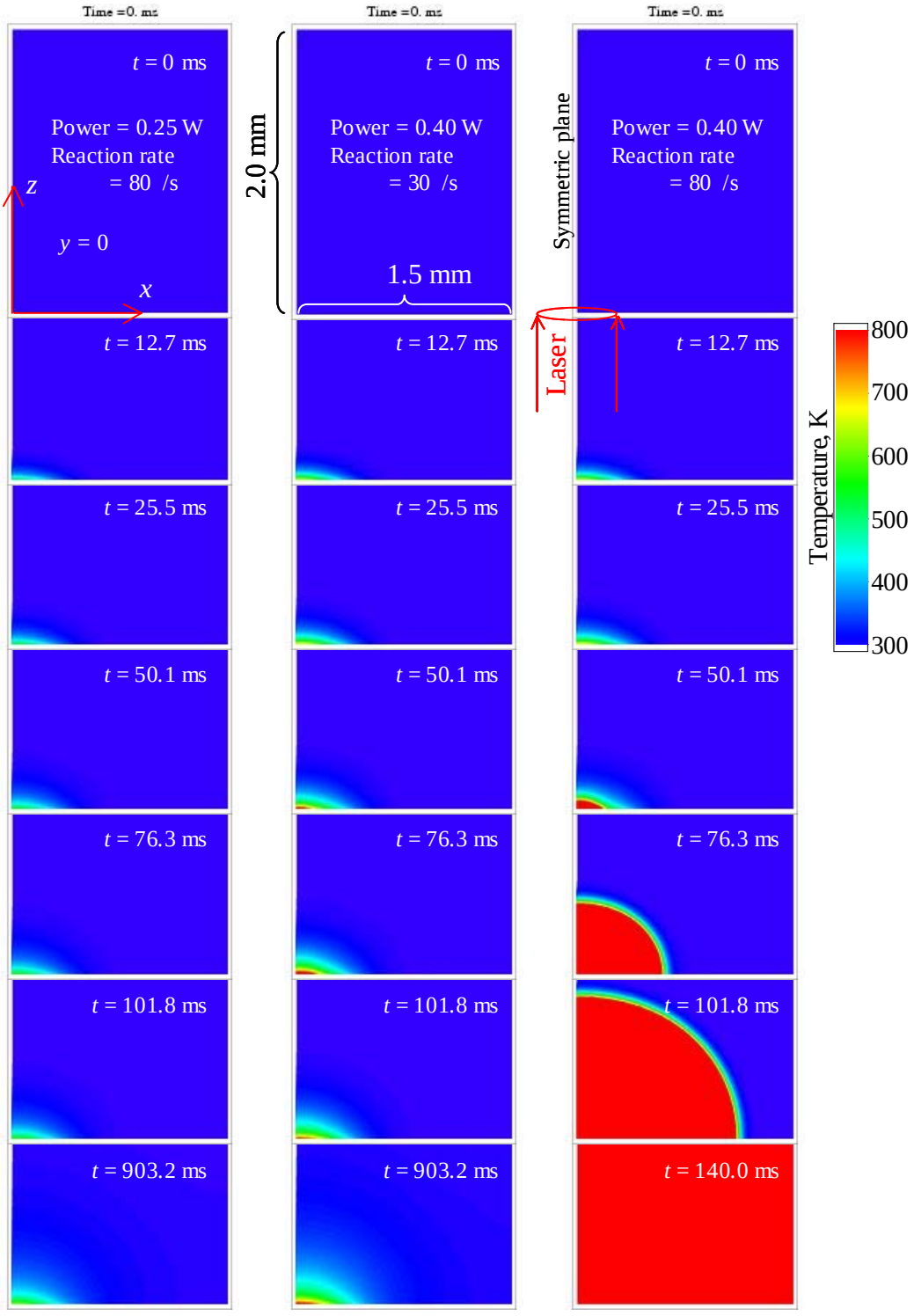

Figure 3.47: Calculated temperature profiles on $y = 0$ plane with changing the power and reaction rate. Three results are shown: no reaction, quenching, and self-sustained combustion.

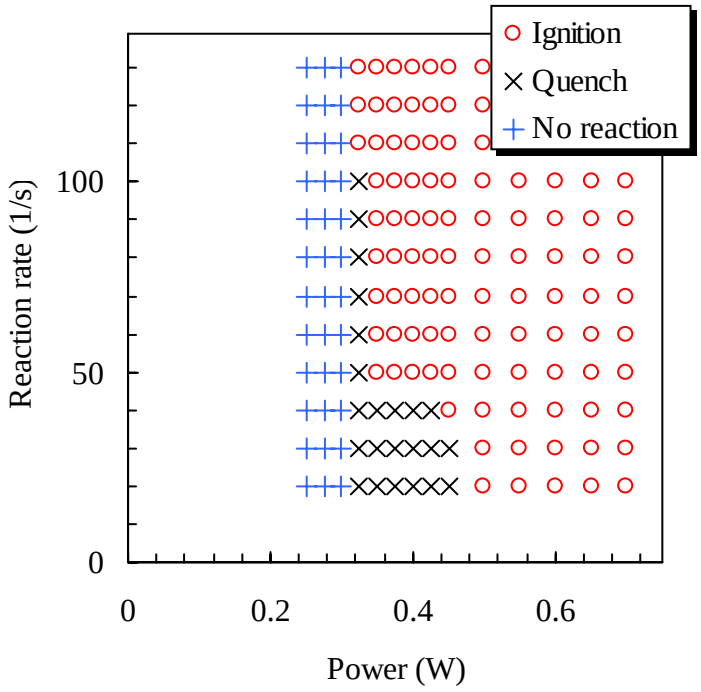

a)

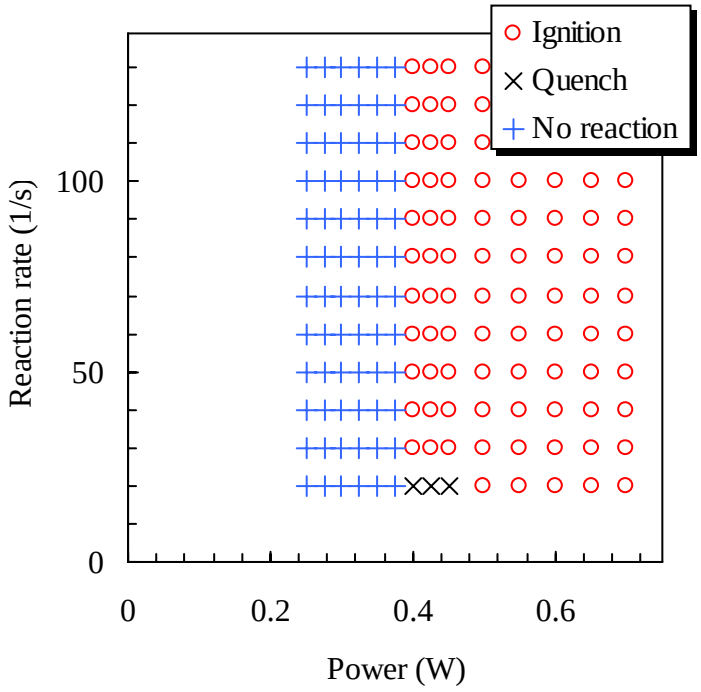

b)

Figure 3.48: Mapping of the calculated result: ignition, quench, or no-reaction, a)W_y =50 μm and b)W_y =110 μm.

The wider is laser width, the more power is required to heat up to the threshold temperature. Hence, in the case of w_y =110 μm, at least 0.4 W is necessary to starts the reaction. However, once the reaction starts, it is easier for the combustion surface to propagate around than narrow laser width, because the area which reacts at a time is larger.

The reaction rate of our B/KNO_3 was estimated as about 100 /s in the above section. That value gives the threshold laser power of 0.35 W for w_y =50 μm and 0.4 W w_y =110 μm. It well agreed with the experimental results of ignition probability measurement (Fig. 3.33). In that experiment, we could not know the accurate vertical laser width of the laser, because it was difficult to accurately set the pyrotechnic for laser. The associated position error would be less than $\pm$ 0.5 mm, and it causes the inaccuracy of laser width from 50 to 110 μm. However, it is shown by the calculation that the threshold power is changed only 0.05 W. even if the width is changed from 50 to 110 μm

The calculation conducted here has another uncertainty, the thermal conductivity. In the above calculation, the conductivity is taken as 1.6 W/mK. Whereas that value is calculated according to the empirical equation, there are other predictive equation and there are large variation of those, as shown in Appendix D. In addition, the conductivity of boron decreased with the increase of the temperature (1.6 W/mK is calculated using one at 400 K). Then to confirm the effect of the conductivity, the threshold power was compared between 1.6 and 1.2 W/mK in Fig. 3.49. Figure 3.49 a) is the case of the thermal conductivity of 1.6 W/mK and b) is 1.2 W/mK. It is shown that decreasing thermal conductivity decreases the threshold power, which is within 0.25 to 0.33 W in the reaction rate around 100 1/s. That value is closer to the experimental results than at 1.6 W/mK.

Another quantitative evaluation of the calculation code was carried out by comparing the ignition time. As an index to evaluate the ignition time, the reactive fraction $\mu_{\rm ce}$ is defined as

$$\mu_{\rm ce}(t) \equiv \frac{\int_V \int_0^t \rho \Delta h_{\rm R} \omega_{\rm R} s(t, \mathbf{x})\ dt\ d\mathbf{x}}{\rho \Delta h_{\rm R} V} \tag{3.84}$$

where the denominator means the total chemical energy included in the system (pellet) and the numerator is the chemical energy released in the time t. Figure 3.50 shows the time when the reactive fraction reaches to 55 %. Figure 3.50 a)

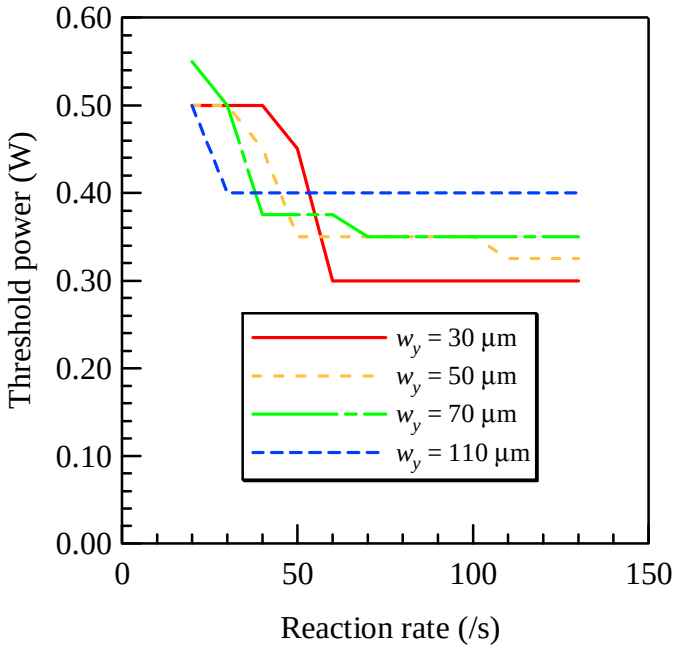

a)

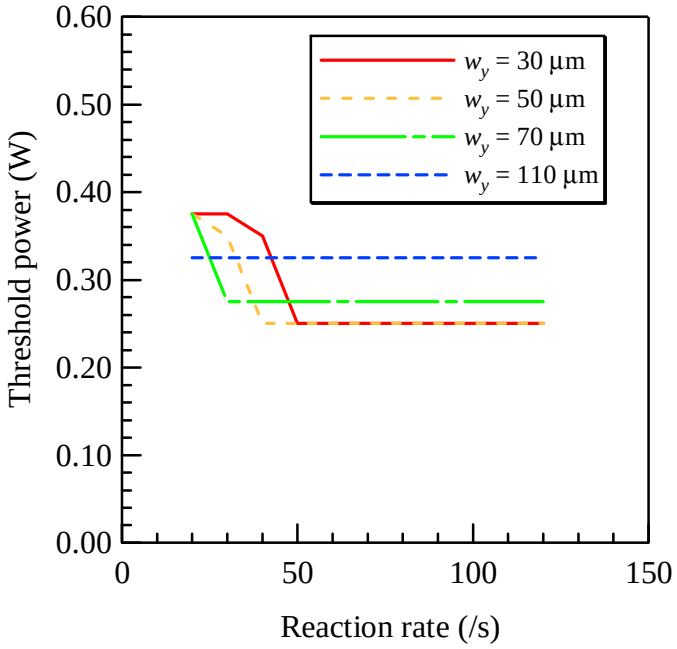

b)

Figure 3.49: Claculated threshold power for the laser ignition of B/KNO_3 pyrotechnic, a)k =1.6 W/mK and b)k =1.2 W/mK.

is in the case of $w_y = 50$ μm and b) is $w_y = 110$ μm. As the laser power goes close to the threshold power, the ignition time is drastically extended. With the enough laser power, the ignition times are ranged from 150 to 350 ms according to the reaction rate. Reaction rate more than 40 /s gives the ignition time around 200 ms. That value almost agrees with the experimentally observed combustion pictures, although it was difficult to precisely determin the ignition time in the experiment.

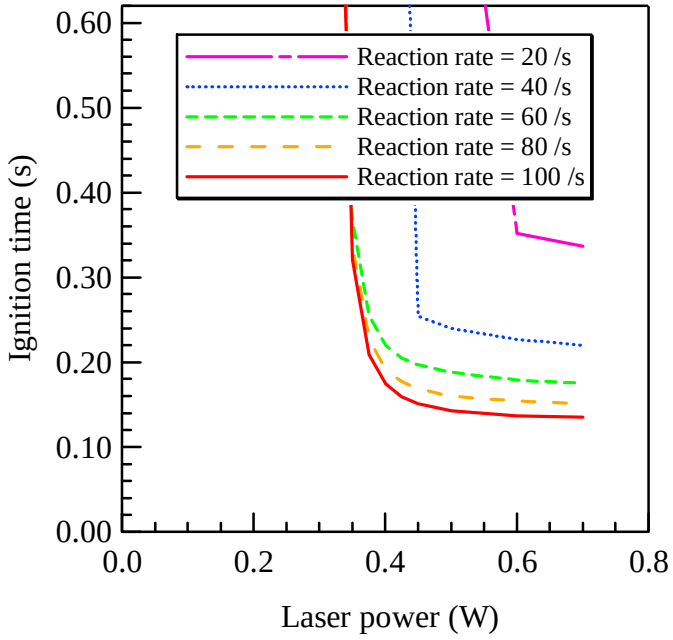

a)

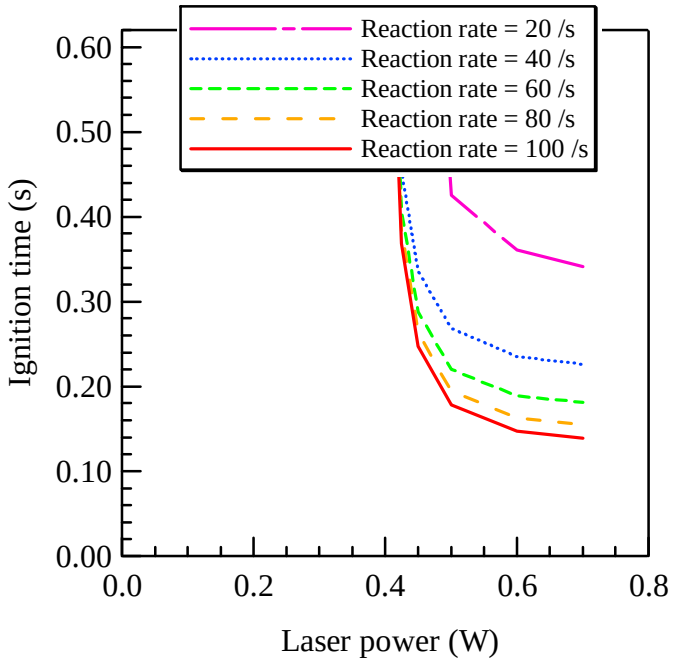

b)

Figure 3.50: Claculated ignition time when 55 % of volume starts the reaction (k =1.6 W/mK), a)W_y =50 μm and b)W_y =110 μm.

3.8 Conclusion of Chapter 3

In this chapter, a dual propulsive mode laser microthruster was proposed and developed, and the following conclusions were obtained.

- Successful operations of the laser ablation mode was verified using polyvinyl chloride propellant. The thrust provided by the laser ablation was proportional to the laser pulse width. The thrust to power ratio ranged from 40 to 150 μNs/J correspoing to the ablative material. Therefore the laser ablation mode provides widely ranged thrust with arbitrary resolution by selecting the ablative material suited with the required thrust resolution.

- Absorption rate of the ablative propellant strongly affected the thrust performance, especially thrust to power ratio. Polyvinyl chloride with rich carbon density showed higher thrust to power ratio. The ablation of PVC by one Watts class diode laser was caused by teh dehydrochlorination, and the degradation of HCl can be explained by the photothermal reaction.

- Boron / potassium nitrate pyrotechnics is suited with laser igntion in vacuum, and it was experimentally verified. The threshold laser power and pulse with for the laser ignition was adequate for the use of microspacecraft, 300 mW and 150 ms. Composite propellant and double-base propellant was not ignited by 1 W diode laser in vacuum. The laser ignition processes of Boron / potassium nitrate was well reproduced with numerical calculation, where three dimensional heat conduction problem was solved with the exothermic reaction.

- That laser ignited combustion provided thrust of 11 mNs when using a 30 mg pyrotechnic and thrust of 600 mNs when using a 1.0 mg pyrotechnic. Those much higher thrust than laser ablation thrusters covers wide range of thrust by combining laser ablation, and it enables a single micropropulsion conducting multiple propulsion tasks.

Chapter 4

Liquid Propellant Pulsed Plasma Thruster

4.1 Introduction

4.1.1 Pulsed plasma thrusters

In recent years, Pulsed Plasma Thrusters (PPTs) have attracted great attention as promising thrusters for microspacecraft. They have compat size suitable with microspacecraft and provide high specific impulse of the order of 1000 s. In stead of the high specific impulse, however, PPTs require a energy storing capacitor and power processing unit (PPU) charging it. Typically ten Joules class PPTs requires weight of 0.2 to 1.0 kg for the capacitor and PPU. Therefore the adequate spacecraft size for PPTs are larger than ones dealt in the previous chapter. That size would be over 10 kg. For instance, a 10-50 J class PPT installed on the Earth Observing 1 (EO-1) spacecraft weighs 4.95 kg with two thruster heads, a common capacitor, and a single power processing unit [95]. A bread-boad model PPT with 1-5 J class, which was developed in Tokyo Metroporitan Institure of Technology, weighs less than 2.0 kg [96]. It has also have two heads, a common capacitor, and single PPU.

A PPT is a pulsed electric propulsion, and can be operated in low power levels of 1 to 100 W, whereas most electric propulsions require high power levels over a few 100 W. Power throttling of PPTs is managed simply by changing the pulse repetition frequency. That throttling does not affect the performance because the

performance of a PPT is determined by a single shot operation. That characteristic is suited with the power limited microspacecraft. In addition, PPTs generate a small digital impulse bit by a single firing. It will enable to constrcut simple control system for the accurate positioning, attitude control, and station keeping.

4.1.2 Ablative PPTs

To date, most common PPTs are using solid polymer propellant, where PTFE (Teflon®) has been empirically selected. Energy stored in a capacitor is released by pulsed discharge initiated in interelectrode space by a spark plug. The current flows adjacent to the polymer surface with ablating it, and supplies working gas into the plasma. The plasma is grown by that propellant feeding, and contributes the more ablation of the polymer. Thus the discharge plasma and polymer ablation interact each other, and propellant is passively fed by the discharge ablation. Hence those kinds of PPTs are called as ablative PPTs or APPTs. The interaction between the discharge current and self-induced magnetic field generates electromagnetic force outward and accelerates the plasma from the electrodes. After every shot the polymer consumed a little, and the ablated polymer is pushed by a spring placed on the back. Because of that simple propellant feeding system, APPTs have a simple structure, which leads to high reliability, toughness, and long life-time. Figure 4.1 is a conceptual drawing of APPTs. Histories, trends, and physics of PPTs were well surmmarized by Burton and Turch in the reference[28].

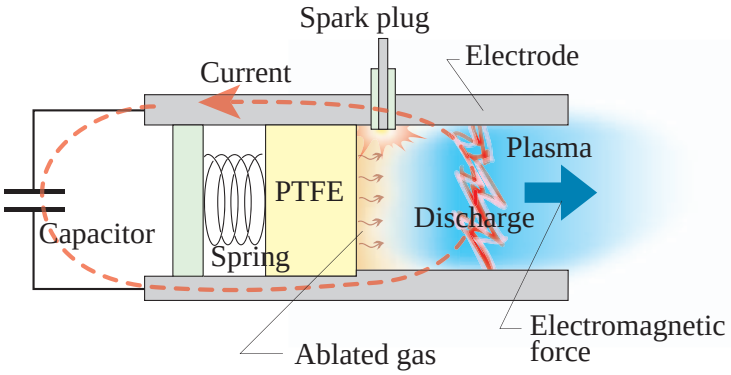

Figure 4.1: Conceptual drawing of an ablative PPT.

However, there are several problems on ablative PPTs: poor thrust performance, contamination, and non-uniform ablation. To improve the performance of APPTs, various studies have been performed. Nevertheless, flight-qualified APPTs have been still remained in the efficiency of less than 10 % [97, 95, 96]. Several researchers in this field have pointed out that the excessive propellant feeding after the main discharge causes the low performance. It was observed that low speed vapor continues to be provided after the main discharge [98, 99]. It would be because the surface temperature remains higher than the boiling point of the propellant. Additionally the emission of large particulates was observed [100], which could not be effectively accelerated. Such kinds of low speed propellants hardly contribute to the thrust and decrease the propellant utilization efficiency. In order to improve the propellant efficiency, it is necessary to supply only an minimum amount of propellant for both ionization and acceleration.

Contamination problems on spacecraft or thruster itself is caused by the exhaust plasma gas of PTFE. PTFE is made of carbon and fluorine. The reason why PTFE was selected of a number of polymers was the charring[101], that is, alternative propellants failed due to the severe carbonization. In the early work on PPTs, carbonization on a spark plug was studied [102], which eventually failed the operation. In these days, failure reports due to charring has not been known, and Myers and Arrington reported that the contamination did not affect on spacecraft [103]. However, contamination issues always remain as potential with using PTFE, especially for applications with highly sensitive diagnostics for ineterferometry missions.

The non-uniform ablation is caused by the profiles of the current density and PTFE surface temperature. There are preferential ablations near the electrodes [104]. Such non-uniform ablation varies the impulse bit trend in successive operation and decreases the amount of usable propellant. That phenomena was remarkable for the small energy levels and small size [96, 105].

After all, the several disadvantages have made scientists hesitate to apply PPTs in spacecraft, whereas PPTs would be only one thruster in electric propulsions applicable to microspacecraft due to their compactness, low power operation, and useful digital impulse. Therefore studies on high performance and contamination free PPTs are very important and such thrusters will be promising micropropulsion providing high delta-v.

4.1.3 Proposal of use of liquid propellant

A pulsed plasma thruster using liquid propellant (LP-PPT) was proposed in our laboratory in 1999 by Prof. Arakawa and the fundamental studies have been conducted [50, 51, 52, 53]. Use of liquid propellant for PPTs is expected to overcome the problems: excessive propellant feeding, contamination, and non-uniform ablation. Figure 4.2 shows a conceptual drawing of a LP-PPT. Liquid droplets are intermittently supplied into interelectrode space usig a liquid injector. Some fractions of the liquid are vaporized into gas. Main discharge is initiated by breakdown according to Paschen's low or with pre-discharge by an spark plug. Several gas or liquid phase propellant are converted into plasma, and are accelerated both electromagnetically and electrothermally.

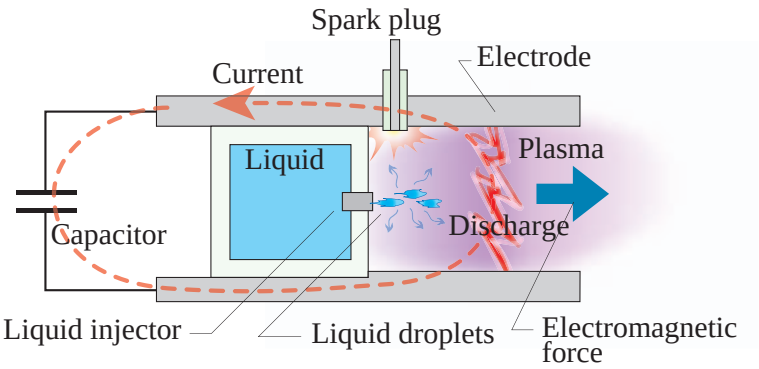

Figure 4.2: Conceptual drawing of a liquid propellant PPT.

The use of liquid is motivated by efficient propellant feeding and clean, contamination free propellant. If the propellant consumed in a single shot is controlled by a liquid injector, the PPTs will have higher performance than usual. Defintaely an liquid injector causes increasing the complexity and weight of the thruster. Hence the injector must provide enough benefits to a thruster to compensate that disadvantage. It was accomplished by the increase of the specific impulse. The early works on LP-PPTs by Kakami and the author showed the successful operation of a PPT using liquid and its higher specific impulse (∼3000 s) than ablative PPTs. The works are reviewed in the references [51, 53]. Liquid propellant is superior than gaseous propellant which should be highly pressurized. Liquid phase propellant will enable a compact propellant feeding system. As a liquid propellant, water

is focused here. Its good handling property, availability, cheapness, and non-toxity are attractive as propellant for microspacecraft. Also it has the potential to be shared with other life-support sytems.

However, disadvantage of a LP-PPT was its lower thrust, thrust to power ratio, in contrast to the higher specific impulse. A LP-PPT addressed in a doctoral thesis by Kakami [52] has the thrust to power ratio (equal to impulse to energy ratio) of 6.0 μNs/J, but typical PPTs have the thrust of about 10 μNs/J. One of the reasons of the low thrust is that LP-PPTs have not been optimized due to their short history, but there is another cause decreasing the thrust. The main objective of this chapter is clarifying plasma acceleration processes and energy partition in a LP-PPT to improve the performance of LP-PPTs. Moreover, based on the result, two methods increasing the performance are proposed and they are experimentally examined.

Recently other institutes have started studies on PPTs using liquid [106, 107, 108, 109]. They employed different liquid feeding systems each other. Scharlemann and York used porous ceramic to feed liquid propellant, where water diffuse through the porous material from the storage tank to the discharge chamber. It has no mechanical component and maintains the simple structure of APPTs, but the liquid is kept to evaporate through the material. Simon et al. developed a micro-PPT using liquid. Water diffuses through membrane and stored in a small cavity with an orifice to the outside. In the cavity small discharge is initiated, which injects vapor into the main chamber.

4.1.4 Theory of electromagnetic acceleration in a PPT

First, to well understand the acceleration mechanism of PPTs, electromagnetic impulse generated by a PPT is formulated. The history of PPTs is not new and a number of theoretical approaches on PPTs have been proposed since 1960s [21, 110, 111]. Here, our interest is in the electromagnetic acceleration not in electrothermal acceleration, whose effect is neglected. The electrohtermal effect can be simply included by adding an additional term to the result obtained here.

We assume a PPT with parallel plate electrodes. A coordinate is taken as x is perpendicular the electrodes, y is the direction of electrodes width, and z is along the electrodes, namely streamwise direction. Figure 4.3 shows the coordinate.

To simplify the problem, it is assumed that the discharge current has the only

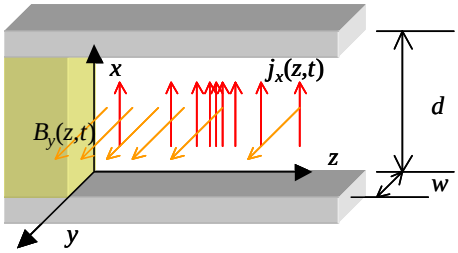

Figure 4.3: Coordinate used in the formulation of electromagnetic acceleration.

component along x direction and the uniform profile on y. Hence the current is a function of only z and t, and $\mathbf{j} = j_x(z,t)\hat{\mathbf{x}}$. As a result, induced magnetic field has only y component, and $\mathbf{B} = B_y(z,t)\hat{\mathbf{y}}$. They are related by Ampere's low as

$$B_y = \mu_0 \int_z^\infty j_x \, dz \tag{4.1}$$

The electromagnetic force per unit length applied to plasma f_{EM} is expressed as

$$f_{\mathrm{EM}} = j_x B_y w d \tag{4.2}$$

where w and d are the electrode width and interelectrode distance. The total electromagnetic force F_{EM} is obtained by integrating it along the streamwise direction.

$$\begin{aligned} F_{\mathrm{EM}}(t) &= \int_0^\infty f_{\mathrm{EM}} \, dz & (4.3)\\ &= \mu_0 w d \int_0^\infty j_x(z) \int_z^\infty j_x(s) ds \, dz & (4.4)\\ &= \mu_0 w d \frac{1}{2} \left[\int_0^\infty j_x(z) dz \right]^2 & (4.5)\\ &= \mu_0 \frac{d}{w} \frac{1}{2} J(t)^2 & (4.6) \end{aligned}$$

where the relations of J_x and B_y (Eq.4.1) and the total current

$$J = w \int_0^\infty j \, dz \tag{4.7}$$

are used. The term $\mu_0 d/w$ is the inductance per unit length for the ideal two dimensional electrode configuration. Equation 4.6 is generallized to

$$F_{\mathrm{EM}}(t) = \frac{1}{2} L' J(t)^2 \tag{4.8}$$

using the inductance per unit length L'. As a result, the squared discharge current and the inductance per unit lenght of the electrode are essential parameters of electromagnetic acceleration.

The power consumed for the electromagnetic acceleration $W_{\rm EM}$ is

$$W_{\rm EM} = \int_0^\infty u(z,t) f_{\rm EM}(z,t)\, dz \tag{4.9}$$

$$\simeq v(t) \int_0^\infty f_{\rm EM}(z,t)\, dz = \frac{1}{2} L' v(t) J(t)^2 \tag{4.10}$$

where $u(z,t)$ is the fluid velocity of the plasma and $v(t)$ is the characteristic velocity over the electrode, which is defined as

$$v(t) \equiv \int_0^\infty u(z,t) f_{\rm EM}(z,t)\, dz \Big/ \int_0^\infty f_{\rm EM}(z,t)\, dz \tag{4.11}$$

The work done on the moving plasma by the electromagnetic force during the pulsed discharge is

$$E_{\rm EM} = \int_0^\infty \frac{1}{2} L' v(t) J(t)^2\, dt \tag{4.12}$$

The term $\frac{1}{2} L' v(t)$ in the integral has the same unit as the resistance, and it is referred as the equivalent resistance of electromagnetic acceleration, and abbreviated to $R_{\rm EM}$.

$$R_{\rm EM}(t) \equiv \frac{1}{2} L' v(t) \tag{4.13}$$

The energy initially stored in the capacitor of the PPT, E_0, is consumed as the electromagnetic work or as the dissipation at the resistance of the plasma $R_{\rm plasma}$ and the resistance of an external circuit $R_{\rm circuit}$. Here the external circuit means the capacitor and feed lines from electrodes, and $R_{\rm circuit}$ includes all of those resistances. Of course, the energy dissipated in the external circuit is hardly used for the acceleration and it becomes energy loss. Expressing the relation of the energy and those resistances,

$$E_0 = \int_0^\infty \left(R_{\rm circuit} + R_{\rm plasma}(t) + \frac{1}{2} L' v(t) \right) J(t)^2\, dt \tag{4.14}$$

$$= \left(R_{\rm circuit} + \bar{R}_{\rm plasma} + \frac{1}{2} L' \bar{v} \right) \int_0^\infty J(t)^2\, dt \tag{4.15}$$

where $\bar{R}_{\rm plasma}$ and $\bar{R}_{\rm EM}$ are averaged resistances of plasma and electromagnetic work, defined by

$$\bar{R}_{\rm plasma} \equiv \int_0^\infty R_{\rm plasma}(t) J^2\, dt \Big/ \int_0^\infty J^2\, dt \tag{4.16}$$

$$\bar{R}_{\rm EM} \equiv \frac{1}{2}L'\bar{v} \tag{4.17}$$

$$\bar{v} \equiv \int_0^\infty v(t)J^2\,dt \Big/ \int_0^\infty J^2\,dt \tag{4.18}$$

$$= \sum_n \int_{n^{\rm th}1/2cycle} v_n J^2\,dt \Big/ \int_0^\infty J^2\,dt \tag{4.19}$$

Here let us define the effective resistance of the plasma $R^*_{\rm plasma}$ and the total resistance of the PPT circuit $R_{\rm total}$ as

$$R^*_{\rm plasma} \equiv \bar{R}_{\rm plasma} + \bar{R}_{\rm EM} \tag{4.20}$$

$$R_{\rm total} \equiv \bar{R}_{\rm circuit} + \bar{R}_{\rm plasma} + \bar{R}_{\rm EM} \tag{4.21}$$

When the energy conversion efficiency is defined as the fraction of the work done by the electromagnetic force to the initial stored energy, it is expressed as

$$\eta_{\rm EM} = \frac{\bar{R}_{\rm EM}}{R_{\rm total}} \tag{4.22}$$

The impulse that the thruster generates (the momentum given to the plasma) is expressed as by using Eqs. 4.8, 4.15, and 4.21,

$$I_{\rm EM} = \int_0^\infty F_{\rm EM}\,dt = \frac{1}{2}L'\int_0^\infty J(t)^2\,dt \tag{4.23}$$

$$\simeq \frac{1}{2}L'\frac{E_0}{R_{\rm total}} \tag{4.24}$$

Therefore it is very important to know the resistances of $R_{\rm circuit}$, $R_{\rm plasma}$, and $R_{\rm EM}$. They determines the energy efficiency (or energy partition) and the thrust to power ratio. Therefore those resistances are estimated in the succeeding sections. The total resistance of the PPT circuit $R_{\rm total}$ is easily calculated using initially stored energy and integral of the squared discharge current according to Eq. 4.15. The $R_{\rm circuit}$ is obtained from the discharge without plasma described in the succeeding section. The equivalent resistance of the electromagnetic work $R_{\rm EM}$ cannot be obtained unless the characteristic velocity of the plasma is calculated according to Eq. 4.11. That velocity is roughly obtained using pictures taken by ultra high-speed camera.

4.2 Experimental setup

4.2.1 Vacuum facilities

Experiments on pulsed plasma thrusters were conducted in a 1.1-m-diam, 1.8-m-long vacuum chamber, UT cylindrical chamber. It is the same chamber used for experiments on the laser ablation. The background pressures were maintained under $1 - 5 \times 10^{-5}$ Torr. The inner pressure was measured using a ionization vacuum gauge. The detailed explanation is described in Appendix B.

The space chamber was electrically connected to the ground due to prevent the possibility charging up to high voltage for the safety. However, the potential of the chamber was instantaneously pulled up and down by the pulsed discharge of PPTs (with a few hundred volts amplitude). It affected the base potential of an oscilloscope and disturbed the measured waveforms of current and voltage. To reduce the effect, the ground line of the oscilloscope used was directly connected to the chamber wall.

4.2.2 Liquid injector

A liquid propellant PPT proposed here requires an intermediate injector to supply liquid in vacuum. The injector should have small and light body to be suited with microspacecraft. In addition the injector must supply very minute liquid a shot, because mass shot required for 10 W class PPTs are very small, a few micro grams. In the study of liquid propellant PPTs, development of such a liquid injector is most important and it will become a key technology to determine the performance.

Ink-jet type injector

In the early stage of this study, we attempted to apply the ink-jet technology in printers into the injector of a LP-PPT. Ink-jet printers inject liquid droplets from a small pinhole with the pressure increase by a piezoelectric device or film boiling of small bubble in the tank. It has no shut off valve and seals liquid by the surface tension. It leads to a simple and compact structure, and supplies a extremely small amount of droplets, of pico-little. Those characters are also suitable with an injector expected for a liquid propellant PPT.

Designed piezoelectric capillary injectors worked well in the atmosphere. It has a small cavity of 640 ml closed by 50 μm-thickness-SUS plate with a 20 μm ejection orifice. An annular piezoelectric oscillator is attached on the plate, and its resonance vibration of 18 - 25 kHz increases the inner pressure in pulses. Its schematic drawing and the picture in the operation are shown in Fig. 4.4.

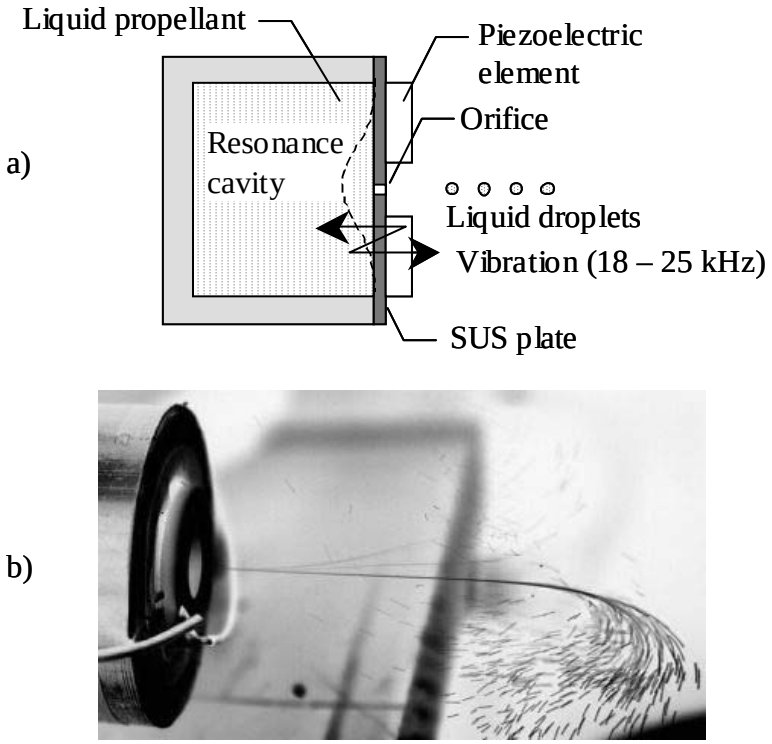

Figure 4.4: Piezoelectric injector: a) schematic drawing and b) picture of the operation in the atmosphere.

In vacuum, however, it could not work well. Pressure difference between the inner tank and vacuuum causes a lot of leak of the liquid. In addition the leaked liquid adhered around the orifice and it prevented the injection of liquid. To seal liquid by surface tension in vacuum, the diameter of an orifice is required to be smaller than 3 μm. However, it is difficult to supply liquid using such a small orifice, because quite high inner pressure is required to eject adequate amount of the propellant from the orifice in the limited time (too slow injection causes inefficient propellant usage).

Closing Valve injector

An injector with closing valve was developed to perform fundamental experiments of a liquid propellant PPT. Figure 4.5 shows a designed valve injector, which injects liquid from an orifice by its inner pressure. In the closing state (normally state), a coil spring presses a flexible membrane via a push-rod, and seals an ejection orifice. The membrane is made of silicone rubber of 1 mm thickness. When the rod is pulled by an solenoid actuator, the orifice is opened and liquid is ejected by the inner pressure. Additional liquid is fueled from a feed line beside the main body, which is not shown in the Fig. 4.5. There was no pressurization device, and inside of the liquid tank would ranged from the atmosphere to the vapor pressure of the installed liquid. In the liquid tank 500 mg water can be reserved, which is enough amount to perform ground testing. The valve injector has the size of 14×20×50

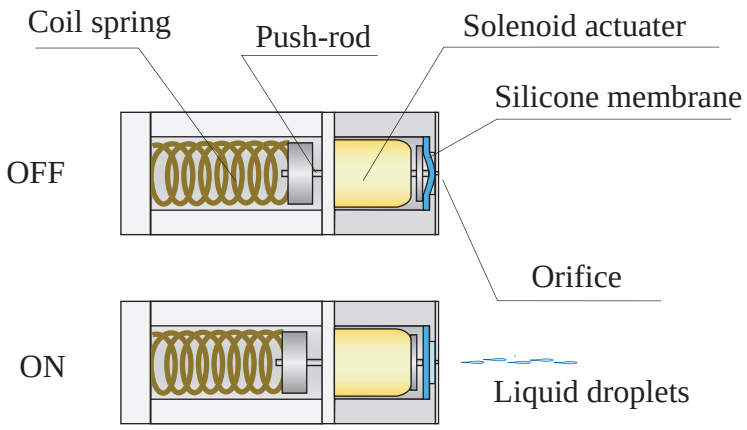

Figure 4.5: Schematic diagram of operation of a valve injector.

mm^3 and weighs about 78 g. The ejection orifice of 25 or 50 μm is opened on a SUS plate of 50 μm thickness. The orifice plated is bound to the valve body. A solenoid actuator used is 11C-12V made by Shindengen Mechatronics Co., Ltd, which characteristics are shown in Table 4.1. A spring to seal the orifice has the spring constant of 1.28 N/mm.

The use of a mechanical valve can lead to lack of the simplicity and reliability. The durability of an injector would restrict life time of the thruster. Here the injector was used to conduct fundamental experiments on liquid propellant PPTs. In the next stage, further advanced liquid injector should be developed. Recent

Table 4.1: Characteristics of a solenoid actuator 11C-12V from Shindengen Mechatronics Co., Ltd..

Total weight	7 g
Plunger weight	1 g
Number of coil turns	1450
Resistance	143 Ω
Attraction force	1.9 N at 0.5 mm stroke
(38 V)	1.0 N at 1.0 mm stroke

growth of MEMS technology has the capability to achieve it. Recently, there are a number of studies of microvalves using MEMS. These researches can be applied to the liquid propellant PPT. For instance, MEMS technology allowed a more miniaturized injector whose size was $7 \times 7 \times 21$ mm^3 [112], with the same mechanism as the injector used here.

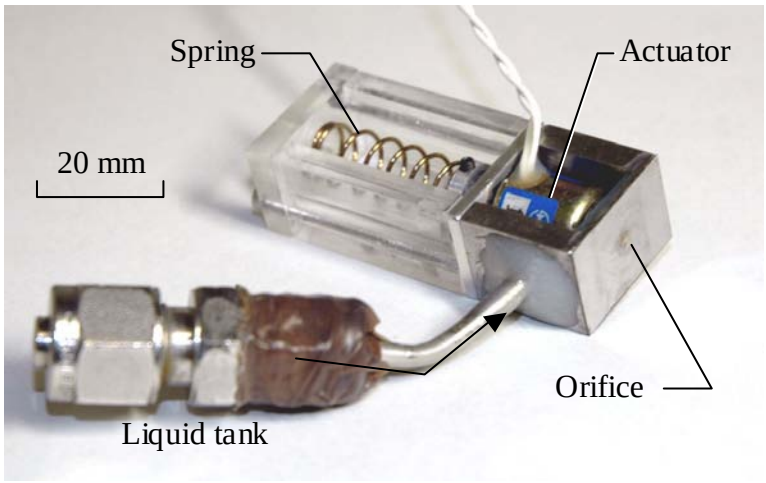

Figure 4.6: Picture of the liquid injector used in this study.

Figure 4.6 shows the picture of the fabricated liquid injector. It successfully injected liquid droplets in vacuum; the minimum mass shot was 3 μg. This injector was used to supply liquid to a liquid propellant PPT through this study. The mass shot was controlled by adjusting the voltage applied to the actuator and its pulse width. The pulsed voltage was controlled using a controlling computer, which

generates TTL signals with arbitrary pulse width, and an injector driven circuit which is a switching circuit. The electrical diagram of the driven circuit is shown in Appendix F. More details are described in the reference[52].

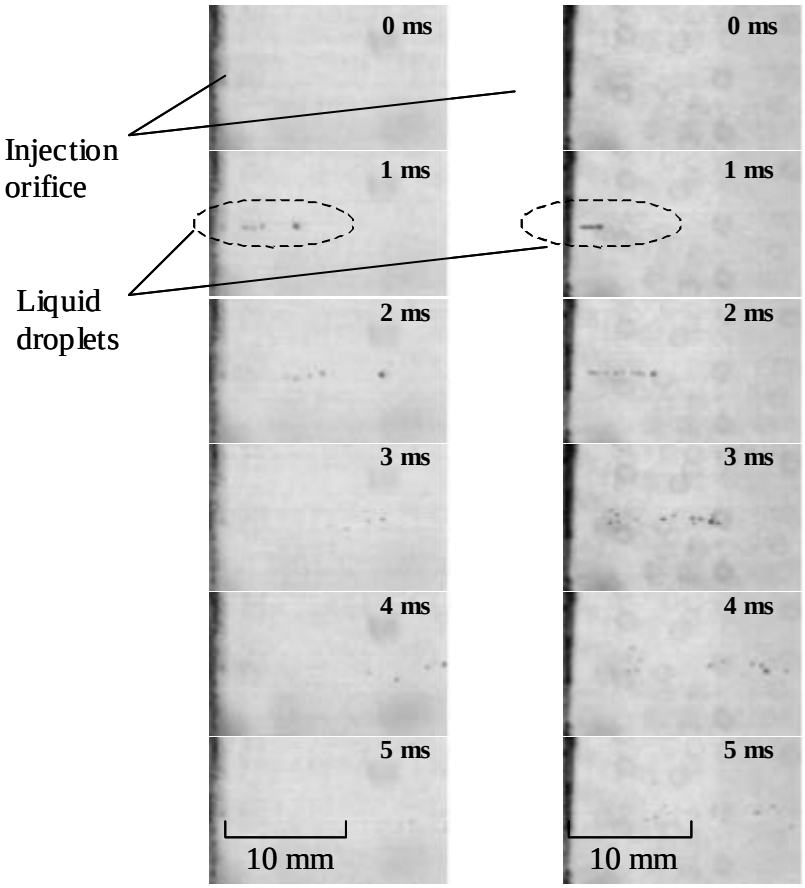

Figure 4.7: Pictures of water droplets ejected from the injector orifice, sequentially taken every one millisecond. a) orifice diameter:50 μm and b) orifice diameter: 25 μm.

The liquid injection of 4 μg in the vacuum chamber was observed using a high-speed camera of 1000 frames/s. Figure 4.7 shows pictures of liquid droplets ejected from the liquid injector in the vacuum chamber. The pictures were sequentially taken by every one millisecond by using a 1000 f/s CCD camera and arc strobe light. Fig. 4.7 a) is the ejection using the orifice of 50 μm and Fig. 4.7 b) is for the orifice of 25 μm. In the both cases, the mass shot was 5.5 μg. The method to observe those small droplets are described in detail in the reference [113].

4.2.3 Thrusters

A liquid propellant pulsed plasma thruster dealt here consists of parallel plate electrodes, glass side walls, spark plug, liquid injector, and capacitor. The schematic diagram of the thruster is shown in Fig. 4.8. The electrodes are made of stainless

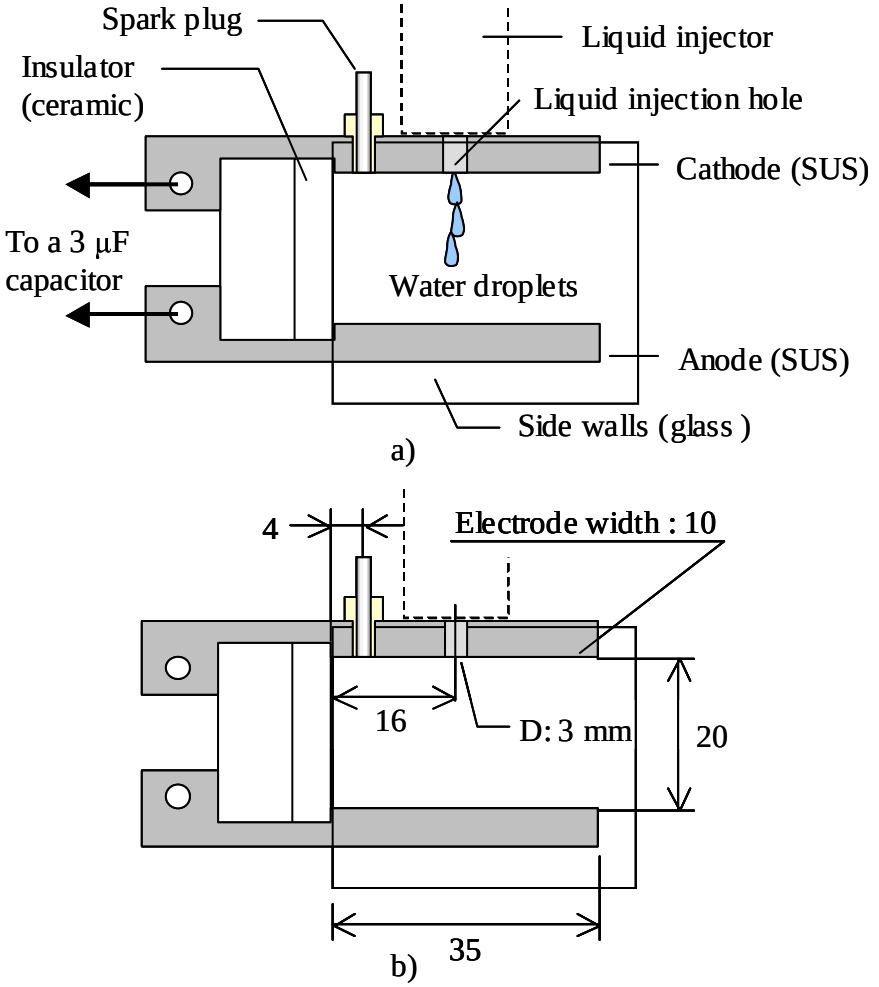

Figure 4.8: Schematig diagram of the liquid PPT used here; a) materials and b) dimensions.

steel and it has the interelectrode space of 20 mm, the length of 34 mm, and the width of 10 mm. The electrode are fixed on a base plate made of polymer (POM). The anode and cathode are insulated by a ceramic back wall (photoveel). The interelectrode space can be changed to 40 mm using another base plate and ceramic back wall. The interelectrode width of 20 mm was applied in this study, if not

otherwise specified. The liquid injector described in the previous section was installed above the cathode. The effect of the injection position was investigated by Furuta in his Maseter thesis [113], and it was shown that that it did not affect the thruster performance. The cathode has a 3-mm-diam hole opened at 4 mm away from the back wall in order to feed liquid droplets into the interelectrode space through that hole. The side walls are installed to help rising up the interelectrode pressure by the liquid injection. A spark plug will be described in the succeeding section.

The capacitor consists of two 1.5 μF capacitors connected in parallel and has the capacitance of 3 μF. They are custom-made mica paper capacitors made by Soshin Electric Co., Ltd.. The one capacitor has the weight of 200 g and the dimensions of $100 \times 80 \times 10$ mm^3. The feed lines has the length of about 35 mm and crimp-type terminals are attached to the end of the lines to connect the electrodes. The capacitor has the dielectric loss tangent ($\tan\delta$) of 0.35 at 1 kHz, the voltage endurance of 4 kV DC of 5 s, and the inductance of about 40 nH.

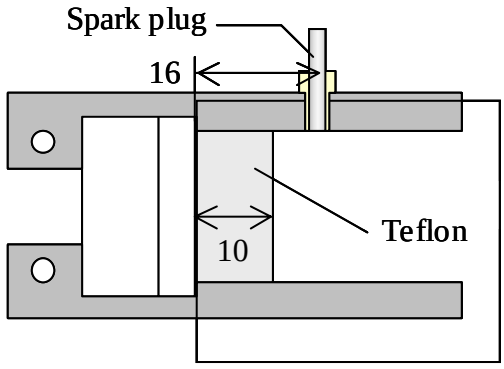

Figure 4.9: Schematic diagram of the ablative PPT used here.

The liquid propellant PPT can be operated as a ablative PPT by installing a PTFE block between the electrodes instead of a liquid injector, as shown in Fig. 4.9. The ablative PPT was prepared to compare the performance to the LP-PPT. The PTFE block has the size of $10\times10\times20$ mm^3. Due to that thickness, the effective electrode length is decreased down to 24 mm. The surface of the PTFE is the almost same position as the liquid injection hole. The spark plug is installed in the liquid injection hole. , which has the same configuration of the electrodes as the LP-PPT.

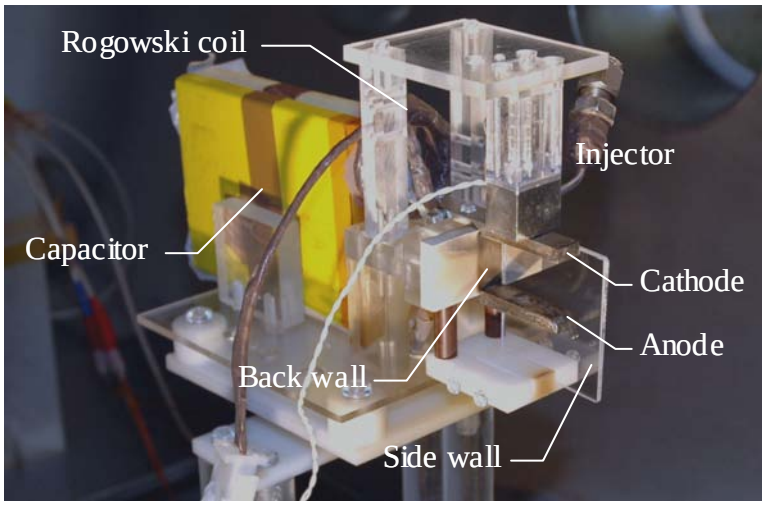

a)

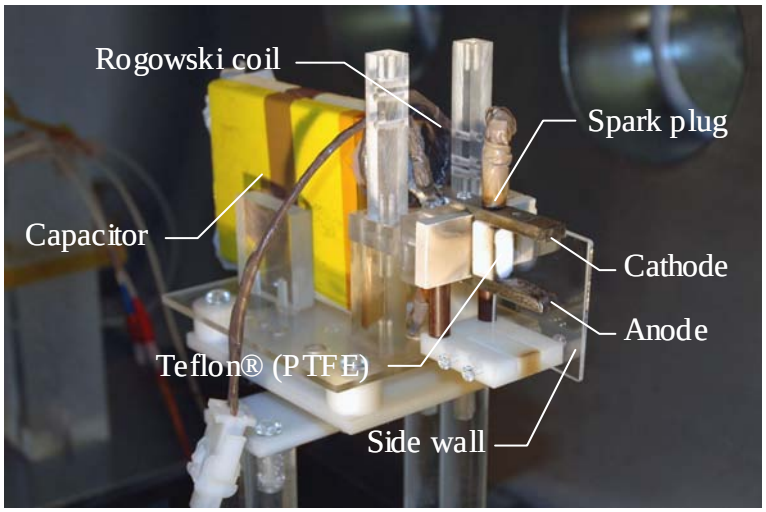

b)

Figure 4.10: Pictures of the thrusters: a) LP-PPT and b) APPT.

Figure 4.10 shows pictures of the LP-PPT and APPT placed on the thrust stand. In the pictures only oneside of the side wall was installed.

4.2.4 Spark plug

A spark plug produces small plasma puff by arc breakdown and initiates arc discharge between electrodes of PPTs. The spark plug used here consisted of coaxial

anode of 2 mm diameter and insulator of 3 mm outer diameter. The plug was mounted into the cathode, which also plays a role of a spark plug cathode. The plug face is aligned in the same plane as the cathode. The configuration is shown in Fig. 4.11. The relative position of the plug anode, plug insulator, and cathode was experimentally determined. The position that all faces are in the same plane showed the best ignition performance and it was employed.

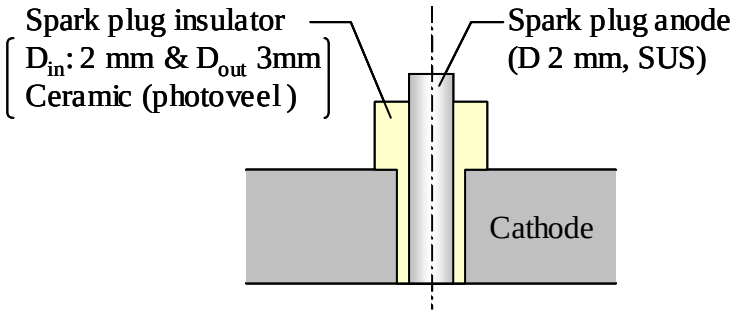

Figure 4.11: Schematic diagram of the spark plug.

About 5 kV pulsed voltage was applied to the plug anode using a high voltage trigger circuit, which is a capacitor discharge ignition. A spark plug capacitor was charged to about 100 V and a SCR switch discharged the charge through a pulsed transformer of the ratio 1:50. Then on the second coil of the transformer, about 5 kV pulsed voltage was applied. The gate timing of the SCR was operated by a control computer, and it was synchronized with the signal of liquid injection. The electrical circuit diagram of the spark plug is shown in Appendix F.

4.2.5 Rogowski coil

The discharge current during a PPT firing was measured using a Rogowski coil (handmade). In this section, the fabricated coils and its calibration method are shown. Its fudnamental principles are shown in Appendix E.

Rogowski coils

In this study, two Rogowski coils were fabricated, Type 1 and Type 2, whose characteristics are tabulated in Table 4.2 and pictures are shown in Fig. 4.12.

First, Type 1 Rogowski coil was fabricated and used in the early experiments.

Table 4.2: Characteristics of Rogowski coils and *RC* integration circuits.

		Type 1	Type2
Rogowski coil	Sensitivity (kA/V)	2.5	1.8
	Winding density (turns/mm)	10.4	2.8
	Number of turns (turns)	490	620
	Wire diameter (mm)	0.25	0.25
	Poloidal diameter (mm)	4.4	5.0
	Toroidal diameter (mm)	28	32
	Number of linkage	1	2
Integration circuit	Resistance (kΩ)	5.1	2.5
	Capacitance (μF)	0.1	0.1

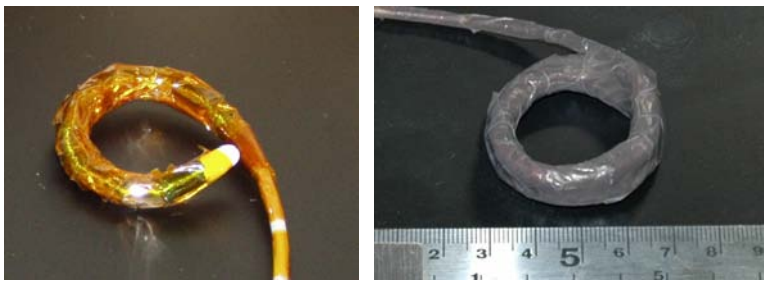

a) b)

Figure 4.12: Pictures of the Rogowski coils: a) Type1 and b) Type2.

A thin wire was wound around a coaxial cable in order to make it easy to bring the wire back through the coils. The winding was performed in three piles to increase the winding density and the sensitivity. As a result it had the sensitivity of 2.5 kA/V. However, Type 1 coil was broken (shorted) after a year, and Type 2 Rogowski coil was fabricated. The short would be caused by high voltage generated on the coil by the electromotive force. If the current with 10 kA amplitude and 1.5 Mrad/s frequency passes through the Type 1 Rogowski coil, the electromotive force of 3.0 kV will be generated. In the fabrication of Type 2, the winding density was decreased down to 2.8 turns/mm with no piling, corresponding to the electromotive force of 1.0 kV. To compensate the decreased sensitivity, the number

of linkages were increased to two and time constant of the integration circuit was decreased by half. The resulted sensitivity of Type 2 coil was 1.8 kA/V. That low winding density contributes also to low inductance of the Rogowski coil. The shapes of both Rogowski coils were maintained by rapping a Kapton®insulating tape.

A Rogowski coil and integration circuit are connected by a twist cable. The integration circuit was installed inside a vacuum chamber, because it decreased the electrical noise induced on the output rather than outside of the chamber. The integration circuit and an oscilloscope were connected by an coaxial cable via a BNC feedthrough on a port of the chamber. Discharge of PPT generates a lot electrical noise and oscillates the potential of the chamber in pulse. To electrically shield out the noise, the chamber was connected to the ground using a copper mesh cable with 50mm width and 3 mm thickness. Nevertheless, the chamber potential was oscillated in pulses, and the noise could not be shielded in perfect. Instead, the base potential of the oscilloscope was set to mutch the chamber potential by directly connecting its ground line to the chamber wall. The configuration is shown in Fig. 4.13.

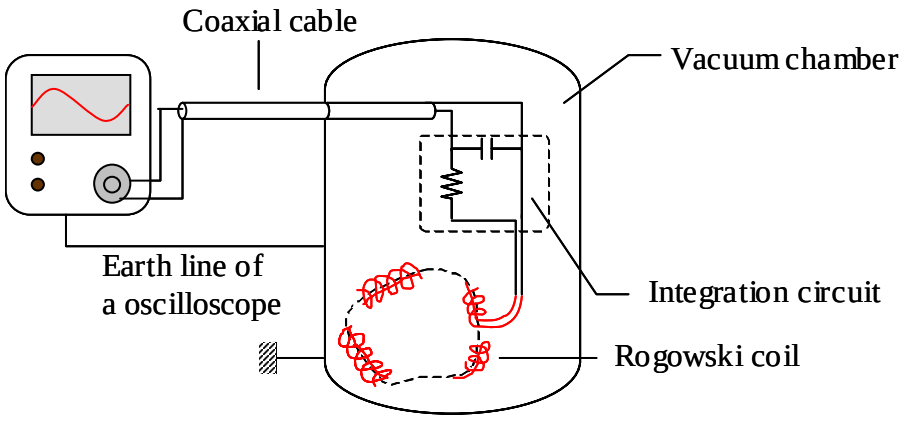

Figure 4.13: Electrical connections assoiated with a Rogowski coil.

Calibration

Calibration of Rogowski coils were performed in the atmosphere by shorting the electrodes of PPTs and using a current monitor. Voltages of 400 to 1000 kV are

applied to the PPT electrodes in the atmosphere and they were shorted using a copper plate. The copper plate directly connects the electrodes to simulate a discharge pass on a PPT. At the same time, a current monitor was installed to the electrode. The current waveform was measured by the current monitor and Rogowski coil, and the outputs were compared. Figure 4.14 shows the setup of the calibration.

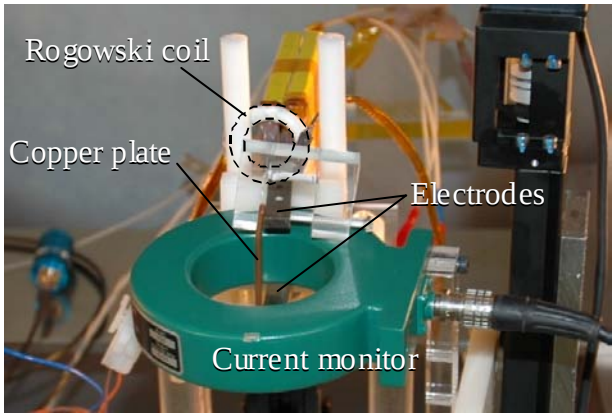

Figure 4.14: Picture of the calibration setup using the current monitor. Copper plate shorts the circuit in the atmosphere.

Table 4.3: Specifications of the current monitor used for the calibration.

Sensitivity	10 A/V
Maximum peak current	5 kA
Frequency range	1 Hz to 20 MHz
Inner (hole) diameter	50.8 mm
Outer diameter	101.6 mm

The current monitor is made by Pearson Electronics, Inc. (the model number is 110), whose specifications are shown in Table 4.3. It measures current by the same principle as Rogowski coils. However, because of its maximum current limit and the large size, it is difficult to directly measure discharge current of PPTs using the current monitor.

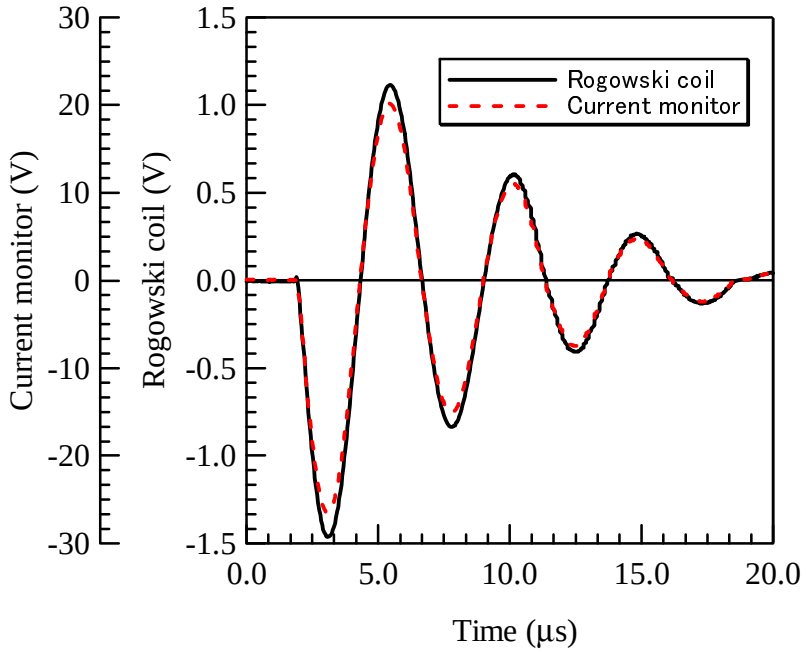

Figure 4.15: Typical waveforms of the calibration of the Rogowski coil.

Figure 4.15 shows typical current waveforms in the calibration. Typically 10 to 20 waveforms are compared between the output from the current monitor and Rogowski coil. In the case of Type 2 Rogowski coil, 16 waveforms were measured with changing the applied voltage from 400 to 1000 V. The obtained sensitivity was 1.813 kA/V in the average with the standard deviation of 0.0047 kA/V. Phase delay of the Rogowski coil output from the current monitor was 19 ns with the standard deviation of 2 ns.

4.2.6 Power supplys

A high voltage DC power source was used to charge a main capacitor of PPTs to 1-3 kV. The power supply FS-3000-1 made by ASTRO Electronic Industry Corporation was used. It supplies the maximum voltage of 3 kV and current of 1 A. That specification is too powerful for 10 W class PPTs, and it was used just for the ground tests. The supply was set outside the space chamber and the voltage was applied using electrical feedthroughs of the chamber. Between the supply and capacitor, a current limiting resistance was installed, which was 25

kΩ. The used capacitor has the capacitance of 3 μF as mentioned later. Hence the characteristic time for the charge was 75 ms and the maximum current was 0.12 A for the charging to 3 kV.

A DC power supply used to charge a capacitor of the spark plug was FS-600-0.2 made by ASTRO Electronic Industry Corporation. It can supply the maximum voltage of 600 V and current 0.2 A. In most case, the spark plug is operated with 90 - 120 V charging. The current limiting resistance was 1 kΩ. The characteristic time was 1 ms and the maximum charging current was 0.1 A. The housing of the power supply FS-600-0.2 is shared with FS-3000-1.

Figure 4.16 shows the electrical connections of the power supply, Rogowski coil, voltage divider, vacuum chamber and PPTs.

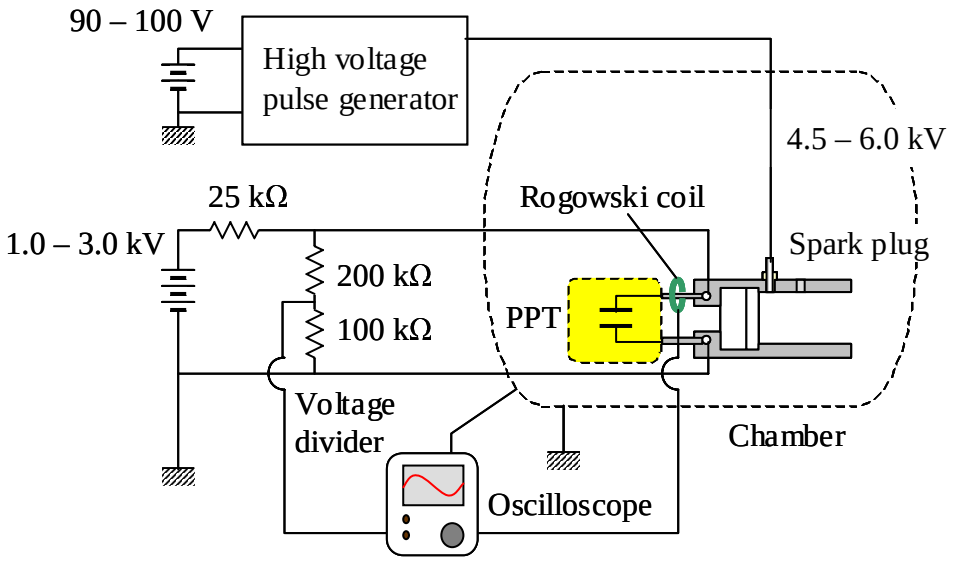

Figure 4.16: Electrical connections of power supplys and PPTs.

4.3 Measurement methods

4.3.1 Mass shot

Among researchers on PPTs, mass consumed during a single shot firing is called as *mass shot*. In the case of a liquid PPT, it corresponds to the ejected liquid propellant for a single shot. Generally the mass shot of 10 J class PPTs are less than

10 μg, and difficult to directly measure such small mass. In most investigations of ablative PPTs, it is evaluated by the weight difference of a solid propellant before and after a few thousands of shots.

In this study, the mass shot Δm was estimated from the pressure increase in the vacuum chamber ΔP, as well as the laser ablated mass measurement in Section 3.2.7. The pressure increase is related as $\Delta m = C\Delta P$, where C is the proportionality constant. The proportionally constant C was determined dividing the averaged mass shot by the averaged pressure increase during the experiment. The averaged mass shot was determined by the weight difference before and after the experiment. Pressure waveforms in the chamber were all recorded during the experiment, and the averaged pressure increase was determined. Once the coefficient was obtained, every mass shot was estimated from the pressure increase.

To obtain the coefficient C, over 2000 shots operation was carried out, which led to about 20 mg weight difference (mass shot was about 5 - 15 μg). That weight difference was measured using a precise balance: AB304S by Mettler tredo Co., Ltd.. It has the minimum resolution of 0.1 mg and the maximum weight of 320 g. However, attachment of several volatile materials caused the much variations of the weight measurement. The actual accuracy of the weight measurement here would be about $\pm$1.0 mg, because the indicator of the balance fluctuated within $\pm$1.0 mg Especially moisture attachment on the injector led to increase of the weight over 100 mg. To avoid the influence from the total mass shot measurement of 20 mg, before the experiment the fueled injector was placed in vacuum during over 2 hours. It vaporized the moisture attached on and stored in the materials of the injector. After that, the weight of injector was measured as quickly as possible, and installed again in the vacuum chamber for the experiment. In addition, when we handled the injector for the weight measurement, we got on latex gloves to avoid moisture attachment to the injector from our hands.

In contrast, it was difficult to measure the mass shot of an ablative PPT. The plume ejected from an ablative PPTs contains carbon and fluorine which attaches on or reacts with a chamber wall. Hence the pressure increase in the chamber is strongly depends on the configurations of the objects inside the chamber. In short, the coefficient C can be changed by experiment to experiment. Therefore, instead of using a pressure, the mass shot was estimated from the energy. It had been confirmed that the mass shot of ablative PPTs is proportional to the capacitor

stored energy [28, 110]. The mass shot of the ablative PPT was measured by the weight difference before and after the 340 shots operation at 6.0 J. As a result, the proportional constant between the energy and mass shot was obtained as 0.97 μg/J. In the experiment after that, the mass shot was estimated from that value, assuming the proportionality between the energy and mass shot.

4.3.2 Impulse bit

PPTs generate their force in pulsed mode, and it is usually dealt as impulse rather than thrust. Moreover, impulse gnerated by the single firing of PPTs are frequently called as *impulse bit*, because it is the minimum impulse which the PPT can provide. PPTs are expected to be used for fine thrust control by throttling their operation frequency. In such a case, the impulse generated by a single shot is regarded as the minimum unit to control the thrust.

Impulse bits of liquid and ablative PPTs were measured using a thrust stand described in Chapter 2. Single shot measurement was performed. Generally 10 J class PPTs have impulse bit of 50 to 100 μNs. The mechanical noise induced on the stand by background vibrations was about 1.0 μNs, and much less than the PPT impulse. Hence the wave analysis was performed by normal sinusoidal curve-fitting. As described there, the stand had the resolution of $\pm$1.0 Ns and the accuracy of 2.0 % caused by the calibration.

4.3.3 Total resistance

The resistance and inductance of a PPT circuit were obtained by curve-fitting a damped oscillation waveform to the current waveform. A PPT can be assumed as an electrical circuit which has discrete elements of inductance, capacitance, and resistance [21]. The resistance consists of the inner resistance of capacitors, resistance of feeding lines, resistance of plasma, and effective resistance of electromagnetic acceleration. The inductance comes from a single loop of the discharge current. The capacitance obviously means the capacitor storing the energy. In the actual discharge, the resistance and inductance are varying with time. However, in the first approximation, the current waveform of PPT discharge is explained using a RLC circuit with constant elements. Actually, most PPTs show damped oscillation current waveforms. Figure 4.17 shows a typical current waveform during the

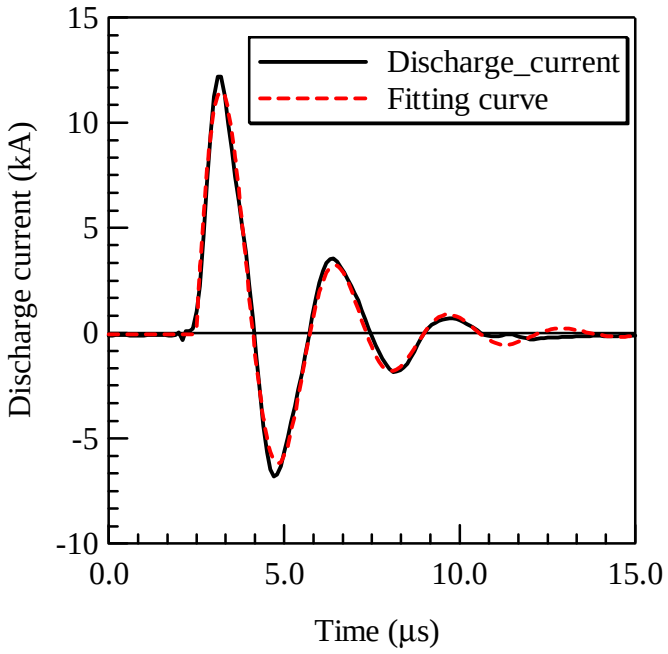

Figure 4.17: Typical discharge current waveform during the firing of the LP-PPT at 11.5 J.

discharge of the LP-PPT. Current waveform of a RLC circuit is

$$J(t) \quad = \quad J_0 \, e^{-\mu t} \sin \omega t \tag{4.25}$$

$$\text{where } \mu = \frac{R}{2L} \quad \text{and} \quad \omega = \sqrt{\frac{1}{LC} - \left(\frac{R}{2L}\right)^2} \tag{4.26}$$

in the case of $C < 4L/R^2$. That damped oscillatory waveform can be used as good approximation of the discharge current of PPTs, in spite of the actual time-varying resistance and inductance. In Fig. 4.17, the curve of Eq. 4.26 fitted to the measured discharge current. The curve-fitting gives a resistance and inductance of the PPT circuit. This resistance includes all the resistances in a PPT, and it is one called total resistance, R_{total}, in Section 4.1.4. In this study, resistance and inductance are obtained using that curve-fitting.

4.3.4 Resistance of an external circuit

The resistance of the external circuit R_{circuit} was obtained by shorting the electrodes using a copper plate in the atmosphere (same as done in the calibration of

Rogowski coil). The end of the copper plate was fixed to cathode using an acrylic vice. Between the anode and the other end of the plate, a piece of insulating sheet was held. Applied voltage of 400 - 1000 V to the capacitor, the insulating sheet was pulled out. Then the plate touched to the anode and current passed with small arc spark. In this experiment, resistance of the current is the summation of the resistances of the external circuit, the copper plate, and arc spark generated between the plate and electrode.

The resistance of the copper plate was less than 0.3 $m\Omega$ and negligible. It was confirmed from the calculation from resistivity of copper with considering the skin depth and also from the experiment changing the length of the plate.

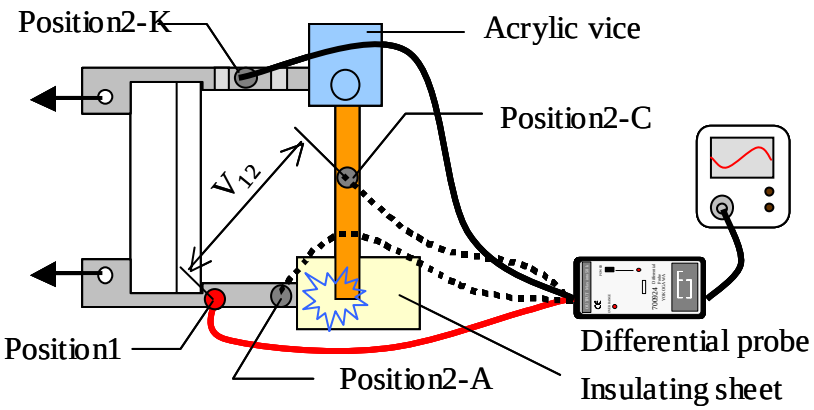

Figure 4.18: Measurement of the arc spark resistance between the anode and copper plate.

The resistance of the arc spark generated between the anode and copper plate was estimated measuring voltage drop over that spark. Figure 4.18 shows that schematic drawing. The voltages between three different points were measured, namely between the root of the anode (Position1 in the figure) and the cathode (Position2-K), the copper plate (Position2-C), or the center of the anode (Position2-A). That voltage drop between the two points V_{12} was measured using a differential probe. The voltage drop is expressed as

$$V_{12} = R_{12}J + L_{12}\frac{dJ}{dt} \tag{4.27}$$

where R_{12} and L_{12} are the resistance and inductance between the measured two points. The voltage drop V_{12}, current J measured by a Rogowski coil, and its time

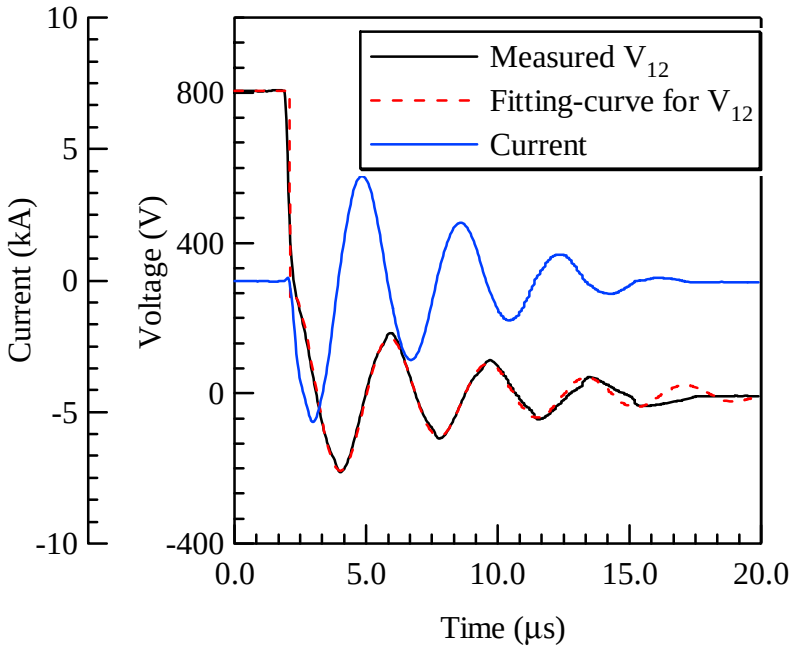

Figure 4.19: Typical waveforms of voltage difference, current, and fitting-curve of the voltage.

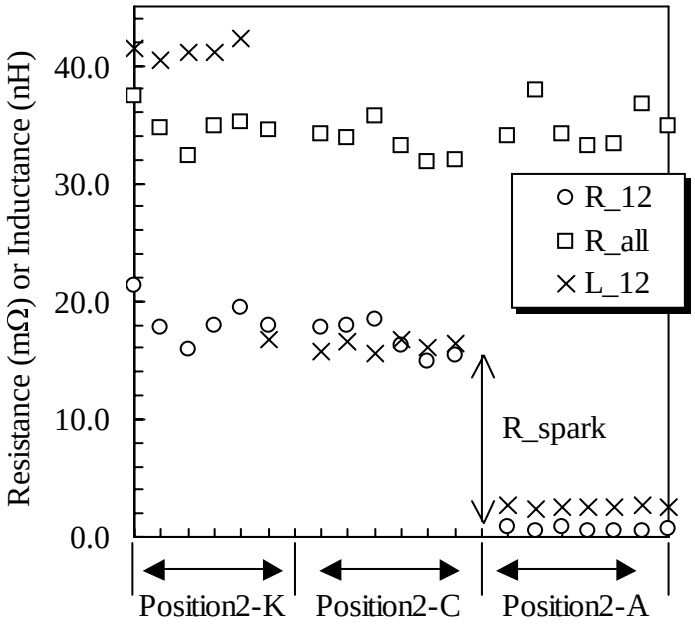

Figure 4.20: Resistance of the arc spark at the gap between the anode and copper plate in the atomosphere.

derivative are fitted to Eq. 4.27 to determin the resistance R_{12} and inductance L_{12}. Figure 4.19 shows typical waveforms of measured voltage difference, current, and fitting-curve of the voltage.

Figure 4.20 is the result of R_{12} and L_{12} measurement. The resistances of Position 2-K and Position 2-C are almost same, whereas the resistance of Position 2-A decreases a lot. This difference of the resistance is attributed from he resistance of arc spark (only Position 2-A did not measure the spark). Therefore, subtracting this resistance from the total resistance R_{all} gives the resistance of external circuit R_{circuit}. As a result, the resistance of an external circuit was 17±3 mΩ. The error comes from the resistance of electrode and the variation of the spark resistance The variation of the resistance R_{12} measured at Position 2-K or 2-C is caused by the arc spark, because the variation of the total resistance R_{all} matches to it. On the other hand, inductances are monotonically decreased from 41 to 2.5 nH with decreases of the measured distance.

4.3.5 Inductance per unit length

The inductance per unit length L' was measured by changing the position of the copper plate as shown in Fig 4.21. Different positions of the plate give different inductances. The dependence of the inductance on the position gives the inductance per unit length. The result is shown in Fig. 4.22 for the case of interelectrode space of 20 and 40 mm. The inductance is linearly increased by shifting the position of the copper plate outward. The inclinations are inductance per unit length L', and they are 0.71 and 1.01 nH/mm for 20 and 40 mm electrode respectively.

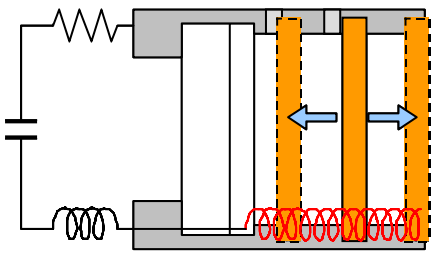

Figure 4.21: Changing the position of the copper plate to measure the inductance per unit length.

Analytical expression for the inductance of a closed circuit of rectangular conductors is [28, 114]

$$L = 0.4\left\{\frac{3}{2}l + l\ln\frac{d}{b+c} - d + 0.22(b+c)\right\} \quad (4.28)$$
$$L\ (\mu H),\ \text{and}\quad l, d, b, c\ (m)$$

where l and d are the length and height of the closed circuit and $b \times c$ is the cross section of the rectangular conductor in meter. Hence, differentiating the equation with respect to l,

$$L' = 0.6 + 0.4\ln\frac{d}{b+c}\ \ (\mu H), \quad (4.29)$$

which does not depend on the length l. The electrode used here, of the cross section of 10×5 mm and the distance of 20 or 40 mm, give L' of 0.72 and 0.99 nH/mm respectively. After all, the analytically estimated L' shows good agreement with the measured L', whereas the PPT used here has a rectangular cross section only with the electrode and the other parts have quite different sections.

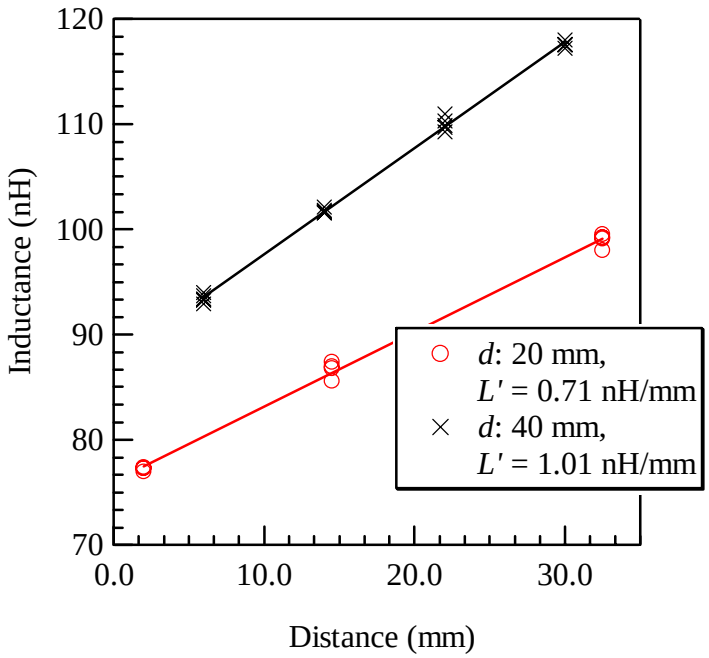

Figure 4.22: Dependence of the inductance on the shorting position.

4.4 Experimental Results

Here fundamental characteristics of a liquid PPT were investigated using the thruster shown in Fig. 4.8. Whereas the thruster had not been optimized, the characteristics of a liquid PPT was clarified by comparing it to an ablative PPT. The used ablative thruster is shown in Fig. 4.9.

4.4.1 Mass shot vs. Impulse bit

The impulse bit of a liquid PPT was shown not to depend on the mass shot, namely injected propellant by liquid injector for a single shot. Essentially the electromagnetic impulse of PPTs does not depend on the mass shot, as indicated by Eq. 4.24. On the other hand, electrothermal acceleration will be proportional to the square root of the mass shot. It means that the impulse by a liquid PPT was produced mainly by electromagnetic acceleration.

Figure 4.23 shows the dependence of impulse bit on the mass shot operated at the energy of 10.0 J (2.6 kV). The error bars in the figure show the standard deviations of five shots. The impulse is slightly increased with the increase of the mass shot. The slope of the regression line is 467 m/s. It corresponds to the expected cold gas velocity. Therefore the slight increase of the impulse would be caused by the increase of the cold gas thrust, not electrothermal acceleration.

Constant impulse bit on the mass shot means that the specific impulse is inversely proportional to it. Figure 4.24 show the specific impulse calculatd from the impulse bit and mass shot. At the mass shot of 3.0 μg, it reaches over 2000 s. At the higher energy operation, it reached to 3000 s (such high Isp operation was investigated by Kakami [52]). It should be noted here that small mass shot operation also causes a lot of varieties of impulse bits. It would be because that too small mass shot makes it difficult to initiate discharge.

4.4.2 Energy vs. Impulse bit

The impulse bit of a liquid PPT was linearly increased with the increase of the capacitor stored energy. It is expected from the theory of electromagnetic impulse Eq. 4.24. Figure 4.25 shows the impulse bit dependence of the energy. There the impulse bit using another electrode distance of 40 mm is also shown. The

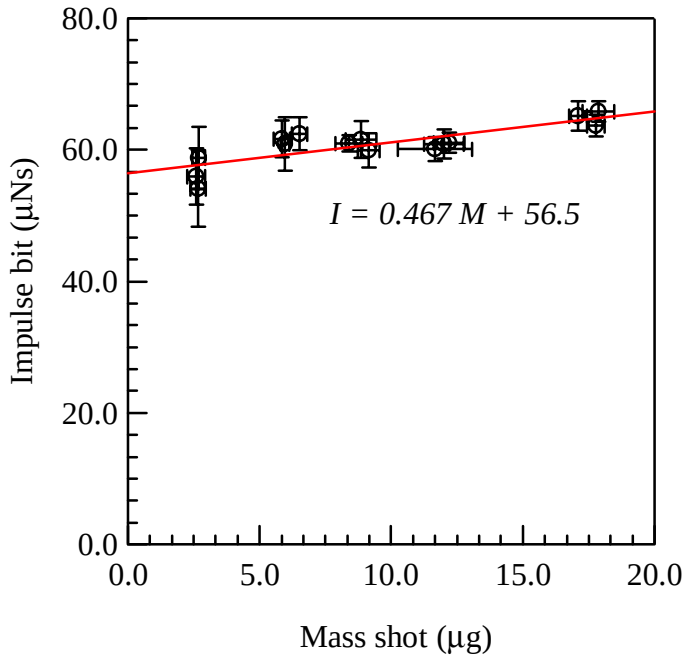

Figure 4.23: Impulse bit dependence on the mass shot in the LP-PPT at 10.0 J (2.6 kV).

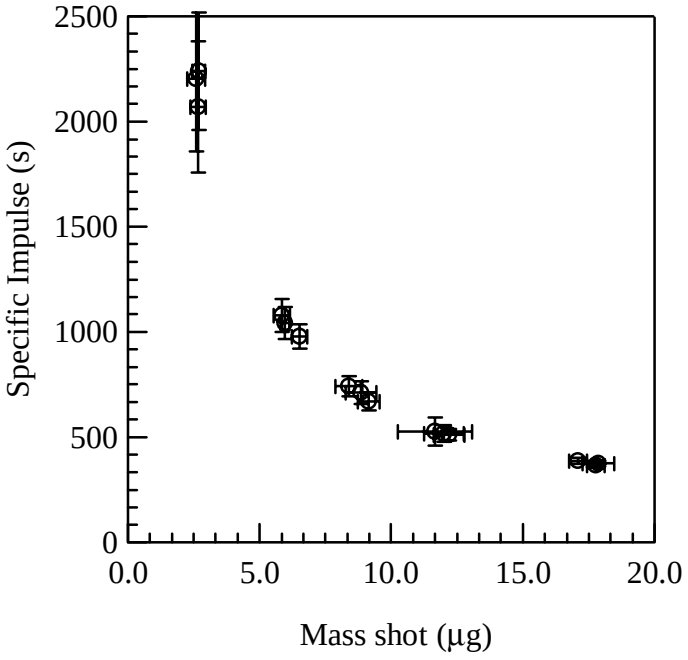

Figure 4.24: Specific impulse dependence on the mass shot in the LP-PPT at 10.0 J (2.6 kV).

electrode with d: 40 mm has higher L' inductance per unit length than d: 20 mm, 0.71 and 1.01 nH/mm respectively. However the impulse bits shows little increase, only 3 %. It would be because that the increase due to L' was cancelled out by the increase of the plasma resistance caused by a long electrode distance.

Figure 4.26 shows the total resistance of PPTs. The resistances are almost constant in the energy (a little decrease). The averaged resistance over the energy is increased from 65 to 75 Ω by increasing the electrode distance from d 20 to 40 mm. However the increase of the resistance (15 %) is not as large as the increase of the inductance per unit length (40 %). The cause of the inconsistency was not sure here. As one of reasons, it can be explained by the difference of discharge current pass. In the case of d 40 mm electrode, oblique current pass was sometimes observed. Inducntance L' evaluated in Section 4.3.5 is based on the assumption that the current straightly flows perpendicular to the electrode. The oblique current pass would decrease the effective L'.

4.4.3 Comparison with an ablative PPT

To compare the characteristics of liquid propellant PPTs to ablative PPTs, The characteristics of an APPTs was measured. In the operation of an ablative PPT, applying voltage more than 2.4 kV led to an unexpected discharge, which means that sometimes breakdown occurred between the electrodes with no ignition by a spark plug. Then the applied voltage of an ablative PPT was limited up to 2.4 kV (8.6 J). Installing a labyrinth between the PTFE block and cathode[115] is one of the methods to solve such unexpected discharge, by preventing creeping discharge.

A liquid PPT has higher specific impulse but lower thrust to power ratio than an ablative PPT. Figure 4.27 compares the impulse bit between a liquid PPT and an ablative PPT (both have 20 mm interelectrode distance). The ablative PPT also shows the linear dependence of impulse bit on the capacitor stored energy, which have been confirmed by a lot of researchers on ablative PPTs [28, 116, 117, 110]. That impulse bit was higher than one of a liquid PPT. Corresponding to it, the total resistance of an ablative PPT was lower than a liquid PPT. Figure 4.28 is the comparison of the measured total resistance of both thrusters.

Instead the specific impulse of the ablative PPT remains under 800 s, and

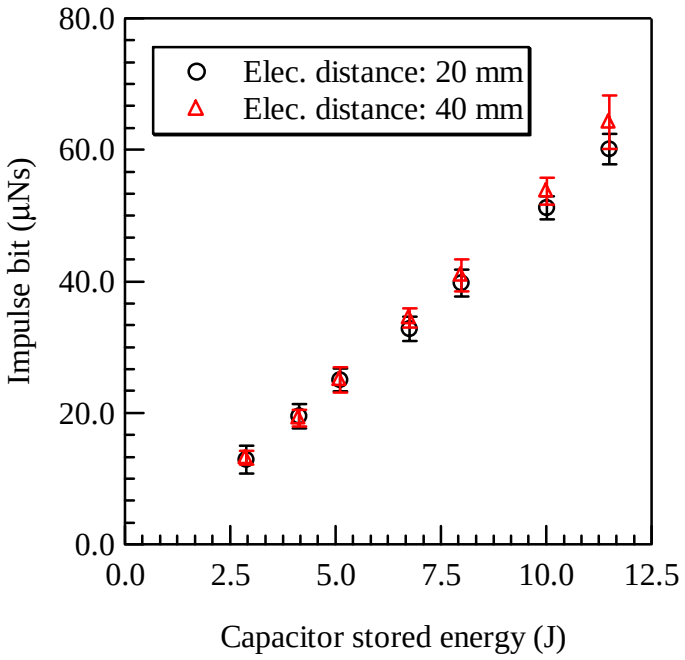

Figure 4.25: Impulse bit dependence on the capacitor stored energy in the LP-PPT with interelectrode space of 20 and 40 mm.

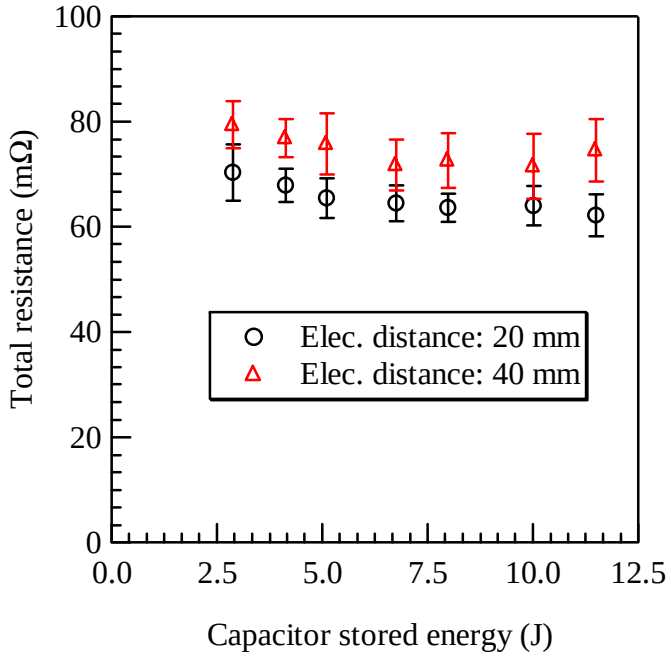

Figure 4.26: Total resistance dependence on the capacitor stored energy in the LP-PPT with interelectrode space of 20 and 40 mm.

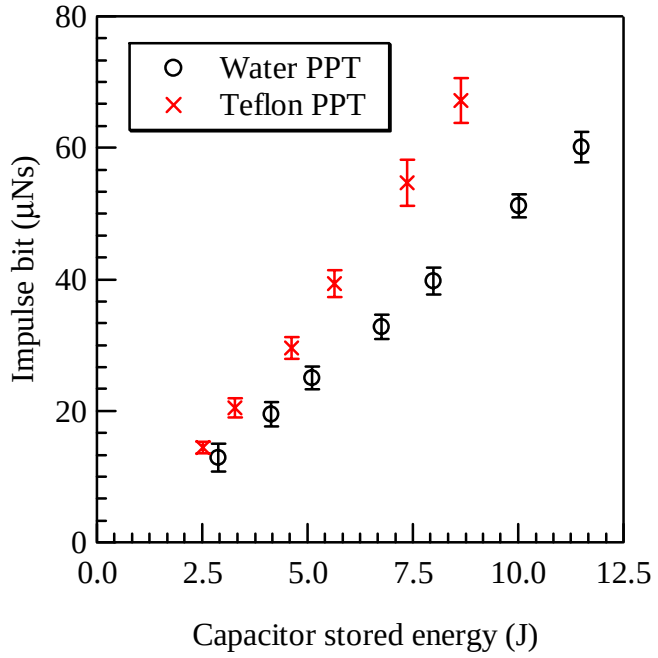

Figure 4.27: Comparison of the impulse bit dependence on the energy between the LP-PPT and APPT.

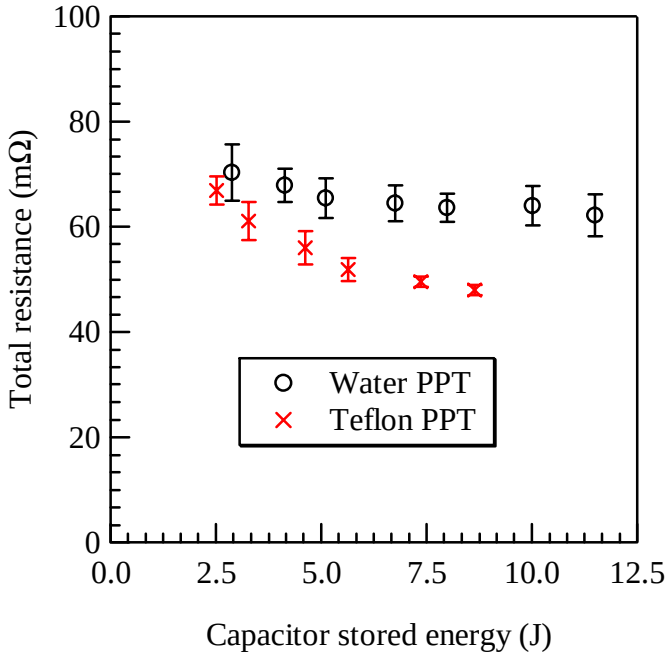

Figure 4.28: Comparison of the total resistance dependence on the energy between the LP-PPT and APPT.

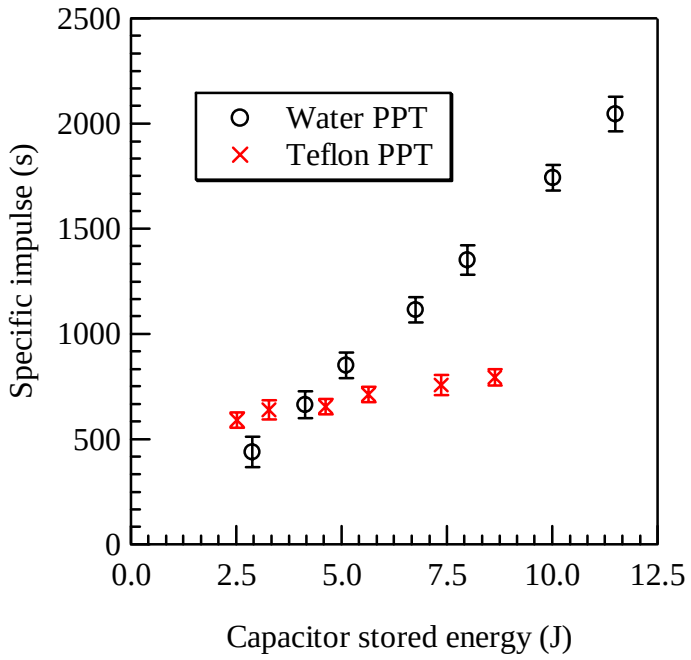

Figure 4.29: Comparison of the specific impulse dependence on the energy between the LP-PPT and APPT.

much lower than the liquid PPT. Figure 4.29 shows the specific impulse of both thrusters calculated from the impulse bit and mass shot. The mass shot of PPTs was obtained by a method described in Section 4.3.1. In ablative PPTs, the mass shot, ablated by the discharge, was linearly proportional to the energy as well as the impulse bit. As a result the specific impulse shows almost constant against the energy (although, in actual, it slightly increases with the energy).

4.4.4 Observation of dicharge plasma

Ultra high speed camera

Discharge plasmas and its acceleration processes on a LP-PPT and Teflon PPT were observed by using an ultra high-speed camera. The camera is NAC Ultra 8, which can take a successive 8 pictures at the maximum frame rate of 100 Mfps. Here the pictures were taken at the frame rate of 10 Mpps (100 ns) and with the exposure time of 100 ns. Pictures taken several times in the same conditions were connected as successive images of one sequence. PPTs dealt here terminate the

most of electromagnetic acceleration during the first and second half cycle of the current waveform (about 4 μs). Then we mainly took pictures during only the first and second half cycle.

Observation system consists of the ultra high-speed camera, a photo detector, a Rogowski coil described in Section 4.2.5, and a controlling computer used to drive the liquid injector. The photo detector detected light emission from the discharge plasma. The output signal from the photo detector was amplified, converted into TTL, and delivered to the Ultra 8 as a trigger signal. Those processings between the detector and camera were performed using an electrical circuit, whose diagram is shown in Appendix F.

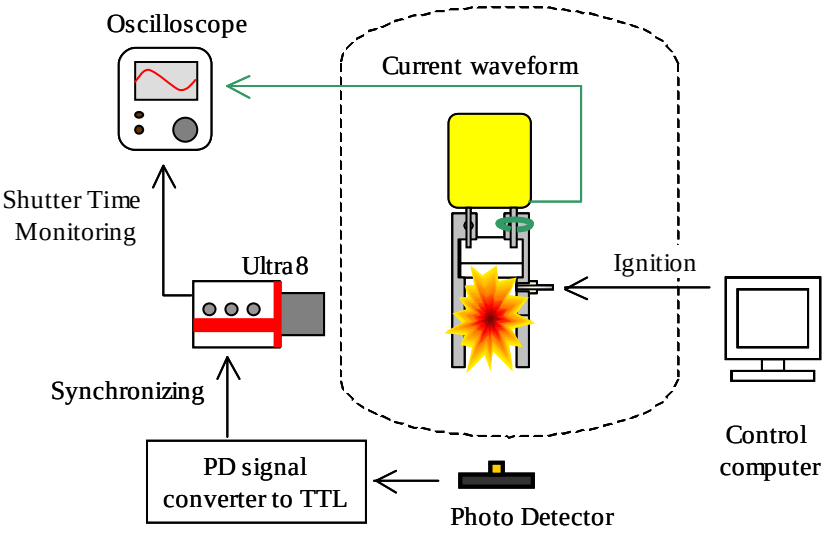

Figure 4.30: Configuration of plasma observation system using a ultra high speed camera.

The electrical system of the photo detector and Ultra 8 was completely isolated from one of the thruster. Generally a spark plug of PPTs generates large and random noise at the ignition before the main discharge. In the experiment, that noise affected all the electrical signals connected to them (current or voltage). The signals with the noise could not be used as the trigger of the camera, because the main discharge was initiated in random after 1 to 5 μs of the pre-discharge of the spark plug. Therefore we needed a trigger completely isolated from the ignitor noise, and it was a photo detector. Current waveform of PPT discharge and signals of shutter time from ULTRA8 were recorded by a digital oscilloscope

at a time. The comparison of the current waveform and shutter time of camera let us know when each picture was taken during the discharge.

Observed images of discharge plasma

Figure 4.31 shows pictures of discharge for several successive times of a liquid propellant PPT, and Fig. 4.32 is for an ablative PPT. The time shown in those figures is the time from the rising of the current. Corresponding current waveforms and the shutter time are shown in those figures. Those pictures were taken by four times of operations in the same conditions.

In LP-PPT, initial plasma was generated between the ignitor and anode. The position that the initial current pass touched on the anode was changed a little on the experimental conditions. It was usually just under the ignitor, but sometimes other places. After the ignition, the plasma expanded into the entire interelectrode space and flowed downstream. The plasma reached to the end of the electrode (35 mm downstream from the back wall) at $t = 0.59$ μs, and most of the plasma ejected from the electrodes before the end of the first half cycle ($t = 1.20$ μs). Just before the second half cycle ($t = 1.40$ μs) there is almost no plasma emission, and breakdown occurred near the back wall and new plasma was generated. This second plasma generation is called as *restriking*. The second plasma was ejected from the electrode in the same way as the first half cycle. Here we can see clearer current sheet than the first half cycle, which expanded outside the electrodes forming an arc current pass.

In contrast, in the APPT, there seemed to be two types of plasma. One was similar to the plasma observed in the LP-PPT, accelerated according to the current ringing. The other was a plasma with strong emission near the PTFE wall. It moves downstream very slowly (about 1 km/s) with no relation to the current reversing. It would be electrothermally accelerated gas sublimated from the PTFE surface and cause of low specific impulse of APPTs. In the LP-PPT, such low velocity plasma was not observed.

Estimation of the exhaust velocity

In order to quantitatively estimate the motion of plasma, intensity profile of the light emission along the flow direction was calculated for LP-PPT. All pictures

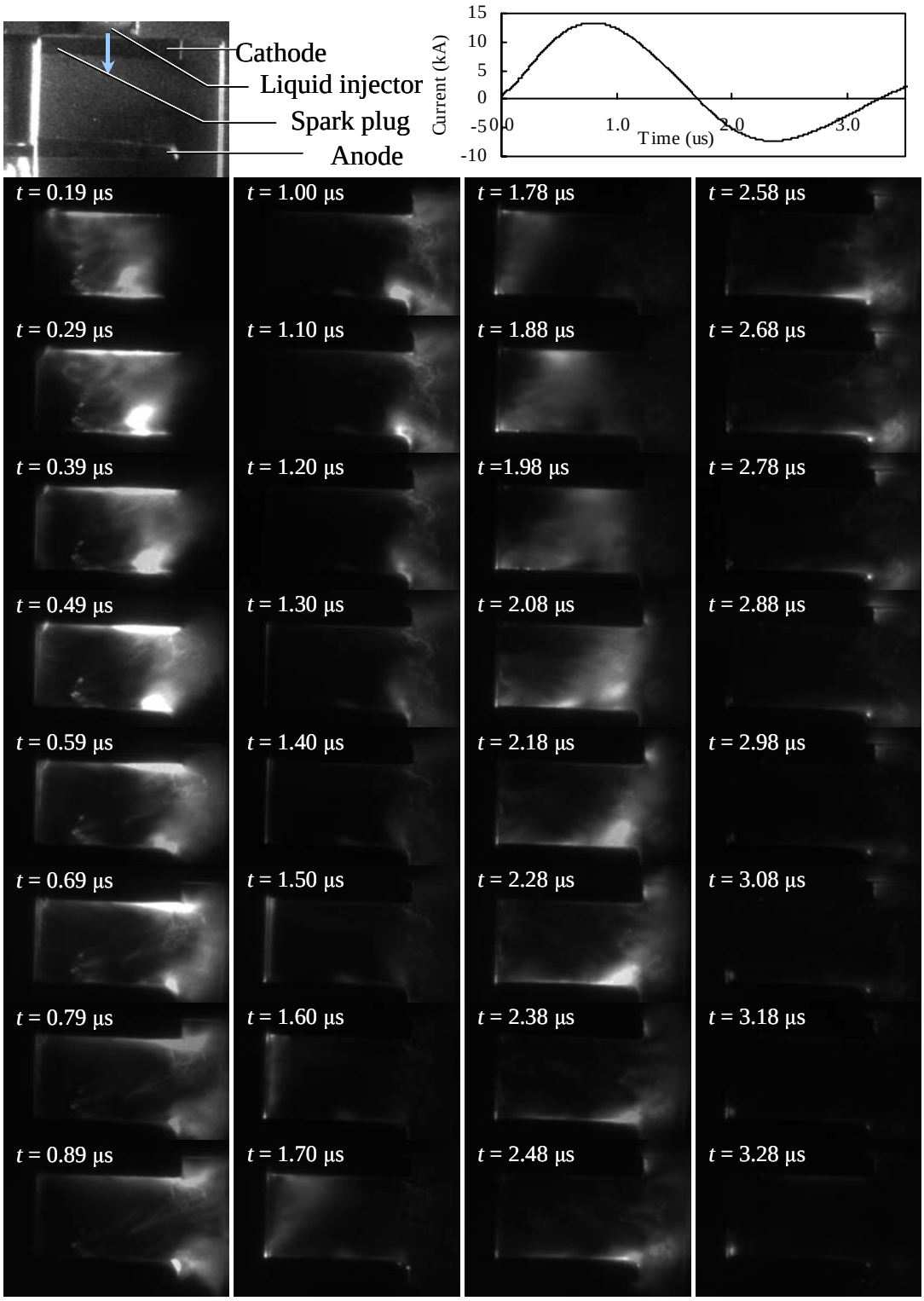

Figure 4.31: Successive images of plasma discharge of LP-PPT at the capacitor stored energy of 10 J.

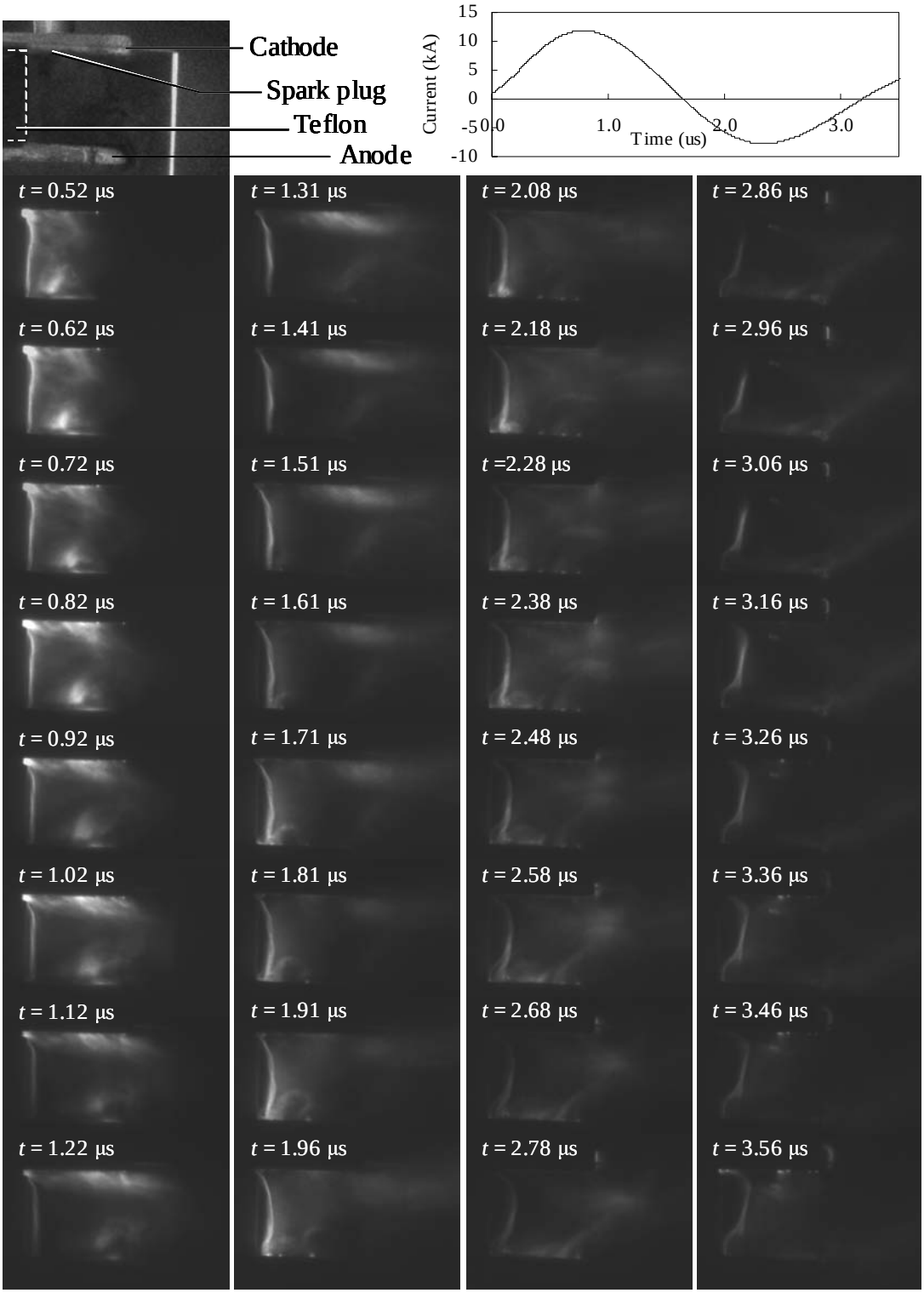

Figure 4.32: Successive images of plasma discharge of APPT at the capacitor stored energy of 7.4 J.

were converted into numerical data of the light intensity. The data were integrated in a longitudinal direction (vertical to the electrode), and intensity profiles of the lateral direction (parallel to the electrode) were obtained. Figure 4.33 shows the lateral direction intensity profiles at the time from 0.2 to 3.3 μs; Fig. 4.33 a) is during the first half cycle and b) is during the second half cycle.

Figure 4.34 shows the time history of an averaged position of the light emission, calculated using the profiles of Fig. 4.33. In the figure, the corresponding squared current waveform is also shown. Here the averaged position of plasma was defined as the gravity center of the intensity profile, expressed by

$$z_{\mathrm{G.C.}}(t) \equiv \int_0^L zI(z,t)\,dx \Big/ \int_0^L I(z,t)\,dx \tag{4.30}$$

where $I(z,t)$ is the intensity profile shown in Fig. 4.33. First, the average position goes downstream with the averaged velocity of 33 km/s. After that, the position remained around 35 mm, whereas the actual plasma is ejected from the electrode. It is because the most of plasma flew outside the observed area and strong emission around the edge of the electrodes. In the second half cycle, a new plasma is generated on the back wall and it proceeds downstream with the averaged velocity of 43 km/s.

That exhaust velocity is much higher than one estimated from the thrust and mass shot. It means the actually accelerated plasma is much less than the mass shot. In other words, only a fraction of the injected liquid was electromagnetically accelerated as plasma.

It should be cared that the above estimated velocities are not the actual plasma velocity, because the emission from plasma does not mean the density. If the electron reaches to the local equilibrium with respect to its excitation temperature, the emission will be proportional to the density. Moreover, the velocities are obtained only in the beginning of the every half cycle. Further acceleration outside the electrode was neglected. Neverthless, let us roughly estimate the equivalent resistance of electromagnetic acceleration using those velocities. Equation 4.19 is further simplified as

$$\bar{v} = \sum_n \int_{n^{\mathrm{th}}1/2cycle} v_n J^2\,dt \Big/ \int_0^\infty J^2\,dt \tag{4.31}$$

$$\simeq \left(\bar{v_1}\int_0^{T/2} J^2\,dt + \bar{v_2}\int_{T/2}^{T} J^2\,dt\right) \Big/ \int_0^T J^2\,dt \tag{4.32}$$

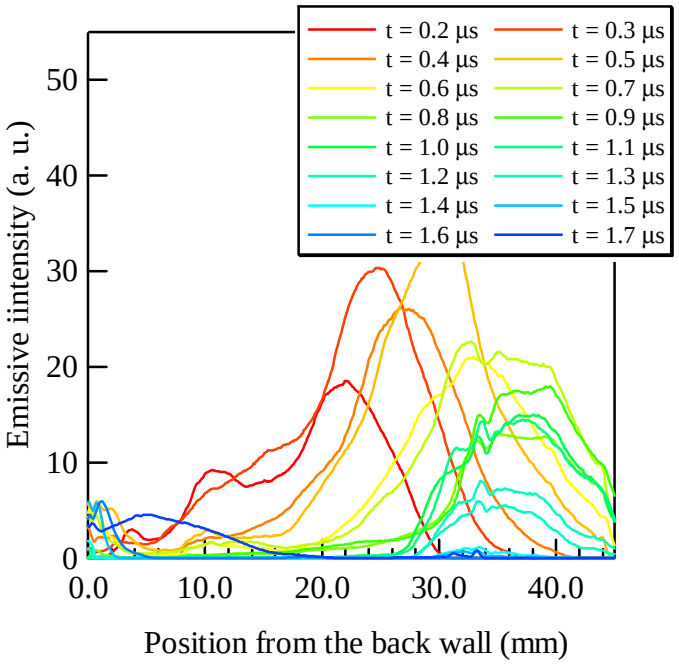

a)

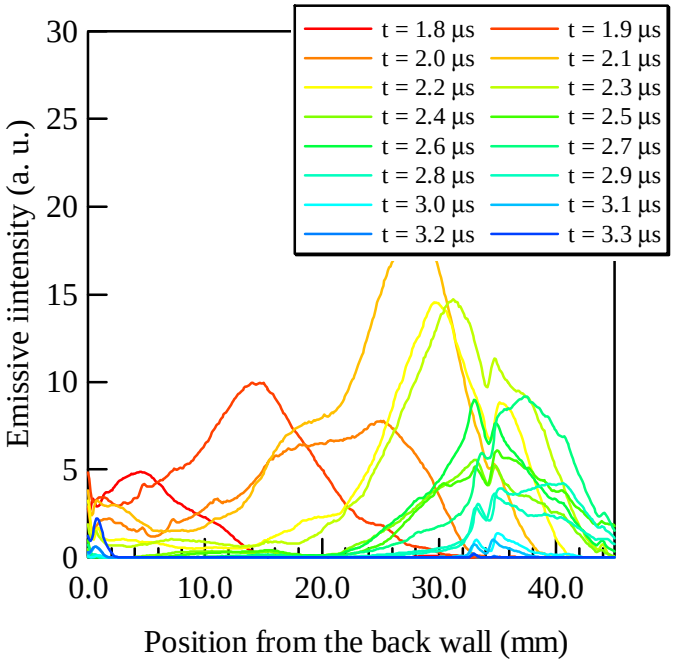

b)

Figure 4.33: Emission intesnsity profile along the electrode.

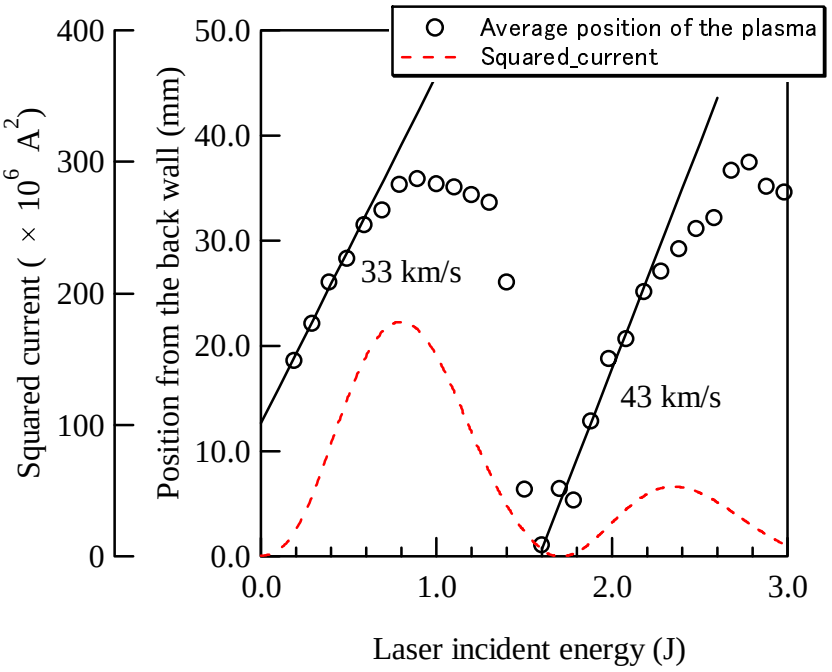

Figure 4.34: Time history of the average position of the plasma emission.

$$= \quad 33\text{km/s} \times 0.78 + 43\text{km/s} \times 0.22 \quad = \quad 35\text{km/s} \tag{4.33}$$

where T is the period of the current oscillation and the integral of the squared current is calculated from the measure current waveform. This averaged velocity 35 km/s and the inductance per unit length 0.71 nH/m give the equivallent resistance of 13 mΩ.

For Teflon PPT, this analysis was not performed due to the above-mentioned two types of plasma flow.

4.4.5 Comparison of plasma resistances

Table 4.4 shows the thrust to power ratios and resistances of the LP-PPT and the Ablative PPT, which were operated by using the same electrodes, electrical feed lines, and a capacitor, shown in Figs. 4.8 and 4.9. The measurement methods of thrust and resistance was explained in the previous sections. The liquid propellant PPT had the total resistance of 64 mΩ, whereas the ablative PPT had only 48 mΩ as shown in the Table. For the LP-PPT, the effective resistance of electromagnetic work was roughly estimated as 13 mΩ from images taken by a high-speed camera.

Subtracting it from $R_{\mathrm{plasma}}+ R_{\mathrm{EM}}$, plasma resistance R_{plasma} was estimated about 33 mΩ for the LP-PPT. As a result, of the energy initially stored in the capacitor, 22 % was used for the electromagnetic acceleation, 27 % was consumed in the external circuit, and the residual 51 % was consumed in the plasma which was the majority of the energy loss. On the other hand, in the case of the APPT, the loss in the plasma was less than the LP-PPT. The resistances of plasma and electromagnetic work of the APPT was lower than one of only plsma of the LP-PPT. Hence, the plasma resistance of the APPT is obviously lower than one of the LP-PPT, although the resistance of the electromagnetic work was not evaluated for the APPT. In my opinion, that value would be around 10 mΩ.

Table 4.4: Partition of resistances in the LP-PPT and APPT.

	Liquid propellant PPT		Ablative PPT	
	Resistance	Fraction	Resistance	Fraction
R_{all}	64±2 mΩ	-	48±1 mΩ	-
R_{circuit}	17±3 mΩ	26.6 %	17±3 mΩ	35.4 %
$R_{\mathrm{plasma}}+ R_{\mathrm{EM}}$	47±5 mΩ	73.4 %	31±4 mΩ	64.6 %
R_{EM}	∼14 mΩ	21.9 %	Not obtained.	21 % if 10 mΩ,

The fact that liquid propellant PPT had a larger total resistance than a Teflon PPT was confirmed also by Scharlemann and York [106, 107].

Here it has been claryfied that a liquid propellant PPT has lower thrust to power ratio than the ablative PPT that has the same thruster configuration, and it is mainly caused by the difference of the plasma resistance. Hence, in order to improve the performance of liquid propellant PPTs, it is necessary to clarify the reason of the high resistance and find the methods to decrease the plasma resistance.

4.5 Performance Improvement for LP-PPTs

In this section, two approaches are examined to decrease the plasma resistance of a liquid propellant PPT and to improve that performance of a liquid propellant PPT. They are seeding of solute into liquid propellant and enhancement of liquid vaporization using a micro-heater.

4.5.1 Seeding on liquid propellant

One of the methods to reduce the plasma resistance is utilization of solute and injecting additives, which can ionize at relatively low temperatures into the plasma. That method had been performed to increase the plasma density of weakly ionized plasma, and called *seeding* [118, 119]. Typically, alkali metals like cesium are selected as seeding material due to its low ionization potential.

Sodium (Na) and ammonia (NH_3) was selected as solute to the water. Water has been used as liquid propellant through this study as promising propellant for PPTs. These materials were chosen because of their ionization potential and handling abilities. The ionization potentials of sodium and ammonia are much lower than that of water (H_2O). Sodium was mixed into water as sodium chloride aqueous solution, and ammonia as ammonia aqueous solution. Table 4.5 shows the ionization potential of H_2O, Na, and NH_3 and the solution concentration to water by mole percent.

Table 4.5: Properties of H_2O, Na, and NH_3.

	Ionization potential	Solution concentration
H_2O	12.7 eV ($H_2O \rightarrow H_2O^+$)	-
Na	5.1 eV ($Na \rightarrow Na^+$)	1.9 %
NH_3	5.9 eV ($NH_3 \rightarrow NH_3^+$)	5.5 %

The above mentioned solution are filled in the liquid injector as well as water propellant. However, thick sodium chloride aqueous solution made the orifice clogged by the adhesion of solid sodium chloride near the orifice. Then the 1.9 % is maximum concentration in performing stable injection of the sodium chloride aqueous solution in vacuum.

4.5.2 Emission spectroscopy

To confirm the presence of solutes in the plasma, emission spectroscopy was conducted. The spectrometer (Hamamatsu; model C5094) has the focal length of 250 mm and 1200 gr/mm grating yielding the reciprocal linear dispersion of 2.5 nm/mm. The dispersed light is detected by a 1024 ch ICCD array. Emission from the discharge was collected into an optical fiber (not focused), and exposure time was set as much longer (2 s) than the PPT discharge. The typical slit width was 100 μm. The spectrogram was scanned at 30 nm increment steps from 320 to 780 nm. The spectral wavelength, and radiance was calibrated using an argon discharge tube and a standard source.

Figure 4.35 shows spectrum lines from PPT discharges for sodium chloride solution and ammonia aqueous solution propellant, where thrusters were operated with capacitor-stored energy of 11.5 J. Sodium (Na I) and ionized chlorine (Cl II) were identified in the plasma of 1.9 % NaCl aqueous propellant by comparing acquired emission lines with a standard reference. Additionally, emission lines from neutral and singly ionized oxygen were identified. They were more intensified than using purified water.

On the other hand, in the case of 5.5 % NH_3 aqueous propellant, spectrum line attributed from ammonia was not identified, and the overall emission lines became weaker than purified water.

4.5.3 Thruster performance

Figure 4.36 shows the dependence of measured thrust power ratio on the capacitor-stored energy for three types of liquid propellants: purified water, sodium chloride aqueous solution, and ammonia aqueous solution. Capacitor-stored energy was varied from 2.9 to 11.5 J. The measured impulse was divided by the energy and averaged over 20 shots for pure water and NaCl seeding or 12 shots for NH_3 seeding. The associated errors mean the 90 % confidence intervals.

Sodium chloride aqueous solution propellant showed higher thrust power ratio than purified water. At the energy of 11.5 J, it increases 9.5 % from 5.2 to 5.7 μNs/J. This increasing tendency become strong as the energy increases. The average increments of impulse was 5.5 %. On the other hand, ammonia aqueous propellant showed lower performance. This result seems to agree with the result

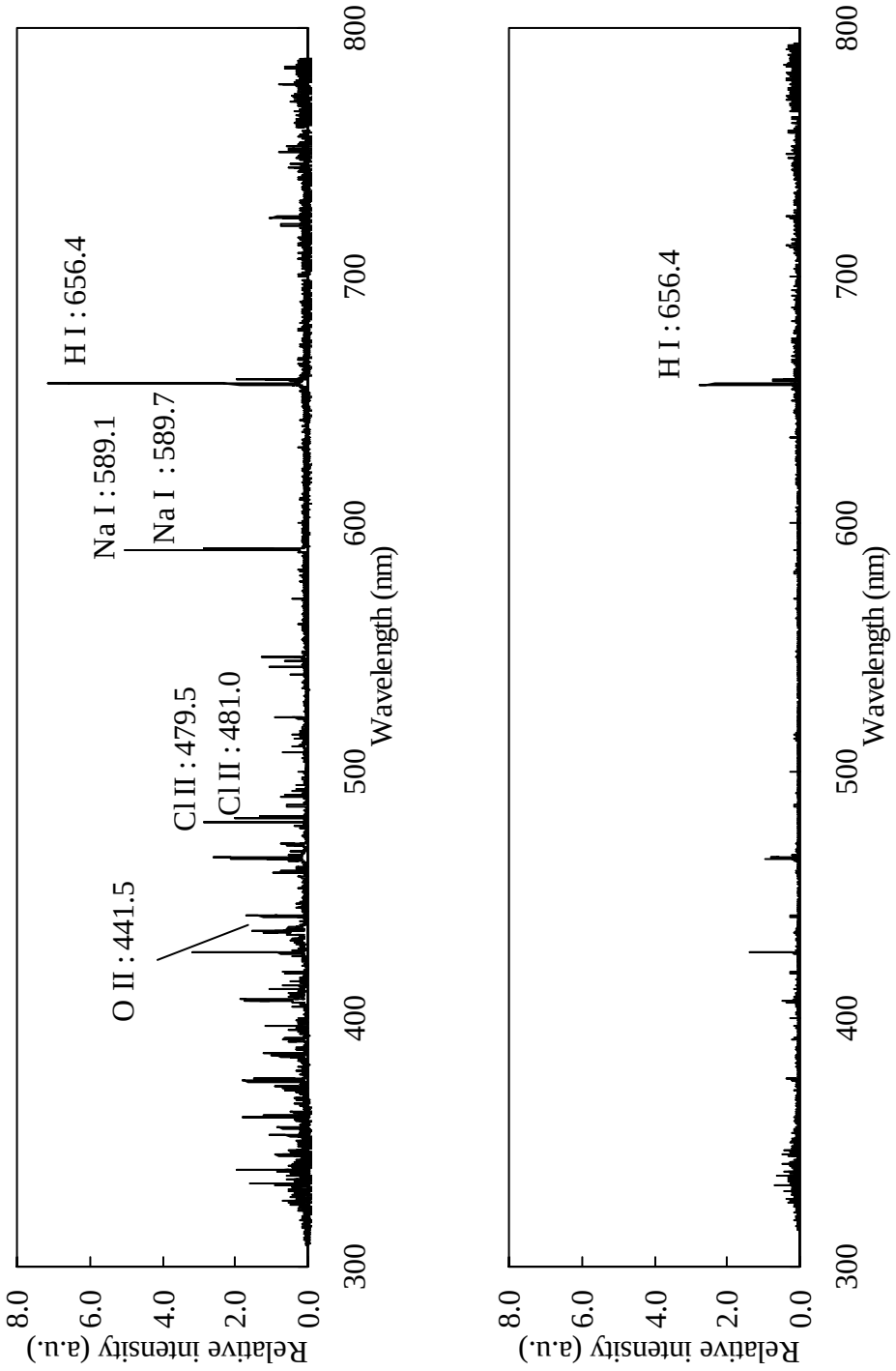

Figure 4.35: Emission spectgrum during the LP-PPT firing with solute mixing liquid; a) NaCl seeding and b) NH_3 seeding.

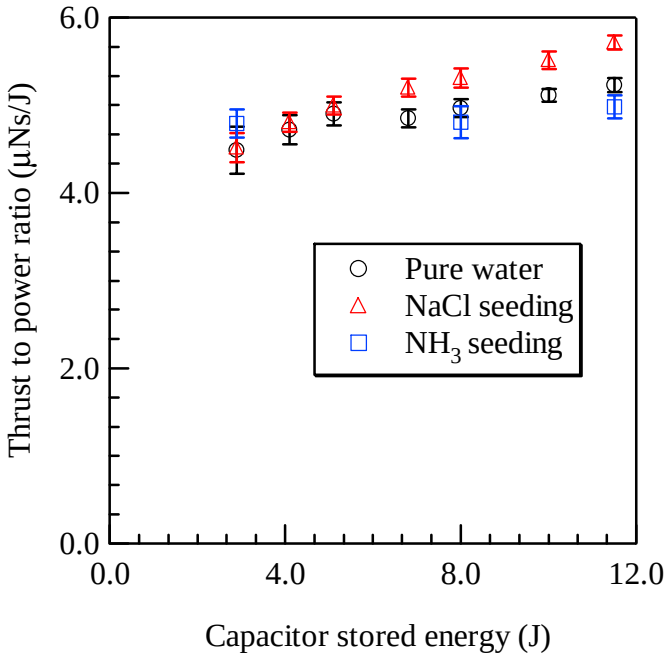

Figure 4.36: Thrust to power ratio dependence on the capacitor stored energy.

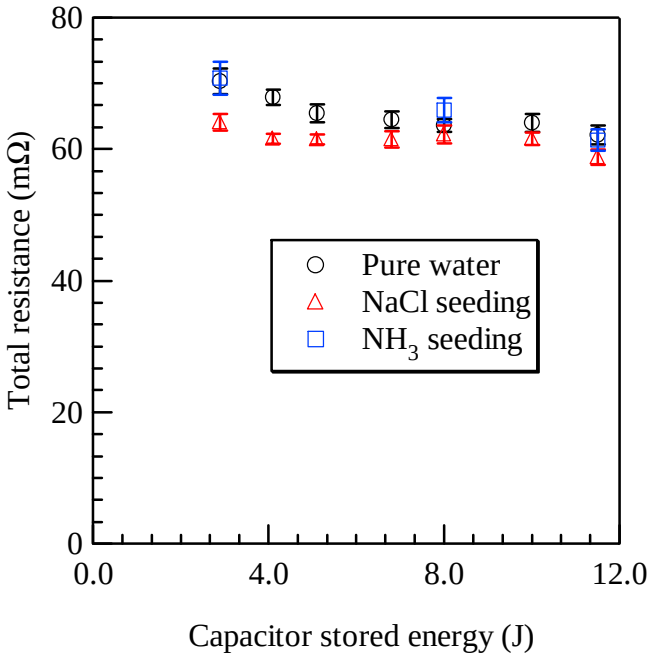

Figure 4.37: Total resistance dependence on the capacitor stored energy.

of strong emission lines from NaCl and weak lines for NH_3.

Figure 4.37 shows the dependence of total resistance of a liquid propellant PPT on the energy. It is obtained from the curve-fit of the current waveform, described in Section 4.3.3. The resistance in Fig. 4.37 shows the average over 20 or 12 shots as well as the thrust power ratio. Sodium chloride aqueous propellant showed smaller resistance than purified water, whose average decrement was 5.7 %. Ammonia aqueous solution had larger resistance than purified water had.

4.5.4 Discussions on the effect of seeding

For the plasma from sodium chloride aqueous solution, emissions from neutral sodium and singly ionized chlorine were observed. Ionized sodium and neutral chlorine were not be observed because they have strong emission lines out of the range of the spectrometer used here, less than 320 nm and higher than 800 nm respectively. Presence of those lines means that some fraction of sodium and chlorine dissolved in water appeared in the plasma.

The results of the impulse and total resistance measurements are consistent with the relation of the electromagnetic impulse and resistance Eq. 4.24, that is small total resistance means high thrust to power ratio. Considering the result of emission spectroscopy, mixing of sodium would increase the plasma density of liquid propellant PPT. Then the total resistance was decreased. However, when ammonia mixing in water, the thrust power ratio was decreased against our expectation. It seems that the plasma density became lower. Some energy might be excessively consumed for dissociation of the ammonia molecule.

Whereas solute mixing succeeded to decrease the total resistance, it is still 20 % larger than a Teflon PPT. Two reasons are considered. Firstly, solutes had only slight effect on the increment of plasma density. Secondly, plasma density was already high but the low electron temperature caused the high resistance (electrical conductivity in fully ionized plasma is proportional to and does not depend on the plasma density). Quantitative measurements for plasma density and temperature are required to clarify those processes.

4.5.5 Enhancement of water vaporization

High resistance of a water propellant PPT can be caused by low propellant density in interelectrode space. It would be not liquid droplets themselves but the evaporated gas which directly contributes to plasma. It is uncertain that how quantity of gas exists before the firing in the interelectrode of a liquid propellant PPT. However, the high plasma velocity observed in Section 4.4.4 indicated the low plasma density. In this section, injecting liquid droplets on a microheater is examined to increase the gaseous propellant density, or pressure, and to decrease the plasma resistance.

Estimation of water droplets evaporation

First, evaporation rate of liquid droplets is estimated. There are the following two evaporation processes of liquid ejected in vacuum: evaporation of flying liquid droplets by the own heat capacity and evaporation of liquid adhering on walls by heat conduction from the walls.

Droplets ejected into the vacuum evaporate by their own heat. The evaporation mass flux: Γ_m is expressed as

$$\Gamma_m = \sqrt{\frac{M}{2\pi RT}} P_{\text{vapor}}(T) \tag{4.34}$$

where P_{vapor} is the vapor pressure of liquid. Return of evaporated gas from the vicinity of the liquid droplets was neglected. Generally vapor pressure has large dependence on the temperature as shown in Fig. 4.38 and the evaporation is suppressed by decrease of temperature due to its latent heat.

For instance, water droplets of 5 μg has the total surface area of 1.2 mm^2 provided that all droplets have the same diameter of 25 μm. They have the evaporation rate of 3.0 μg/ms at 293 K and 0.4 μg/ms at 263 K. Then flying droplets is rapidly cooled and the evaporation is almost stopped within a few mili second. According to the calculation, only 20 % of the mass will be evaporated within 5 ms and the most is evaporated within 0.5 ms.

Droplets adhering on a wall can obtain heat from the wall and can keep to evaporate. In this case, the characteristic time of evaporation is determined by the heat conduction of both the wall and droplets. The heat penetration depth:

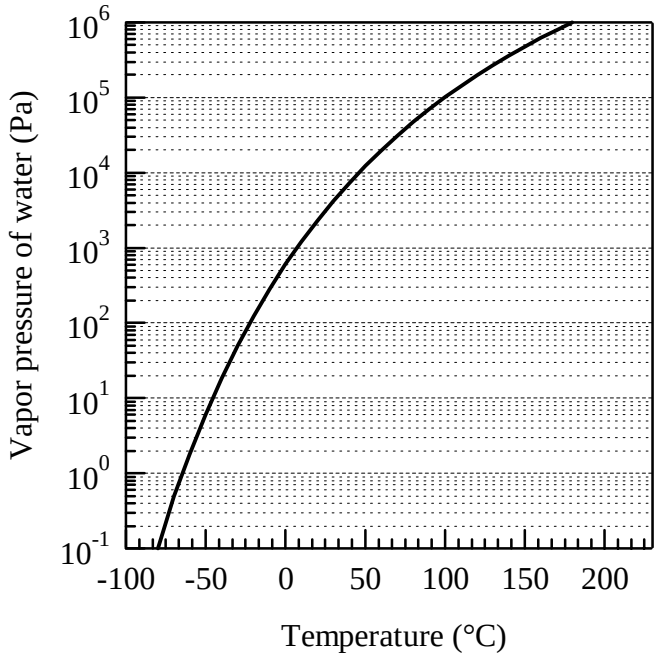

Figure 4.38: Dependence of vapor pressure of water on temperature.

λ defined by the following equation is useful for evaluation.

$$\lambda_{heat} = \sqrt{\kappa t} \tag{4.35}$$

where κ is the thermal diffusivity and t is the time. Table 4.6 shows the thermal properties of water, ethanol, SUS, copper, photoveel, and alumina. Assuming that the energy required to vaporize droplets is supplied from the wall by decreasing the temperature ΔT, that energy: E_{vaporize} is roughly estimated as

$$E_{\text{vaporize}} \sim C_p \Delta T \sqrt{\kappa t}^3 \tag{4.36}$$

Hence, the wall with large heat capacity and high thermal conductivity deliver the heat to the adhered droplets in a short time. For instance, when a wall is copper and the temperature drop is 30 K, vaporization of 5 μg of water requires 11 mJ of the energy, 0.5 mm^3 of the volume, and 2 ms. On the other hand, in the case of stainless steel plate, the time is extended to 320 ms. It is much longer than the scale of gas escaping from the electrodes, and the pressure rise between electrodes becomes a little.

Table 4.6: Thermal properties of solid materials.

	Water	Ethanol	SUS	Copper	Photoveel*	Alumina
$\kappa(\mathrm{m}^2/\mathrm{s})\times10^6$	0.13	0.085	4.0	120	0.53	11
K (W/m K)	0.56	0.17	16	400	1.7	34
C_p(J/kg K)	4200	2480	499	380	1218	800
$\rho(\mathrm{kg}/\mathrm{m}^3)$	1000	785	7920	8920	2590	3930
$\lambda(\mu\mathrm{m})$ at=4 ms	23	18	130	690	50	210

machinable ceramics produced by SUMIKIN CERAMICS & QUARTZ co.,ltd

Enhancement of liquid vaporization by a heater

Pressure between the electrodes is determined by the evaporation rate, not by total mass shot. It is because the time scale for gas filling in the interelectrode space is less than 0.5 ms in our electrode configuration, which is much shorter than the characteristic time of the liquid injection. Droplets adhering on solid surface are more rapidly vaporized than flying ones in vacuum, and its vaporization rate depends on the temperature of the solid. Hence making liquid adhere on heated surface would raise up the interelectrode pressure.

The enhancement of vaporization rate by using a heater gives two benefits. One is increase of the interelectrode pressure, as mentioned. The other is breakdown by that pressure increase according to Paschen's low. There is a potential of a spark-plug-less PPT, which initiates main discharge by only liquid injection. High voltage sparks of a spark plug cause electromagnetic interference, and spark-pluge-less PPTs are attractive.

Heater used to vaporize liquid droplets must have small heat capacity, high thermal isolation, and high thermal diffusivity of the liquid-adhering-surface. The energy to raise the heater up to the operational temperature should be small in comparison with the capacitor stored energy. However, even if the heat capacity is large, high thermal isolation of the heater gives advantage for continuous operation with low power consumption for the heater. The surface on which liquid droplets adhere should have high thermal diffusivity to quickly conduct the energy to the droplets.

Microheater assembly

A commercially available microheater was used to heat up solid surface receiving liquid droplets. It consists of platinum thin film photo-ithographically structured on a 0.15 mm thick alumina substrate. The microheater was bound on a copper main body by Torr Seal®with thermocouple lines. The main body consists of a circular plate with 0.8 mm thickness and 3.7 mm diameter and a rectangular plate with 3.7 mm width, 11mm length, 0.6 mm thickness. Liquid droplets is ejected toward the surface of the circular plate. The copper body was surrounded by a shell made of photoveel. The glued component, a microheater, copper main body, thermocouple lines, and photoveel shell, is referred as a microheater assembly, which is shown in Fig. 4.39. Only the top of the ceramic shell is fixed to the electrode, to avoid the electrical coupling to electrode and insulate from the electrode.

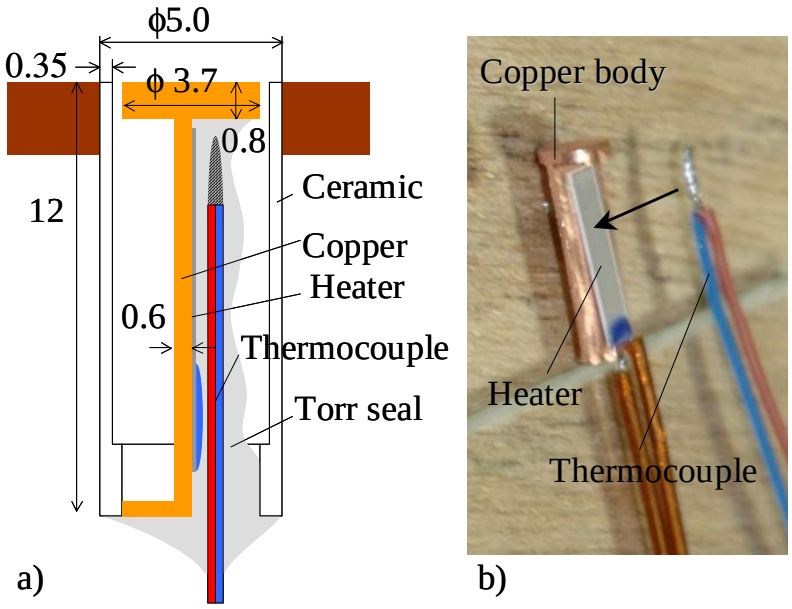

Figure 4.39: Microheater assembly. a) schematic drawing of a microheater assembly and b) photograph before the gluing.

Temperature of the microheater was controlled to be constant using a set point controller. The temperature was measured using a monolithic thermocouple conditioner from Analog Devices (AD597). The temperature output was compared

to the set-point temperature and a switching circuit of the heater was controlled. That electrical diagram is shown in Appendix F. The temperature was ranged from 20 to 100 °C. The maximum temperature was restricted by the temperature limit of the glue dealt here, Torr Seal.

Designed LP-PPTs with using a microheater.

Two varieties of LP-PPTs were designed to enhance the vaporization rate of liquid droplets using the microheater assembly. Those schematic diagrams are shown in Fig. 4.40. Both LP-PPTs have no spark plug and initiate discharge by breakdown by raising the interelectrode pressure.

Figure 4.40 a) is referred as single discharge LP-PPT and Fig. 4.40 b) is referred as double discharge LP-PPT. The first, single discharge LP-PPT, has two parts of parallel plate electrodes as shown in the figure: ignition part and acceleration part. Ignition part has the narrow interelectrode distance of 1 mm and the length of 12 mm. Following the ignition part, acceleration part has the electrodes of 20 mm distance and 35 mm length (cathode is 57 mm). These electrodes are made of copper plates with the thickness of 2 mm.

The ignition part is designed to effectively raise the interelectrode pressure. The microheater assembly is installed 4 mm away from the back wall on the anode. Injection hole for liquid droplets was aligned along the center of the receive plate of the microheater. The ejected liquid droplets exactly hit on the plate because of the short interelectrode distance. Moreover the short distance decreases conductance of the channel. Thin parallel plates channel has the following conductance for rarefied gas stream[120].

$$C_{\text{parallel}} = 116 \ln(l/d) \frac{wd^2}{l} \quad (\text{m}^3/\text{s}) \quad \text{for } l/d > 10 \tag{4.37}$$

where d is the distance between the plates, l is the length, and w is the width. Therefore the electrode distance quadratically decreases the conductance.

The acceleration part is designed to effectively accelerate the plasma by electromagnetic force. The inductance per unit length: L' for a rectangle circuit with parallel plates is given by Eq. 4.29. According to that equation, the acceleration electrodes have L' of 0.8 nH/mm. For the ignition part, Eq. 4.29 cannot be applied due to its too narrow distance. Instead, L' for two dimensional case can be used: $\mu_0 d/w$. Then ignition part has the L' of 0.13 nH/mm.

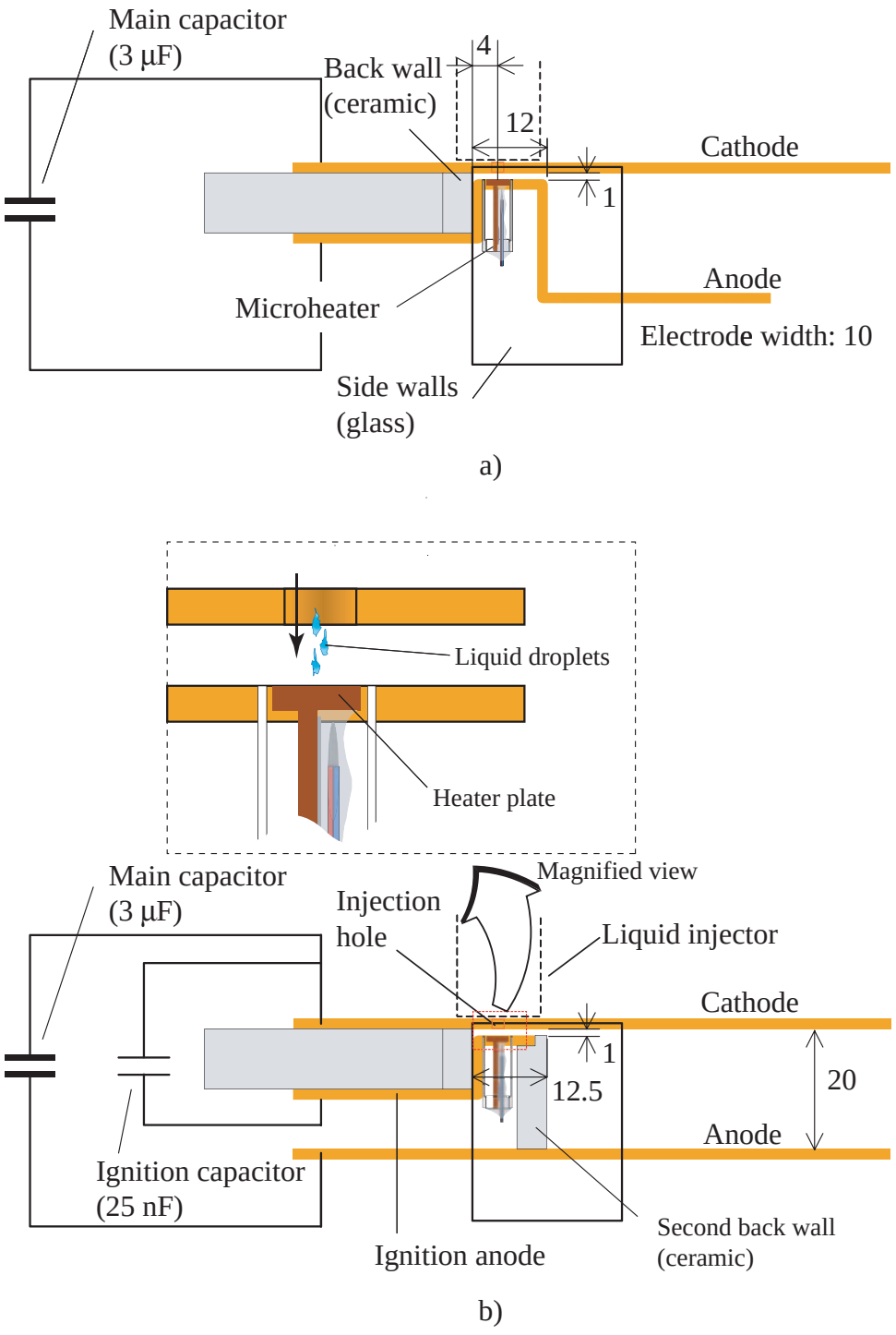

Figure 4.40: Schematic diagrams of the LP-PPT using the microheater.

The double discharge LP-PPT has two capacitors as shown in Fig. 4.40 b), main capacitor of 3 μF and ignition capacitor of 25 nF. Whereas it has two parts as well as the single discharge LP-PPT, anodes of those parts are electrically separated and respectively connected to the capacitors. This design is motivated to prevent the energy excessively consumed in the ignition part. Because the ignition part has lower L' than typical PPTs, discharge current passing there hardly contributes to the acceleration. Small discharge plasma generated in ignition part induces main discharge between main electrodes. After all the ignition part behaves similar to a spark plug. The advantages over a spark plug are that there is no need of high voltage for the discharge, because the breakdown occurs automatically when the pressure reaches up to the certain value.

Another benefit of the double discharge LP-PPT is to use low voltage for the charge of a main capacitor. The single discharge LP-PPT requires high voltage enough to make breakdown. Therefore it restricts the capacitor applied voltage. On the other hand, in the double discharge LP-PPT, the voltage of the main capacitor can be set under the breakdown voltage, and only the ignition capacitor requires higher voltage. Thus the capacitor stored energy can be widely ranged from low level. In this study, 3.0 kV was constantly applied to the ignition capacitor and the voltage applied to the main capacitance was ranged from 1.5 to 3.0 kV.

4.5.6 Experimental results of PPT using a microheater

Operation.

First, the ignition probability was investigated using a heater for the enhancement of the liquid vaporization. A parallel plate electrode with only ignition part was used to clarify the threshold. The voltage of 3 kV was applied the electrode and the liquid was ejected on the heater assembly. The temperature and mass shot of the liquid was changed.

At the standard temperature around 20 °C, there was no breakdown by injecting water droplets of 20 μg. Increasing the temperature, breakdown occured by less liquid injection, and at 100 °C it was accomplished by 6 μg liquid injection. In less mass shot of 4 to 6 μg, the breakdown was accomplished in several times at the heater temperature of 100 °C. Under the 4 μg of mass shot, no breakdown

occurred. Figure 4.41 shows how the threshold changing against the heater temperature and mass shot. In that figure, probability means a fraction of number of ignitions over number of trials. The trial number was 15 or 30. For instance, liquid injection of 7 μg required the temeperature of more than 70 °C for the exact breakdown.

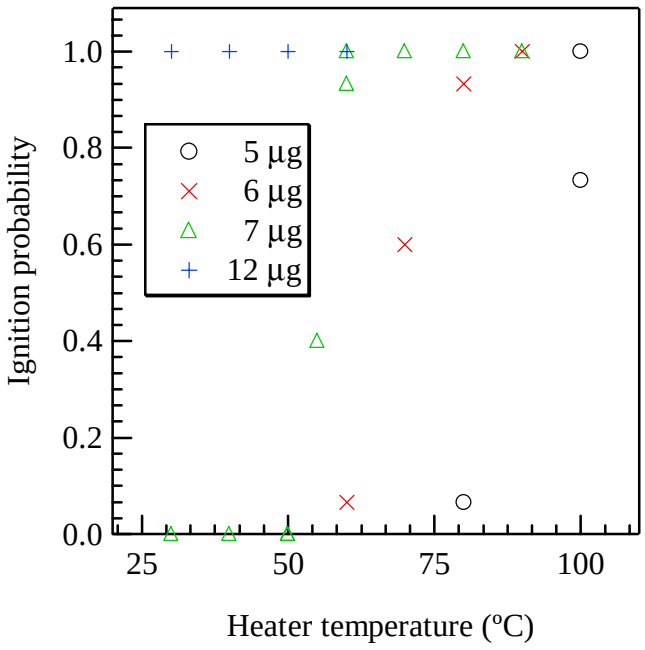

Figure 4.41: Ignition probability dependence on the heater temperature.

Both LP-PPTs using microheater, single discharge and double discharge, were successfully operated with the mass shot over 6 μg with keeping the heater temperature at 100 °C. By injecting liquid droplets on the microheater, breakdown occurred between electrodes. Figure 4.42 shows pictures during the firing with the exposure time of camera over 200 ms. In double discharge LP-PPT, if there is no applied voltage on the main capacitor, only small discharge occurred between the ignition electrodes.

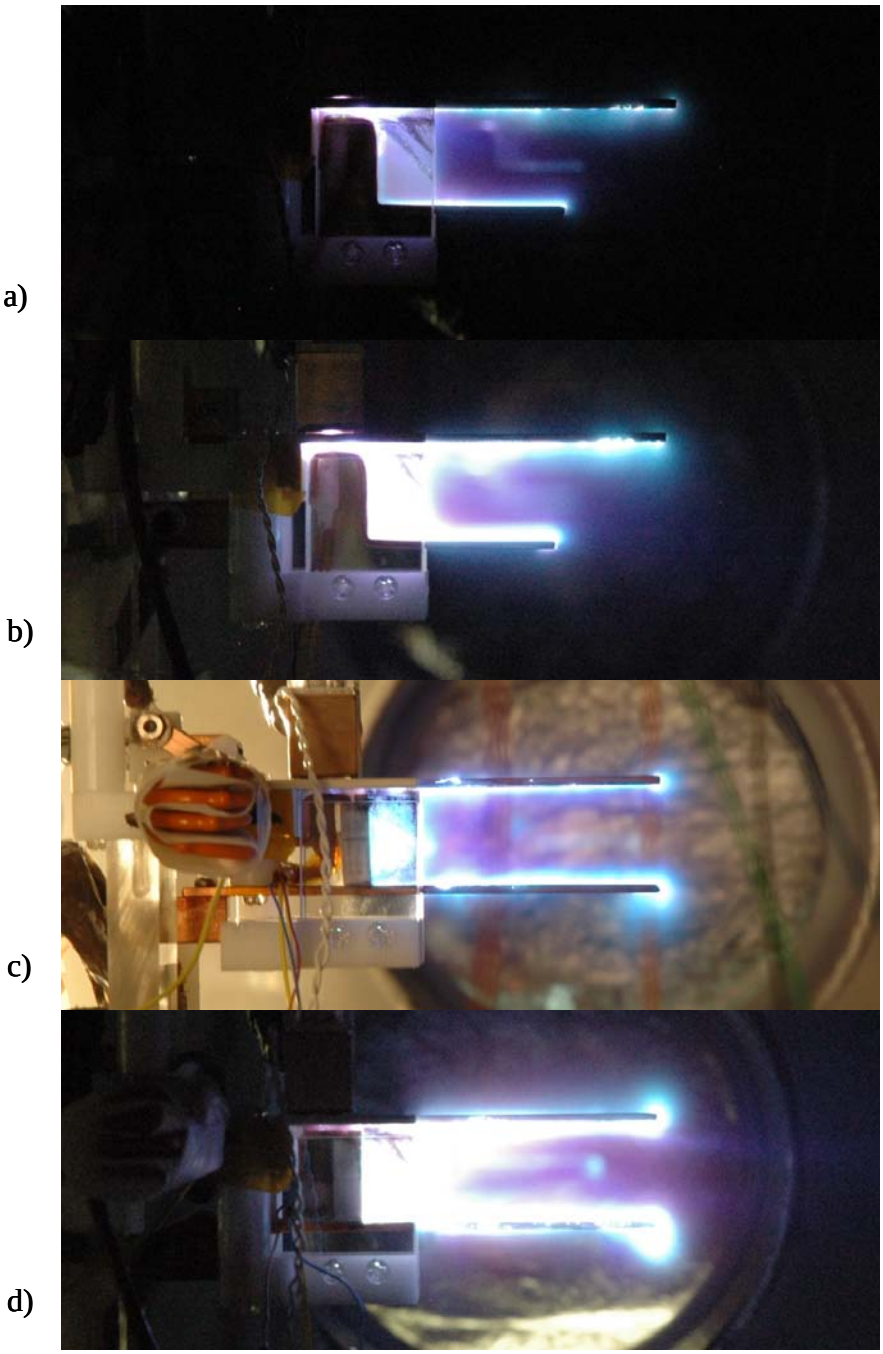

Figure 4.42: Pictures during the firing of LP-PPT using microheater; a) and b): single discharge LP-PPT with close and open diaphragm of the camera and c) and d) double discharge LP-PPT with close and open diaphragm respectively (only c) with back ground light).

Thruster performance

Figure 4.43 shows the thrust to power ratio, impulse bit per energy, for single and double discharge LP-PPT. Every plot was averaged over 10 single shots measurement and the error bar means the standard deviation. In this experiment the mass shot was kept constant of 6 μg.

Double discharge LP-PPT showed higher thrust to power ratio than the previously studied LP-PPT. The thrust to power ratio was gradually increase with increasing the energy, and saturated around 10 J, where they reaches up to 8 μNs/J. Our previous study had showed the maximum thrust to power ratio of 6 μNs/J. In contrast, single discharge LP-PPT showed poor thrust to power ratio below 2 μNs/J, which is less than half of the previous LP-PPT.

In addition, the thrust to power was a little increased using small liquid injection orifice. For double discharge LP-PPT, two sizes of liquid injection orifice of 25 and 50 μm were examined Figure 4.44 shows the total resistance of double discharge LP-PPT for two sizes of the orifice. Their energy dependence was investigated. Every plot was averaged over 5 shots and the error bar means the standard deviation. Theses resistances were consistent with the result of thrust to power ratio. The resistances gradually decreased with increasing the energy, and saturated around 10 J, where they reached down to 50 mΩ. Moreover, the difference in the orifice diameter also consisted with the result of thrust to power. Orifice diameter of 25 μm showed a little smaller resistance than 50 μm.

4.5.7 Discussion on the results of PPT using a microheater

Effect of the Enhancement of Vaporization

It is clear that high thrust to power ratio of double discharge LP-PPT is caused by its low plasma resistance. Moreover this reduction of plasma resistance would be due to the increasing of the interelectrode pressure. From Fig. 4.41 the breakdown between electrodes are clearly affected by the heater temperature. It means the interelectrode pressure was increased by the heater temperature. In short, the interelectrode pressure was raised up to the point to satisfy Paschen's low. Instead, in the caser using a spark plug, the interelectrode pressure is always lower than Paschen's breakdown. It would be the reason that LP-PPT in the previous

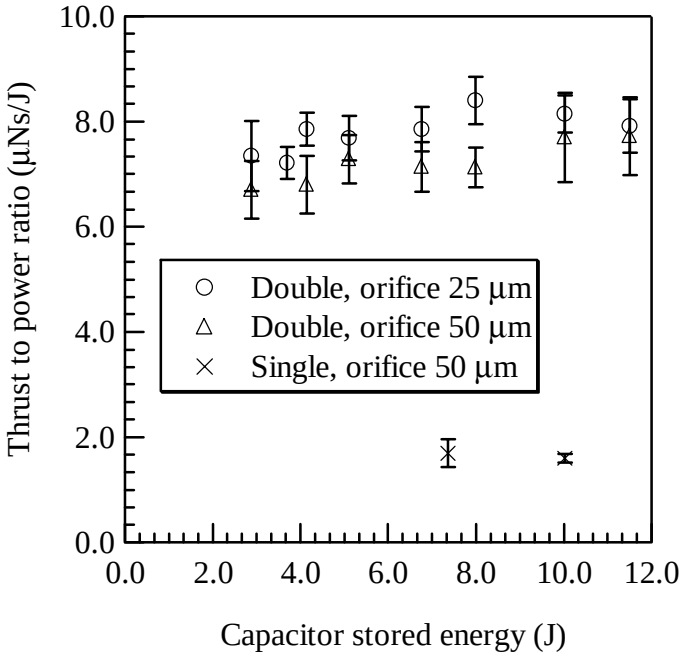

Figure 4.43: Thrust to power ratio dependence on the capacitor stored energy in LP-PPT using microheater.

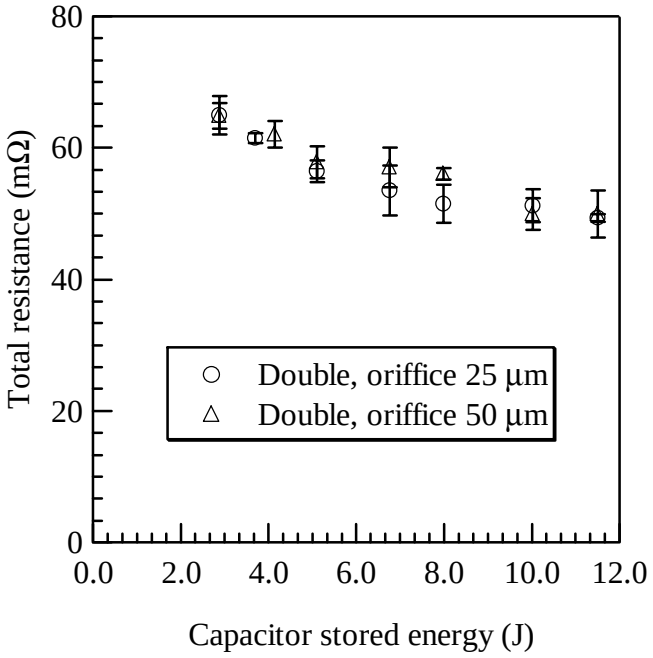

Figure 4.44: Total resistance depdendence the capacitor stored energy in double discharge LP-PPT using microheater.

research had higher resistance than an ablative PPT and also the reason that the seeding did not have so much effect. In Fig. 4.46, the resistances of the ablative PPT, LP-PPT with spark plug , and double discharge LP-PPT are compared. It is shown that the resistances of double discharge LP-PPT is decreased down close to the ablative PPT. Figure 4.45 shows the thrust to power ratio with comparing the other thrusters.

As interesting result, the orifice diameter of the injector affected the resistances and performance, whereas, in our previous study, the state of liquid droplets had no influence on the performance. It would be caused by the difference in the diameter of the droplets. The orifice of the diameter of 25 μm provides smaller droplets than 50μm as shown in images of Fig. 4.7. Small droplets on a heater is more rapidly heated and vaporized than lager droplets. This would be a reason that the injector of the 25 μm orifice provides the higher performance. However, there were larege shot to shot variations associated with the double discharge LP-PPT, and more experiments should be conducted to confirm that effect.

Compatibility of an Ignition Capacitor and Microheater Assembly

Compatibility of a double discharge LP-PPT is examined as a micropropulsion system. A double discharge LP-PPT requires an ignition capacitor and a microheater instead of a spark plug. To apply it for microspacecraft, energy and weight needed for those additional components must be small in comparison with those required for the propulsion system.

The increment of weight and energy for the ignition capacitor is negligible. Actually the capacitor used was much smaller than main capacitor. The ignition capacitor used here consumed the energy of 0.11 J and weighed 25 g.

Thermal capacity of the microheater used here had not attained to enough level in this study. The main copper body on which the microheater was glued weighs 260 mg, and required 10 J to heat 100 K gap. It is comparative with the energy for a single shot. Hence further miniaturization of the heater is necessary. The capacity would be decreased less than a few Joules by eliminating waste part. The microheater itself, consisted of thin alumina, requires 0.09 J for 100 K heating. The main body had too many mass, which was caused by our fabarication ability. Indeed it needs only the surface to receive liquid droplets. A circular plate of 2

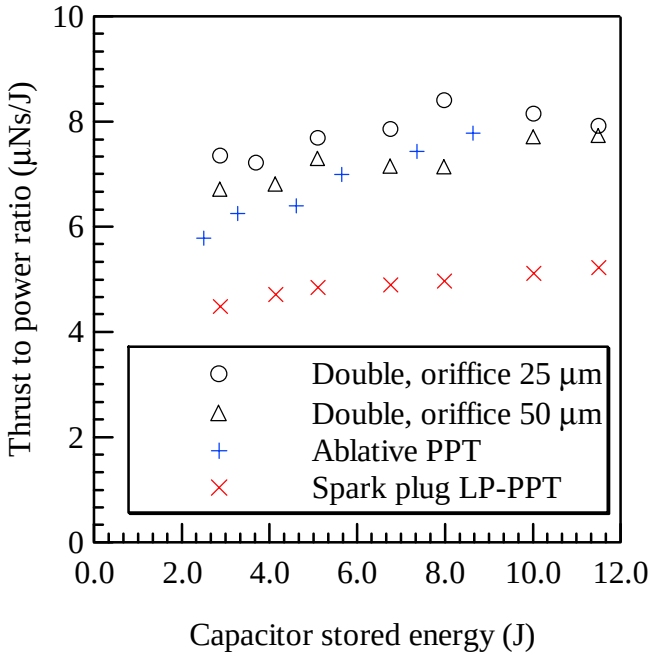

Figure 4.45: Comparison of the thrust to power ratio of Teflon PPT, spark plug LP-PPT (pure water), and double discharge LP-PPT(the orifice of D25 and D50 μm).

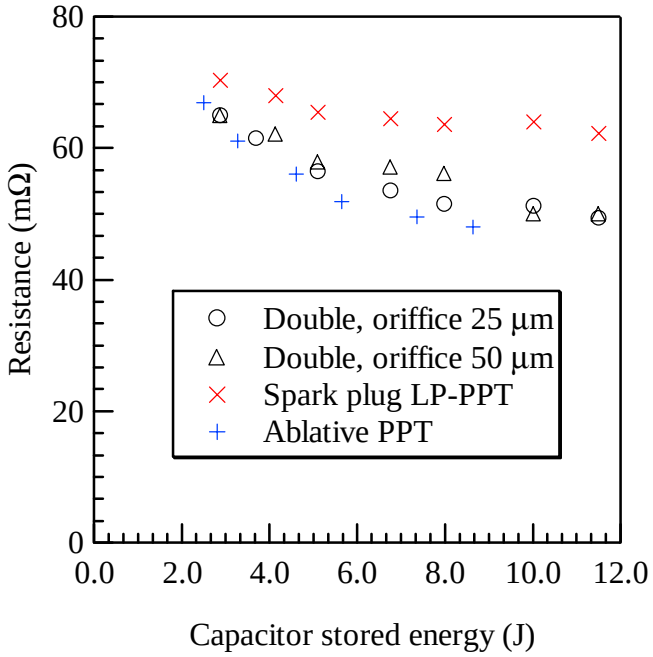

Figure 4.46: Comparison of the total resistances of Teflon PPT, spark plug LP-PPT (pure water), and double discharge LP-PPT(the orifice of D25 and D50 μm).

mm diameter and 0.5 mm thickness is enough size as droplets receiver, and such a plate needs 1.1 J to heat up 100 K.

However, the initial heating energy can be neglected in repetitious operation, if the heater has enough thermal insulation. The heat is escaped from a heater by thermal conduction and radiation. The microheater assembly in this study had those heat losses less than 200 mW. The heat conduction through the photoveel circular tube was 110 mW under the 100 K temperature gap. Black body radiation from the heater surface into the space is 90 mW at the heater temperature of 373 K. Those losses would be neglected in a typical operation of 10 W class PPTs.

4.6 Comparison of LP-PPTs and APPTS

In the last of this chapter, let us compare the charcteristics of LP-PPTs and APPTs. As shown in the previous work, the most advantage of LP-PPTs is their higher specific impulse, reaching to 3000 s by throttling the ejection liquid. However the too small amount of liquid inejction forces discharge occuring under extremely low pressure, and it would cause the wide variations of impulse, see Fig. 4.23. As a result, the adequate operation will be accomplished with over 5 μ g mass shot with the specific impulse around 2000 s in my opinition. That three times higer Isp than APPTs reduces the propellant mass, and the reduction of the propellant should be larger than the weight increment by the liquid injector intalling. The liquid injecter dealt here weighs 78 g, but further miniaturization will be easily accomplished, about down to 50 g. On the other hand, APPTs requires constant force springs to push PTFE block, which would weigh about 10 g. Usually, PPTs are mounted on spacecraft with several heads to increase the mobility of spacecraft, typically 8 heads. Each head requires liquid injector for LP-PPTs or spring system for APPTs. As a result, LP-PPTs cause the 320 (40×8) g weight increase. Threfore if APPTs has the propellant PTFE more than 500 g, the weight increase by the injector will be compensated by the increment of the specific impulse, and that system will be advantaged by using LP-PPT instead It corresponds the missions with delta-V more than 80 m/s on 50 kg spacecraft.

In addtion to the weight reduction by higer Isp, liquid propellant has the advantage of the arbitrary configurations of the fuel. APPTs requires long polymer bolck as the propellant, and it may give difficulty in the integration to spacecraft.

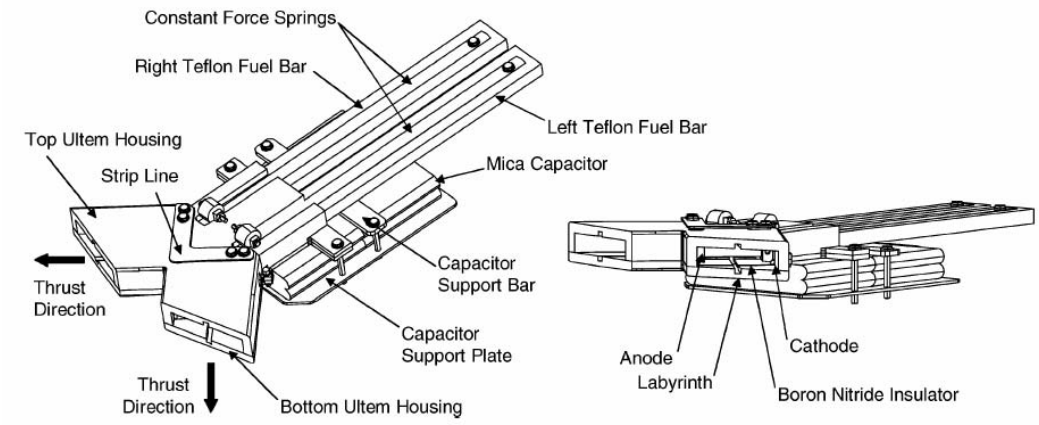

Figure 4.47: Dawgstar APPT desinged in University of Washington.

Typical 10 J class APPTs has the 2 cm^2 cross section of PTFE bolck. It means 100 g PTFE block has the length of about 25 cm (the density of PTFE is about 2 g/cm^3). Figure 4.47 shows an APPT designed in Univesity of Washington for Dawgstar satellite[115]. If much more propellant is needed, the longer PTFE block may conflict with the other spacecraft hardwares.

Moreover, other advantages of using liquid propellant are avoinding non uniform ablation of the polymer and use of no charring or toxic material. The polymer material is likely to attach on solid walls of thruster and spacecraft rather than liquid propellant. On the contrary, disadvantages of liquid propellant are risks of leaking and clogging of liquid. Additionally, water has the capability of icing in sapce. The use of heater to melt the ice will increase a lot of power. In terms of stabel propellant selection, alcohol propellant is attractive. Previous work on liquid propellant PPTs showed the successful operation using ethanol and methanol propellant with the equivalent performance.

4.7 Conclusion of Chapter 4

In this chapter, a liquid pulsed plasma thruster was investigated and its performance improvement methods were proposed, and the following conclusions were obtained.

- Energy partitions in a liquid propellant PPT was evaluated. Of the energy, 22 % was used as the electromagnetic acceleration of plasma, 27% was consumed as the energy loss in the external circuit was 27 %, and 51 % was consumed in the plasma. The energy loss in the plasma was higher than one of the ablative PPT with the same configuration. As a result, lower thrust power ratio using water was caused by the higher plasma resistance than using PFFE.

- Seeding sodium chloride in water decreased the plasma resistance and increased the thrust by 5.5 %. Emission spectrum from discharge plasma was also strengthened by the seeding. In contrast, ammonia seeding showed no a little decrease of the thrust.

- Liquid vaporization rate was enhanced using a micro heater and it enabled breakdown by the pressure rising injecting 6 μg water droplets.

- The enhanced water vaporization increased the thrust by 30 % with double discharge mode. It was because that the interelectrode pressure was increased by enhancing the water vaporization.

Chapter 5

Conclusions

This study has been performed to propose and develop micropropulsions suited with 1 - 00 kg microspacecraft. In order to reach to the goal, the following studies were conducted. First, a high accuracy thrust stand was developed to exactly evaluate the performance of micropropulsions. Secondly, a dual propulsive mode laser microthruster was proposed for microspacecraft less than 10 kg and the fundamental characteristics were clarified. A pulsed plasma thruster using liquid was investigated for microspacecraft over 10 kg by clarifying energy partitions, and the performance improvements were conducted. The major conclusions of this study are:

Thrust stand for micropropulsions

- A thrust stand with high resolution and accuracy was developed. The resolution was less than 1.0 μNs and the accuracy is within 2.0 %. That thrust measurement was examined using thrusters of the weight up to 2.0 kg (the stand was designed to endure thruster weight over 10 kg).

- Tight adjustment of the gravity center (<10 μ m) and effective damping of the stand enabled the high resolution and high usability.

- A curve-fitting method was newly proposed to removing the mechanical noises induced by background vibrations. That effect was analytically clarified and experimentally verified.

Dual propulsive mode laser microthruster

- The successful operation of laser ablation mode was verified using polyvinyl chloride propellant. The thrust provided by the laser ablation was proportional to the laser pulse width with the thrust to power ratio of 40 to 150 μNs/J according to the ablative material. It enabled the laser ablation mode to provide lower thrust with high resolution.

- Absorption rate of the ablative propellant strongly affected the thrust performance, especially thrust to power ratio. Polyvinyl chloride with rich carbon density showed higher thrust to power ratio.

- Laser ignited combustion of pyrotechnic in vacuum was verified using boron / potassium nitrate. The laser ignition processes of Boron / potassium nitrate was well reproduced with numerical calculation, where three dimensional heat conduction problem was solved with the exothermic reaction.

- The threshold laser power and pulse with for the laser ignition was adequate for the use of microspacecraft, 300 mW and 150 ms. That laser ignited combustion enabled laser microthruster to provide higher thrust of 11 mNs and 600 mNs according to the size of the pyrotechnics.

Pulsed plasma thruster using liquid propellant

- Energy partitions of a liquid propellant pulsed plasma thruster was evaluated and the most energy loss was the dissipation in the plasma (51 %). It was revealed that the higher plasma resistance when using liquid propellant caused the low thrust power.

- Seeding sodium chloride in water decreased the plasma resistance and increased the thrust by 5.5 %. Emission spectrum from discharge plasma was also strengthened by the seeding. In contrast, ammonia seeding showed no a little decrease of the thrust.

- Liquid vaporization was enhanced using a micro heater and it enabled breakdown by the pressure rise with the adequate mass shot. The enhanced water vaporization increased the thrust by 30 % with a double discharge mode. It was because of the increased interelectrode pressure.

References

[1] M. M. Micci and A. D. Ketsdever, editors. *Micropropulsion for Small Spacecraft*, volume 187 of *Progress in Astronautics and Aeronautics*. American Institute of Aeronautics and Astornautics, Inc., 2000.

[2] Y. Nojiri, M. Nagai, Y. Nakamura, R. Funase, T. Eishima, E. Takei, C. Yuliang, A. Enokuchi, K. Nakada, and S. Nakasuka. University of tokyo's nanosatellite cubesat-xi and its on-orbit experiment results. In *24^{th} International Symposium on Space Science and Technology*, Miyazaki, Japan, 2004. ISTS 2004-f-05.

[3] C. Kitts, R. Twiggs, F. Pranajaya, B. Palmintier, and J. How. Emerald: a low-cost spacecraft mission for validating formation flying technologies. *1999 IEEE Aerospace Conference Proceedings*, **2**, pp.217–226, 1999.

[4] A. Valdez, C. Hu, C. Kitts, M. Breiling, A. Slaughterbeck, J. Ota, D. Hadi, T. Kuhlman, and S. Lyons. The artemis project: Picosatellites and the feasibility of the smaller, faster, cheaper approach. *1999 IEEE Aerospace Conference Proceedings*, **2**, pp.235–243, 1999.

[5] S.C. Solomon, S.M. Bailey, C.A. Barth, R.L. Davis, J.A. Donnelly, T.E. Holden, M.S. Kelley, R.A. Kohnert, M.T. McGrath, A.W. Merkel, H.L. Reed, S.M. Ryan, M.A. Salada, S.R. Steg, G.A. Tate, J.C. Westfall, J.J. Westphal, and P.R. Withnell. The snoe spacecraft: Integration, test, launch, operation, and on-orbit performance. In *Proceedings of the 12th Annual AIAA/USU Conference on Small Satellites*, Logan, Utah, USA, 1998. ISTS 2004-f-05.

[6] K. T. Alfriend, S. R. Vadali, and H. Schaub. Formation flying satellites: Control by an astrodynamicist. *Celestial Mechanics and Dynamical Astronomy*, **81**, pp.57–62, 2001.

[7] C. Sabol, R. Burns, and C. A. McLaughlin. Satellite formation flying design and evolution. *Journal of Spacecraft and Rocket*, **38**(2), pp.270–278, 2001.

[8] R. S. Smith and F. Y. Hadaegh. Control of deep-space formation-flying spacecraft; relative sensing and switched information. *Journal of Guidance, Control, and Dynamics*, **28**(1), pp.106–114, 2005.

[9] W. Ren and R. W. Beard. Decentralized scheme for spacecraft formation flying via the virtual structure approach. *Journal of Guidance, Control, and Dynamics*, **27**(1), pp.73–82, 2004.

[10] P. R. Lawson. The terrestrial planet finder. *2001 IEEE Aerospace Conference Proceedings*, **4**, pp.2005–2011, 2001.

[11] C. V. M. Fridlund. Darwin - the infrared space interferometry mission. *ESA Bulletin*, **103**, pp.20–25, 2000.

[12] K. Danzmann and LISA Study Team. Lisa: laser interferometer space antenna for the detection and observation of gravitational waves. In *2nd ed., Max-Planck Inst. fur Quantenoptik*, Garching, Germany, 1998. ISTS 2004-f-05.

[13] S. Nakasuka. Requirement for microthruster. Private meeting with Nakasuka lab in University of Tokyo, 2004.

[14] M. Nakano. Mission using electric propulsions. In K. Kuriki and Y. Arakawa, editors, *Introduction to Electric Propulsion*, chapter 10. University of Tokyo Press, 2003.

[15] J. Muller. Thruster options for microspacecraft: A review and evaluation of evaluation of state-of-the-art and emerging technologies. In M. M. Micci and A. D. Ketsdever, editors, *Micropropulsion for Small Spacecraft*, volume 187 of *Progress in Astronautics and Aeronautics*, chapter 3. American Institute of Aeronautics and Astornautics, Inc., 2000.

[16] A. P. London, A. H. Epstein, and J. L. Kerrebrock. High-pressure bipropellant microrocket engine. *Journal of Propulsion and Power*, **17**(4), pp.780–787, 2001.

[17] D. H. Lewis, S. W. Janson, R. B. Cohen, and E. K. Antonsson. Digital micropropulsion. *Sensors and Actuators*, **80**, pp.143–154, 2000.

[18] C. Rossi, T. D. Conto, D. Esteve, and B. Larangot. Design, fabrication and modeling of mems-based microthrusters for space application. *Smart Materials and Structures*, **10**(6), pp.1156–1162, 2001.

[19] S. Tanaka, R. Hosokawa, S. Tokudome, K. Hori, H. Saito, M. Watanabe, and M. Esashi. Mems-based solid propellant rocket array thruster. *Transactions of the Japan Society for Aeronautical and Space Sciences*, **46**(151), pp.47–51, 2003.

[20] K. L. Zhang, S. K. Chou, and S. S. Ang. Development of a solid propellant microthruster with chamber and nozzle etched on a wafer surface. *Journal of Micromechanics and Microengineering*, **14**, pp.785–792, 2004.

[21] R. G. Jahn. *Physics of Electric Propulsion*. McGraw-Hill, New York, 1968.

[22] K. Kuriki and Y. Arakawa, editors. *Introduction to Electric Propulsion*. University of Tokyo Press, 2003.

[23] A. Sengupta, J. Brophy, J. Anderson, and C. Garner. An overview of the results from the 30,000 hr life test of deep space 1 flight spare ion engine. In *40th AIAA/ASME/SAE/ASEE Joint Propulsion Conference*, Fort Lauderdale, Florida, USA, July 11-14, 2004. AIAA-2004-3608.

[24] H. Kuninaka, Y. Shimizu, T. Yamada, I. Funaki, and K. Nishiyama. Flight report during two years on hayabusa explorer propelled by microwave discharge ion engines. In *41st AIAA/ASME/SAE/ASEE Joint Propulsion Conference*, Tucson, Arizona, USA, July 10-13, 2005.

[25] C. Koppel, F. Marchandise, M. Prioul, D. Estublier, and F. Darnon. The smart-1 electric propulsion subsystem around the moon: In flight experience. In *41st AIAA/ASME/SAE/ASEE Joint Propulsion Conference*, Tucson, Arizona, USA, July 10-13, 2005. AIAA-2005-3671.

[26] H. Kuninaka, K. Nishiyama, I. Funaki, ?. Tetsuya, Y. Shimizu, and J. Kawaguchi. Asteroid rendezvous of hayabusa explorer using microwave discharge ion engines. In *29th International Electric Propulsion Conference*, Princeton university, USA, October 31 - November 4, 2005. IEPC-2005-10.

[27] C. R. Koppel and D. Estublier. The smart-1 hall effect thruster around the moon: In flight experience. In *29th International Electric Propulsion Conference*, Princeton university, USA, October 31 - November 4, 2005. IEPC-2005-119.

[28] R. L. Burton and P. J. Turchi. Pulsed plasma thruster. *Journal of Propulsion and Power*, **14**(5), pp.716–735, 1998.

[29] A. Smirnov, Y. Raitses, and N.J. Fisch. Eparametric investigation of miniaturized cylindrical and annular hall thrusters. *Journal of Applied Physics*, **92**(10), pp.5673–5679, 2002.

[30] A. Smirnov, Y. Raitses, and N.J. Fisch. The effect of magnetic field on the performance of low-power cylindrical hall thrusters. In *29th International Electric Propulsion Conference*, Princeton university, USA, October 31 - November 4, 2005. IEPC-2005-099.

[31] A. Shirasaki and H. Tahara. Plume measurements and miniaturization of the hall thrusters with circular cross-sectional discharge chambers. In *29th International Electric Propulsion Conference*, Princeton university, USA, October 31 - November 4, 2005. IEPC-2005-051.

[32] Y. Nakayama, I. Funaki, and H. Kuninaka,. A miniaturized microwave discharge ion thruster with high hole number density grid system. In *29th International Electric Propulsion Conference*, Princeton university, USA, October 31 - November 4, 2005. IEPC-2005-149.

[33] N. Yamamoto, H. Kataharada, T. Chikaoka, H. Masui, H. Nakashima, and Y. Takao. Effect of antenna configuration on thrust performance in a miniature microwave discharge ion engine. In *29th International Electric Propulsion Conference*, Princeton university, USA, October 31 - November 4, 2005. IEPC-2005-036.

[34] S. Marcuccio, A. Genovese, and M. Andrenucci. Experimental performance of field emission microthrusters. *Journal of Propulsion and Power*, **14**(5), pp.774–781, 1998.

[35] M. Tajmar, A. Genovese, and W. Steiger. Indium field emission electric propulsion microthruster experimental characterization. *Journal of Propulsion and Power*, **20**(2), pp.211–218, 2004.

[36] C. D. Hendricks Jr, R. S. Carson, J. J. Hogan, and J. M. Schneider. Photomicrography of electrically sprayed heavy particles. *AIAA Journal*, **2**(4), pp.733–737, 1964.

[37] R. J. Pfeifer and C. D. Hendricks Jr. Parametric studies of electrohydrodynamic spaying. *AIAA Journal*, **6**(3), pp.496–502, 1968.

[38] J. Stark, B. Stevens, M. Alexander, and B. Kent. Fabrication and operation of microfabricated emitters as components for a colloid thruster. *Journal of Spacecraft and Rocket*, **42**(4), pp.628–639, 2005.

[39] M. Gamero-Castano and V. Hruby. Electrospray as a source of nanoparticles for efficient colloid thrusters. *Journal of Propulsion and Power*, **17**(5), pp.977–987, 2001.

[40] R. Bocanegra, J. F. De La Mora, and M. Gamero-Castano. Ammonium electrolytes quench ion evaporation in colloidal propulsion. *Journal of Propulsion and Power*, **20**(4), pp.728–735, 2004.

[41] H. Horisawa and I. Kimura. Very low power arcjet testing. *Vacuum*, **59**, pp.106–117, 2000.

[42] H. Horisawa, H. Ashiya, and I. Kimura. Very low powr micro arc-jet thruster. *Aeronaitical and Space Sciences Japan*, **52**(610), pp.4–8, 2004. in Japanese.

[43] H. Horisawa, T. Noda, K. Onodera, and I. Kimura. Micro-arcjet: microfabrication with uv lasers and thrust characteristics. In *29th International Electric Propulsion Conference*, Princeton university, USA, October 31 - November 4, 2005. IEPC-2005-123.

[44] A. Kantrowitz. Propulsion to orbit by ground-based lasers. *Astronautics and Aeronautics*, **10**(March), pp.74–76, 1972.

[45] R. J. Glumb and H. Krier. Concepts and status of laser-supported rocket propulsion. *Journal of Spacecraft*, **21**(1), pp.70–79, 1984.

[46] A. V. Pakhomov and D. A. Gregory. Ablative laser propulsion: an old concept revisited. *AIAA Journal*, **38**(4), pp.725–727, 2000.

[47] A. V. Pakhomov, D. A. Gregory, and M. S. Thompson. Specific impulse and other characteristics of elementary propellants for ablative laser propulsion. *AIAA Journal*, **40**(11), pp.2305–2311, 2002.

[48] C. Phipps, J. Luke, and G. G. McDuff. A diode-laser-driven microthruster. In *27thInternational Electric Propulsion Conference*, Pasadena, California, USA, October 15 - 19, 2001. IEPC-01-220.

[49] C. Phipps and J. Luke. Diode laser-driven microthrusters: a new departure for micropropulsion. *AIAA Journal*, **40**(2), pp.310–318, 2002.

[50] H. Koizumi. *Study on a Micro Plasma Thruster Using a Liquid Propellant.* Master's thesis, University of Tokyo, 2001. in Japanese.

[51] H. Koizumi, A. Kakami, Y. Furuta, K. Komurasaki, and Y. Arakawa. Liquid propellant pulsed plasma thruster. In *28thInternational Electric Propulsion Conference*, Toulouse, France, March 17-21, 2003. IEPC-03-087.

[52] A. Kakami. *Study on a Pulsed Plasma Thruster Using a Liquid Propellant.* PhD thesis, University of Tokyo, 2003. in Japanese.

[53] H. Koizumi, A. Kakami, K. Komurasaki, and Y. Arakawa. Design and performance of liquid propellant pulsed plasma thruster. *Vacuum*, **73**, pp.419–425, 2004.

[54] K. W. Stark, T. Dennis, D. McHugh, and T. Williams. Design and development of a micropound extended range thrust stand (merts). Nasa technical note, National Aeronautics and Space Administration, August, 1971. NASA TN D-7029.

[55] T. W. Haag. Thrust stand for pulsed plasma thruster. *Review of Scientific Instruments*, **68**(5), pp.2060–2067, 1997.

[56] E. A. Cubbin, J. K. Ziemer, E. Y. Choueiri, and R. G. Jahn. Pulsed thrust measurements using laser interferometry. *Review of Scientific Instruments*, **68**(6), pp.2339–2346, 1997.

[57] M. J. Wilson, S. S. Bushman, and R. L. Burton. A compact thrust stand for pulsed plasma thrusters. In *25th International Electric Propulsion Conference*, Cleveland, Ohio, USA, Auguts 24-28, 1997. IEPC-97-122.

[58] M. Gamero and V. Hruby. A torsional balance that resolves sub-micro-newton forces. In *27th International Electric Propulsion Conference*, Pasadena, California, USA, October 15-19, 2001. IEPC-01-235.

[59] A. J. Jamison, A. D. Katsdever, and E. P. Muntz. Accurate measurement of nano-newton thrust for micropropulsion system characterization. In *27th International Electric Propulsion Conference*, Pasadena, California, USA, October 15-19, 2001. IEPC-01-236.

[60] J. K. Ziemer. Performance measurement using a sub-micronewton resolution thrust stand. In *27th International Electric Propulsion Conference*, Pasadena, California, USA, October 15-19, 2001. IEPC-01-238.

[61] D.E. Newland. *Random Vibrations, Spectral and Wavelet Analysis.* Longman, Harlow, 3rd edition, 1993.

[62] E. N. Sobol. *Phase Transformations and Ablation in Laser-Treated Solids.* Wiley, New York, 1995.

[63] S. I. Anisimov and B. S. Luk'yanchuk. Selected problems of laser ablation theory. *Physics-Uspekhi*, **45**(3), pp.293–324, 2002.

[64] R. K. Singh and J. Narayan. Pulsed-laser evaporation technique for deposition of thin films: physics and theoretical model. *Physical Review B*, **41**(13), pp.8843–8859, 1990.

[65] G. H. Pettit and R. Sauerbrey. Pulsed ultraviolet laser ablation. *Applied Physics A*, **56**, pp.51–63, 1993.

[66] G. D. Mahan, H. S. Cole, Y. S. Liu, and H. R. Philipp. Theory of polymer ablation. *Applied physics letters*, **53**(24), pp.2377–2379, 1988.

[67] N. Bityurin, N. Arnold, B. Luk'yanchuk, and D. Bauerle. Bulk model of laser ablation of polymers. *Applide Surface Science*, **127**, pp.164–170, 1998.

[68] N. K. Bourne. On the laser ignition and initiation of explosives. *Proceedings of the Royal Society of London. Ser. A, Mathematical and physical sciences*, **457**(2010), pp.1401–1426, 2001.

[69] L. D. Yong and F. Lui. Radiative ignition of pyrotechnics: Effect of wavelength on ignition threshold. *Propellants, Explosives, Pyrotechnics*, **23**(6), pp.328–332, 1998.

[70] C. Zanotti and P. Giuliani. Composite propellant ignition and extinction by co_2 laser at subatmosheric pressure. *Propellants, Explosives, Pyrotechnics*, **23**(5), pp.254–259, 1998.

[71] F. Opdebeck and P. Gillard. Optimization of interface conditions in the case of laser diode ignition of pyrotechnic mixtures. *Propellants, Explosives, Pyrotechnics*, **26**, pp.196–200, 2001.

[72] F. Opdebeck, P. Gillard, and E. Radenac. Influence of interface conditions of laser diode ignition of pyrotechnic mixtures: Application to the design of an ignition device. *International Journal of Thermal Sciences*, **42**, pp.47–56, 2003.

[73] S. R. Ahmad and D. A. Russell. Studies into laser ignition of unconfined propellants. *Propellants, Explosives, Pyrotechnics*, **26**, pp.235–245, 2001.

[74] C. Phipps, J. Luke, T. Lippert, M. Hauer, and A. Wokaun. Micropropulsion using a laser ablation jet. *Journal of Propulsion and Power*, **20**(6), pp.1000–1010, 2004.

[75] T. Venkatesan, X. D. Wu, A. Inam, and J. B. Wachtman. Observation of two distinct components during pulsed laser deposition of high tc superconducting films. *Applied Physics Letters*, **52**(14), pp.1193–1195, 1988.

[76] L. V. Zhigilei. Dynamics of the plume formation and parameters of the ejected clusters in short-pulse laser ablation. *Applied Physics A*, **76**, pp.339–350, 2003.

[77] C.S.C. Castro, A.C.P. Azevedo, E.E.C. Monteiro, R. R. Phinho, and G.G.B. Souza. Gas emission from chlorinated polymers induced by synchrotron radiation. *Polymer Degradation and Stability*, **71**, pp.233–242, 2001.

[78] R. Miranda, J. Yang, C. Roy, and C. Vasile. Vacuum pyrolysis of pvc I. kinetic study. *Polymer Degradation and Stability*, **64**, pp.127–144, 1999.

[79] F. Kokai, Y. Koga, Y. Kakudate, M. Kawaguchi, S. Fujiwara, M.Kubota, and K. Fukuda. Laser-ionization mass-spectrometric studies on laser ablation of a nitrogen-rich polymer at 532 nm and 1064 nm. *Applied Physics A*, **59**, pp.299–304, 1994.

[80] H. S. Carslaw and J. C. Jaeger. *Conduction of Heat in Solids.* Clarendon Press, Oxford, 2^{nd} edition, 1986.

[81] Nihon Kagakukai, editor. *Kagaku Binran*, volume 2. Maruzen, 2004. in Japanese.

[82] N. Kubota. *Engineering of Rocket Combustion.* Nikkan Kogyo Shinbun, Ltd., 1995. in Japanese) .

[83] Yutaka Yano. Condensed phase reaction of boron with potassium nitrate. *Propellants, Explosives, Pyrotechnics*, **14**, pp.187–189, 1989.

[84] Yutaka Yano. Boron combustion (I) solid phase reaction of boron/potassium. *Technical report of Technical Research and Development Institute Technical report*, **1033**, pp.1–6, 1988. in Japanese.

[85] Yutaka Yano. Boron combustion (II) burning rate characteristics of boron. *Technical report of Technical Research and Development Institute Technical report*, **1026**, pp.1–7, 1988. in Japanese.

[86] Yutaka Yano. Burning rate characteristics of b/kno_3 mixture. *Journal of the Industrial Explosives Society, Japan*, **49**(2), pp.129–133, 1988. in Japanese.

[87] M. Kobayashi, H. Maekawa, H. Nakamura, and Y. Kondou. Calculation of the mean thermal conductivity of heterogenious solid mixture with the voronoi-polyhedron element method. *Transactions of the Japan Society of Mechanical Engineers. B*, **57**(537), pp.271–277, 1991. in Japanese.

[88] Yoshio Yuge. Three-dimensional site percolation problem and effective-medium theory: A computer study. *Journal of Statistical Physics*, **16**(4), pp.339–347, 1977.

[89] S. C. Cheng and R. I. Vachon. The prediction of the thermal conductivity of two and three phase solid heterogeneous mixtures. *International journal of heat and mass transfer*, **12**, pp.249–264, 1969.

[90] W. Woodside. Calculation of the thermal conductivity of porous media. *Canadian journal of physics*, **36**, pp.815–823, 1958.

[91] H.W. Russel. Principles of heat flow in porous insulators. *Journal of the American Ceramic Society*, **18**, pp.1–5, 1935.

[92] D. Ding. A study on the ignition of boron/potassium nitrate mixture. *Science and Technology of Energetic Materials: journal of the Japan Explosive Society*, **67**(1), pp.23–27, 2006.

[93] K. Miyata and N. kubota. Boron combustion (IV) combustion of boron/potassium nitrate and boron/potassium perchlorate. *Technical report of Technical Research and Development Institute Technical report*, pages 1–12, 1991. in Japanese.

[94] K. Hasue and H. Tamura. Combustion aspects of the consolidated mixtures of boron and potassium nitrate at cryogenic temperatures. *Journal of the Japan Explosives Society: explosion, explosives and pyrotechnics*, **58**(6), pp.252–257, 1997. in Japanese.

[95] C. Zakrzwski, S. Benson, P. Sanneman, and A. Hoskins. On-orbit testing of the eo-1 pulsed plasma thruster. In *38th AIAA/ASME/SAE/ASEE Joint Propulsion Conference*, Indianapolis, Indiana, USA, July 7-10, 2002. AIAA 2002-3973.

[96] H. Takegahara, M. Igarashi, N. Kumagai, K. Sato, and K. Tamura. Evaluation of pulsed plasma thruster system for μ-lab sat II. In *27th International Electric Propulsion Conference*, Pasadena, California, USA, Octorber 15-19, 2001. IEPC-01-153.

[97] R. J. Vondra. The mit lincoln laboratory ppt, 1976. AIAA76-998.

[98] G. G. Spanjers, K. A. McFall, F. S. Gulczinski III, and R. A. Spores. Investigation of propellant inefficiencies in a pulsed plasma thruster. In *32nd AIAA/ASME/SAE/ASEE Joint Propulsion Conference*, Lake Buena Vista, Florida, USA, 1996. July 1-3.

[99] P. G. Mikellides and P. J. Turchi. Modeling of late-time ablation in teflon pulsed plasma thrusters. In *32nd AIAA/ASME/SAE/ASEE Joint Propulsion Conference*, Lake Buena Vista, Florida, USA, 1996. July 1-3.

[100] G. G. Spanjers, J. S. Lotspeich, K. A. McFall, and A. Spores. Propellant losses because of particulate emission in a pulsed plasma thruster. *Journal of Propulsion and Power*, **14**(4), pp.554–559, 1998.

[101] D. J. Palumbo and W. J. Guman. Effects of propellant and electrode geometry on pulsed ablative plasma thruster performance. *Journal of Spacecraft*, **13**(3), pp.163–167, 1976.

[102] G. Aston and C. Pless. Ignitor plug operation in a pulsed plasma thruster. *Journal of Spacecraft*, **19**(3), pp.250–256, 1982.

[103] R. M. Myers and A. Arrington. Pulsed plasma thruster contamination. In *32nd AIAA/ASME/SAE/ASEE Joint Propulsion Conference*, Lake Buena Vista, Florida, USA, 1996. July 1-3.

[104] F. Gluczinski, M. Dulligan, J. Lake, and G. G. Spangers. Micropropulsion research at afrl. In *36th AIAA/ASME/SAE/ASEE Joint Propulsion Conference*, Huntsville, Alabama, USA, 2000. July 16-19.

[105] M. Keidar and D. I. Boyd. Analysis of teflon surface charring and near field plume of a micro-pulsed plasma thruster. In *27th International Electric Propulsion Conference*, Pasadena, California, USA, 2001. Octorber 15-19.

[106] C.A. Scharlemann and T.M. York. Investigation of a ppt utilizing water as component propellant. In *28th International Electric Propulsion Conference*, Toulouse, France, March 17-21, 2003. IEPC 03-112.

[107] C.A. Scharlemann and T.M. York. Pulsed plasma thruster using water propellant, parti: investigation of thrust behavior and mechanism. In *39nd AIAA/ASME/SAE/ASEE Joint Propulsion Conference*, Huntsville, Alabama, USA, July 20-23, 2003. AIAA-2003-5022.

[108] C.A. Scharlemann and T.M. York. Pulsed plasma thruster using water propellant, partii: thruster operation and performance evaluation. In *39nd AIAA/ASME/SAE/ASEE Joint Propulsion Conference*, Huntsville, Alabama, USA, July 20-23, 2003. AIAA-2003-5023.

[109] D.H. Simon and H.B. Land III. Micro pulsed plasma thruster technology development. In *40nd AIAA/ASME/SAE/ASEE Joint Propulsion Conference*, Fort Lauderdale, Florida, USA, July 12-14, 2004. AIAA-2004-3622.

[110] A. Solbes and R. J. Vondra. Performance study of a solid fuel-pulsed electric microthruster. *Journal of Spacecraft*, **10**(6), pp.406–410, 1973.

[111] R.L. Burton, F. Rysanek, E.A. Antonsen, M.J. Wilson, and S. S. Bushman. Pulsed plasma thruster performance for microspacecraft propulsion. In M.M. Micci and A.D. Ketsdever, editors, *Micropropulsion for Small Spacecraft*, volume 187 of *Progress in Astronautics and Aeronautics*, chapter 13. American Institute of Aeronautics and Astornautics, Inc., 2000.

[112] S. Bohm, G.J. Burger, M.T. Korthors, and F. Roseboom. A micromachined silicon valve driven by a miniature bi-stable electro-magnetic actuator. *Sensors and Actuators*, **80**, pp.77–83, 2000.

[113] Y. Furuta. *Study on the Liquid Injection and Plsma Discharge in a Liquid Propellant Pulsed Plasma Thruster.* Master's thesis, University of Tokyo, 2003. in Japanese.

[114] H.L. Anderson, editor. *Physics Vade Mecum.* American Institute of Physics, New York, 1981.

[115] C. D. Rayburn, M. E. Campbell, and A. T. Mattick. Pulsed plasma thruster system for microsatellites. *Journal of Spacecraft and Rocket*, **42**(1), pp.161–170, 2005.

[116] W. J. Guman. Solid propellant pulsed plasma propulsion system design. *Journal of Spacecraft*, **13**(1), pp.96–100, 1976.

[117] R. J. Vondra and K. I. Thomassen. Performance improvements in solid fuel microthrusters. *Journal of Spacecraft*, **9**(10), pp.738–742, 1972.

[118] A.B. Cambel, editor. *Plasma Physics and Magnetofluid-Mechanics*. McGraw-Hill, New York, 1963.

[119] R.J. Rosa. Physical principles of magnetohydrodynamic power generation. *The Phyics of Fluids*, **4**(2), pp.182–194, 1961.

[120] ULVAC, Inc., editor. *Vacuum Handbook*. Ohm-sha, Tokyo, 1992. (in Japanese) .

[121] S. Kitabe, Y. Kobayashi, Y. Nagasaka, and A. Nagashima. Thermal conductivity measurement of molten salts by the transient hot-wire method. *Transactions of the Japan Society of Mechanical Engineers. B*, **55**(516), pp.2411–2416, 1989.

Acknowledgments

During conducting this dissertation, I have been supported by many people. In order to show my best gratitude, I would like to express the acknowledgments in my mother language.

本研究は多くの方々のご支援をいただき完成させることができました．ここに全ての皆様に深く感謝の意を示します．

はじめに，本研究を行う機会を与えていただいた荒川義博教授に深く感謝いたします．折りあるたびに交わしていただいた先生との議論の中で，推進機およびプラズマに対する物理的な解釈から直感的なイメージにいたるまで研究に関する多くのことを学ばせていただきました．なかでも，新しい研究テーマに対する先見の目には驚かされるばかりでした．幅広く分野をみつめ，常に新しい研究を探していく姿勢をいつまでも見習っていきたいと思います．直接の研究の他にも，国内外における会議への出席，新しい真空装置の構築，新規実験装置の購入，予算の申請，３年生の見学旅行への同伴，など多くの貴重な経験をさせていただきました．これまで，自由に好きな研究を行う機会を与えていただき，研究を行う喜びを失わせないまま研究をつづけさせていただいたことを大変嬉しく思います．成功だけではなく数多くの失敗しながらも様々なことを学びつづけてきたこの６年間は，今後，研究者として人生を歩んでいく上で大きな糧になることと思います．小紫公也助教授には輪講の際に毎回するどい指示・質問をいただいたり，多くのことを学ばせていただきました．小紫研究室の学生に接する厳しくも真摯な研究姿勢は，大きな刺激となると共に研究者，指導者として見習いたいと思います．また，共に行動していただいた学会で楽しい時間を過ごさせていただことや，英語雑誌への投稿の際に原稿チェックをしていただいたこと等，深く感謝しています．中須賀真一教授には，荒川研と中須賀研によるマイクロスラスタミーティングにおいて，衛星側からの的確な要求および助言をいだただきました．レーザー着火モードのアイディアが生まれたこのミーティングは，極めて有意義なものだったと感謝しております．小林さんには研究物品の購入に関わる多くの手続きをしていただき感謝しております．

研究室の中で一緒に過ごし研究した皆様にも多くのことでお世話になりました．はじめに PPT 班の先輩としてご指導いただいた各務さんに感謝いたします．修士一年の何も知らない自分に，真空知識，機械工作，そして電気回路と多くの事をお教えしていただき大変感謝しています．なかでも，電気・電子回路に関する知識の広さ深さには，カルチャーショックとも言うべき驚きと多大な尊敬の念を感じずにはいられませんでした．細田さんには頼りになる先輩として研究だけでなく，いろいろとお世話になりました．自分だけでなく研究室全体の兄貴分として荒川・小紫研を引っ張っていただいたと感じています．学部四年生の際に荒川研に見学にきた自分に優しく接していただいたことは忘れられません．山本さん，森さんにも多くのことを教わると同時に，一つ上の研究者として大きな刺激をいただきました．山本さんには，その幅広い知識から同じ電気推進に関す

る先輩研究者として実験装置・プラズマに関する多くのご指導を賜りました．また，その様々な細かい気遣いによって，研究室の皆が十分に研究に取り組むことができていたのだと思っています．森さんには同じ二階実験室で実験をする先輩として大変お世話になりました．輪講や議論の際にみせる鋭い洞察と思考は，研究者としてお手本にしたいと感じています．実験室では陣取り合戦を繰り広げたりと迷惑・小生意気な自分でしたが，優しく楽しく接していただき大変感謝しております．福田くん，上原くんとは研究だけでなく個人的なことを相談したりと，一緒に楽しい時間を過ごさせてもらいましたいました．上田くんとは，数値計算の話を多くしたおかげで，物理的洞察の視点を大きく広げることができたと思います．

PPT 班で研究を共にした後輩の皆様に感謝の意を示します．しっかりものの吉村君，いつでもにぎやかな古田君，焼酎大好き高柳君，たこ焼きの上手な川添さん，何事もクールにこなす野地君，熱い研究意欲をもつ瀧口君，執念で卒論を書いた杉山君．先輩としてを指導をしてきましたが，実際にはその中で自分の方が多くのことを学んでこれたのだたと感じています．一緒に研究を行うことができ大変嬉しく思います．特に古田君には，はじめての後輩をもち右往左往する自分についてきてくれて，研究だけではなく遊びも含めて一緒に楽しく過ごせたことを嬉しく思います．

レーザーマイクロスラスタにおいて共に研究した中野さん，井上君，小島君，久米君に感謝の意を示します．航空高専において行った実験では，時折折りに中野さんから実験，計算，宇宙開発そして経済にいたるまで様々なお話を聞き大変勉強になりました．井上君と三人で何度もかわした熱い議論は大変貴重なものだったと感じています．そして，井上君にはレーザーマイクロスラスタおよび ICP カソードの共同テーマはもちろんのこと，研究全般から私生活まで大変お世話になりました．井上君がきてからの四年間の中で，研究から社会問題に至るまで数多くの議論を交わしてきましたが，どれもこれまで得たことのない楽しく充実したものでした．長いようで短い期間でしたが，どれだけのものを培うことができたか測り知れません．しばしば無茶を言ったりやったりしてきた自分ですが，公私ともに楽しく付き合っていただき誠に感謝しています．また，レーザー着火を成功させる鍵となった B/KNO_3 ペレットを提供していただき実験にも協力していただいた日油技研工業の渡辺さんに感謝致します．

最後に，自分をここまで育ててくれた両親，および支援してくれた親戚に感謝の意を示します．これまで，好き勝手に進路を選ぶ自分のわがままを快く聞き入れ，そしていつでも温かく支え見守っていてくれた両親がいたからこそ今日の自分があります．幼少より多くの興味深い話を聞かせてくれ科学の道に導いてくれた父，どんなつらいことがあっても優しく接し支えてくれた母に，言葉では表せないほどの感謝の念を感じています．俊昌とは，兄として不甲斐ない自分でしたが，楽しく健やかに共に成長できたことを嬉しく思います．

昨年はじめに他界した祖父が父の博士論文をこの上なく誇りにしていたという話を知人から聞きました．願わくば本論文が父母にとってそのような誇りとなりますよう，本論文を父母に捧げます．

2006 年 5 月 16 日

小泉　宏之

Appendix A

Force transducer discharge

Discharge constant

A piezo type force transducer has its discharge constant. A piezoactuator used as a force detector can be assumed a capacitance, and the stored charge is changed by the exerted force. Discharge constant is a period in which the charge discharges. Typical pulse response of a piezo type force transducer is shown in Fig. A.1. When

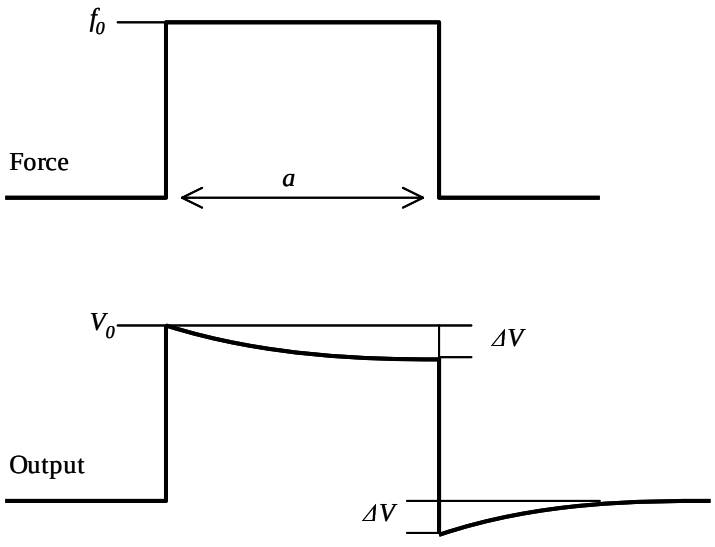

Figure A.1: Pulse response of a piezo force transducer.

constant force is applied, its output exponentially decreases, and, after the pulse, output is shifted to not zero but -ΔV, corresponding to the decrease of the output

at the end of the force pulse. ΔV is given by

$$\Delta V = V_0 \left(1 - \exp(-t_0/\tau)\right) \tag{A.1}$$

We consider impulse response to obtain the response for arbitrary waveform. For a very shot-time pulse, the voltage drop ΔV is given by

$$\Delta V \cong V_0 t_0/\tau \tag{A.2}$$

, and the tail after the impulse is

$$V_{tail}(t; t_0) \cong -V_0 \frac{t_0}{\tau} e^{(t-t_0+\Delta t)/\tau} \tag{A.3}$$

At $t = t$, there is a residual voltage $V(t; t_0)$ from an impulse response of $t = t_0$. Therefore, an arbitrary waveform force $f(t)$ has an accumulated residual voltage at $t = t$

$$\begin{aligned} V_{\text{res}} &= -\sum_{t_0<t} f(t_0) \frac{\Delta t}{\tau} e^{(t-t_0+\Delta t)/\tau} && \text{(A.4)} \\ &= -\int_0^t f(t_0) \frac{1}{\tau} e^{(t-t_0)/\tau} dt_0 \quad (\Delta t \to 0) && \text{(A.5)} \\ &= -\frac{1}{\tau} e^{-t/\tau} \int_0^t f(t_0) e^{t_0/\tau} dt_0 && \text{(A.6)} \end{aligned}$$

As a result, the actual output voltage $V^*(t)$ against the ideal output voltage $V(t)$ is

$$V^*(t) = V(t) - \frac{1}{\tau} e^{-t/\tau} \int_0^t f(t_0) e^{t_0/\tau} dt_0 \tag{A.7}$$

Inverse transform

Multiplying $\exp(t/\tau)$ on the both side of Eq. A.7 and differentiating it, we obtain

$$\frac{dV}{dt} = \frac{dV^*}{dt} + \frac{V^*(t)}{\tau} \tag{A.8}$$

Again integrating this equation,

$$V(t) = V^*(t) + \frac{1}{\tau} \int_0^t V^*(s) ds \tag{A.9}$$

From this equation, we can calculate the ideal output voltage $V(t)$ from $V^*(t)$

Application to the actual ouput from FT.

Figure A.2 shows the measured output voltage of force transducer, and the corrected voltage according to the Eq. (A.9). Here, we have to know the discharge constant to perform the inverse transform of Eq.(A.9). In the data sheet of our force transducer, however, discharge constant was described only as "more than 1 s". Hence we need more accurate description about the discharge constant. The measured output by the impact of calibration hammer shows off set after the impact. This off set would causes the discharge of piezoelectric element, which gradually decrease according to the discharge constant of more than 1 s. The ideal force by impact hammer must have zero at this point. Therefore if we carry out inverse transform using an appropriate discharge constant, the obtained waveform would show no off set. I determined such discharge constant that the inversely transformed waveform has zero after the impact, using 7 data during 20 data we measured. As a result I obtained the discharge constant as 1.8 s, and all data were corrected using this time constant and the impulse was calculated.

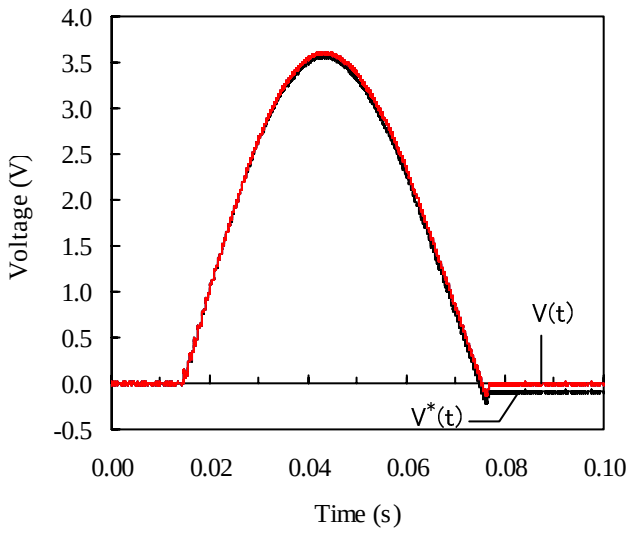

Figure A.2: Measured output voltage of the force transducer and its modified output according to Eq. A.9.

Appendix B

Vacuum Facilities

UT space chamber

UT (University of Tokyo) space chamber has the volume of 1.0-m-diam and 1.5-m-long. Figure B.1 shows the picture of that chamber. The chamber is made of stainless steel and evacuated using two stage pumps: rotary pump and turbo molecular pump. The rotary pump is VD-401 from ULVAC, Inc. which has the

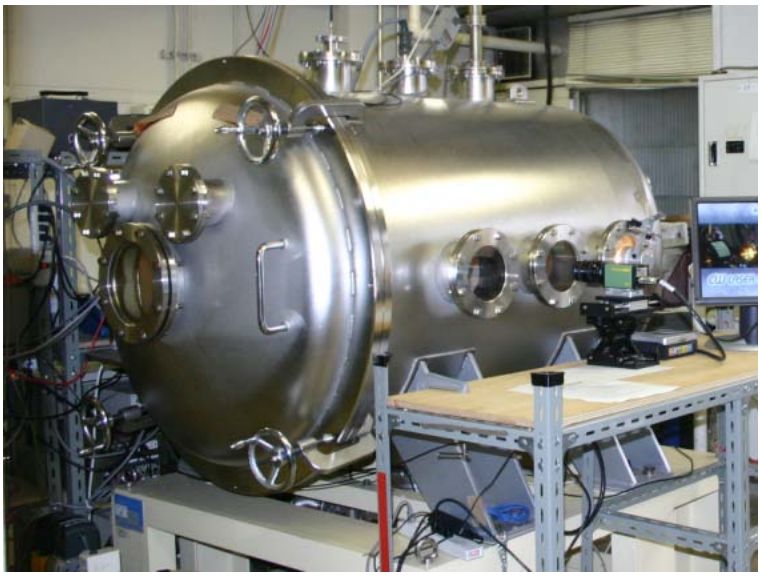

Figure B.1: Picture of UT space chamber.

pumping speed of 670 L/min. The turbo molecular pump is TMP-403M from Shimadzu Corporation which has the pumping speed of 340 and 420 L/s for H_2

and N_2 respectively. The pressure can be evacuated down to 5×10^{-6} Torr with no thruster in it. The pressure was measured using a Pirani gauge for $0.1 \sim 760$ Torr and an ionization vacuum gauge under 10^{-3} Torr. Fig. B.2 shows the schematic diagram of the evacuating system. That chamber has three electrical ports to

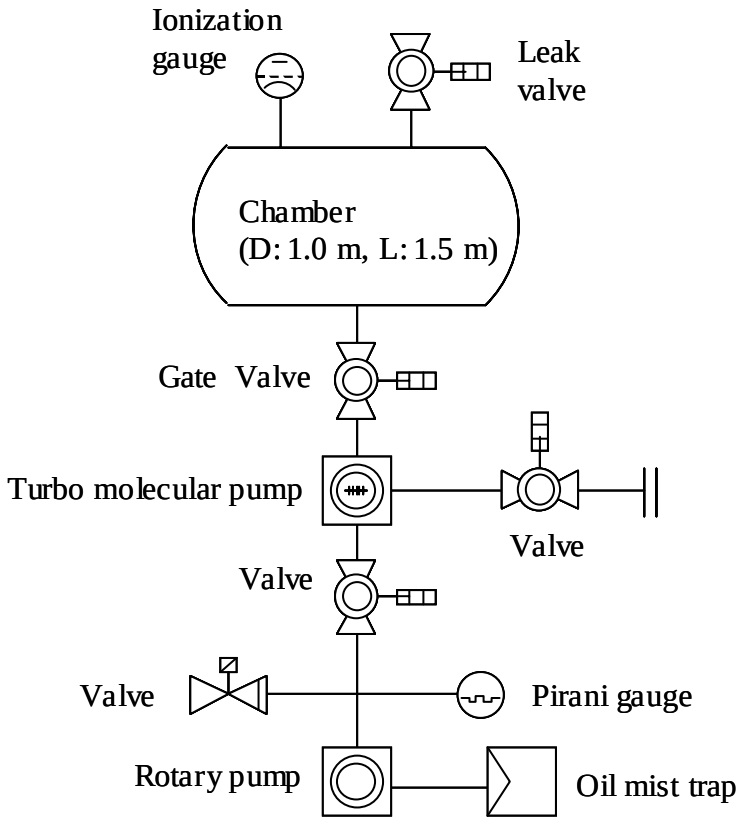

Figure B.2: Schematic diagram of the evacuating system of UT space chamber.

introduce electrical feed lines into the chamber. The specifications of the three ports are shown in Table B.1, B.2, and B.3.

TMAE cubic space chamber

TMAE (Tokyo Metropolitan of Aeronautical Engineering) chamber has the volume of a 0.9-m-cubic. The chamber is also made of stainless steel and evacuated using two stage pumps: rotary pump and turbo molecular pump. The turbo molecular pump is TG220F from Osaka Vacuum, Ltd. and has the pumping speed of 100 and 220 L/s for H_2 and N_2 respectively. The pressure can be evacuated down to

Table B.1: Specifications of electrical ports on UT space chamber; 6 inch (DN150) side port for high voltage.

Manufacurer	Greentec Co., Ltd.	
Product Number	804B4275-14	802C6530
Number of conductors	1	1
Number of plugs	2	2
Maximum voltage	12 kV	30 kV
Maximum current	30 A	2 A

Table B.2: Specifications of electrical ports on UT space chamber; 6 inch (DN150) side port for low voltage.

Manufacurer	Greentec Co., Ltd.	
Product Number	9999-10	BNC-JJ
Number of conductors	10	1
Number of plugs	2	2
Maximum voltage	1 kV	-
Maximum current	3 A	-

Table B.3: Specifications of electrical ports on UT space chamber; 4 inch (DN100) top port.

Manufacurer	Greentec Co., Ltd.	CeramaTec NA Corporation
Product Number	9999-20	9216-08-W
Number of conductors	20	4
Number of plugs	1	2
Maximum voltage	1 kV	6 kV
Maximum current	3 A	27 A

1×10^{-4} Torr with no thruster in it. The inner pressure was measured using a compact fullrange^{TM} CC gauge: PKR 251 from Pfeiffer Vacuum GmbH. It contains two types of vacuum gauge and can measure the pressure from the atmosphere to high vacuum. In high vacuum, cold cathode ionization vacuum gauge works. That chamber has two electrical ports, which are the same as those shown in Table B.1 and B.2

Figure B.3: Picture of TMAE cubic space chamber.

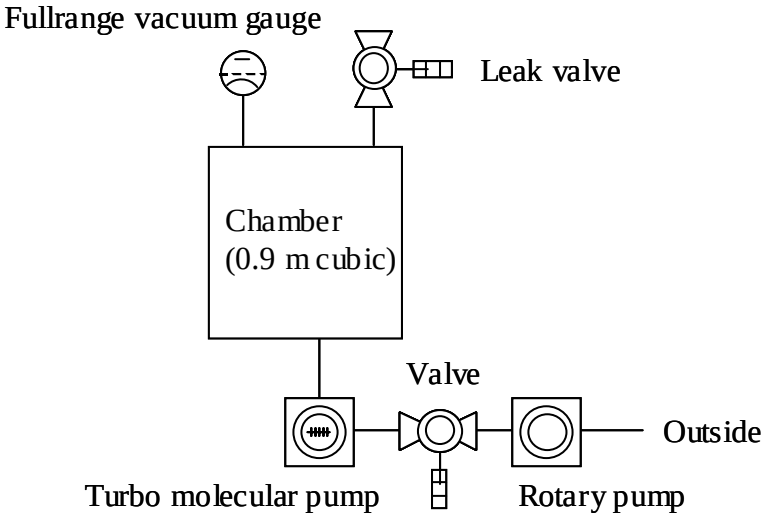

Figure B.4: Schematic diagram of the evacuating system of TMAE space chamber.

Appendix C

Amplitudes of Random Process Noise

Amplitudes of periodic random process noise is related to the power spectrum and corelation function. Arbitrary function $x(t)$ with a finite period of $(-l/2, l/2)$ can be expressed using the Fourier serie

$$x(t) = \sum_{n=1}^{\infty} (a_n \cos \omega_n t + b_n \sin \omega_n t) \quad , \quad \omega_n = \frac{2n\pi}{l} \tag{C.1}$$

$$\begin{cases} a_n = \dfrac{2}{l} \displaystyle\int_{-2/l}^{2/l} x(t) \cos \omega_n t dt \\ \\ b_n = \dfrac{2}{l} \displaystyle\int_{-2/l}^{2/l} x(t) \sin \omega_n t dt \end{cases} \tag{C.2}$$

Here we will obtaine the ensembel average of the squared amplitude, A_n^2.

$$\begin{aligned} A_n^2 &= a_n^2 + b_n^2 \\ &= \frac{4}{l^2} \int_{-2/l}^{2/l} dt \int_{-2/l}^{2/l} dt' \Big[x(t)x(t') \left\{ \cos \omega_n t \cos \omega_n t' + \sin \omega_n t \sin \omega_n t' \right\} \Big] \\ &= \frac{4}{l^2} \int_{-2/l}^{2/l} dt \int_{-2/l}^{2/l} dt' \Big[x(t)x(t') \cos \omega_n (t - t') \Big], \end{aligned} \tag{C.3}$$

and

$$\begin{aligned} < A_n^2 > &= \frac{4}{l^2} \int_{-2/l}^{2/l} dt \int_{-2/l}^{2/l} dt' \Big[< x(t)x(t') > \cos \omega_n (t - t') \Big] \\ &= \frac{4}{l^2} \int_{-2/l}^{2/l} dt \int_{-2/l-t}^{2/l-t} d\tau \Big[R(\tau) \cos \omega_n \tau \Big] \end{aligned}$$

$$
\begin{aligned}
&= \frac{4}{l^2}\int_0^l R(\tau)\cos\omega_n\tau(l-\tau)\ d\tau + \frac{4}{l^2}\int_{-l}^0 R(\tau)\cos\omega_n\tau(l+\tau)\ d\tau \\
&= \frac{4}{l^2}\int_{-l}^l R(\tau)\cos\omega_n\tau(l-|\tau|)\ d\tau \\
&= \frac{4}{l}\int_{-l}^l R(\tau)\cos\omega_n\tau\ d\tau \underbrace{-\frac{4}{l^2}\int_{-l}^l R(\tau)\tau\cos\omega_n\tau\ d\tau}_{I_R(1/l^2)} \qquad \text{(C.4)}
\end{aligned}
$$

where the definition of the corelation function, $R(t) \equiv < x(t)x(t') >$, was used. Assuming that the integral of socond term converges and has a finite value,

$$< A_n^2 >= \frac{4}{l}\int_{-l}^l R(\tau)\cos\omega_n\tau\ d\tau + I_R(1/l^2) \qquad \text{(C.5)}$$

Hence, in the limit of $l \to \infty$,

$$< A_n^2 >= \frac{4}{l}\int_{-\infty}^{\infty} R(\tau)\cos\omega_n\tau\ d\tau \qquad \text{(C.6)}$$

Using the above epression, summation of the amplitude weighted by an arbitrary function can be converted to the integral of the power spectrum.

$$
\begin{aligned}
\sum_{n=1}^{\infty} < A_n^2 > f(\omega_n) &= \sum_{n=1}^{\infty}\left[\frac{2}{\pi}\Delta\omega\int_{-l}^l R(\tau)\cos\omega_n\tau\ d\tau + I_R(\Delta\omega^2)\right]^2 f(\omega_n) \\
&= \int_0^{\infty} d\omega\left[\frac{2}{\pi}f(\omega)\int_{-\infty}^{\infty} R(\tau)\cos\omega\tau\ d\tau\right] \qquad (l\to\infty) \\
&= 2\int_{-\infty}^{\infty} f(\omega)S(\omega)\ d\omega \qquad \text{(C.7)}
\end{aligned}
$$

where,

$$
\begin{aligned}
S(\omega) &= \frac{1}{2\pi}\int_{-\infty}^{\infty} R(\tau)e^{-i\omega\tau}\ d\tau \qquad \text{(C.8)} \\
&= \frac{1}{2\pi}\int_{-\infty}^{\infty} R(\tau)\cos\omega\tau\ d\tau \qquad \text{(C.9)}
\end{aligned}
$$

was used.

Appendix D

Thermal Conductivity of Mixture Solid

Predictions of the thermal conductivity of heterogeneous solid mixture have been developed by several authors [87, 88, 89, 90, 91]. To date, however, no general equation exisits to predict it. The thermal conductivity of heterogeneous solid mixture depends on the phase geometry as well as the on the properties of materials. Here, several predictions are summerized.

Nomenclature

p: volume fraction of mixed solid
k_{c}: thermal conductivity of continuous phase
k_{d}: thermal conductivity of discontinuous phase
k_{m}: thermal conductivity of mixed phase
λ : ratio of thermal conductivities of discontinuous phase $(k_{\mathrm{d}}/k_{\mathrm{c}})$
λ_{m} : ratio of thermal conductivities of mixed solid$(k_{\mathrm{m}}/k_{\mathrm{c}})$

Maxwell

$$\lambda_{\mathrm{m}} = \frac{\lambda + 2 - 2p(1-\lambda)}{\lambda + 2 + p(1-\lambda)} \tag{D.1}$$

which is derived from the electrostatic field problem on the dielectric with porus $(p \ll 1)$.

Kobayashi et. al [87] conducted the numerical analysis in heterogeneous solid mixture with the voronoi-polyhedron element method, and derived the following

empirical equation

$$\lambda_{\rm m} = \frac{C_1\lambda_1 + C_2\lambda_2 + C_3\lambda_3}{C_1 + C_2 + C_3} \tag{D.2}$$

$$F = \ln\left(\frac{\lambda + 1/\lambda}{2}\right) \quad , \quad G = 5(1-2p)((1-p)p)^{0.75} \ \ln\lambda + 1$$
$$\lambda_1 = \frac{\lambda}{(1-p)\lambda + p} \quad , \quad C_1 = Fp^{1.1}$$
$$\lambda_2 = p\lambda^{0.75} + (1-p)^{1.25} \quad , \quad C_2 = 0.9F(1-p)^{1.5}$$
$$\lambda_3 = \lambda^p \quad , \quad C_3 = p\lambda^{(2-3p)/2}$$

Woodside [90]

$$\lambda_{\rm m} = \left\{\left(\frac{a^1 - 1}{2a}\ln\left(\frac{a+1}{a-1}\right) - 1\right)R + 1\right\}^{-1} \tag{D.3}$$
$$R = \left(\frac{6p}{\pi}\right)^{1/3} \quad , \quad a = \sqrt{\frac{4}{\pi(\lambda-1)R^2} + 1}$$

Russel [91]

$$\lambda_{\rm m} = \frac{\lambda p^{2/3} + (1 - p^{2/3})}{\lambda(p^{2/3} - p) + (1 - p^{2/3} + p)} \tag{D.4}$$

Yuge [88]

$$\lambda_{\rm m} = \frac{d_x + \sqrt{d_x^2 + 8d_1d_2}}{4} \tag{D.5}$$
$$d_1 = (1-p) + pd_0 d_0 = \frac{2\lambda}{\lambda + 1}$$
$$d_2 = p\lambda + (1-p)d_0 \quad , \quad d_x = (2-3p)d_1 + (3p-1)d_2$$

Cheng and Vachon [89]

$$\lambda_{\rm m} = \left\{\frac{1}{\alpha\beta}\ln\left(\frac{2\alpha + \beta B}{2\alpha - \beta B}\right) + 1 - B\right\}^{-1} \tag{D.6}$$
$$B = \sqrt{3p/2} \quad ,$$
$$\alpha = \sqrt{(\lambda-1)B + 1} \quad , \quad \beta = \sqrt{4|\lambda - 1| + B}$$

Boron potassium nitrate that is a pyrotechnic used in this study is mixture of boron in potassium nitrate. The thermal conductivity of boron is listed in Table D.1. It largely depdends on the temperature from 27.6 to 6.29 W/mK correspoindg temperature of 300 to 1000 K. On the other hand, the thermal conductivity of

molten potassium nitrate remained around 0.4 $\sim$ 0.5 W/mK [121]. The diameter of the mixed boron particle was less than 1.0 μm and the weight fraction of 0.30 and the volume fractionof 0.27. Due to its large difference of the conductivities and not small volume fraction, the accurate prediciton of the B/KNO_3 pellet is difficult.

Table D.1: Thermal conductivity of boron.

Temperature (K)	Thermal conductivity (W/mK)
300	27.6
400	18.7
700	9.41
1000	6.29

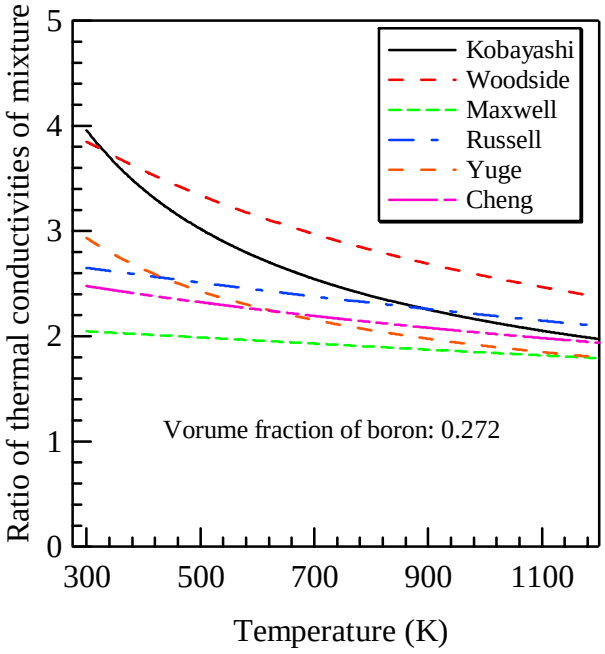

Figure D.1: Thermal conductivity of boron-mixed-KNO_3, temperature dependence

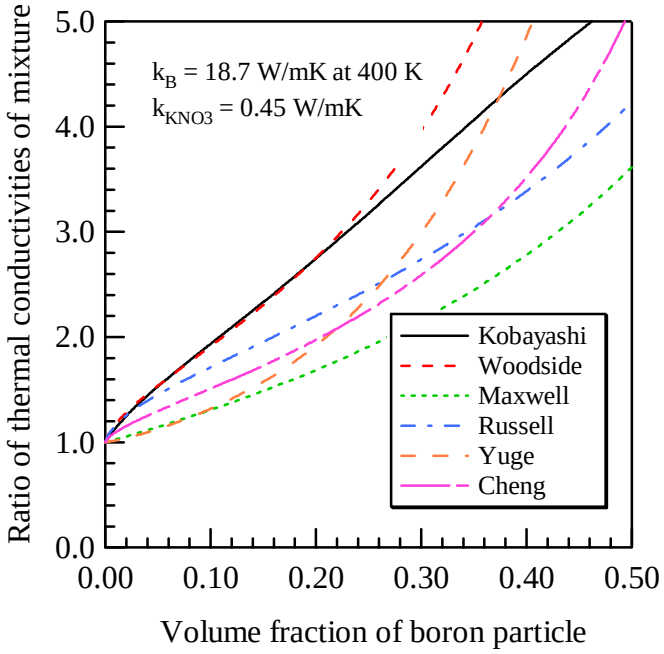

Figure D.2: Thermal conductivity of boron-mixed-KNO_3, dependence on the volume fraction of boron at 400 K.

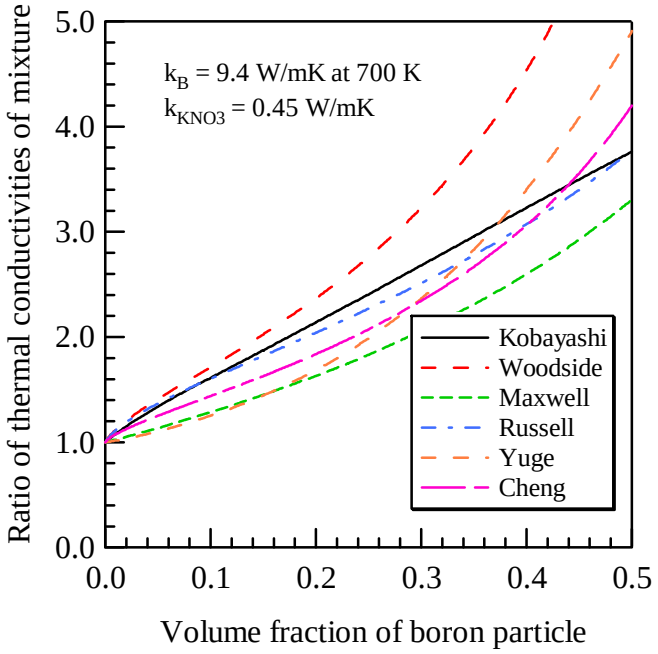

Figure D.3: Thermal conductivity of boron-mixed-KNO_3, dependence on the volume fraction of boron at 700 K.

Appendix E

Rogowski Coil

Principle of a Rogowski coil

A Rogowski coil is essentially multi-turn solenoid deformed into a torus which encircles the current to be measured and the end of the coil winding wire is brought back through the turns of the coil to the initial end. Figure E.1 shows the cenceptual drawing of a Rogowski coil. Putting the torus as a loop C, let us calculate the

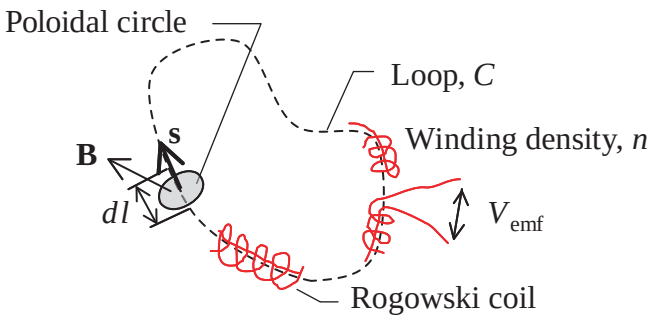

Figure E.1: Conceptual drawing of a Rogowski coil.

linkage flux, namely magnetic flux threading the coil element along a line element dl.

$$d\Phi \;=\; \mathbf{B}\cdot\mathbf{s}ndl \;=\; sn\mathbf{B}\cdot d\mathbf{l} \tag{E.1}$$

where $\mathbf{B}$ is the magnetic field through the poloidal circle (coil element), $\mathbf{s}$ is the normal on the poloidal, n is the number density of coil turns, and $d\mathbf{l}$ is the line element vector. It is assumed that the poloidal circle is so small that the magnetic

field can be assumed to be uniform on the circle and that the poloidal circle is perpendicular to the line element. Magnetic flux threading all of the coil is the sum of $d\Phi$ over the loop C, and

$$\Phi \;=\; \oint_C d\Phi \;=\; sn \oint \mathbf{B} \cdot d\mathbf{l} \;=\; sn\mu_0 I \tag{E.2}$$

where s and n are assumed to be constant over the loop and Ampere's low is applied . I is the current penetlating the loop C, which is the current to be measured. Equation E.2 is the linkage flux by the magnetic field induced by the discharge current. Hence $\mu_0 sn$ is the mutual inductance between the circuit to be measured and the Rogowski coil. Expressing the mutual inductance as M, the electromotive force V_{emf} is

$$V_{\text{emf}} = \frac{d\Phi}{dt} = M\frac{dI}{dt} = \mu_0 sn\frac{dI}{dt} \tag{E.3}$$

After all, output voltage of a Rogowski coil is proportional to the derivative of the threading current, and its proportional constant is the mutual inductance of them.

In the deviation of the above relation, the following are assumed,

- Winding density and poloidal area are constant over the loop.
- Magnetic flux is uniform on the poloidal circle.
- Poloidal circle is perpendicular to the lien element of the loop.

Then it must be cared that the fabricated Rogowski coil satisfies those assumptions. In other words, a Rogowski coil can be arbitrarily deformed and the measured current can pass through any point in the loop so that those assumptions are satisfied. Large poloidal circle increases the sensitivity but decreases the uniformity of magnetic flux on the circle. Current through the center of the loop is likely to give uniform magnetic field on the poloidal because the field has large space gradient near the current.

Integration circuit

It is necessary that a integrating device is interposed between a Rogowski coil and a recording oscilloscope because a Rogowski coil delivers a voltage proportional to

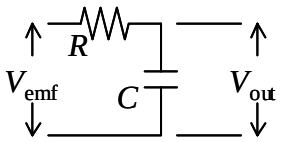

Figure E.2: RC integration circuit.

the derivative of the current. Generally a passive RC integration circuit is used to integrate the output of a Rogowski coil, as shown in Fig.E.2. Output voltage of the integration circuit, $V_{\rm out}$, is related to the input voltage, electromotive force of a Rogowski coil $V_{\rm emf}$ as

$$V_{\rm out} = \frac{1/(iC\omega)}{R+1/(iC\omega)}V_{\rm emf} \tag{E.4}$$

$$V_{\rm emf} = (iRC\omega+1)V_{\rm out} = \left(RC\frac{d}{dt}+1\right)V_{\rm out} \tag{E.5}$$

Integrating it using the relation of the current and electromotive force, Eq. E.3,

$$I = \frac{\mu_0}{sn}\left(RCV_{\rm out}+\int V_{\rm out}\ dt\right) \tag{E.6}$$

In the case that the time constant of the RC integration circuit is much larger than the time scale of the phenomenon, the second term of Eq. E.6 can be neglected, and

$$V_{\rm out} = \mu_0\frac{sn}{RC}I = \frac{M}{RC}I \tag{E.7}$$

Effect of the self inductance of a Rogowski coil

In general, a Rogowski coil is connected to an integration circuit and the electromotive force causes current passing through the Rogowski coil itself. The electromotive current induces magnetic field opposite to the field by measuring current. That field leads to an error, and the effect is considered here.

Electromotive force on a Rogowski coil obeys the actual magnetic field generated in the coil which is the summation of magnetic field by the current to be measured and by the current through the Rogowski coil itself. Hence the actual electromotive force is

$$V_{\rm emf} = \frac{d}{dt}\Phi = \frac{d}{dt}\oint_C(\mathbf{B}-\mathbf{B}_{\rm emf})\cdot d\mathbf{l} \tag{E.8}$$

where $\mathbf{B}_{\rm emf}$ is the magnetic field induced by the current passing through the Rogowski coil, $I_{\rm emf}$. Putting the self inductance of the Rogowski coil as L,

$$\oint_C \mathbf{B}_{\rm emf} \cdot d\mathbf{l} = LI_{\rm emf} = L\frac{V_{\rm emf}}{R} \tag{E.9}$$

where the right hand side is in the case that the Rogowski coil is connected to an resistance R. Combining it to Eq. E.3,

$$V_{\rm emf} = \frac{d}{dt}\Phi = M\frac{dI}{dt} - \frac{L}{R}\frac{d}{dt}V_{\rm emf} \tag{E.10}$$

Solving it about $V_{\rm emf}$,

$$V_{\rm emf} = M\frac{e^{-t/\tau}}{\tau}\int_0^t \frac{dI}{dt}e^{t/\tau}dt, \qquad \text{where } \tau = \frac{L}{R} \tag{E.11}$$

For instance, if the current is a sinusoidal wave $I = I_0\sin(\omega t)$, the electromotive force becomes

$$V_{\rm emf} = M\frac{\omega I_0}{1+(\omega\tau)^2}\left(\cos(\omega t) + \omega\tau\sin(\omega t) - e^{-t/\tau}\right) \tag{E.12}$$

Hence, the effects of the self inductance of a Rogowski coil are decreasing the amplitude (denominator in the r.h.s of Eq. E.12), phase shit (second term in the parentheses), and distortion of the waveform (third term in the parentheses). If $\omega\tau \ll 1$, Eq. E.12 becomes Eq. E.3. Figure E.3 shows the effect of finite inductance of a Rogowski coil. In the case of $\omega\tau = 0.2$, The sinusoidal curve shows the delay of the rising and phase from the $\omega\tau = 0$ case.

As a result, the time constant on a Rogowski coil, $\tau = L/R$, distorts the waveform, and it should be set to be much smaller than the characteristic time of the system. The self inductance of a Rogowski coil is expressed as

$$L = \mu_0 s n^2 l_C \tag{E.13}$$

where l_C is the effective length of the deformed solenoid. Because L is quadratically and M is linearly increased with the inrcease of the winding density, increasing winding density to improve the sensitivity leads to large time constant. Increasing the number of linkages of loop C and the measured current is better a method. If there are multiple linkages between the current to be measured and the Rogowski loop C, the self inductance and mutual inductance are

$$L = \mu_0 s n^2 N_C l_C \quad \text{and} \quad M = \mu_0 s n N_C. \tag{E.14}$$

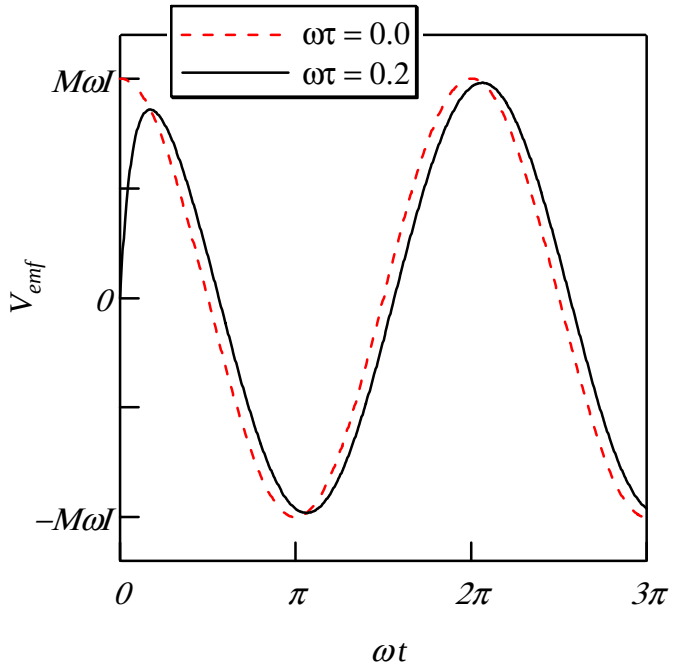

Figure E.3: Effect of the self inductance of a Rogowski coil on the output of the RC integration circuit.

where N_C is number of linkage of loop C. Bothe are linearly incresed with the increase of the linkage number. In the study of PPTs, the secondly fabricated Rogowski coil had two linkages with decreasing the winding density.

Appendix F

Electrical Circuit Diagrams

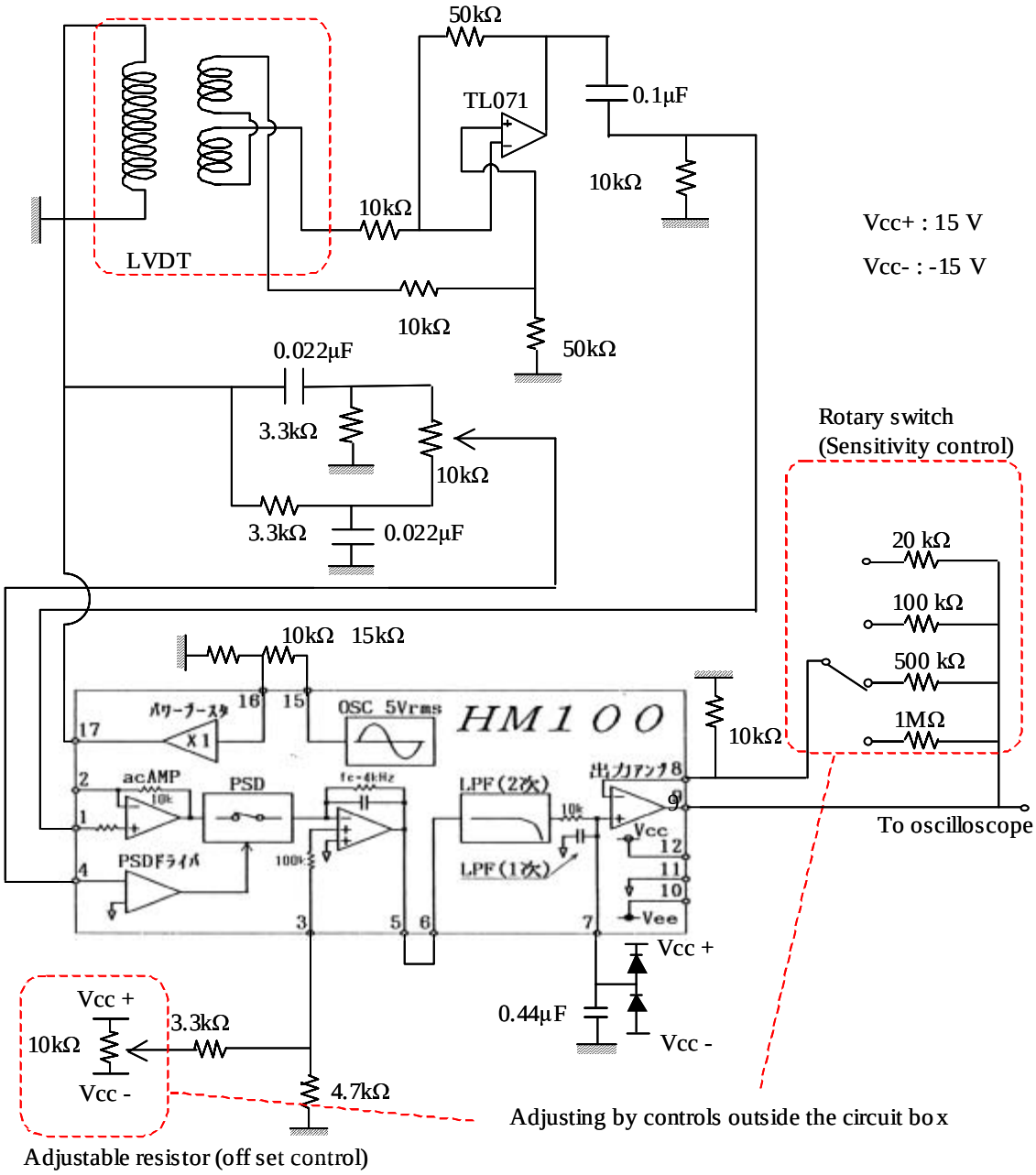

Figure F.1: LVDT signal conditioner.

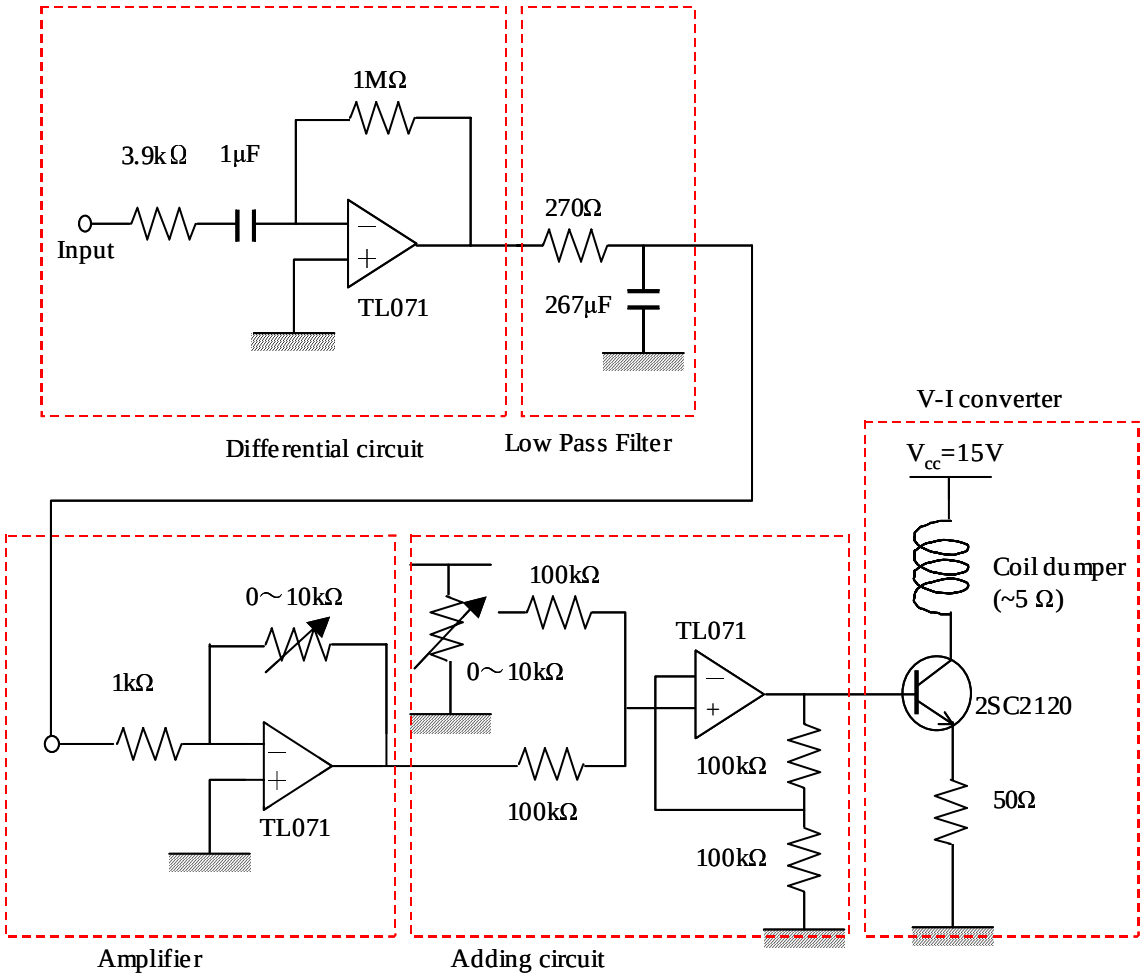

Figure F.2: Electromagnetic damper circuit.

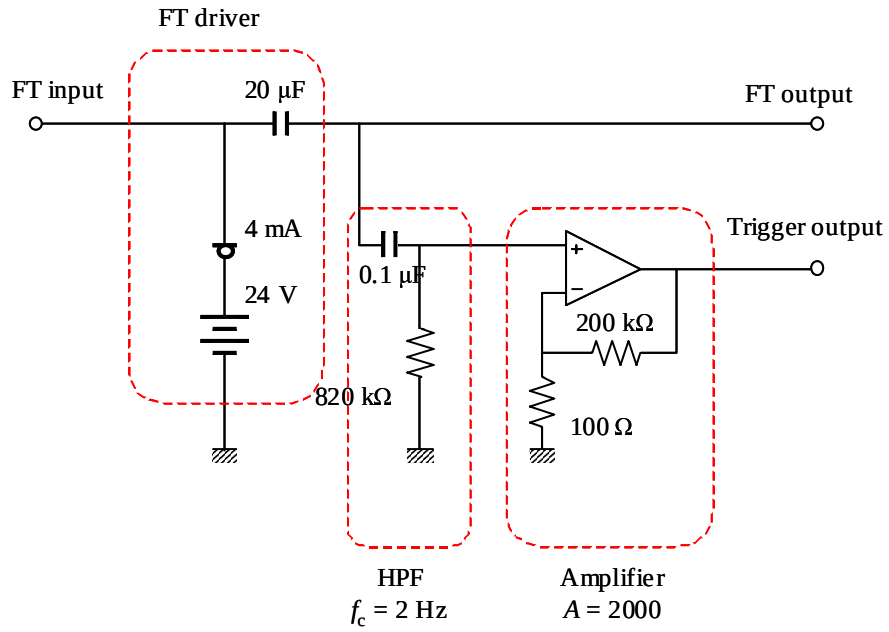

Figure F.3: Power supply of the piezoelectric force transducer.

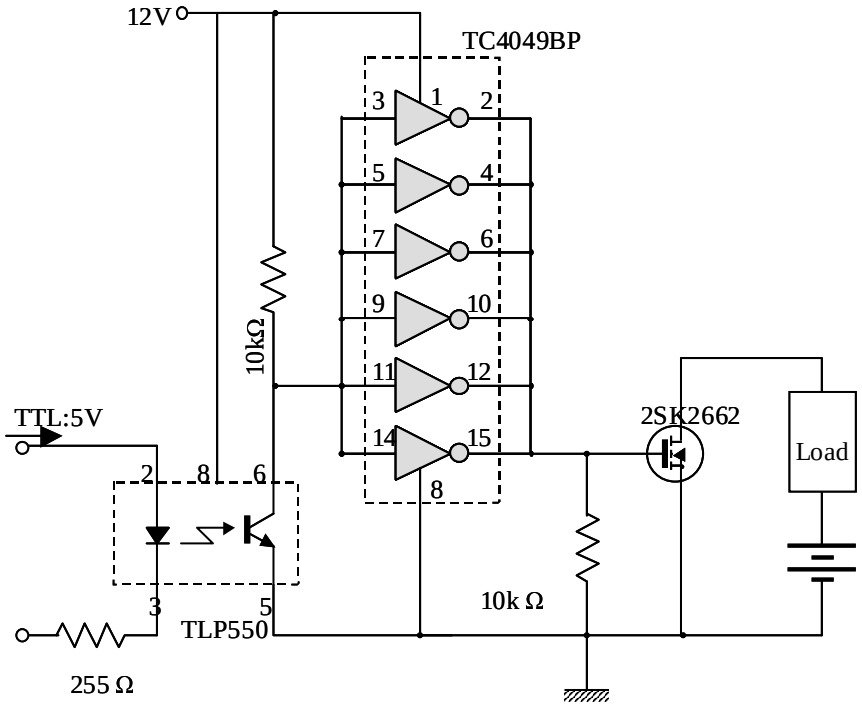

Figure F.4: Driving circuit of the liquid injector.

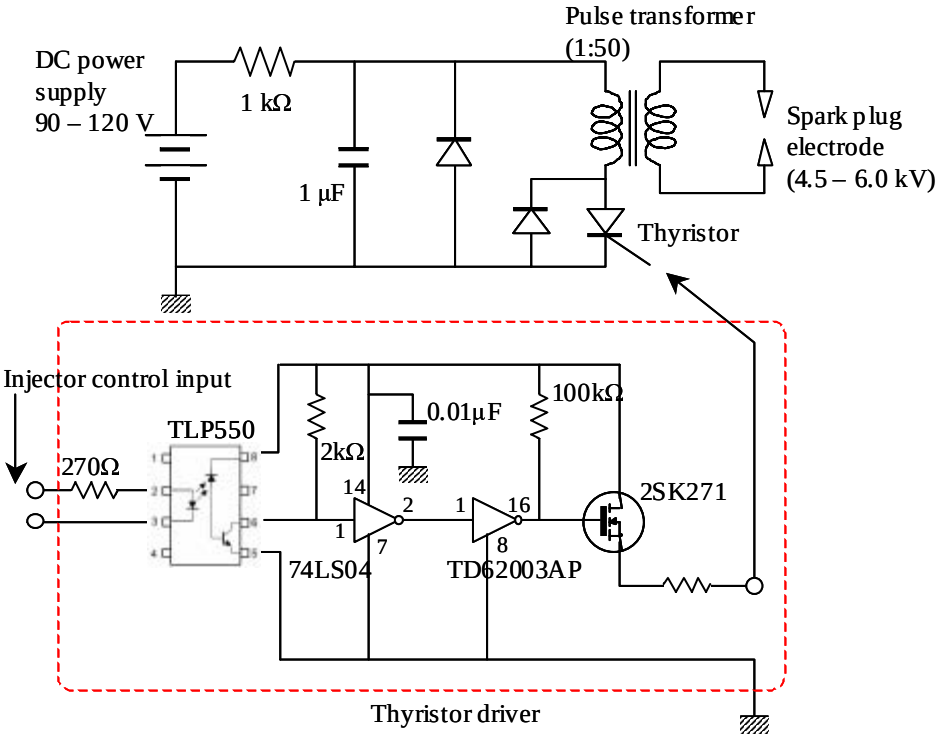

Figure F.5: High voltage pulse generator for the spark plug.

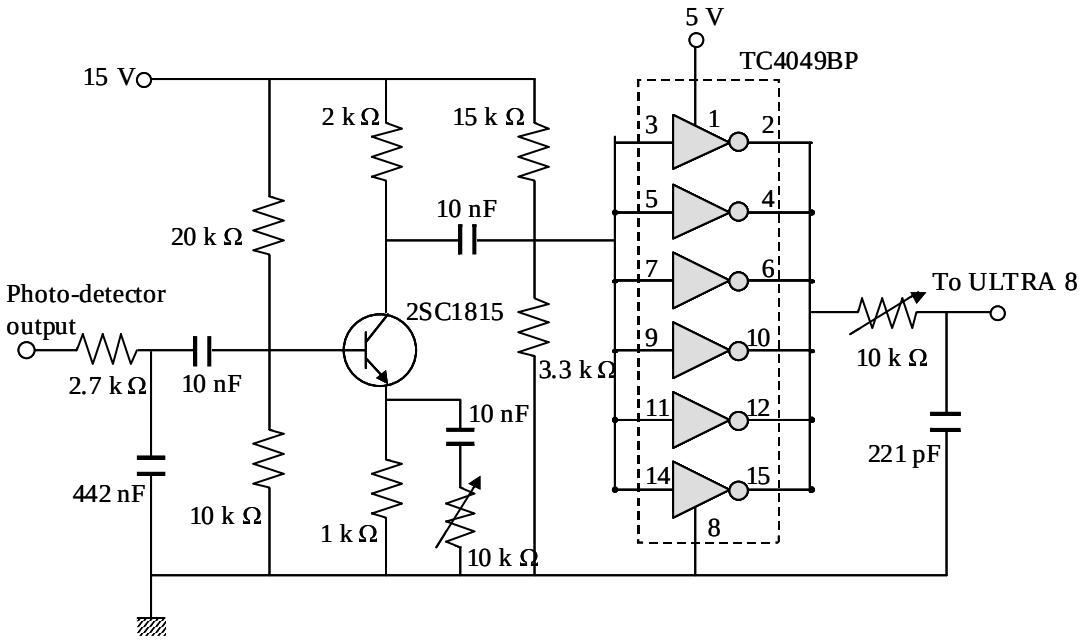

Figure F.6: Photo amplifier to generate TTL signal.

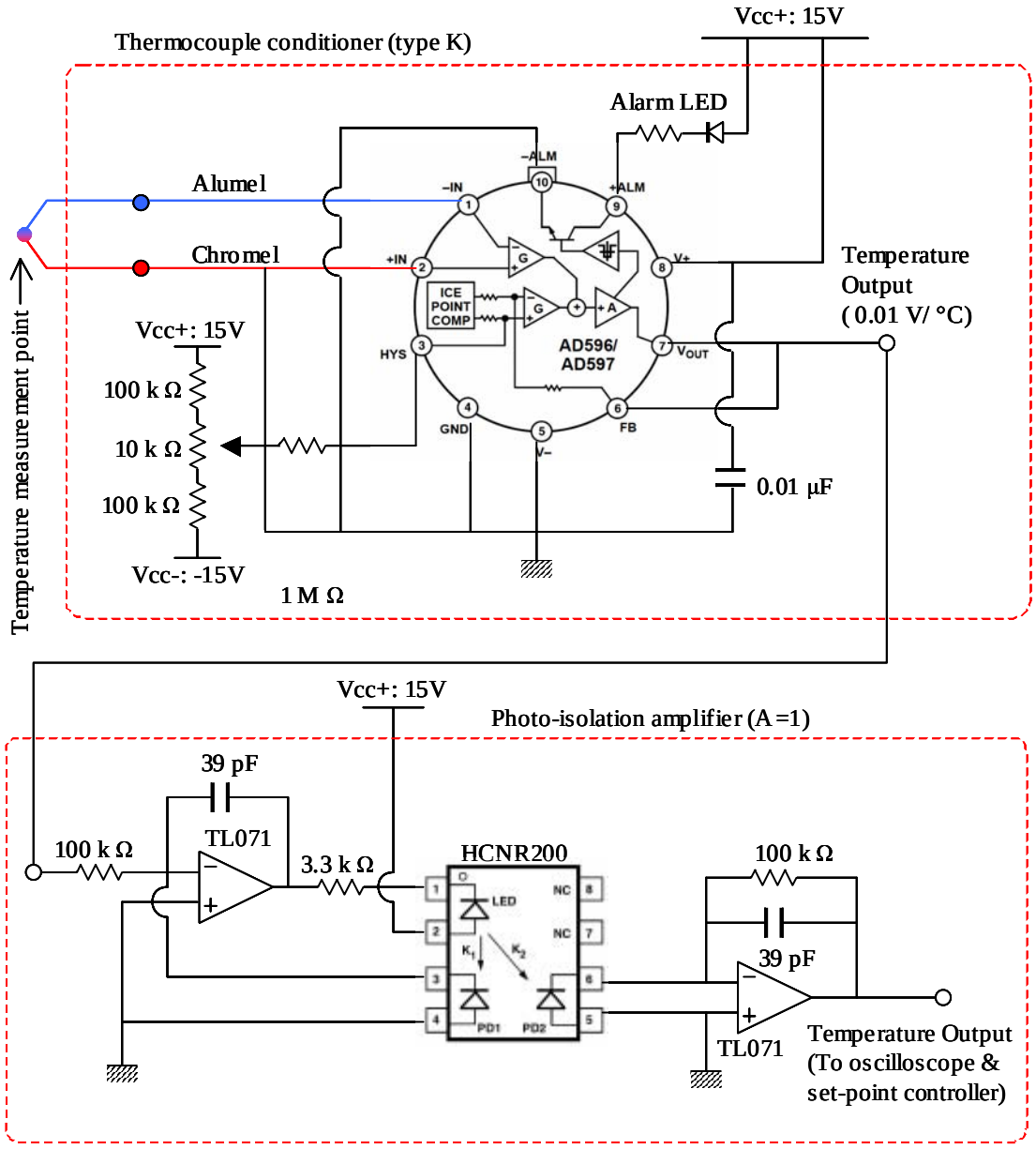

Figure F.7: Thermocouple conditioner.

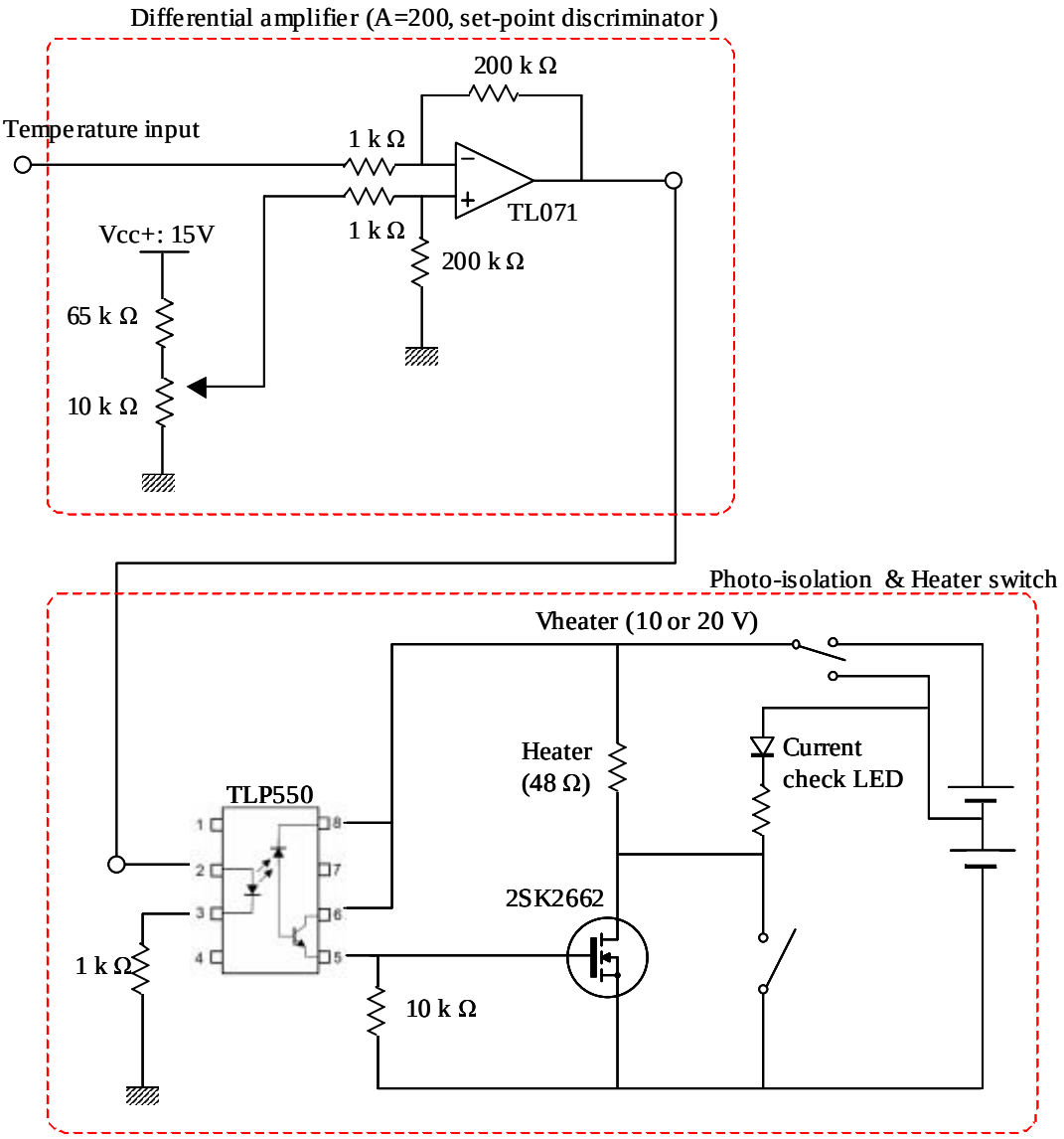

Figure F.8: Temperature set-point controller.